Advanced Controllable Solid-State Raman Lasers

Ran Li

Department of Electronic and Electrical Engineering

Centre for Microsystems & Photonics

A thesis submitted to the Department of Electronic and Electrical Engineering
at the University of Strathclyde for the degree of Doctor of Philosophy

November 2015

Declaration of Authenticity & Author's rights

This thesis is the result of the author's original research. It has been composed by the author and has not been previously submitted for examination which has led to the award of a degree.

The copyright of this thesis belongs to the author under the terms of the United Kingdom Copyright Acts as qualified by University of Strathclyde Regulation 3.50. Due acknowledgement must always be made of the use of any material contained in, or derived from, this thesis.

Signed:

Date:

This thesis is dedicated to the memory of my dear grandfather, Li Heling

Acknowledgements

This thesis could not have been possible without the support, guidance and contribution from all the people who have helped me throughout this unforgettable PhD journey.

First of all, I want to express the sincerest gratitude to my supervisor, Dr Walter Lubeigt who has always been supportive and encouraging, and provided me with invaluable guidance in my research and life over the past four years. His enthusiasm and perfectionism in work set an excellent role model for me. Meanwhile, I would also like to thank him for lots of golden memories we shared together in Scotland, Australia and China...I would never have become who am I today without him.

I would also like to express my thanks and gratitude to Dr Ralf Bauer for his many contributions and generous assistance in the years. His knowledge and experience have been a reliable source of constant feedback to my research projects, job applications and daily life. He is also very kind to have organised some wonderful group activities for friend-gathering and relaxation. Without his contributions and help, my PhD road could have had many more challenges and difficulties.

I am very grateful to Prof Deepak Uttamchandani, and thank for his care, cultivation and support, especially over the last year when I had to deal with a few unfortunate situations. I would also like to thank Mrs Josephine Hamilton for her always kind management of lots of financial transactions and shipments. The whole atmosphere within the Centre for Microsystems and Photonics (CMP) was one of the greatest support throughout my PhD life. Thanks to all the academic staff and researchers, Mick, Gordon (F), Michele, Ian, Bob, David, Gordon (B), Walter (J) and George for readily sharing their knowledge, tips, equipment, tricks and life experience with me. I have learned much from them that I will value for years to come. I'm also very grateful to the group's students: Ania, Barbara, Graham, Cameron, LiLi, Jamie, Kay, Alan,

Abstract

This thesis presents work on developing advanced controllable continuous-wave (CW) solid-state Raman lasers operating at near-infrared and visible wavelengths for astronomy and medical applications. An adaptive-optics (AO) technique, which is commonly applied in astronomy, was for the first time integrated within self-Raman lasers for improving the Raman laser output performances and wavelengths control.

Over the last decade, intracavity solid-state Raman lasers have been widely utilised to extend the spectral coverage of common crystalline laser materials, especially when they are combined with second harmonic generation or sum frequency generation. However, due to the non-elastic nature of stimulated Raman scattering, a significant thermal lensing is generated within the Raman gain medium, which results in parasitic thermo-optical distortions inside the cavity. The magnitude of this effect scales directly with the Raman laser output power and has been identified as the main limitation in power-scaling crystalline Raman lasers. In this thesis, an AO-based feedback control loop system, consisting of an intracavity bimorph deformable mirror, a photodiode sensor and a PC-based control program using a random-search algorithm, has been implemented inside several Raman laser platforms demonstrating its potential for Raman laser output power-scaling. A power improvement of up to ~ 45 % is reported for a $Nd:YVO_4$ self-Raman laser at $\lambda = 1176$ nm using an intracavity AO optimisation. Moreover, a frequency-doubled $Nd:GdVO_4$ self-Raman laser in the yellow waveband ($\lambda = 586.5$ nm) has also been power-scaled using the intracavity AO technique, achieving a total power enhancement of ~ 41 %. These represent the potential to significantly alleviate the detrimental thermal lens effect and open avenues which will enable solid-state Raman lasers to reach new output power levels.

In addition, several CW $Nd:YVO_4$ self-Raman lasers based on the primary and secondary Raman shifts of YVO_4 (893 cm^{-1} and 379 cm^{-1} respectively) were

characterised and reported in this thesis. For the first time an on demand wavelengths selection between laser output at λ = 1109 nm and λ = 1176 nm has been achieved with hundreds of milliwatts output power using an intracavity AO control technique. This represents an important step on the way towards automatic wavelength selectable high power Raman lasers.

Table of Contents

List of Acronyms (In Alphabetic Order)

ADC	Analog to Digital Converter
AO	Adaptive Optics
AR	Anti-Reflective
ASOM	Adaptive Scanning Optical Microscope
$Ba:(NO_3)_2$	Barium Nitrate
$Ba:WO_4$	Barium Tungstate
BBO	Beta Barium Borate
$Ca:(NO_3)_2$	Calcium Nitrate
CCD	Charge-Coupled Device
CH_4	Methane
CW	Continuous-Wave
D_2	Deuterium
DAC	Digital to Analog Converter
DM	Deformable Mirror
DMM	Deformable Membrane Mirror
DRL	Diamond Raman Laser
ESO	European Southern Observatory
FBG	Fibre Bragg Grating
FWHM	Full Width at Half Maximum
H_2	Hydrogen
HR	High-Reflectivity
InGaAs	Indium Gallium Arsenide
KTP	Potassium Titanium Oxide Phosphate
LBO	Lithium Triborate
LC	Liquid Crystal
$LiIO_3$	Lithium Lodate
M^2	Beam quality factor
MEMS	Micro-Electro-Mechanical System
$MgO:LiNbO_3$	Magnesium-doped Lithium Niobate

MMDM	Micro-machined Membrane Deformable Mirrors
N_2	Nitrogen
NA	Numerical Aperture
$Na:NO_3$	Sodium Nitrate
$Nd:GdVO_4$	Neodymium-doped Gadolinium Orthovanadate
Nd:KGW	Neodymium-doped Potassium Gadolinium Tungstate
Nd:KYW	Neodymium-doped Potassium Yttrium Tungstate
$Nd:LuVO_4$	Neodymium-doped Lutetium Orthovanadate
Nd:YAG	Neodymium-doped Yttrium Aluminium Garnet
$Nd:YALO_3$	Neodymium-doped Yttrium Orthoaluminate
Nd:YLF	Neodymium-doped Yttrium Lithium Fluoride
$Nd:YVO_4$	Neodymium-doped Yttrium Orthovanadate
OC	Output Coupler
OCT	Optical Coherence Tomography
$Pb:WO_4$	Lead Tungstate
PRF	Pulse Repetition Frequency
Q	Quality-factor
QCW	Quasi-Continuous-Wave
ROC	Radius of Curvature
SBS	Stimulated Brillouin Scattering
SDL	Semiconductor Disk Lasers
SFG	Sum Frequency Generation
SHG	Second Harmonic Generation
SPS	Stimulated Polariton Scattering
SRS	Stimulated Raman Scattering
$Sr:WO_4$	Strontium Tungstate
SSL	Solid-State Laser
T	Transmission
TEM	Transverse Electromagnetic Mode
TMT	Thirty Meter Telescope

VECSEL	Vertical External-Cavity Surface Emitting Laser
WFM	Wavefront Modulator
WFS	Wavefront Sensor
Yb:KGW	Ytterbium-Doped Potassium Gadolinium Tungstate

Chapter 1

Introduction

Lasers, an acronym for "Light Amplification by Stimulated Emission of Radiation", have completely changed the world since they were firstly demonstrated by Maiman in 1960s [1.1]. Nowadays they have become an integral part of our daily lives used in a wide range of applications, from disc players to eye surgery [1.2], from colorful laser pointers to high-power military weapons [1.3] (see Fig. 1.1) and many more.
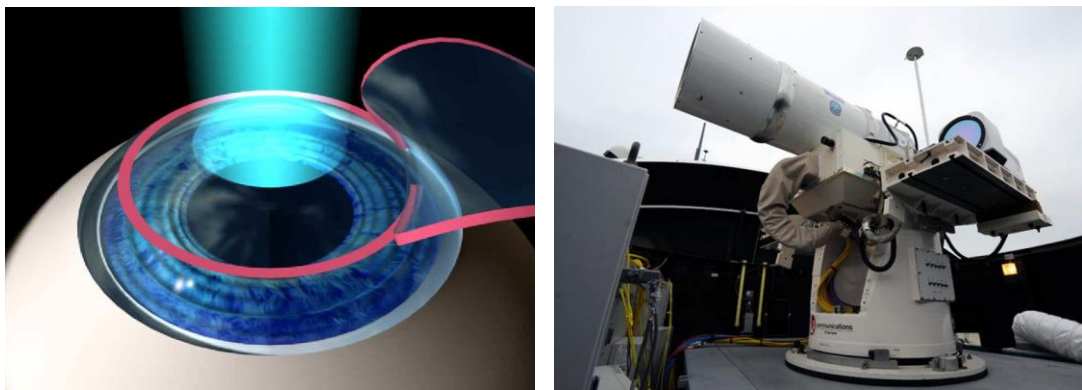
| (a) | (b) |

Fig. 1.1 (a) laser eye surgery; (b) a laser weapon sits on the guided-missile destroyer USS Dewey in San Diego [Pictures taken from http://www.theeyepractice.com.au/optometrist-sydney/behind-laser-eye-surgery-excimer-laser and http://www.nydailynews.com/news/national/navy-deploy-futuristic-laser-weapon-time-year-article-1.1617389]

The sub-category of Solid-State Lasers (SSLs) describe a type of laser source which utilise solid-state gain media such as crystals or glasses doped with rare earth or transition metal ions to generate different laser outputs (although semiconductor lasers are also included in the term of SSLs, they are generally divided into a separate class of laser sources due to their specific lasing

principle) [1.4]. Over the last five decades, SSLs have been widely employed in a variety of practical applications due to their high-quality output performance (i.e. Watt-level output power with a beam quality factor M^2 less than 1.1) and compact optical configurations. However, the output wavelengths generated by SSLs show a certain limitation due to the specific material-dependent energy levels of the laser crystals. Only few crystalline laser gain media (particularly those with transition-metal-doped crystals) achieve a broad wavelength range, with the main example being Titanium-doped sapphire which is widely used for wavelength tuning between approximately 650 to 1100 nm [1.5, 1.6]. Further extension of SSLs spectral coverage still remains an important requirement for a large number of application demands. Next to the development of new crystalline laser active materials, there are also other approaches being developed to access new wavelengths; one way is by achieving additional laser frequency conversions with conventional crystalline materials via nonlinear optical processes such as Stimulated Raman Scattering (SRS), Second Harmonic Generation (SHG) or Sum Frequency Generation (SFG).

This thesis presents the work on intracavity solid-state Raman lasers, which is an efficient and practical approach to access further laser output wavelengths by using SRS. The work was mainly focused on investigating and managing two major issues (i.e. thermal lens effect and spectral effects) that currently strongly restrict the performance of intracavity Raman lasers operating in the Continuous-Wave (CW) regime. An Adaptive Optics (AO)-based feedback control system was implemented into several intracavity Raman laser configurations for two objectives, 1) Raman laser output power-scaling and 2) Raman output wavelengths selection.

This first chapter contains a general introduction of the thesis. At first, the theoretical physical description of Raman scattering is presented in section 1.1. Then different types of Raman laser configurations are described in section 1.2. Section 1.3 discusses the main limitations of all-solid-state intracavity self-Raman lasers which are the focus of this thesis, while a brief introduction of

AO systems will be given in section 1.4. Finally, the thesis outline will be presented at the end of this chapter.

1.1 Theory of Raman scattering

1.1.1 Spontaneous Raman scattering

Raman scattering is an inelastic light scattering process whereby the scattered photons have a different frequency than the incident photons. Spontaneous Raman scattering was discovered by C. V. Raman in liquids [1.7], and independently by Landsberg and Mandelstam in crystals [1.8] in 1928. Since then, Raman spectroscopy techniques have been built and developed as an indispensable approach for observing the information about molecular vibrations, which is widely used to identify or quantify different material samples [1.9].

In general, when photons are scattered from an atom or molecule, the energy of the scattered photons is dominantly equal to the energy of the incident photons, which is called an elastic scattering process. However, in the Raman scattering process incident photons interact with the atoms or molecules and a small fraction of the scattered photons are causing a material excitation which leads to the scattered photons having a different frequency (or wavelength) from the incident photons. These internal excitation modes of the material can be a pure electronic excitation, a spin flip, a lattice vibration or a vibrational or rotational excitation of a molecule [1.10]. As shown in Fig. 1.2 (a), if a scattered photon loses in energy due to the changes in the molecular energy levels of the material it is called "Stokes scattering", whereby a Stokes photon which has a lower frequency (or longer wavelength) than the incident photon and a phonon (i.e. a quantised lattice vibration) will be generated. The angular frequency of a scattered photon (or Stokes photon) ω_S can be written as

$$\omega_S = \omega_L - \omega_R \tag{1-1}$$

where ω_L is the angular frequency of the incident photon and ω_R is the angular frequency of the Raman shift which matches the molecular vibration mode of the Raman active material.
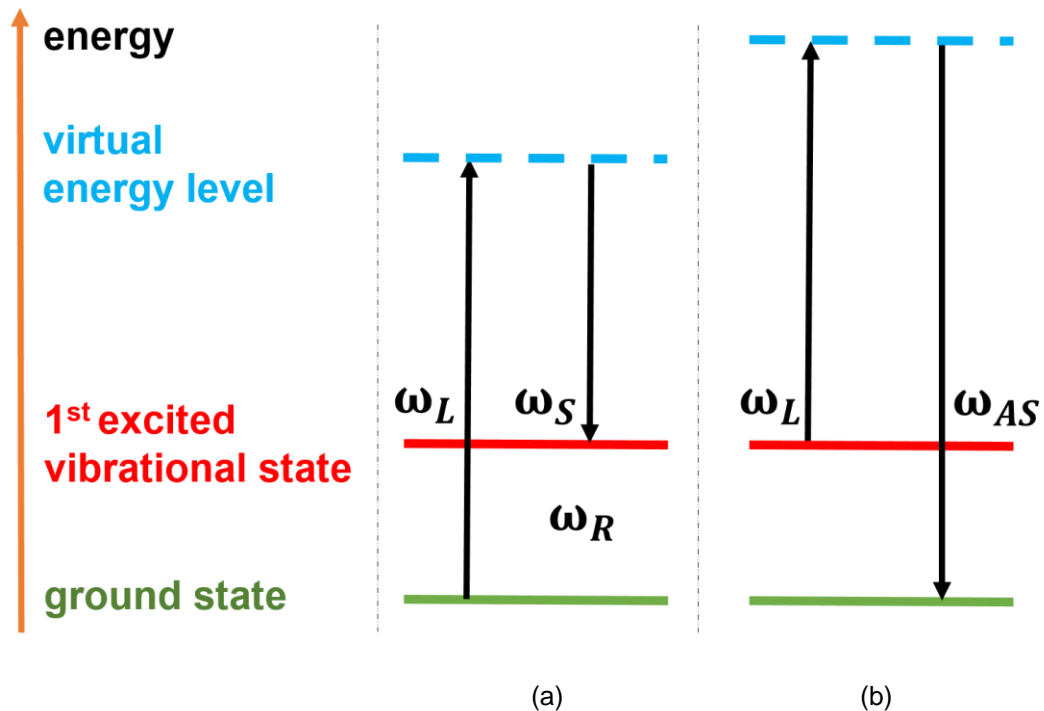
Fig. 1.2 Schematic diagram of spontaneous Raman scattering: (a) Stokes scattering and (b) Anti-Stokes scattering

If a molecule is already in an excited state, then the reverse scattering process can take place as displayed in Fig. 1.2 (b). In this case, the scattered photon additionally obtains the energy difference between the excited and ground state of the molecule and has a higher frequency ω_{AS} (or shorter wavelength), which is called "Anti-Stokes scattering".

$$\omega_{AS} = \omega_L + \omega_R \tag{1-2}$$

It should be noted that the intensity of Anti-Stokes scattering lines are generally much weaker compared with Stokes scattering. That is because the population

of the excited level is much smaller than that of the ground level in the thermal equilibrium, which can be represented by the Boltzmann factor F(state) [1.11]:

$$\mathbf{F(state)} \propto \mathbf{e}^{-\frac{\hbar\omega}{K_B T}} \qquad (1\text{-}3)$$

where h is the Planck constant, K_B is the Boltzmann constant and T the temperature.

Spontaneous Raman scattering is a weak process that typically only 1 part in 10^6 of the incident radiation is involved in within condensed matter [1.12]. However, to efficiently improve the intensity of the Raman scattering process, a high-intensity pump light can be used to generate a significantly higher number of pump and scattered photons, enabling the creation of the SRS process.

1.1.2 Stimulated Raman scattering

When the intensity of the incident pump becomes sufficiently high, the induced polarisation P in the optical medium will be influenced by nonlinear processes which can be summarised as [1.12]:

$$\mathbf{P = \varepsilon_0 \chi_1 * E + \varepsilon_0 \chi_2 * |E|^2 + \varepsilon_0 \chi_3 * |E|^3 + \cdots} \qquad (1\text{-}4)$$

where ε_0 is the dielectric constant, E is the intensity of the electric field, χ_1 is the linear optical susceptibility, and χ_2, χ_3, etc. represent the different orders of nonlinear optical susceptibility of the medium. The second-order nonlinear polarisability (i.e. $P_2 = \varepsilon_0\ \chi_2\ |E|^2$) gives rise to the nonlinear optical processes of SHG, SFG, difference frequency generation and optical parametric oscillation, while the SRS process arises from the third-order nonlinear optical polarisability (i.e. $P_3 = \varepsilon_0\ \chi_3\ |E|^3$).

SRS originates and is building up from spontaneous Raman scattering noise combined with a high-intensity pump light or an initial Stokes beam. The basic

theory of SRS has been presented and developed in several publications [1.12-1.15] and was also well reviewed by Basiev [1.16] and Pask [1.10].

Typically, SRS operation can be divided into two temporal regimes due to the response time of the Raman medium to the incident light field. If the duration of the pump pulse τ_P is much longer than the dephasing time of the vibrational excitation T_R, then the Raman laser is operated in a steady-state regime. On the other hand, if the pump pulse duration becomes comparable to or even shorter than the dephasing time of the vibrational excitation (typically in the pico-second range), then the Raman laser is operating in the transient regime. For most of the crystalline Raman materials, the dephasing time is in the order of ~ 10 ps, which means the steady-state Raman laser regime can be normally achieved when the pump pulse duration is longer than ~ 1 ns [1.14]. Since all work in this thesis deals entirely with all-solid-state Raman lasers operated in the CW regime, the relevant theory of the SRS steady-state regime will now be reviewed in more details, while the detailed theory of SRS in the transient regime can be found in Refs [1.14, 1.15, 1.17].

In the steady-state regime the Raman gain coefficient g_R can be expressed as:

$$g_R = N * \frac{4\pi^2 \omega_S}{\mu_P \mu_S c^2 m \omega_R (\frac{\Delta \omega_R}{2})} * (\frac{\partial \alpha}{\partial q})^2 \qquad (1\text{-}5)$$

where N is the number density of Raman-active molecules (in a solid-state medium that can be quantised as the number of phonons), μ_P and μ_S are the refractive indices of the Raman medium at the pump and Stokes wavelength respectively, c is the speed of light, m is the reduced mass for the oscillating molecule, $\Delta \omega_R$ is the full width at half maximum of the Raman peak which is related to the dephasing time of the vibrational excitation T_R (i.e. $\Delta \omega_R / 2 = 1 / T_R$). $\partial \alpha / \partial q$ is the normal-mode derivative of the molecule polarisability tensor.

With the integrated Raman scattering cross-section $\partial \sigma / \partial \Omega$ defined as:

$$\frac{\partial \sigma}{\partial \Omega} = \frac{\omega_S{}^4 \mu_S}{\mu_P c^4} * \frac{h}{2m\omega_R} * \left(\frac{\partial \alpha}{\partial q}\right)^2 \tag{1-6}$$

we can take equations (1-6) and (1-5), and re-write the Raman gain coefficient g_R as:

$$g_R = N * \frac{8\pi^2 c^2}{h\mu_S{}^2 \omega_S{}^3 \left(\frac{\Delta\omega_R}{2}\right)} * \left(\frac{\partial \alpha}{\partial \Omega}\right) \tag{1-7}$$

Equation (1-7) points out that three main factors can be beneficial to achieve a higher steady-state Raman gain coefficient, which are a shorter Stokes wavelength due to larger values of ω_R, a narrower Raman linewidth corresponding to the term of $\Delta\omega_R / 2$ and a larger Raman scattering cross-section. It should be also noted that the Raman scattering cross-section can be strongly dependent on the orientation of the Raman medium with respect to the polarisation of the incident pump beam. The highest Raman scattering cross-section is in practice normally obtained when the Stokes line is polarised parallel to the pump polarisation.

The intensity of the generated Stokes light $I_s(z)$ along the incident light direction z can be expressed as:

$$I_s(z) = I_s(0) * e^{(g_R I_P z)} \tag{1-8}$$

where z is the interaction length of the Raman gain medium, I_P is the intensity of pump light, and $I_S(0)$ is the initial spontaneous Stokes noise scattered into a solid angle $\Delta\Omega$. In the absence of any initial Stokes signal or "seed" injection, it can be written as:

$$I_s(0) = \frac{h\omega_S{}^3 \mu_S{}^3}{(2\pi)^3 C^2} * \Delta\Omega \tag{1-9}$$

It should be noted that the intensity of a SRS cascading effect can be generated when the intensity of a low-order Stokes output ω_{S1} reaches the

SRS threshold for a higher-order Stokes conversion, thereby producing high-order Stokes light at ω_{S2} (see equation 1-10).

$$\omega_{S2} = \omega_{S1} - \omega_R \qquad (1\text{-}10)$$

In practice, multiple-Stokes lines can be observed in Raman lasers, especially in the case of short pulse pumped Raman lasers with high pulse energy or intracavity CW Raman lasers constructed by a high-quality-factor (Q) cavity for the low-order Stokes wavelengths but relative high coupling losses for the adjacent high-order Stokes wavelengths [1.18].

1.2 Raman laser configurations

Since the first discovery of SRS in a ruby laser cavity by Woodbury and Ng in 1962 [1.19], SRS became an efficient and widely used approach to expand the spectral coverage of crystalline lasers. A variety of solid-state Raman laser designs have been developed since then, including single or double-pass Raman generation, the use of an extracavity Raman resonator and the use of an intracavity Raman resonator.

1.2.1 Raman generator

As shown in Fig. 1.3, the Raman generator configuration is the simplest design for generating a Raman laser output. The pump light is directly focused into the Raman active crystal to produce spontaneously scattered Stokes light which is amplified (but does not oscillate in a resonator) as it makes a single pass through the Raman active crystal. Due to the high intensity pump requirement ($\sim$ 100 MW cm^{-2}), typically, the pump source for Raman generator is a pulsed laser operating in the picosecond or nanosecond range [1.10, 1.18]. The pump to Raman conversion efficiency can be improved by a double-pass configuration, where a reflecting mirror is placed behind the output face of the

crystal at a slight angle to recycle the output radiation. For instance, Cerny and Jelinkova reported a Ba:WO$_4$ Raman generator pumped by a frequency-doubled, pulsed Nd:YAG laser in 2002 [1.20]. A first Stokes conversion efficiency of 38 % was obtained in a single pass configuration while a near-quantum-limit efficiency of 85 % was achieved using a double-pass configuration.
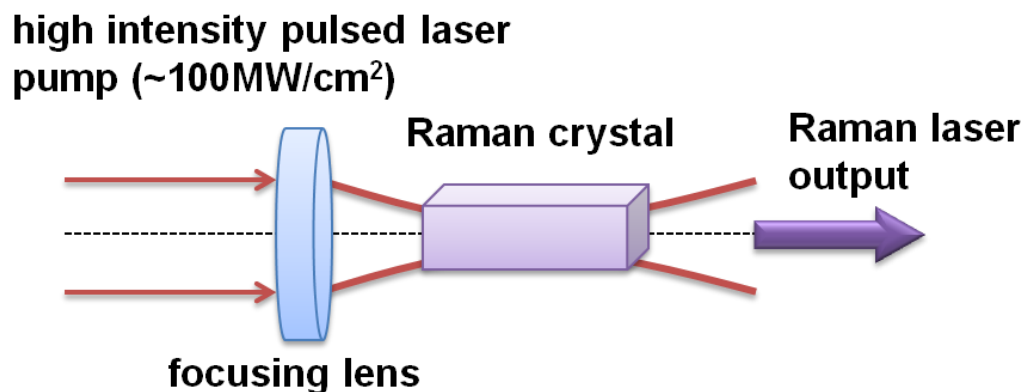
Fig. 1.3 Raman generator configuration

Although high conversion efficiency can be realised using a Raman generator, two major drawbacks restrict its applications. First, high pump intensity is required to achieve SRS. More importantly though the cascading nature of SRS means that higher Stokes outputs are also generated simultaneously in an uncontrolled manner.

1.2.2 Extracavity Raman laser configuration

In an extracavity laser configuration, an optical cavity is constructed around the Raman crystal to resonate the Raman Stokes field. As shown in Fig. 1.4, typically the end mirror has a high reflectivity (HR) at the desired Stokes wavelength, while the transmission of the output coupler is selected to optimise the Raman laser output.
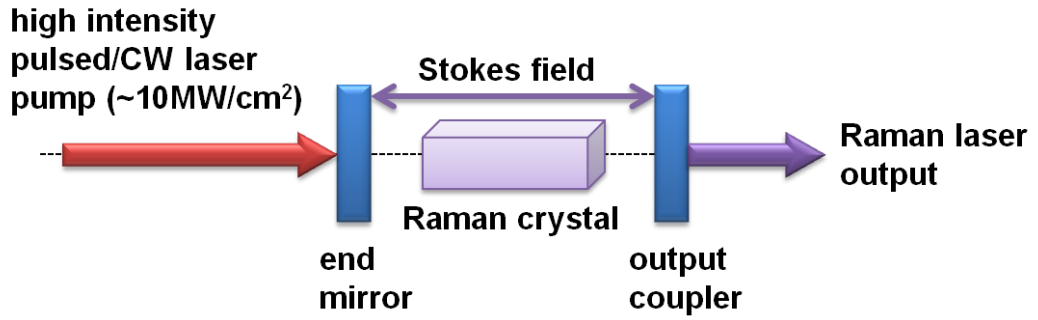
Fig. 1.4 Extracavity Raman laser configuration

Assuming the cavity losses are dominated by the transmission of the end mirror and output coupler, the SRS threshold condition can be expressed as:

$$R_1 R_2 \exp(2 g_R I_L l_R) \geq 1 \qquad (1\text{-}11)$$

where, R_1, R_2 presented the reflectivities of the end mirror and output coupler at the Stokes wavelength respectively, I_L is the intensity of the laser pump and l_R is the length of the Raman active crystal.

Ideally, an additional HR coating at the pump wavelength is required for the output coupler to allow a further pass of the pump signal through the gain medium, increasing the Stokes conversion efficiency. In general either a CW or pulsed laser with high power intensity ($\sim$ 1 - 10 MW cm^{-2}) can be utilised as the pump source.

This type of configuration has three main advantages compared to the Raman generator configuration. First, due to the significant enhancement of the intracavity Stokes field intensity, the SRS threshold can be achieved with reduced pump intensities. Second, higher Stokes orders can be obtained by appropriate selection of the cavity mirror coatings. And third, adjusting the curvatures of the cavity mirrors and the cavity length can lead to improved Raman output beam quality, resulting from an arrangement where the pump and Stokes modes are matched in their spatial distribution.

The performance of extracavity Raman lasers has been described in several articles such as by Pask in 2003 [1.10], Cerny in 2004 [1.16] and Piper in 2007 [1.18]. Theoretical modelling of the performance of CW external cavity Raman lasers is also provided in [1.21]. In 2014, a 108 W first Stokes Raman laser output at $\lambda = 1240$ nm operating in the quasi-CW (QCW) regime with on-time durations of 200 µs was reported in an extracavity diamond Raman laser (DRL) by Williams et al. [1.22]. This is the highest output power for any crystalline Raman laser reported so far, and is an order of magnitude above all previous results in the QCW range. The highest truly-CW crystalline Raman laser was also demonstrated in an extracavity DRL by Kitzler et al. in 2013 [1.23]. A maximum first Stokes ($\lambda = 1240$ nm) CW Raman output of 15 W was demonstrated using a 42 W single frequency fibre laser ($\lambda = 1064$ nm) as fundamental beam. This corresponded to a fundamental to first Stokes conversion efficiency of 35.7 %. Recently, another notable extracavity Raman laser work was reported by Reilly et al. in 2015 [1.24] who demonstrated a monolithic DRL with a pump to Raman conversion efficiency of 84%. Up to 136 mW of yellow Raman laser power emitting at $\lambda = 573$ nm was achieved with a 1.5 ns pulsed laser pump ($\lambda = 532$ nm). The Raman laser resonator consisted of a HR-coated, 2 mm-long, synthetic diamond with a 13 mm Radius of curvature (ROC) micro-lens structure etched onto its end face to improve the cavity stability during SRS oscillation.

1.2.3 Intracavity Raman laser configuration
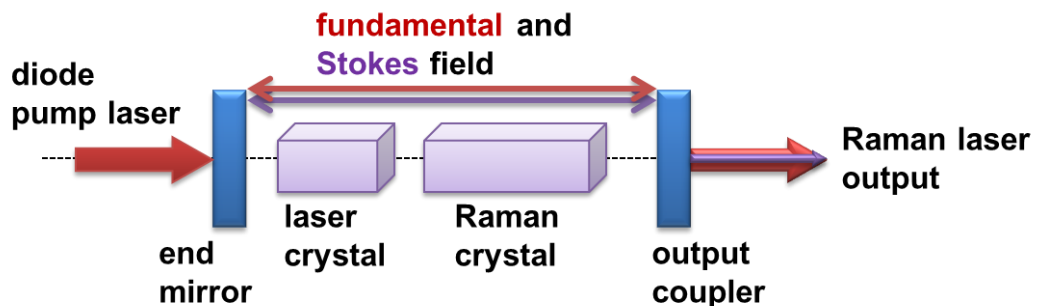
(a)
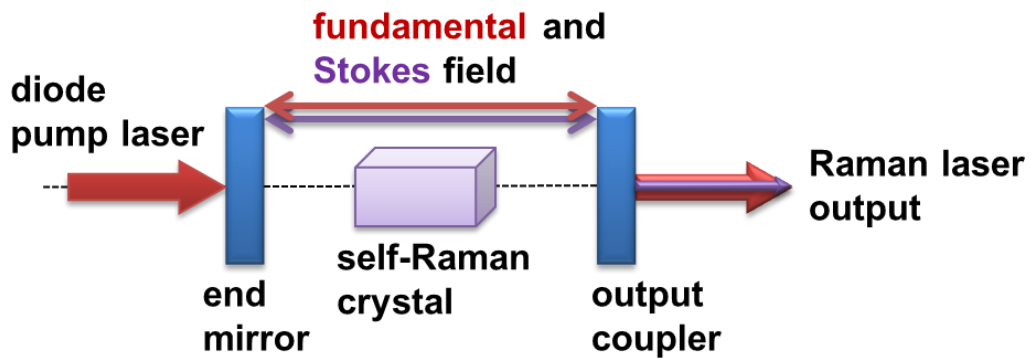
(b)

Fig. 1.5 (a) Intracavity Raman laser configuration; (b) self-Raman laser configuration

In an intracavity Raman laser configuration, both the laser and Raman active crystals are placed in the same resonator (see Fig. 1.5). This configuration makes use of the high intracavity fundamental laser field intensity inside the basic laser cavity to reach the SRS Raman threshold with minimal diode pump power. Therefore, SRS thresholds can be obtained with diode pump powers as low as 2 W [1.18]. However, the efficiency of this type of Raman lasers is strongly dependent on intracavity optical losses. The use of separate active crystals within the Raman laser cavity will introduce additional losses. Moreover, the management of different spatial laser modes needing to be matched in each crystal is also another challenge for the Raman laser output optimisation. However, these problems can be avoided in a self-Raman laser which is a particular case of intracavity laser configurations (see Fig. 1.5 (b)). Since the laser crystal is also the Raman gain medium in a self-Raman laser, it can provide a simpler and more compact design with reduced optical losses.

Due to the different laser output modes, intracavity Raman lasers can be divided into two regimes, pulsed and CW. Before 2004, all solid-state Raman laser work was focused on the pulsed regime since high peak powers available from pulsed lasers were required to reach the SRS threshold. However, over the last decade the rapid development of ion-beam sputtered coating technologies [1.25] allowed the creation of laser cavities with high-Q for the fundamental laser field. These provide ideal platforms for intracavity CW

Raman lasers. The work in this thesis deals entirely with CW intracavity Raman lasers and a performance review of this type of lasers will be presented in chapter 2.

1.3 Challenges in designing CW intracavity Raman lasers

1.3.1 Theoretical description

Understanding the physics of Raman lasers is vital for laser configuration design and setup. However, the behaviour of CW intracavity Raman lasers is complex due to a significant thermal lens effect, spectral effects and the strong coupling between the fundamental and Stokes fields. Therefore it is difficult to precisely match the experimental results with a comprehensive model.

In 2007, Spence et al. developed a simplified model describing the trends underlying the behaviour of CW intracavity Raman lasers [1.26]. This model takes into account the interplay relationships between the Raman conversion efficiency and crucial parameters such as the Raman gain coefficient, optical cavity losses and the mode size of the fundamental field. This work significantly simplified the design of CW intracavity Raman lasers.

A laser configuration containing a laser crystal pumped by a CW laser diode and a Raman crystal is the basis of the model (see Fig. 1.6). All intracavity laser modes are assumed to be perfectly matched with each other with top-hat transverse profiles. They can have different spot radii in each active crystal, but each spot radius is assumed to remain constant during the laser process.
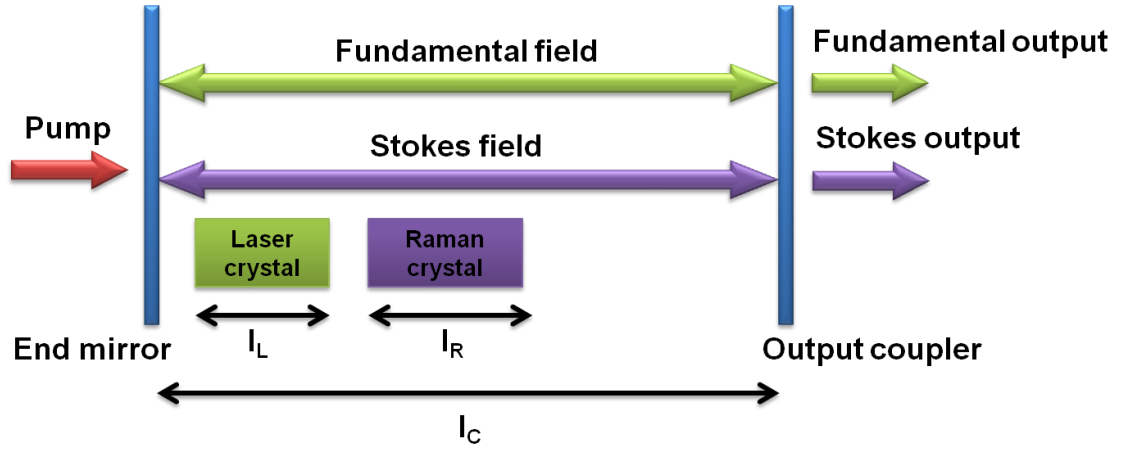
Fig. 1.6 Schematic diagram of a CW intracavity Raman laser configuration (image extracted from [1.26])

These assumptions result in three rate equations for the fundamental field, Stokes field and population inversion which are given in equation (1-12) to (1-15) respectively:

$$\frac{dP_F}{d_t} = \frac{c\sigma_G N^* P_F l_L}{l} - \frac{2cP_F P_S g_R l_R}{l A_R \lambda_F/\lambda_S} - \frac{cP_F(T_F+L_F)}{2l} \qquad (1\text{-}12)$$

$$\frac{dP_S}{d_t} = \frac{2cP_F P_S g_R l_R}{l A_R} - \frac{cP_S(T_S+L_S)}{2l} \qquad (1\text{-}13)$$

$$\frac{dN^*}{d_t} = \frac{P_P \lambda_P}{hcA_L l_L} - \frac{2\lambda_F \sigma_G N^* P_F}{hcA_L} - \frac{N^*}{\Gamma_T} \qquad (1\text{-}14)$$

$$l = [l_C + l_L(n_L - 1) + l_R(n_R - 1)] \qquad (1\text{-}15)$$

where P_S, P_F, P_P are the intracavity powers of the Stokes, fundamental and diode pump fields respectively, l_R, l_L, are the Raman and fundamental crystal lengths, and l is the overall optical cavity length. T_F and T_S are the transmission of the output couplers for the fundamental and Stokes field respectively. L_F and L_T are the optical losses during a cavity round-trip for the fundamental and Stokes field respectively. N^* and σ_G are the population inversion density and the emission cross-section of the fundamental laser gain medium, g_R is the stimulated Raman gain coefficient of the Raman gain medium and Γ_T is the

lifetime of the upper state level. λ_S, λ_F are the wavelengths of the Stokes and fundamental fields respectively. A_R, A_L are the Stokes, and fundamental field spot areas.

Two analytic model expressions of the Stokes Raman threshold P_{th} and Raman laser output power P_S can be derived from the equations above by neglecting the upper level life time Γ_T:

$$P_{th} = \frac{A_R}{g_R l_R} \frac{\lambda_F}{\lambda_P} \frac{(T_S+L_S)(T_F+L_F)}{4} \qquad (1\text{-}16)$$

$$P_S = P_P * \frac{T_S}{(T_S+L_S)} \frac{\lambda_P}{\lambda_S} - \frac{T_S(T_F+L_F)}{4} \frac{\lambda_F}{\lambda_S} \frac{A_R}{g_R l_R} \qquad (1\text{-}17)$$

Several points of crystalline Raman laser resonator design are indicated by these two equations. At first, it can be seen from equation (1-16) that, the optical cavity losses for both fundamental and Stokes fields (corresponding to the parametres of T_S, L_S, T_F and L_F) can significantly impact the threshold of SRS. Since these losses are commonly caused by the misalignment of resonator elements or some undesired transmission or absorption from either the cavity mirrors or the laser and Raman active crystals, the use of self-Raman materials is highly advantageous. Moreover, a smaller mode size of the fundamental radiation ($\sim A_R$), a larger Raman gain coefficient ($\sim g_R$), a longer length of the active crystal ($\sim l_R$) and a smaller ratio between the diode pump and fundamental laser photon energies ($\sim \lambda_F / \lambda_P$) could be also beneficial to reduce the Raman pump threshold. It should be also noted that, although a long Raman crystal enables to provide a low SRS threshold due to its high Raman gain, it could also involve some extra optical losses. Moreover, it is always difficult to keep the required small focus over a long crystal distance. In general, 5 to 20 mm long Raman crystals are most commonly used in CW intracavity solid-state Raman lasers.

In equation (1-17), the first term expresses that the Raman output power is set by the output coupling of Stokes photons and the quantum defect between the

diode pump and Stokes wavelengths. The second term is determined by the resonator losses, ratio between the diode pump and Stokes laser photon energies and the Raman coupling parameter which can be expressed as $K_R = P_P \frac{g_R l_R}{A_R}$.

In conclusion, the important factors for CW crystalline intracavity Raman laser configuration design can be summarised into four main influencing aspects: low optical cavity losses, small mode size of the fundamental field, high Raman gain and low quantum defect between the diode pump and Stokes wavelengths. However, it should be noted that a higher intracavity power intensity, especially in self-Raman laser materials, can produce a significant thermal lensing which enables to constrain the SRS conversion efficiency or/and lead to some optical damage on the anti-reflective (AR) coatings of the crystal surfaces.

Typically, three main issues that strongly restrict the performance of crystalline Raman lasers operating in the CW regime are: 1) optical cavity losses, 2) spectral effects and 3) thermal lens effects.

1.3.2 Optical losses

Reducing optical cavity losses for the fundamental and Stokes fields is crucial for both obtaining a low Raman threshold and a high conversion efficiency as seen in equation (1-16) and (1-17). The cavity mirrors are in general all coated to be HR for the fundamental wavelength (i.e. R > 99.99 %) while the transmission of the output coupler is commonly less than 1 % at the Stokes output wavelength. Two methods are commonly used to minimise the reflective losses on the crystal surfaces: one is using a right-angle cut crystal with high quality AR coatings on the end-facets of the crystal, and another is employing a Brewster-angle cut crystal.
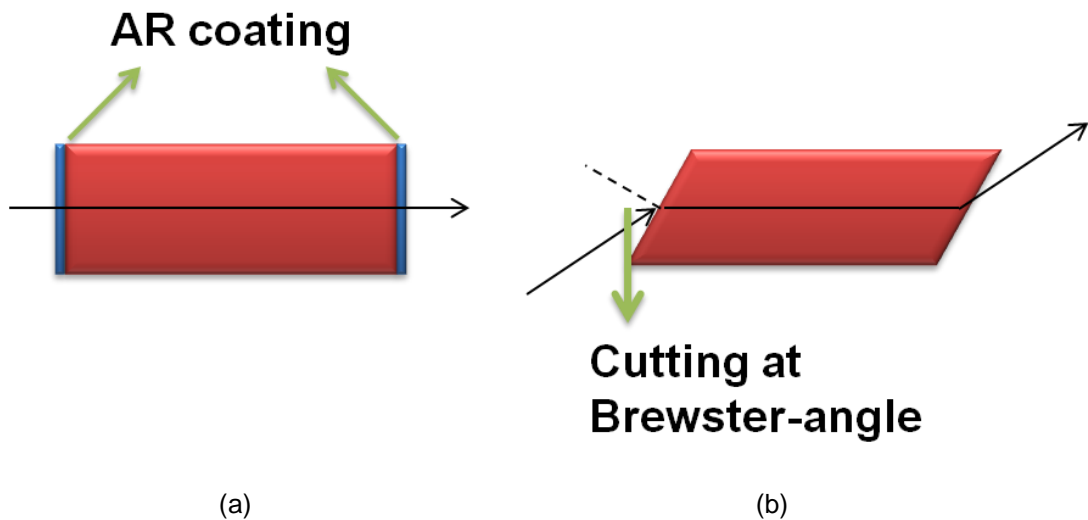
Fig. 1.7 Two different types of cut for Raman laser crystals, a) Right-angle cut with HR coating; and b) Brewster-angle cut

For the right-angle cut crystal, the polished ends are perpendicular to the axis of light propagation (see Fig. 1.7 (a)) which permits a simpler alignment for laser cavities. To minimise the reflective losses on the crystal surfaces, high quality AR coatings (i.e. R < 0.1 %) are required for both sides of the crystal. However, the laser power density, especially in an intracavity laser configuration, is then mainly restricted by the damage threshold of the AR coatings (~ 100 MW cm^{-2}). For the second cut option, the polished end facets of the laser crystal are cut at a Brewster angle between the normal axis of the polished face and the axis of light incidence (see Fig. 1.7 (b)). In this way, the reflective losses on the crystal surfaces are ideally zero for an incoming laser beam with a particular linear polarisation. Therefore, higher laser power densities can be utilised with a Brewster-angle cut crystal since there is no coating damage limitation. The main drawback however is the specific incidence angle of incoming light which can lead to some astigmatism on the beam mode profiles inside the laser active crystal, which will increase the Raman threshold and degrade the laser conversion efficiency. It should be also noted that in a Raman laser cavity at least two different Brewster angles are presented due to the refractive index variation with the wavelength change between the fundamental and Stokes radiation. This leads in practice to the choice of a "compromise angle" to minimise losses for both the fundamental

and Stokes field. Keeping this in mind, the Brewster angle configuration will also be more affected by a depolarisation of the fundamental or Stokes field.

As the scattering cross-section of a Raman gain medium strongly depends on the polarisation of the pump light (or the fundamental light for intracavity laser configurations) it is crucially important to manage the relationship between the orientation of the Raman active crystal and the polarisation of the pump or fundamental laser field. For most intracavity Raman laser configurations, the strongest Stokes scattering (corresponding to the highest Raman gain coefficient) can be achieved for the Stokes polarisation being parallel to the pump polarisation [1.18]. Moreover, it is also critical to minimise any thermal-induced birefringence effects. For this reason it is common to use some low-birefringent crystals (i.e. synthetic diamond) or intrinsic birefringent crystals (i.e. vanadate or tungstate crystals) for attaining a linearly polarised output without depolarisation loss.

Compared with the separate laser and Raman gain media configuration, self-Raman active crystals exhibit a significant advantage in reducing the optical losses corresponding to a simpler laser cavity design. Moreover, the bulk crystal losses can also significantly affect the Raman laser output performance as reported by Li et al. in [1.27]. Therefore, the length of the active crystal, which controls the Raman gain, and also the bulk losses must be carefully chosen. The bulk crystal losses can be reduced by some novel artificial Raman active materials such as low-loss, low birefringent synthetic diamonds which have been used in Lubeigt et al.'s [1.28, 1.29] and Parrotta et al.'s work [1.30, 1.31].

1.3.3 Spectral effects

The interaction between the different intracavity fields in the same resonator will also lead to spectral effects which will influence the Raman conversion

efficiency of the desired Stokes output. These effects can be divided into two types: generation of unwanted spectral lines and spectral broadening effect.

Firstly, as discussed previously, minimising the optical cavity losses is critical to improve the Raman laser output conversion efficiency. In this way, high quality HR coatings (i.e. R > 99.99 %) are necessary to be used for all cavity mirrors at the fundamental wavelength. However, the resulting increased intracavity power intensity can lead to some undesired SRS processes producing secondary Raman emission lines. These lines will therefore compete with the desired intracavity Stokes output and significantly reduce the Raman conversion efficiency. For instance, cascaded Stokes Raman outputs will appear as an extra optical loss for the first Stokes Raman field. Also, the first Stokes Raman output based on the secondary Raman transition may be generated in parallel to the desired Raman output. Optimising the output coupling for each intracavity field is therefore vital to minimise the detrimental effects from undesired wavelengths. Experimental results and discussions regarding this topic will be highlighted in chapter 4. A similar problem can also be observed when SRS is used in conjunction with SHG or SFG techniques. For example, in [1.32] Lee et al. reported a selectable visible Raman laser configuration including the generation of light at λ = 532 nm (i.e. SHG of the fundamental field), λ = 559 nm (i.e. SFG between the fundamental and first Stokes fields), and λ = 586 nm (i.e. SHG of the first Stokes field). In this case, the visible Raman laser output conversion efficiency between the fundamental to the green line (λ = 532 nm) was impeded by undesired SRS conversion from the fundamental (λ = 1064 nm) to the first Stokes wavelengths (λ = 1173 nm). A similar situation also occurred when the generation of light at λ = 559 nm and λ = 586 nm was constrained by the appearance of an unwanted second Stokes line.

The SRS process can be treated as a nonlinear output coupling for the fundamental field since the fundamental laser conversion and SRS process occur within the same resonator. Therefore the behaviour of the fundamental field will tend to "shift away" from the original peak conversion wavelength to

avoid the SRS-dependent loss. This will lead to a spectral broadening of the fundamental linewidth which has been observed in a variety of intracavity Raman lasers [1.33-1.38]. This effect will ultimately degrade the Raman conversion efficiency. For example, in 2009, Fan et al. observed the spectral broadening occurring in a Nd:YVO$_4$/BaWO$_4$ Raman laser [1.36]. As the Raman power improved from the SRS threshold to the maximum Stokes power, the fundamental linewidth was broadened from 0.2 nm to 1.05 nm, while the first Stokes linewidth was extended from 0.15 nm to 0.5 nm. Moreover, a separate transition of the fundamental can also be generated due to the SRS-induced loss occurring on the main transition of the fundamental gain medium. For instance, in 2011, Li et al. observed a secondary λ = 1086 nm fundamental emission while the primary λ = 1064 nm fundamental emission was efficiently converted into the first Stokes Raman output at λ = 1176 nm [1.39].

The investigation of spectral broadening effects was just proposed in the last couple of years, leading to a trade-off situation: ideally, a narrow Stokes bandwidth is desired, however, it can aggravate the spectral broadening effect of the fundamental field which in turn reduces the effective Raman gain as demonstrated by Bonner et al. [1.40]. In 2014, Savitski demonstrated that this spectral broadening can be significantly reduced by using either an intracavity narrowing element (i.e. a Volume Bragg Grating or a Fabry-Perot Etalon) or by using an injection seed laser [1.41]. The author also pointed out that a wider linewidth of the Raman transition may have the potential to increase the effective Raman gain by restricting the spectral broadening effect. This effect will be experimentally shown in the chapter 4 by comparing two first Stokes Raman laser outputs based on different Raman shifts of a Nd:YVO$_4$ crystal which have different Raman transition linewidths.

1.3.4 Thermal loading effects

During the solid-state laser amplification process, a significant portion of energy is inevitably dissipated as heat and deposited within the laser active

crystal. It is caused by a series of phenomena including quantum defect [1.4], non-radiative decay [1.42], excited state absorption [1.43], up-conversion [1.42, 1.44, 1.45], concentration quenching [1.42, 1.44] and impurities absorption [1.34]. The quantum defect is normally set as the minimum heat load occurring during laser process; up-conversion and concentration quenching usually become more problematic at high doping concentration in host materials. This thermal loading within the gain medium can lead to a range of thermo-optic effects which are displayed in Fig. 1.8.
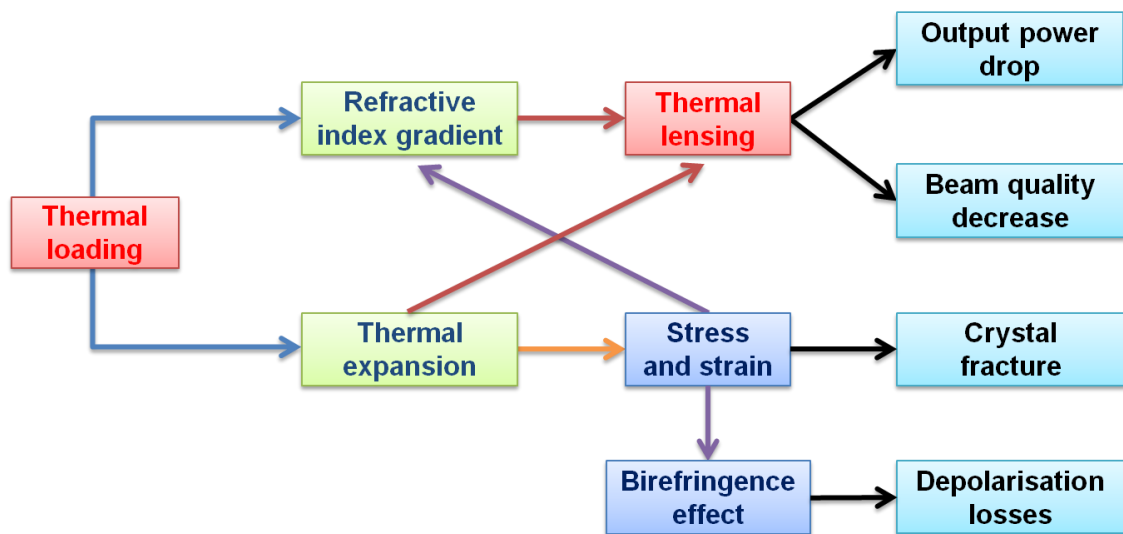
Fig. 1.8 Flow chart of the thermal loading effects

For the commonly-used end-pumped laser configuration, the heat loading will lead to a rise of the material temperature which is conducted away from the centre of the crystal (where the diode pump power is focused). Transverse temperature gradients and physical thermal expansion will therefore be present throughout the length of the crystal and hence a refractive index profile will be created due to both of these effects, acting as an aberrated lens [1.44, 1.46, 1.47]. In this way, the thermal lens will build-up and lead to a strong thermo-optical distortion inside the laser cavity which can significantly degrade the laser output performance. Thermal expansion leads to a physical bulge outwards on the end faces of the laser crystal, performing like a positive lens. The strain and temperature gradients cause additionally gradients of refractive

index which correspond to a further lens effect, which can be positive or negative due to the elasto-optic coefficient and thermo-optic coefficient respectively [1.42].

Due to the non-elastic nature of SRS, even more heat can be generated within the Raman material, especially in a CW intracavity laser configuration. The effective focal length $f_{thermal}$ of the thermal lens can be estimated for an end-pumped Raman laser system, when only considering the thermo-optic contribution to the thermal lens, using [1.10]:

$$\frac{1}{f_{thermal}} = \left(\frac{d_n}{d_T} \right) \frac{1}{K_C} \frac{P_S}{\pi \omega_S^2} \left(\frac{\lambda_S}{\lambda_P} - 1 \right) \qquad (1\text{-}18)$$

where d_n/d_T is the thermo-optic coefficient which represents the varying refractive index corresponding to the temperature change. K_C is the thermal conductivity of the crystal and ω_S is the $1/e^2$ Gaussian radius of the Stokes field inside the Raman gain medium.

As shown in equation (1-18), the focusing power of the thermal lens is proportional to the thermo-optic coefficient of the Raman active crystal and inversely scales with the square of the Stokes mode radius and the thermal conductivity of the Raman material. Most notably, it scales directly with the Raman Stokes average power density, which expresses the existence of a strong coupling trade-off between power-scaling and the thermal lens. This thermal issue is more complex in self-Raman lasers since a residual pump loading and the non-elastic nature of SRS are occurring simultaneously within the same active gain medium. Therefore, finding an efficient approach to alleviate the thermal lens effect is crucial for power-scaling CW intracavity solid-state Raman lasers.

1.3.5 Previous approaches to reduce thermal lensing

Over the last decade, the thermal issue was commonly approached through utilising QCW lasers to significantly reduce the thermal loading within the Raman gain medium [1.34, 1.48]. In this way, the pump source was switched on only for a certain duty cycle (i.e. 50 %, 20 %, 10 %), which was short enough to reduce the thermal lens effect but also long enough to ensure the laser oscillation was close to its steady state behaviour. In this way, higher on-time Raman laser output powers could be achieved with a higher pump level allowance

However, to improve truly CW Raman laser outputs several methods to alleviate the thermal lensing have been reported for a range of specific Raman crystals. One approach to avoid strong thermal lensing is to choose a Raman active material with high performance thermal properties. Due to the outstanding thermo-mechanical properties of diamond (high thermal conductivity of 2200 W / m · K, low thermal expansion coefficient of 1.1×10^{-6} K^{-1} and high damage threshold [1.49]) in combination with its high Raman gain ~ 10 cm / GW at $\lambda = 1$ µm [1.50], the synthetic diamond materials have been demonstrated to significantly reduce the SRS-induced thermal lensing for power-scaling of CW Raman lasers [1.28-1.31]. However, it is still challenging to obtain diamond samples with good and repeatable optical properties (i.e. low absorption losses < 0.1 % per pass and low-birefringence, $\Delta n < 10^{-6}$ per pass) and desired coatings [1.51].

Several methods were also investigated for Neodymium-doped-orthovanadate Raman lasers, which have been used for a large number of CW intracavity Raman lasers over the last decade. In 2008, Lee et al. used a diode pump source at $\lambda = 880$ nm (instead of the conventional pump source at $\lambda = 808$ nm) and a longer Nd:GdVO$_4$ crystal to reduce the thermal lens effect thanks to a reduced quantum defect and a higher Raman gain [1.52]. In 2010, L. Fan et al. efficiently enhanced the CW Raman laser output power by alleviating the thermal lens effect using a composite YVO$_4$/Nd:YVO$_4$/YVO$_4$ crystal [1.38]. In

2012, the focusing powers of the thermal lens for the fundamental ($\lambda = 1063$ nm) and first Stokes ($\lambda = 1173$ nm) lasing field originating from different pump wavelengths ($\lambda = 808$ nm or 880 nm) were directly measured for the first time by Omatsu et al. using lateral shearing interferometry [1.50]. These measurement showed a clear reduced thermal lens effect when using the pump wavelength at $\lambda = 880$ nm rather than at $\lambda = 808$ nm.

Moreover, in 2012 Loiko et al. reported a 14 W CW solid-state Yb:KGW laser emitting at a wavelength of $\lambda = 1024$ nm with low thermo-optic aberrations [1.53]. They found that in addition to the low quantum defect with a pump wavelength at $\lambda = 980$ nm, the Ng-cut Yb:KGW crystal could self-compensate for the thermal lens effect due to an interaction between the negative impact of the temperature dependence of the refractive index and the positive impact of its thermal expansion coefficient. This led to an impressive slope efficiency of 76 %. Although this is not a Raman laser case It should be noted that due to the high Raman gain coefficients of tungstate (i.e. 3.3 cm / GW @ 901 cm^{-1} or 4.4 cm / GW @ 768 cm^{-1} [1.54]), this "near-athermal" crystal has great potential to be used in self-Raman lasers for power-scaling Raman laser outputs in the future.

In this thesis, a novel approach of implementing an AO-based feedback control system is proposed and demonstrated, featuring an intracavity Deformable Mirror (DM) inside self-Raman lasers to compensate for the complex thermal lensing occurring within the gain medium.

1.4 AO system

AO is a technique used to improve the performance of optical systems by correcting for the effects of variable optical aberrations. Historically it was developed to enhance the sharpness of astronomical images from ground-based telescopes by compensating for the incoming wavefront distortions

induced by atmospheric turbulences [1.55]. This concept was firstly proposed by Babcock in 1953 [1.56] and demonstrated by Leighton et al. in 1957 [1.57].

As shown in Fig. 1.9, a typical AO system features three main components arranged in a closed-loop: a wavefront sensor (WFS), a wavefront modulator (WFM) and a control system. The WFS assesses the optical aberrations of an incoming wavefront and provides a feedback signal to the control system. The WFM can then be driven by the control system to correct for the distorted wavefront according to the information from the WFS. A literature review of the AO principle and its applications will be fully introduced in the following chapter 3.
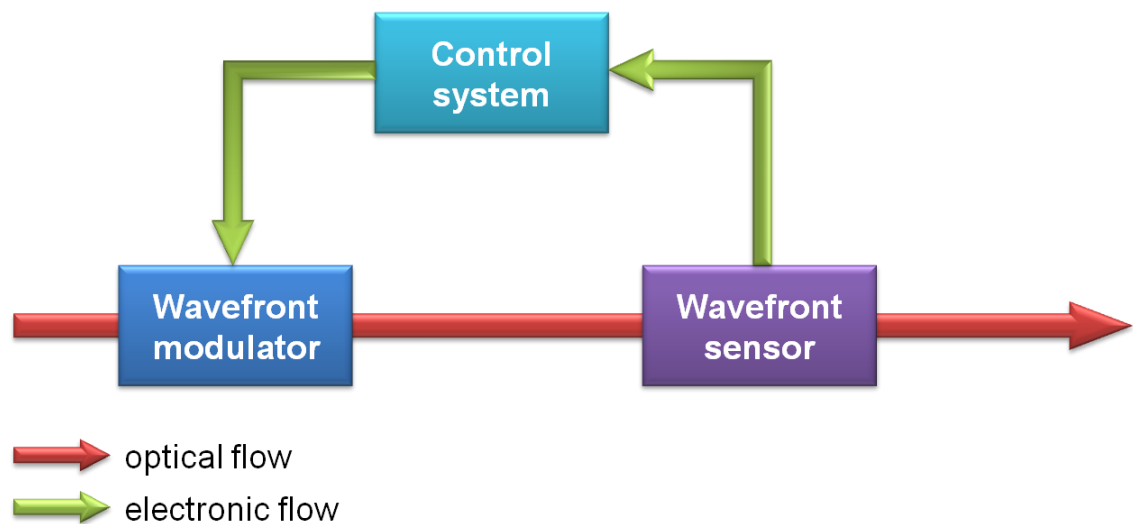
Fig. 1.9 Schematic diagram of an AO control loop system

In this thesis, an AO-based feedback control loop system was integrated inside an intracavity self-Raman laser to significantly compensate for the strong thermal lens effect within the Raman gain medium and power-scale the Raman laser output performance. A variety of bespoke bimorph DMs (see Fig. 1.10) manufactured by BAE systems advanced technology centre [1.58] were utilised in this work as the key element.
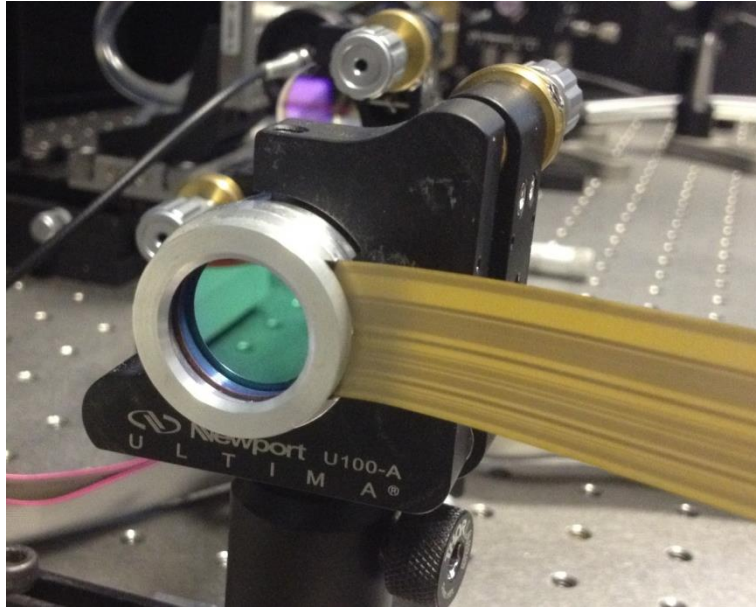
Fig. 1.10 37-actuator bimorph DM produced by BAE systems advanced technology centre

1.5 Research motivation and thesis outline

In this chapter, the SRS theory and various types of different Raman laser configurations have been introduced with theoretical equations. Three main issues which crucially affect the performance of CW intracavity Raman lasers were discussed, including the optical cavity losses, spectral effects and the thermal lens effect.

The work presented in this thesis is entirely focused on dealing with these three limitations and developing an advanced controllable CW intracavity Raman laser system either for extending its spectral coverage or power-scaling the Raman laser output by using AO techniques. To minimise the optical cavity losses in the Raman laser resonator and provide a simpler Raman laser configuration design, all Raman gain media utilised in this thesis were self-Raman laser crystals (i.e. $Nd:YVO_4$ and $Nd:GdVO_4$).

In chapter 2, the development of crystalline Raman lasers will be reviewed. As the work related to this thesis is only focused on all-solid-state CW intracavity Raman lasers, a performance review of this type of Raman laser sources

reported in the last decade (from 2005 to 2015) is summarised. A literature review of the development of AO techniques and their application is introduced in chapter 3.

In chapter 4, several intracavity Nd:YVO$_4$ self-Raman lasers based on the primary or/and secondary Raman shifts of YVO$_4$ (i.e. 893 cm^{-1} and 379 cm^{-1} respectively) are presented corresponding to a number of novel crystalline Raman output wavelengths (λ = 1109 nm, 1158 nm and 1231 nm) operated in the CW regime with Watt level output powers. These Raman lines represent an attractive potential to access more-closely spaced sets of visible wavelengths in the green-lime-yellow region by employing additional SHG, which can significantly benefit many applications in medicine and bio-photonics [1.59, 1.60]. In addition, by comparing the first Stokes Raman laser outputs based on either the primary or secondary Raman shifts, it will be proved that a wider linewidth of the Raman transition may have the potential to improve the Raman conversion efficiency by restricting the described spectral broadening effect.

In chapter 5, an intracavity CW Nd:YVO$_4$ self-Raman laser combined with an AO-based feedback control loop featuring a bimorph DM and a closed-loop search algorithm is reported. This method represents a novel approach to significantly alleviate the strong thermal lensing within the self-Raman crystal and enable the power-scaling of the Raman laser output. Moreover, a wavelength selection between two Raman laser outputs (λ = 1109 and λ = 1176 nm) by manually changing the intracavity DM shape is also presented. Some additional experimental results utilising a new advanced bimorph DM in either a CW Nd:YVO$_4$ self-Raman laser or a CW frequency-doubled Nd:GdVO$_4$ Raman laser are reported in chapter 6. This series of proof-of-concept experiments show the significant potential to improve the Raman laser output to new power levels either in the visible or the near-infrared spectral bands, which is beneficial to a wide range of applications such as in astronomy and medical fields [1.61, 1.62].

Finally, the work in this thesis will be summarised and concluded in chapter 7 with presenting several promising ideas for future work.

1.6 References

1.1   T. H. Maiman, "Stimulated Optical Radiation in Ruby," Nature. **187**, 493-494 (1960).

1.2   D. Aron-Rosa, J. J. Aron, M. Griesemann, R. Thyzel, "Use of the neodymium-yag laser to open the posterior capsule after lens implant surgery: a preliminary report," J Am Intraocul Implant Soc. **6**, 352-354 (1980).

1.3   J. R. Cook, J. R. Albertine, "The Navy's high-energy laser weapon system," Proc. SPIE. **2988**, 264 (1997).

1.4   W. Koecher, *Solid-state laser Engineering*, 5th edition (Springer Series in Optical Sciences, New-York, 1999).

1.5   P. Moulton, "Ti-doped sapphire: a tunable solid-state laser," Opt. News. **8**, 9 (1982).

1.6   P. Albers, E. Stark, and G. Huber, "Continuous-wave laser operation and quantum efficiency of titanium-doped sapphire," J. Opt. Soc. Am. B. **3**, 134-139 (1986).

1.7   C. V. Raman, "A new radiation," Indian. J. Phys. **2**, 387-398 (1928).

1.8   G. Landsberg, L. Mandelstam, "New phenomenon in scattering of light (preliminary report)," J Russian Physico-Chemical Soc. **60**, 335 (1928).

1.9   D. J. Gardiner, P. R. Graves, *Practical Raman Spectroscopy*, (Springer-Verlag, Berlin Heidelberg, 1989).

1.10   H. M. Pask, "The design and operation of solid-state Raman lasers," Prog. Quant. Electron. **27**, 3-56 (2003).

1.11   C. Kittel, *Thermal Physics*, (John Wiley & Sons, New York, 1969).

1.12   R. W. Boyd, *Nonlinear Optics*, (Academic Press, San Diego, 1992).

1.13   N. Bloembergen, "The stimulated Raman effect," Am. J. Phys. **35**, 989 (1967).

1.14 W. Kaiser, and M. Maier, "Stimulated Rayleigh, Brillouin and Raman spectroscopy," Laser Handbook, **2**, North-Holland, Amsterdam, 1077 (1972).

1.15 C. S. Wang, "The stimulated Raman process," Quantum. Electron. **1**, 447-472 (1975).

1.16 P. Cerny, H. Jelinkova, P. G. Zverev, T. T. Basiev, "Solid state lasers with Raman frequency conversion," Prog. Quant. Electron. **28**, 113-143 (2004).

1.17 R. L. Carman, F. Shimizu, C. S. Wang, N. Bloembergen, "Theory of Stokes pulse shapes in transient Raman scattering," Phys. Rev. A. **2**, 60-72 (1970).

1.18 J. A. Piper and H. M. Pask, "Crystalline Raman Lasers," IEEE J. Sel. Topics Quantum Electron. **13**, 692-704 (2007).

1.19 E. J. Woodbury and W. K. Ng, "Ruby laser operation in the near IR," Proc. IRE. **50**, 2347-2348 (1962).

1.20 P. Cerny, H. Jelinkova, T. T. Basiev, and P. G. Zverev, "Highly Efficient Picosecond Raman Generators Based on the $BaWO_4$ Crystal in the Near Infrared, Visible, and Ultraviole," IEEE J. Quant. Electron. **38**, 1471-1478 (2002).

1.21 O. Kitzler, A. McKay, D. J. Spence and R. P. Mildren, "Modelling and Optimization of Continuous-Wave External Cavity Raman Lasers," Opt. Express. **23**, 8590-8602, (2015).

1.22 R. J. Williams, O. Kitzler, A. McKay, and R. P. Mildren, "Investigating diamond Raman lasers at the 100 W level using quasi-continuous-wave pumping," Opt. Lett. **39**, 4152-4155 (2014).

1.23 O. Kitzler, A. McKay, R. P. Mildren, "Characterization of a Single-frequency-pumped Continuous-wave Extracavity Diamond Raman Laser," European Conference on Lasers and Electro-Optics. Paper CD_P_37 (2013).

1.24   S. Reilly, V. G. Savitski, H. Liu, E. Gu, M. D. Dawson, and A. J. Kemp, "Monolithic diamond Raman laser," Opt. Lett. **40**, 930-933 (2015).

1.25   B. Denker, E. Shklovsky, *Handbook of Solid-State Lasers: Materials, Systems and Applications*, (WPL Press 2013).

1.26   D. J. Spence, P. Dekker, and H. M. Pask, "Modeling of Continuous Wave Intracavity Raman Lasers," IEEE J. Sel. Topics Quantum Electron. **13**, 756-763 (2007).

1.27   X. Li, H. M. Pask, A. J. Lee, Y. Huo, J. A. Piper, and D. J. Spence, "Miniature wavelength-selectable Raman laser: new insights for optimizing performance," Opt. Express. **19**, 25623-25631 (2011).

1.28   W. Lubeigt, G. M. Bonner, J. E. Hastie, M. D. Dawson, D. Burns, and A. J. Kemp, "Continuous-wave diamond Raman laser," Opt. Lett. **35**, 2994-2996 (2010).

1.29   W. Lubeigt, V. G. Savitski, G. M. Bonner, S. L. Geoghegan, I. Friel, J. E. Hastie, M. D. Dawson, D. Burns, and A. J. Kemp, "1.6W continuous-wave Raman laser using low-loss synthetic diamond," Opt. Express. **19**, 6938-6944 (2011).

1.30   D. C. Parrotta, A. J. Kemp, M. D. Dawson, and J. E. Hastie, "Tunable continuous-wave diamond Raman laser," Opt. Express. **19**, 24165-24170 (2011).

1.31   D. C. Parrotta, A. J. Kemp, M. D. Dawson, and J. E. Hastie, "Multiwatt, Continuous-Wave, Tunable Diamond Raman Laser With Intracavity Frequency-Doubling to the Visible Region," IEEE J. Sel. Topics Quantum Electron. **19**, 1400108 (2013).

1.32   A. J. Lee, D. J. Spence, J. A. Piper, and H. M. Pask, "A wavelength-versatile, continuous-wave, self-Raman solid-state laser operating in the visible," Opt. Express. **18**, 20013-20018 (2010).

1.33   P. Dekker, H. M. Pask, and J. A. Piper, "All-solid-state 704mW continuous-wave yellow source based on an intracavity, frequency-doubled crystalline Raman laser," Opt. Lett. **32**, 1114-1116 (2007).

1.34   P. Dekker, H. M. Pask, D. J. Spence and J. A. Piper, "Continuous-wave, intracavity doubled, self-Raman laser operation in Nd:GdVO$_4$ at 586.5 nm," Opt. Express. **15**, 7038-7046 (2007).

1.35   V. A. Lisinetskii, A. S. Grabtchikov, A. A. Demidovich, V. N. Burakevich, V. A. Orlovich, A. N. Titov, "Nd:KGW/KGW crystal: efficient medium for continuous-wave intracavity Raman generation" Appl. Phys. B. **88**, 499-501 (2007).

1.36   L. Fan, Y. Fan, Y. Li, H. Zhang, Q. Wang, J. Wang, and H. Wang, "High-efficiency continuous-wave Raman conversion with a BaWO$_4$ Raman crystal," Opt. Lett. **34**, 1687-1689 (2009).

1.37   L. Fan, Y. X. Fan, Y. H. Duan, Q. Wang, H. T. Wang, G. H. Jia, C. Y. Tu, "Continuous-wave intracavity Raman laser at 1179.5 nm with SrWO$_4$ Raman crystal in diode-end-pumped Nd:YVO$_4$ laser," Appl. Phys. B. **94**, 553-557 (2009).

1.38   L. Fan Y. X. Fan H. T. Wang, "A compact efficient continuous-wave self-frequency Raman laser with a composite YVO$_4$/Nd:YVO$_4$/YVO$_4$ crystal," Appl. Phys. B. **101**, 493-496 (2010).

1.39   X. Li, A. J. Lee, H. M. Pask, J. A. Piper and Y. Huo, "330 mW CW yellow emission from miniature self-Raman laser based on direct HR-coated Nd:YVO$_4$ crystal," IQEC/CLEO Pacific Rim 1250-1252 (2011).

1.40   G. M. Bonner, J. Lin, A. J. Kemp, J. Wang, H. Zhang, D. J. Spence, and H. M. Pask, "Spectral broadening in continuous-wave intracavity Raman lasers," Opt. Express. **22**, 7492-7502 (2014).

1.41   V. G. Savitski, "Experimental analysis of emission linewidth narrowing in a pulsed KGd(WO$_4$)$_2$ Raman laser," Opt. Express. **22**, 21767-21774 (2014).

1.42   D. Brown, "Heat, fluorescence, and stimulated-emission power densities and fractions in Nd:YAG," IEEE J. Quant. Electron. **34**, 560-572 (1998).

1.43   Y. Guyot, H. Manaa, J. Y. Rivoire, R. Moncorge, N. Garnier, E. Descroix, M. Bon, and P. Laporte, "Excited-state-absorption and upconversion studies of Nd^{3+}-doped single crystals $Y_3Al_5O_{12}$, $YLiF_4$, and $LaMgAl_{11}O_{19}$," Phys. Rev. B. **51**, 784-799 (1995).

1.44   W. A. Clarkson, "Thermal effects and their mitigation in end-pumped solid-state lasers," J. Phys. D - Appl. Phys. **34**, 2381-2395 (2001).

1.45   S. Guy, C. Bonner, D. Shepherd, D. Hanna, A. Tropper, and B. Ferrand, "High-inversion densities in Nd:YAG-upconversion and bleaching," IEEE J. Quant. Electron. **34**, 900-909 (1998).

1.46   M. E. Innocenzi, H. T. Yura, C. L. Fincher, and R. A. Fields, "Thermal modelling of continuous-wave end-pumped solid-state laser," Appl. Phys. Lett. **56**, 1831-1833 (1990).

1.47   A. K. Cousins, "Temperature and thermal stress scaling in finite-length end-pumped laser rods," IEEE J. Quant. Electron. **28**, 1057-1069 (1992).

1.48   J. Lin and H. M. Pask, "Cascaded self-Raman lasers based on 382 cm^{-1} shift in $Nd:GdVO_4$," Opt. Express. **20**, 15180-15185 (2012).

1.49   A. Sabella, J. A. Piper, and R. P. Mildren, "1240nm diamond Raman laser operating near the quantum limit," Opt. Lett. **35**, 3874-3976 (2010).

1.50   T. Omatsu, M. Okida, A. Lee, H. M. Pask, "Thermal lensing in a diode-end-pumped continuous-wave self-Raman Nd-doped $GdVO_4$ laser," Appl. Phys. B. **108**, 73-79 (2012).

1.51   Element Six GmbH, Hanauer Landstrasse 291-293, 60314 Frankfurt, Germany. www.e6.com/wps/wcm/connect/e6_content_en/home.

1.52   A. J. Lee, H. M. Pask, P. Dekker, J. A. Piper, "High efficiency, multi-Watt CW yellow emission from an intracavity-doubled self-Raman laser using $Nd:GdVO_4$," Opt. Express. **16**, 21958-21963 (2008).

1.53   P. A. Loiko, V. E. Kisel, N. V. Kondratuk, K. V. Yumashev, N. V. Kuleshov, A. A. Pavlyuk, "14 W high-efficiency diode-pumped cw Yb:KGd(WO$_4$)$_2$ laser with low thermo-optic aberrations," Opt. Mater. **35**, 582-585 (2012).

1.54   EKSMA, "Full Laser Components 2014 Catalogue," www.eksmaoptics.com/catalogues.

1.55   R. K. Tyson, *Principles of adaptive optics*, (Academic Press, 1991).

1.56   H. W. Babcock, "The possibility of compensating astronomical seeing," Publ. Astron. Soc. Pac. **65**, 229-236 (1953).

1.57   C. C. Wilcox, J. R. Andrews, S. R. Restaino, T. Martinez, S. W. Teare, "Atmospheric Turbulence Generator Using a Liquid Crystal Spatial Light Modulator," Proceedings of the IEEE 2007 Aerospace Conference, 1-8 (2007).

1.58   BAE systems advanced technology centre, Stirling Square, 6 Carlton Gardens, London, SW1Y 5AD United Kingdom, www.baesystems.com.

1.59   H. Yu, K. Wu, H. Zhang, Z. Wang, J. Wang, and M. Jiang, "Nd:YGG crystal laser at 1110 nm: a potential source for detecting carbon monoxide poisoning," Opt. Lett. **36**, 1281-1283 (2011).

1.60   M. F. Garcia-Parajo, M. Koopman, E. M. van Dijk, V. Subramaniam, and N. F. van Hulst, "The nature of fluorescence emission in the red fluorescent protein DsRed, revealed by single-molecule detection," Proc. Natl. Acad. Sci. U.S.A. **98**, 14392-14397 (2001).

1.61   S. Wada, N. Saito, M. Kato, K. Akagawa, A. Takazawa, Y. Hayano, H. Takami, "High Power Yellow Light Generation for Laser Guide Star," in Advanced Solid-State Photonics, paper MB5, (2006).

1.62   J. H. Lock and K. C. S. Fong, "Retinal Laser Photocoagulation," Med. J. Malaysia. **65**, 88-95, (2010).

Chapter 2

Solid-state Raman lasers

2.1 Introduction

Since the first discovery of SRS by Woodbury and Ng in 1962 [2.1], Raman lasers have become an efficient and widely used approach to expand the spectral coverage of lasers [2.2]. Over the recent decades, a variety of active gain media including gases, liquids and solids have been employed in Raman lasers [2.3, 2.4].

Molecular gases such as H_2, D_2 N_2 and CH_4, have been widely employed to produce Raman lasers thanks to their low scattering losses, large Raman scattering cross sections and narrow spectral linewidths (i.e. For CH_4, $\partial\sigma / \partial\Omega = 7.0 \times 10^{-36}$ m^2 / sr when it is pumped at $\lambda = 1.06$ µm under 30 atmospheres, the Raman linewidth can be calculated as $\Delta\omega_R = 0.32 + 0.012*p$ cm^{-1} where p is in atmospheres) [2.4-2.6]. A large number of gaseous Raman media can produce a frequency conversion with transitions ranging from 1000 to 4000 cm^{-1} as listed in [2.7]. However, the use of gas-based Raman lasers is mainly restricted by the typically-low particle concentration in the gas of interest. As a result, high-pressure (up to ~ 100 atmospheres) and large gas cells with interaction length in the metre range are required to achieve efficient SRS conversion. In addition, because of the low thermal conductivity (K_C) of most gases (i.e. at 300 K, $K_C = 0.182W / mK$ for H_2 and $K_C = 0.026W / mK$ for N_2), the repetition rate of high power gas Raman lasers is significantly constrained (usually < 50 Hz). While the development of a flow-through system can alleviate this thermal distortion, parasitic problems such as the competition between SRS and Stimulated Brillouin Scattering

(SBS) processes [2.8] also occurs. In addition, the risk of gas explosion and the chemical instabilities especially for high pressure gas vessel under high power laser pumping have limited the use of gas Raman lasers.

A larger concentration of active particles can be achieved in liquid Raman media leading to a more efficient SRS conversion than in gases. However, due to the broader vibrational transitions, the Raman scattering cross-section is commonly lower in liquids. In general, the influence of increased particle density can efficiently compensate for the decrease of the Raman scattering cross-section resulting in a high Raman gain coefficient in the liquid media [2.3]. However, in addition to the limiting factors also encountered in gas lasers, such as thermal lensing and competition between SBS and SRS, liquid-based Raman lasers additionally suffer from the self-focusing effect, another $\chi^{(3)}$ nonlinear effect [2.9, 2.10].

Solid Raman gain media present favorable properties of relatively-high thermal conductivity (i.e. 5.5 for YVO$_4$, 10.5 for YAG, 2000 for diamond, unit: W m^{-1} K^{-1}) and mechanical hardness (i.e. 53 for YVO$_4$, 280 for YAG, 2860 for diamond, unit: MPa) with especially a high concentration of Raman active particles ($\sim 10^{22}$ - 10^{23} cm^{-3}) [2.11]. Moreover, high steady-state Raman gain coefficients, listed in [2.11], can be achieved in certain crystals due to the high Raman scattering cross-section combined with the narrow vibrational transitions. In this way, highly efficient SRS conversion with a low SRS pump threshold will be achieved within crystals such as KGW, YVO$_4$, and diamond. Therefore, compact and simple Raman laser configurations can be obtained using this type of crystals. The work in this thesis will be only focused on solid-state Raman lasers using Nd:YVO$_4$ and Nd:GdVO$_4$ as Raman media.

In addition, optical fibres are also attractive Raman active media since the long interaction length in fibre can make it easy to achieve the SRS threshold, especially in a low-loss laser resonator [2.12]. They are normally pumped by a rare-earth-doped fibre laser or directly pumped by a high-brightness laser diode. Due to the long interaction area corresponding to a high gain, the output power of Raman fibre lasers operated in the CW regime can reach up to the

order of hundreds of watts [2.13, 2.14]. Fibre Bragg Gratings (FBGs) are commonly nested inside fibres to act as reflecting cavity mirrors, constructing the Raman fibre laser resonator and selecting the Raman output wavelength with a narrow bandwidth. In addition, multiple SRS cascading lines can be easily accessed by using multiple pairs of FBGs. Therefore, a quite attractive output spectral range emitting in the near- to mid-infrared (i.e. 1.5 - 4 µm) can be obtained, which are beneficial to a wide range of applications such as LIDAR, gas sensing, and optical communication [2.15-2.18]. The main limitation of Raman fibre lasers is the involvement of undesired nonlinear processes due to the high gain and intensity inside the fibre, such as SBS, Kerr effect and four-wave mixing [2.12]. However, more and more Raman fibre lasers are now available commercially, either in CW or pulsed mode emitting from the visible to the mid-infrared spectral band.

This chapter is concerned with reviewing the experimental works of crystalline Raman lasers, especially focusing on the all-solid-state CW intracavity Raman lasers which will be utilised in this thesis. Section 2.2 looks back at the history of crystalline Raman lasers development, with reviewing several pioneering works based on different Raman active crystals. A thorough performance review of all-solid-state CW intracavity Raman lasers over the last decade is presented in section 2.3, while some of the specific intracavity Raman laser devices will be highlighted with more specifics.

2.2 Development of crystalline Raman lasers

SRS occurring within crystalline materials was first observed in diamond, calcite and α-sulfur by G. Eckhardt et al. in 1963 [2.19]. However, a practical and efficient solid-state Raman laser was not achieved until a decade later. Since high power densities ($\sim$ 100 MW cm^{-2}) are required to obtain SRS, crystalline Raman lasers were all pulsed devices, at least until 2005. From 1975 to 1979, a number of pioneering works were reported by Ammann et al. In 1975, they reported the first intracavity crystalline Raman laser operating at

1 kHz of Pulse Repetition Frequency (PRF) [2.20]. Nd:YAlO$_3$ and LiIO$_3$ crystals were then employed as laser and Raman gain media respectively. A total average power of 20 mW containing both first Stokes (λ = 1180 nm) and second-Stokes outputs (λ = 1340 nm) was obtained. In 1977, using the same active crystals, the Raman laser output was significantly power-scaled using appropriate output couplers for the Stokes outputs [2.21]. A first Stokes average output power of 0.9 W was measured at 3.2 kHz of PRF corresponding to ~ 77 % fundamental to first-Stokes conversion efficiency. Moreover, 200 mW of average output power at the second-Stokes output was obtained in another configuration operating at PRF = 1 kHz. In 1979, they demonstrated the first visible solid-state Raman lasers using intracavity SHG and SFG [2.22]. A Nd:YALO$_3$ crystal was used as fundamental laser gain medium while LiIO$_3$ was utilised as both a Raman and SHG/SFG medium. As a result, a variety of visible Raman laser outputs at λ = 540 nm (1.13 W), 565 nm (78 mW), 592 nm (685 mW), 622 nm (98 mW) and 655 nm (107 mW) were obtained operating at a PRF of 3 kHz. During the 1980s, solid-state Raman lasers entered a steady development period. In 1985, Andryunas et al. achieved stimulated self-Raman conversion in Nd:KGW and Nd:KYW crystals operating in the picosecond range [2.23]. One year later, several Raman lasers using a range of crystals such as Ba:(NO$_3$)$_2$, Na:NO$_3$ and Ca:(NO$_3$)$_2$ and operating in the nanosecond domain were reported by Karpukhin et al. [2.24]. This work exploited the potential of these Raman active crystals previously demonstrated by Eremanko et al in 1980 [2.25]. In 1993, an improved Ba:(NO$_3$)$_2$ Raman laser operating in the picosecond range was reported by Zverev et al. [2.26]. In 1995, the development of crystalline Raman lasers significantly picked up with the report by Murray et al. of an eye-safe Raman laser delivering a first Stokes output at λ = 1535 and 1556 nm [2.27] simultaneously with pulse energies as high as 0.25 J at PRF = 1 Hz. In this work, a Ba:(NO$_3$)$_2$ active crystal was pumped by a Nd:YAG laser operating at λ = 1318 and 1338 nm. Second Stokes outputs at λ = 1820 and 1860 nm were also achieved. Both Raman Stokes outputs operated in a picosecond range. This work opened up a range of new applications for Raman laser devices

[2.11]. After that, a large number of relevant investigations were reported in the following years, especially with the use of tungstate-based Raman active crystals [2.28-2.34]. For instance, in 1999, Pask et al. developed an all-solid-state yellow Raman laser source delivering up to 1.2 W of average output power at $\lambda = 578$ nm [2.30]. LiIO$_3$ and LBO crystals were utilised in a Q-switched Nd:YAG laser cavity as Raman and SHG gain media respectively. This demonstration provided an efficient method to produce yellow light for medical applications such as blood monitoring since hemoglobin strongly absorbs this wavelength. During the same year, an all-solid-state Nd:KGW self-Raman laser pumped by a CW diode source was demonstrated by Grabtchikov et al [2.32]. Up to 4.8 mW of Raman laser average output operating at $\lambda = 1181$ nm was obtained at PRF = 1 kHz. Finally, in 2004, the first solid-state CW Raman laser was reported by the same group [2.35]. 164 mW of first Stokes Raman output power at $\lambda = 543$ nm was obtained with ~ 5.5 W of argon-ion laser pumping ($\lambda = 514$ nm). One year later, the first all-solid-state intracavity Raman lasers operating in the CW region were demonstrated by Demidovich et al [2.33] and Pask [2.34] separately.

The recent blossoming of crystalline Raman laser research was significantly impacted by the development of Neodymium-doped orthovanadates crystals, such as Nd:YVO$_4$ and Nd:GdVO$_4$ as firstly predicted by Kaminskii et al. in 2001 [2.36]. Three years later, Chen successfully demonstrated the use of vanadate-based Raman lasers operating in a sub-nanosecond range [2.37, 2.38]. This led to a rapid development of practical and compact all-solid-state Raman lasers operating in the CW regime as reviewed in next section.

2.3 Review of CW intracavity all-solid-state Raman lasers

Time [Ref]	Laser crystal (doubling crystal)	Raman crystal	Output wavelength (nm)	Max output power (W)	Conversion efficiency (pump to Raman output power)
2005 [2.33]	Nd:KGW	Nd:KGW	$\lambda = 1181$	0.054	2.6 %
2005 [2.34]	Nd:YAG	KGW	$\lambda = 1176$	0.8	4 %
2006 [2.39]	Nd:YVO$_4$	Pb:WO$_4$	$\lambda = 1177$	0.178	13 %
2007 [2.40]	Nd:YVO$_4$	Nd:YVO$_4$	$\lambda = 1177$	0.05	5 %
2007 [2.41]	Nd:GdVO$_4$ (LBO)	KGW	$\lambda_1 = 1176$ $\lambda_2 = 588$	1.56 0.704	8.7 % 5.1 %
2007 [2.42]	Nd:GdVO$_4$ (LBO)	Nd:GdVO$_4$	$\lambda_1 = 1173$ $\lambda_2 = 586.5$	2 0.678	9.1 % 4.2 %
2007 [2.43]	Nd:KGW /KGW	Nd:KGW /KGW	$\lambda = 1181$	0.277	14 %
2007 [2.44]	Nd:YVO$_4$ (LBO)	Nd:YVO$_4$	$\lambda_1 = 1176$ $\lambda_2 = 588$	0.32 0.14	7.6 % 4.4 %
2008 [2.45]	Nd:GdVO$_4$ (LBO)	Nd:GdVO$_4$	$\lambda = 586.5$	2.51	12.2 %
2009 [2.46]	Nd:YVO$_4$	Ba:WO$_4$	$\lambda = 1180$	3.36	13.2 %
2009 [2.47]	Nd:YVO$_4$	Sr:WO$_4$	$\lambda = 1179.5$	2.23	10.5 %
2010 [2.48]	Nd:YVO$_4$ (LBO)	Sr:WO$_4$	$\lambda = 590$	0.23	1.5 %
2010 [2.49]	Nd:GdVO$_4$ (LBO)	Nd:GdVO$_4$	$\lambda = 559$	5.3	21 %
2010 [2.50]	Nd:GdVO$_4$ (LBO)	Ba:WO$_4$	$\lambda_1 = 1180$ $\lambda_2 = 590$	2.1[1] 2.9[2]	7.8 %[1] 11 %[2]
2010 [2.51]	Nd:YVO$_4$ (LBO)	Nd:YVO$_4$	$\lambda = 559$	0.89	4.9 %
2010 [2.52]	LuVO$_4$ /Nd:LuVO$_4$ /LuVO$_4$	LuVO$_4$ /Nd:LuVO$_4$ /LuVO$_4$	$\lambda = 589$	3.5	13.3 %

	(LBO)				
2010 [2.53]	Nd:YVO$_4$	Diamond	$\lambda = 1240$	0.2	2 %
2010 [2.54]	Nd:GdVO$_4$ (LBO)	Nd:GdVO$_4$	$\lambda_1 = 532$ $\lambda_2 = 559$ $\lambda_3 = 586$	4.6$_{(1)}$ 5.3$_{(2)}$ 4.3$_{(3)}$	16 %$_{(1)}$ 20.4 %$_{(2)}$ 17.1 %$_{(3)}$
2010 [2.55]	Nd:GdVO$_4$ (LBO)	Nd:GdVO$_4$	$\lambda_1 = 1308$ $\lambda_2 = 620$	0.95$_{(1)}$ 1.027$_{(2)}$	6.8 %$_{(1)}$ 4.9 %$_{(2)}$
2010 [2.56]	YVO$_4$ /Nd:YVO$_4$ /YVO$_4$	YVO$_4$ /Nd:YVO$_4$ /YVO$_4$	$\lambda = 1175$	2.8	11 %
2011 [2.57]	YVO$_4$ /Nd:YVO$_4$	YVO$_4$ /Nd:YVO$_4$	$\lambda = 1176$	1.84	7.8 %
2011 [2.58]	Nd:KGW (LBO)	Nd:KGW	$\lambda = 561$	0.57	3.3 %
2011 [2.59]	Nd:YVO$_4$ (KTP)	Nd:YVO$_4$	$\lambda_1 = 1176$ $\lambda_2 = 558.6$	1.53$_{(1)}$ 0.48$_{(2)}$	6.8 %$_{(1)}$ 4 %$_{(2)}$
2011 [2.60]	Nd:GdVO$_4$ (LBO)	Sr:MoO$_4$	$\lambda_1 = 1173.5$ $\lambda_2 = 586.8$	2.18$_{(1)}$ 3.1$_{(2)}$	8.8 %$_{(1)}$ 12.4 %$_{(2)}$
2011 [2.61]	InGaAs	KGW	$\lambda = 1143$	0.8	7.5 %
2011 [2.62]	Nd:YVO$_4$ (BBO)	Nd:YVO$_4$	$\lambda_1 = 1176$ $\lambda_2 = 587.8$	0.16$_{(1)}$ 0.22$_{(2)}$	4.7 %$_{(1)}$ 5.8 %$_{(2)}$
2011 [2.63]	Nd:YVO$_4$	Diamond	$\lambda = 1240$	1.6	11 %
2011 [2.64]	Nd:YVO$_4$ (BBO)	Nd:YVO$_4$	$\lambda_1 = 1176$ $\lambda_2 = 587.8$	0.7$_{(1)}$ 0.33$_{(2)}$	18.4 %$_{(1)}$ 8.6 %$_{(2)}$
2011 [2.65]	InGaAs	Diamond	$\lambda = 1227$	1.3	14.4 %
2011 [2.66]	Nd:YVO$_4$ (LBO)	Nd:YVO$_4$	$\lambda_1 = 588$ $\lambda_2 = 559$	0.32$_{(1)}$ 0.66$_{(2)}$	8.4 %$_{(1)}$ 17 %$_{(2)}$
2012 [2.67]	GaAs /InGaAs (LBO)	KGW	$\lambda_1 = 560$ $\lambda_2 = 592.5$	0.8$_{(1)}$ 0.52$_{(2)}$	4.2 %$_{(1)}$ 2.9 %$_{(2)}$
2012 [2.68]	Nd:YLF	Diamond	$\lambda = 1217$	5.1	3.3 %
2012 [2.68]	Nd:YLF	KGW	$\lambda = 1139$	6.1	4.1 %
2012 [2.69]	Nd:YLF (LBO)	KGW	$\lambda_1 = 1163$ $\lambda_2 = 1147$ $\lambda_3 = 549$ $\lambda_4 = 552$ $\lambda_5 = 573$ $\lambda_6 = 581$	0.95$_{(1)}$ 0.7$_{(2)}$ 0.65$_{(3)}$ 1.9$_{(4)}$ 0.6$_{(5)}$ 1.1$_{(6)}$	7.7 %$_{(1)}$ 5.4 %$_{(2)}$ 5 %$_{(3)}$ 14.6 %$_{(4)}$ 4.6 %$_{(5)}$ 8 %$_{(6)}$
2012 [2.70]	Nd:GdVO$_4$ (BBO)	Nd:GdVO$_4$	$\lambda_1 = 1173$ $\lambda_2 = 559$ $\lambda_3 = 586.5$	4.1$_{(1)}$ 4.05$_{(2)}$ 3.46$_{(3)}$	11.2 %$_{(1)}$ 12.5 %$_{(2)}$ 10.7 %$_{(3)}$

2012 [2.71]	Nd:YVO$_4$ /Ba:WO$_4$ (LBO)	Nd:YVO$_4$ /Ba:WO$_4$	$\lambda = 590$	0.194	5.1 %
2013 [2.72]	Nd:LuVO$_4$ (LBO)	Nd:LuVO$_4$	$\lambda = 560$	4.2	22.9 %
2013 [2.73]	Nd:YVO$_4$	Nd:YVO$_4$	$\lambda_1 = 1109$ $\lambda_2 = 1156$ $\lambda_3 = 1176$ $\lambda_3 = 1231$	1.0$_{(1)}$ 0.7$_{(2)}$ 0.54$_{(3)}$ 1.14$_{(4)}$	8.4 %$_{(1)}$ 5.4 %$_{(2)}$ 5.4 %$_{(3)}$ 9.3 %$_{(4)}$
2013 [2.74]	InGaAs (LBO)	Diamond	$\lambda_1 = 1228$ $\lambda_2 = 614$	4.4$_{(1)}$ 1.5$_{(2)}$	14.2 %$_{(1)}$ 5.4 %$_{(2)}$
2013 [2.75]	Yb:KGW	Yb:KGW	$\lambda = 1099.6$	1.7	21.8 %
2014 [2.76]	Nd:YLF (LBO)	KGW	$\lambda_1 = 990$ $\lambda_2 = 474$	0.027$_{(1)}$ <0.001$_{(2)}$	0.15 %$_{(1)}$ -
2015 [2.77]	Nd:YVO$_4$	Nd:YVO$_4$	$\lambda = 1176$	1.8	7.3%

Table 2.1 Summary of the most significant CW all-solid-state intracavity Raman lasers developed from 2005 to 2015

A performance review of the most significant all-solid-state intracavity Raman lasers operating in the CW regime is displayed in Table 2.1. Over the last decade, the development of CW Raman lasers was mainly undertaken at the near-infrared and visible regions of the spectrum, achieving multi-Watt power levels. In addition, several specific intracavity Raman laser devices such as miniature selectable self-Raman lasers, double-end-pumped Raman lasers or the continuously-tunable intracavity Raman laser systems combined with semiconductor disk lasers, have been developed for a wide range of applications. A selection of crucial demonstrations is given in the following paragraphs.

In 2005, the first CW Raman output produced by an all-solid-state laser device was demonstrated by Demidovich et al. in a Nd:KGW self-Raman laser [2.33]. A first Stokes Raman output at $\lambda = 1181$ nm was achieved with a threshold of 1.15 W diode pump power. A maximum Raman laser output of 54 mW was measured for a diode pump power of 2.06 W, corresponding to a pump diode-to-Stokes conversion efficiency of 2.6 %. In the same year and independently

from Demidovich's work, Pask reported a 800 mW CW intracavity Raman laser with an overall conversion efficiency of 4 % using a Nd:YAG laser crystal and a Nd:KGW Raman gain medium [2.34]. The Raman threshold at $\lambda = 1176$ nm was measured at 4 W of diode pump power.

To date, the highest output power of a CW intracavity crystalline Raman laser was reported by Savitski et al. in 2012 [2.68]. In this work, a KGW Raman gain medium was combined with a side-pumped Nd:YLF laser medium leading to a maximum CW Raman output power of 6.1 W with 150 W of side-pump power. A similar experimental setup was also constructed using a diamond Raman crystal and resulting in a Raman output of 5.1 W for a side-pumped pump power of 153 W.
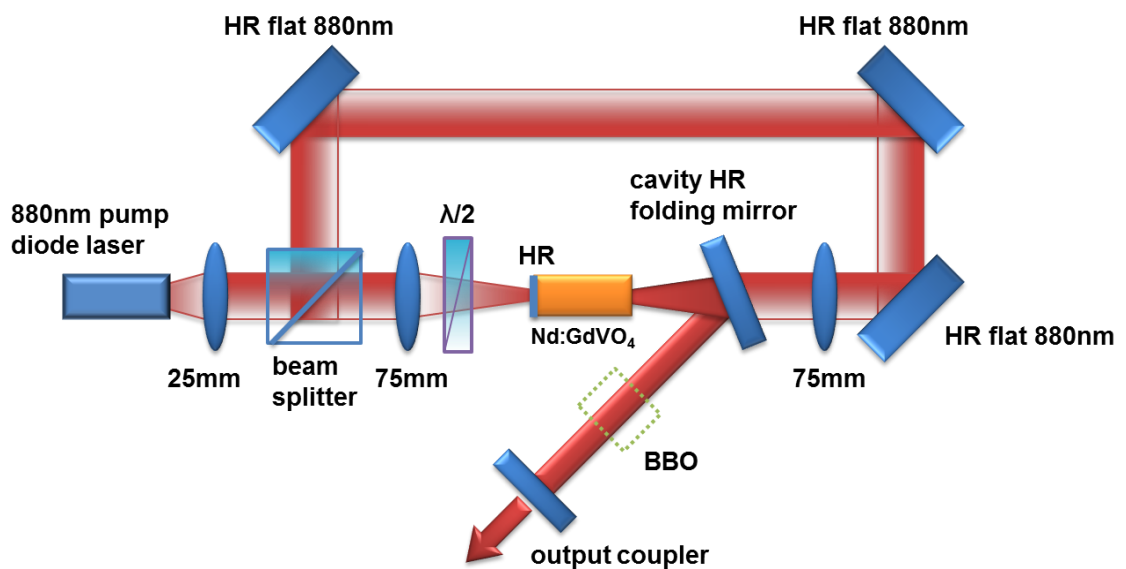
Fig. 2.1 Cascaded Nd:GdVO$_4$ self-Raman laser configuration with double-end polarised pumping, (Image extracted from [2.70])

Although the highest CW intracavity solid-state Raman laser output power was reported by a side-pumped laser system, end-pumped laser systems are utilised in most intracavity crystalline Raman lasers. This end-pumping configuration can provide good quality mode matching in the active crystals between the diode pump beam and the fundamental laser beam, which is favourable to achieve a low Raman threshold, high Raman conversion

efficiency and high beam quality. The highest Raman output power from an end-pump laser configuration was reported by Lin et al. in 2012 [2.70] using a double-end-pumped system displayed in Fig. 2.1.

A maximum first Stokes Raman laser output power of 4.1 W was obtained for a diode pump power of 36 W, corresponding to a diode-to-Stokes conversion efficiency of 11.2 %. The Raman threshold was measured as low as a 1.6 W diode pump power emitting at λ = 880 nm. The authors noted that, compared with the single-end-pump configuration, this double-end polarised pumping approach provided improved pump power absorption (by ~ 20 %), lower crystal temperature and better overlap (~ 60 %) between the pump beam and (Transverse Electromagnetic Mode (TEM$_{00}$)) fundamental mode.

The highest CW intracavity Raman laser output based on a single-end-pump system was reported by Fan et al [2.46] using a Nd:YVO$_4$ crystal combined with a BaWO$_4$ crystal in 2009. The Raman threshold was reached with 3.6 W of diode pump power while a maximum first Stokes Raman laser output power of 3.36 W was obtained leading to a diode-to-Stokes conversion efficiency of 13.2 %.

In 2013, Chang et al. reported the first Yb:KGW intracavity self-Raman laser operating in the CW regime [2.75]. The Raman threshold was measured at a diode pump power of 1.47 W. A maximum first Stokes Raman laser output power of 1.7 W emitting at λ = 1099.6 nm was attained for a diode pump power of 7.8 W which results in a diode-to-Stokes Raman conversion efficiency of 21.2 %. However, a wide spectral bandwidth of 8 nm was observed at the maximum first Stokes Raman output power due to the broad absorption bandwidth of the Yb:KGW crystal.

For CW visible intracavity crystalline Raman lasers, the highest CW Raman laser output performance associated with an intracavity SHG or SFG was reported by Lee et al. in 2010 [2.49]. In this work, a 5.3 W yellow Raman output (λ = 559 nm) was obtained in a Nd:GdVO$_4$ self-Raman laser configuration corresponding to a high diode-to-visible conversion efficiency of 21 %.

In addition to the high power Raman laser outputs, some applications may require a few more specific desirable parameters such as a low Raman threshold, a miniature cavity structure, or a continuous tunable output Raman wavelength. This leads to a variety of specific Raman laser device developments.

In 2011, Li et al. demonstrated a miniature, CW wavelength-selectable crystalline Raman laser including a Nd:YVO$_4$ self-Raman gain medium (with a HR coating at the pumped face), a LBO doubling crystal and a curved output coupler [2.66]. The total cavity length was only ~ 15 mm. Two visible Raman laser outputs emitting at $\lambda = 588$ nm (yellow) or 559 nm (lime) were obtained by simply adjusting the temperature of an intracavity LBO crystal (i.e. 98 °C for $\lambda = 559$ nm and 45 °C for $\lambda = 588$ nm). The Raman thresholds (0.34 W of diode pump power) were identical for these two visible wavelengths. The maximum Raman laser outputs were measured at 660 mW (for $\lambda = 559$ nm) and 320 mW (for $\lambda = 588$ nm) corresponding to diode-to-visible conversion efficiencies of 17 % and 8.4 % respectively.

The lowest Raman threshold was reported by Lisinetskii et al using a Nd:KGW/KGW composite crystal [2.43]. The diode pump threshold for the first Stokes Raman output emitting at $\lambda = 1181$ nm was measured at only 230 mW. A maximum Raman output of 277 mW was obtained at 2 W corresponding to a diode-to-Stokes conversion efficiency of 13.9 %.

To further extend all-solid-state Raman output spectral coverage in the CW regime and make it continuously adjustable, a variety of novel intracavity crystalline Raman lasers combined with Semiconductor Disk Lasers (SDLs, also known as Vertical External-Cavity Surface Emitting Lasers, (VECSELs)) were developed. It was first demonstrated by Parrotta et al. in 2011 using an intracavity KGW Raman laser pumped by an InGaAs SDL [2.65]. The Raman laser output wavelength could be tuned between $\lambda = 1133$ nm and 1157 nm by rotating the intracavity birefringent filter. The Raman laser threshold was achieved for a diode pump power of 5.6 W. A maximum Raman laser output

power was measured at 0.8 W emitting at λ = 1143 nm with a diode-to-Stokes conversion efficiency of 7.5 %.

In 2012, Lin et al. reported a compact SDL-pumped, CW, visible KGW Raman laser combining SHG and SFG techniques [2.67]. A GaAs material was used to fabricate the semiconductor disk with a strained InGaAs quantum well structure, which produced tunable emission between 1040 and 1076 nm. By tuning the temperature of an intracavity LBO crystal, two separate tunable emitting bands could be obtained, either between λ = 548.5 nm to 566 nm based on SFG of the fundamental and first Stokes fields or between λ = 577.5 nm to 596 nm based on the SHG of the first Stokes field. The maximum Raman laser output power for SFG and SHG were achieved at 0.8 W for λ = 560 nm and 0.52 W for λ = 592.5 nm corresponding to diode-to-visible conversion efficiencies of 4.2 % and 2.9 % respectively.

In 2013, a SDL pumped intracavity CW diamond laser operating from λ = 1209 nm to 1256 nm was demonstrated by Parrotta et al. [2.74]. Over 10 nm of tuning of the Raman laser output was achieved with an output power above 4 W. A maximum Raman laser output power of 4.4 W was obtained while emitting at λ = 1228 nm, corresponding to a diode-to-Stokes conversion efficiency of 14.2 %. Using this laser in conjunction with a doubling crystal of LBO, an orange-red visible light (λ = 604.5 nm to 619.5 nm) was observed. Up to 1.5 W emitting at λ = 614 nm was measured, corresponding to a diode-to-visible conversion efficiency of 5.4 %.

2.4 Conclusion

As the work in this thesis is entirely focused on all-solid-state CW intracavity Raman lasers, the most recent and significant developments of this type of Raman laser configuration have been thoroughly reviewed in this chapter. Over the last decade, it has been widely utilised as an efficient approach to extend the spectral coverage of solid-state lasers emitting at near-infrared and

visible spectra. This leads to a range of applications in retinal laser photocoagulation [2.78], single-molecule detection [2.79], laser projection displays, and remote sensing (bathymetry or underwater detection) [2.2]. However, due to the main limitations of intracavity solid-state Raman lasers operating in the CW regime, which were described in section 1.3, the Raman laser output performances were typically restrained to be less than ~ 6 W. Overcoming the restricting issues (i.e. mainly due to the significant thermal lens effect within Raman active materials) and power-scaling the intracavity crystalline Raman lasers to new power levels (> 10 W) is highly required for many high-profile applications, notably astronomic guide stars [2.80] and large-scale laser projection displays [2.2].

2.5 References

2.1   E. J. Woodbury and W. K. Ng, "Ruby laser operation in the near IR," Proc. IRE. **50**, 2347–2348 (1962).

2.2   H. M. Pask, P. Dekker, R. P. Mildren, D. J. Spence, J. A. Piper, "Wavelength-versatile visible and UV sources based on crystalline Raman lasers," Prog. Quant. Electron. **32**, 121-158 (2008).

2.3   C. Webb, J. Jones, *Handbook of Laser Technology and Applications, Volume II: Laser design and laser systems*, (IOP Press, 2004).

2.4   A. J. Glass, "Design Considerations for Raman Lasers," IEEE J. Quant. Electron.**3**, 516-520 (1967).

2.5   H. M. Pask, "The design and operation of solid-state Raman lasers," Prog. Quant. Electron. **27**, 3-56 (2003).

2.6   D. C. Hanna, D. J. Pointer, and D. J. Pratt, "Stimulated Raman Scattering of Picosecond Light Pulses in Hydrogen, Deuterium, and Methane," IEEE J. Quant. Electron. **22**, 332-336 (1986).

2.7   G. Eckhardt, "Selection of Raman Laser Materials," IEEE J. Quant. Electron. **2**, 1-8 (1966).

2.8   K. Sentrayan and V. Kushawaha, "Competition between steady state stimulated Raman and Brillouin scattering processes in CH_4 and H_2," J. Phys. D: Appl. Phys. **26**, 1554-1560 (1993).

2.9   S. R. J. Brueck and H. Kildal, "Efficient Raman Frequency Conversion in Liquid Nitrogen," IEEE J. Quant. Electron. **18**, 310-312 (1982).

2.10   M. Cardona (Ed), *Light Scattering in Solids, Volume. I*, (Springer Press, 1983).

2.11   J. A. Piper and H. M. Pask, "Crystalline Raman Lasers," IEEE J. Sel. Topics Quantum Electron. **13**, 692-704 (2007).

2.12   G. P. Agrawal, *Nonlinear Fiber Optics*, （Academic Press, San Diego, 1995).

2.13   Y. Feng, L. R. Taylor, and D. B. Calia, "150 W highly-efficient Raman fiber laser," Opt. Express. **17**, 23678-23683 (2009).

2.14   R. J. Williams, J. Nold, M. Strecker, O. Kitzler, A. McKay, T. Schreiber and R. P. Mildren, "Efficient Raman frequency conversion of high-power fiber lasers in diamond," Laser Photon. Rev. **9**, 405-411 (2015).

2.15   H. Jiang, L. Zhang, and Y. Feng, "Silica-based fiber Raman laser at > 2.4 µm," Opt. Lett. **40**, 3249-3252 (2015).

2.16   D. Faucher, M. Bernier, N. Caron, and R. Vallée, "Erbium-doped all-fiber laser at 2.94 µm," Opt. Lett. **34**, 3313-3315 (2009).

2.17   C. Carbonnier, H. Tobben, and U. B. Unrau, "Room temperature cw fibre laser at 3.22 µm," Electron. Lett. **34**, 893-894 (1998).

2.18   J. Schneider, C. Carbonnier, and U. B. Unrau, "Characterization of a Ho^{3+}-doped fluoride fiber laser with a 3.9 µm emission wavelength," Appl. Opt. **36**, 8595-8600 (1997).

2.19   G. Eckhardt, D. P. Bortfeld and M. Geller, "Stimulated emission of Stokes and anti-Stokes Raman lines from diamond, calcite and α-sulfur single crystals," Appl. Phys. Lett. **3**, 137-138 (1963)

2.20   E. O. Ammann and J. Falk, "Stimulated Raman scattering at kHz pulse repetition rates," Appl. Phys. Lett. **27**, 662-664 (1975).

2.21   E. O. Ammann and C. D. Decker, "0.9-W Raman oscillator," J. Appl. Phys. **48**, 1973-1975 (1977).

2.22   E. O. Ammann, "Simultaneous stimulated Raman scattering and optical frequency mixing in lithium iodate," Appl. Phys. Lett **34**, 838-840 (1979).

2.23   K. Andryunas, Y. Vishakas, V. Kabelka, I. V. Mochalov, A. A. Pavlyuk, G. T. Petrovskii, and Y. Syrus, "Stimulated-Raman self-conversion of Nd^{3+} laser light in double tungstenate crystals," JETP Lett. **42**, 410-412, (1985).

2.24   S. N. Karpukhin, and A. I. Stepanov, "Generation of radiation under conditions of stimulated Raman scattering in $Ba(NO_3)_2$, $NaNO_3$ and $CaCO_3$ crystals," Kvantovaya Elektronika **13**, 1572-1577 (1986) (Quant. Electron. **16**, 1027-1031 (1986)).

2.25   A. S. Eremenko, S. N. Karpukhin, and A. I. Stepanov, "Stimulated Raman scattering of the second harmonic of a neodymium laser in nitrate crystals," Kvantovaya Elektronika **7**, 196-197 (1980) (Quant. Electron. **10**, 113-114 (1980)).

2.26   P. G. Zverev, J. T. Murray, R. C. Powell, R. J. Reeves, "Stimulated Raman scattering of picosecond pulses in barium nitrate crystals," Opt. Commun. **97**, 59-64 (1993).

2.27   J. T. Murray, R. C. Powell, N. Peyghambarian, D. Smith, W. Austin, and R. A. Stolzenberger, "Generation of 1.5 μm radiation through intracavity solid-state Raman shifting in $Ba(NO_3)_2$ nonlinear crystals," Opt. Lett. **20**, 1017-1019 (1995).

2.28   C. He, T. H. Chyba, "Solid-state barium nitrate Raman laser in the visible region," Opt. Commun. **135**, 273-278 (1997).

2.29   H. M. Pask, J. A. Piper, "Practical 580nm source based on frequency doubling of an intracavity-Raman-shifted Nd:YAG laser," Opt. Commun. **148**, 285-288 (1998).

2.30   H. M. Pask and J. A. Piper, "Efficient all-solid-state yellow laser source producing 1.2 W average power," Opt. Lett. **24**, 1490-1492 (1999).

2.31   I. V. Mochalov, "Laser and nonlinear properties of the potassium gadolinium tungstate laser crystal $KGd(WO_4)_2:Nd^{3+}$-(KGW:Nd)," Opt. Eng. **36**, 1660-1669 (1997).

2.32   A. S. Grabtchikov, A. N. Kuzmin, V. A. Lisinetskii, V. A. Orlovich, and G. I. Ryabtsev, "All solid-state diode-pumped Raman laser with self-frequency conversion," Appl. Phys. Lett **75**, 3742-3744 (1999).

2.33   A. A. Demidovich, A. S. Grabtchikov, V. A. Lisinetskii, V. N. Burakevich, V. A. Orlovich, W. Kiefer, "Continuous-wave Raman generation in a diode-pumped Nd^{3+}:$KGd(WO_4)_2$," Opt. Lett. **30**, 1701-1703 (2005).

2.34   H. M. Pask, "Continuous-wave, all-solid-state, intracavity Raman laser," Opt. Lett. **30**, 2454-2456 (2005).

2.35   A. S. Grabtchikov, V. A. Lisinetskii, and V. A. Orlovich, M. Schmitt, R. Maksimenka, and W. Kiefer, "Multimode pumped continuous-wave solid-state Raman laser," Opt. Lett. **29**, 2524-2526 (2004).

2.36   A. A. Kaminskii, K. Ueda, H. J. Eichler, Y. Kuwano, H. Kouta, S. N. Bagaev, T. H. Chyba, J. C. Barnes, G. M. A. Gad, T. Murai, and J. Lu, "Tetragonal vanadates YVO_4 and $GdVO_4$ – new efficient $\chi^{(3)}$ - materials for Raman lasers," Opt. Commun. 1**94**, 201-206 (2001).

2.37   Y. F. Chen, "Compact efficient self-frequency Raman conversion in diode-pumped passively Q-switched Nd:$GdVO_4$ laser," Appl. Phys. B **78**, 685-687 (2004).

2.38   Y. F. Chen, "Efficient subnanosecond diode-pumped passively Q-switched Nd:YVO_4 self-stimulated Raman laser," Opt. Lett. **29**, 1251-1253 (2004).

2.39   V. A. Orlovich, V. N. Burakevich, A. S. Grabtchikov, V. A. Lisinetskii, A. A. Demidovich, H. J. Eichler, and P. Y. Turpin, "Continuous-wave intracavity Raman generation in $PbWO_4$ crystal in the Nd:YVO_4 laser," Laser Phys. Lett. **3**, 71-74 (2006).

2.40   V. N. Burakevich, V. A. Lisinetskii, A. S. Grabtchikov, A. A. Demidovich, V. A. Orlovich, V. N. Matrosov, "Diode-pumped continuous-wave Nd:YVO_4 laser with self-frequency Raman conversion," Appl. Phys. B **86**, 511-514 (2007).

2.41   P. Dekker, H. M. Pask, and J. A. Piper, "All-solid-state 704 mW continuous-wave yellow source based on an intracavity, frequency-doubled crystalline Raman laser," Opt. Lett. **32**, 1114-1116 (2007).

2.42   P. Dekker, H. M. Pask, D. J. Spence and J. A. Piper, "Continuous-wave, intracavity doubled, self-Raman laser operation in Nd:GdVO$_4$ at 586.5 nm," Opt. Express. **15**, 7038-7046 (2007).

2.43   V. A. Lisinetskii, A. S. Grabtchikov, A. A. Demidovich, V. N. Burakevich, V. A. Orlovich, A. N. Titov, "Nd:KGW/KGW crystal: efficient medium for continuous-wave intracavity Raman generation," Appl. Phys. B **88**, 499-501 (2007).

2.44   A. J. Lee, H. M. Pask, T. Omatsu, P. Dekker, J. A. Piper, "All-solid-state continuous-wave yellow laser based on intracavity frequency-doubled self-Raman laser action," Appl. Phys. B **88**, 539-544 (2007).

2.45   A. J. Lee, H. M. Pask, P. Dekker, J. A. Piper, "High efficiency, multi-Watt CW yellow emission from an intracavity-doubled self-Raman laser using Nd:GdVO$_4$," Opt. Express. **16**, 21958-21963 (2008).

2.46   L. Fan, Y. Fan, Y. Li, H. Zhang, Q. Wang, J. Wang, and H. Wang, "High-efficiency continuous-wave Raman conversion with a BaWO$_4$ Raman crystal," Opt. Lett. **34**, 1687-1689 (2009).

2.47   L. Fan, Y. X. Fan, Y. H. Duan, Q. Wang, H. T. Wang, G. H. Jia, C. Y. Tu, "Continuous-wave intracavity Raman laser at 1179.5 nm with SrWO$_4$ Raman crystal in diode-end-pumped Nd:YVO$_4$ laser," Appl. Phys. B **94**, 553-557 (2009).

2.48   F. G. Yang, Z. Y. You, Z. J. Zhu, Y. Wang, J. F. Li, and C. Y. Tu, "End-pumped continuous-wave intracavity yellow Raman laser at 590 nm with SrWO$_4$ Raman crystal," Laser Phys. Lett. **7**, 14-16 (2010)

2.49   A. J. Lee, H. M. Pask, D. J. Spence, and J. A. Piper, "Efficient 5.3 W cw laser at 559 nm by intracavity frequency summation of fundamental and first Stokes wavelengths in a self-Raman Nd:GdVO$_4$ laser," Opt. Lett. **35**, 682-684 (2010).

2.50   A. J. Lee, H. M. Pask, J. A. Piper, H. Zhang, and J. Wang, "An intracavity, frequency-doubled BaWO$_4$ Raman laser generating multi-watt continuous-wave, yellow emission," Opt. Express. **18**, 5984-5992 (2010).

2.51   Y. F. Lu, W. B. Cheng, Z. Xiong, J. Lu, L. J. Xu, G. C. Sun, and Z. M. Zhao, "Efficient CW laser at 559 nm by intracavity sum-frequency mixing in a self-Raman Nd:YVO$_4$ laser under direct 880 nm diode laser pumping," Laser Phys. Lett. **7**, 787-789 (2010).

2.52   Y. Lu, X. Zhang, S. Li, J. Xia, W. Cheng, and Z. Xiong, "All-solid-state cw sodiumD$_2$ resonance radiation based on intracavity frequency-doubled self-Raman laser operation in double-end diffusion-bonded Nd^{3+}:LuVO$_4$ crystal," Opt. Lett. **35**, 2964-2966 (2010).

2.53   W. Lubeigt, G. M. Bonner, J. E. Hastie, M. D. Dawson, D. Burns, and A. J. Kemp, "Continuous-wave diamond Raman laser," Opt. Lett. **35**, 2994-2996 (2010).

2.54   A. J. Lee, D. J. Spence, J. A. Piper, and H. M. Pask, "A wavelength-versatile, continuous-wave, self-Raman solid-state laser operating in the visible," Opt. Express. **18**, 20013-20018 (2010).

2.55   A. J. Lee, J. Lin, and H. M. Pask, "Near-infrared and orange-red emission from a continuous-wave, second-Stokes self-Raman Nd:GdVO$_4$ laser," Opt. Lett. **35**, 3000-3002 (2010).

2.56   L. Fan, Y. X. Fan H. T. Wang, "A compact efficient continuous-wave self-frequency Raman laser with a composite YVO$_4$/Nd:YVO$_4$/YVO$_4$ crystal," Appl. Phys. B **101**, 493-496 (2010).

2.57   H. Y. Zhu, Y. M. Duan, G. Zhang, C. H. Huang, Y. Wei,·W. D. Chen, L. X. Huang, Y. D. Huang, "Efficient continuous-wave YVO$_4$/Nd:YVO$_4$ Raman laser at 1176 nm," Appl. Phys. B **103**, 559-562 (2011).

2.58 J. Xia, Y. F. Lu, X. H. Zhang, W. B. Cheng, Z. Xiong, J. Lu, L. J. Xu, G. C. Sun, Z. M. Zhao, and Y. Tan, "All-solid-state CW Nd:KGd(WO$_4$)$_2$ self-Raman laser at 561 nm by intracavity sum-frequency mixing of fundamental and first-Stokes wavelengths," Laser Phys. Lett. **8**, 21-23 (2011).

2.59 Y. Zhu, G. Zhang, Y. Duan, C. Huang, Y. Wei, "Compact Continuous-Wave Nd:YVO$_4$ Laser with Self-Raman Conversion and Sum Frequency Generation," Chin. Phys. Lett. **28**, 1-3 (2011).

2.60 H. Yu, Z. Li, A. J. Lee, J. Li, H. Zhang, J. Wang, H. M. Pask, J. A. Piper, and M. Jiang, "A continuous wave SrMoO$_4$ Raman laser," Opt. Lett. **36**, 579-581 (2011).

2.61 D. C. Parrotta, W. Lubeigt, A. J. Kemp, D. Burns, M. D. Dawson, and J. E. Hastie, "Continuous-wave Raman laser pumped within a semiconductor disk laser cavity," Opt. Lett. **36**, 1083-1085 (2011).

2.62 X Li, A. J. Lee, H. M. Pask, J. A. Piper, and Y. Huo, "Efficient, miniature, cw yellow source based on an intracavity frequency-doubled Nd:YVO$_4$ self-Raman laser," Opt. Lett. **36**, 1428-1430 (2011).

2.63 W. Lubeigt, V. G. Savitski, G. M. Bonner, S. L. Geoghegan, I. Friel, J. E. Hastie, M. D. Dawson, D. Burns, and A. J. Kemp, "1.6 W continuous-wave Raman laser using low-loss synthetic diamond," Opt. Express. **19**, 6938-6944 (2011).

2.64 X. Li, A. J. Lee, H. M. Pask, J. A. Piper and Y. Huo, "330 mW CW yellow emission from miniature self-Raman laser based on direct HR-coated Nd:YVO$_4$ crystal," IQEC/CLEO Pacific Rim 1250-1252 (2011).

2.65 D. C. Parrotta, A. J. Kemp, M. D. Dawson, and J. E. Hastie, "Tunable continuous-wave diamond Raman laser," Opt. Express. **19**, 24165-24170 (2011).

2.66 X. Li, H. M. Pask, A. J. Lee, Y. Huo, J. A. Piper, and D. J. Spence, "Miniature wavelength-selectable Raman laser: new insights for optimizing performance," Opt. Express. **19**, 25623-25631 (2011).

2.67   J. Lin, H. M. Pask, D. J. Spence, C. J. Hamilton, and G. P. A. Malcolm, "Continuous-wave VECSEL Raman laser with tunable lime-yellow-orange output," Opt. Express. **20**, 5219-5224 (2012).

2.68   V. G. Savitski, I. Friel, J. E. Hastie, M. D. Dawson, D. Burns, and A. J. Kemp, "Characterization of Single-Crystal Synthetic Diamond for Multi-Watt Continuous-Wave Raman Lasers," IEEE J. Quant. Electron. **48**, 328-337 (2012).

2.69   J. Jakutis-Neto, J. Lin, N. U. Wetter, and H. Pask, "Continuous-wave watt-level Nd:YLF/KGW Raman laser operating at near-IR, yellow and lime-green wavelengths," Opt. Express. **20**, 9841-9850 (2012).

2.70   J. Lin, H. M. Pask, "Nd:GdVO$_4$ self-Raman laser using double-end polarised pumping at 880 nm for high power infrared and visible output," Appl. Phys. B **108**, 17-24 (2012).

2.71   X. Li, A. J. Lee, Y. Huo, H. Zhang, J. Wang, J. A. Piper, H. M. Pask, and D. J. Spence, "Managing SRS competition in a miniature visible Nd:YVO$_4$/BaWO$_4$ Raman laser," Opt. Express. **20**, 19305-19312 (2012).

2.72   Y. Tan, X. H. Fu, P. Zhai and X. H. Zhang, "An efficient cw laser at 560 nm by intracavity sum-frequency mixing in a self-Raman Nd:LuVO$_4$ laser," Laser Phys. **23**, 1-4 (2013).

2.73   R. Li, R. Bauer, and W. Lubeigt, "Continuous-Wave Nd:YVO$_4$ self-Raman lasers operating at 1109 nm, 1158 nm and 1231 nm," Opt. Express. **21**, 17745-17750 (2013).

2.74   D. C. Parrotta, A. J. Kemp, M. D. Dawson, and J. E. Hastie, "Multiwatt, Continuous-Wave, Tunable Diamond Raman Laser With Intracavity Frequency-Doubling to the Visible Region," IEEE J. Sel. Topics Quantum Electron. **19**, 1400108 (2013).

2.75   M. T. Chang, W. Z. Zhuang, K. W. Su, Y. T. Yu, and Y. F. Chen, "Efficient continuous-wave self-Raman Yb:KGW laser with a shift of 89 cm^{-1}," Opt. Express. **21**, 24590-24598 (2013).

2.76   D. Geskus, J. Jakutis-Neto, H. M. Pask, and N. U. Wetter, "Intracavity frequency converted Raman laser producing 10 deep blue to cyan emission lines with up to 0.94 W output power," Opt. Lett. **39**, 6799-6802 (2014).

2.77   C. C. Kores, J. Jakutis-Neto, D. Geskus, H. M. Pask, and N. U. Wetter, "Diode-side-pumped continuous wave Nd^{3+}: YVO4 self-Raman laser at 1176 nm," Opt. Lett. **40**, 3524-3527 (2015).

2.78   J. H. Lock, K. C. Fong, "Retinal Laser Photocoagulation," Med J. Malaysia. **65**, 88-93 (2010).

2.79   M. F. Garcia-Parajo, M. Koopman, E. M. van Dijk, V. Subramaniam, and N. F. van Hulst, "The nature of fluorescence emission in the red fluorescent protein DsRed, revealed by single-molecule detection," Proc. Natl. Acad. Sci. U.S.A. **98**, 14392-14397 (2001).

2.80   S. Wada, N. Saito, M. Kato, K. Akagawa, A. Takazawa, Y. Hayano, H. Takami, "High Power Yellow Light Generation for Laser Guide Star," in Advanced Solid-State Photonics, paper MB5, (2006).

Chapter 3

Adaptive optics principle and applications

3.1 Introduction

AO is a technique used to compensate for variable optical aberrations [3.1]. This concept was firstly proposed by Horace Babcock, an astronomer who worked at Mount Wilson Observatory, in 1953 [3.2]. He described a dynamic optical system, featuring a deformable optical element cooperating with a wavefront sensor (WFS), which can be utilised to correct for the degradations of astronomical images induced by atmospheric turbulence. However, the experimental realisation of his idea was not achieved due to the technological limitations for a successful AO system at that time.

In 1957, Robert Leighton et al. achieved the first step to include an AO system in an astronomy setup by implanting a tiltable secondary reflecting mirror inside the 60-inch telescope at Mount Wilson Observatory (see Fig. 3.1) [3.3]. By tilting the reflecting mirror, they demonstrated the potential to partially correct for the atmospheric turbulence distortions and successfully obtained the clearest images of Jupiter and Saturn up to that time. This can be treated as the earliest "proof-of-concept" for an AO technique utilised in astronomy. However, to further remove the atmospheric turbulence effects, a new technology was required to correct the incoming wavefront distortion with more controllable flexibility.
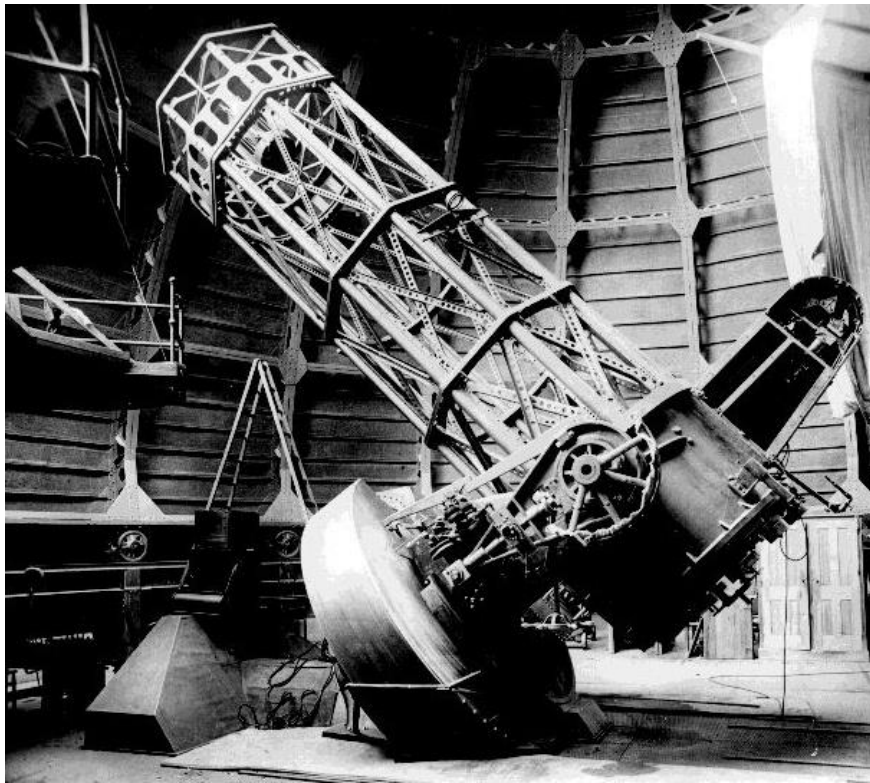
Fig. 3.1 60-inch telescope at Mount Wilson Observatory [Picture taken from http://spiff.rit.edu/classes/phys301/lectures/expand/expand.html]

Fig. 3.2 3.6 m-diameter ESO telescope at La Silla [Picture taken from http://www.eso.orgin /public/unitedkingdom/images/3m60-pan2-cc/]

In the late 1980s, a major technological breakthrough of AO was achieved by the European Southern Observatory (ESO). The first AO DM consisting of 19 individual surfaces and actuators was developed and implemented inside the 3.6 m-diameter ESO telescope at La Silla, Chile (see Fig. 3.2) [3.4]. It has been demonstrated that this more flexible AO technique can efficiently compensate for further atmospheric turbulences, which significantly improves the sharpness of optical imaging.

In 1991, the US Department of Defense declassified most of their AO investigations which had been running since 1970 [3.3]. After that, AO techniques stepped into a rapid development and have been utilised in most astronomical telescopes. Nowadays, with the rapid growing demand in astronomical observation for theoretical physics and cosmology, novel astronomical telescopes are required to collect more light with sharper focusing abilities which can be achieved by including AO systems. One of the well-known observatory projects is the "Thirty Meter Telescope (TMT)" [3.5]. In its plan, an extremely large aperture (~ 30 m-diameters) astronomical telescope will be constructed using 492 segmented mirrors to create the whole reflecting surface. Each segmented mirror will be adjusted separately to correct for any involved optical aberrations from the atmosphere and space. It is estimated to be functional in 2022 and its schematic diagram is shown in Fig. 3.3.
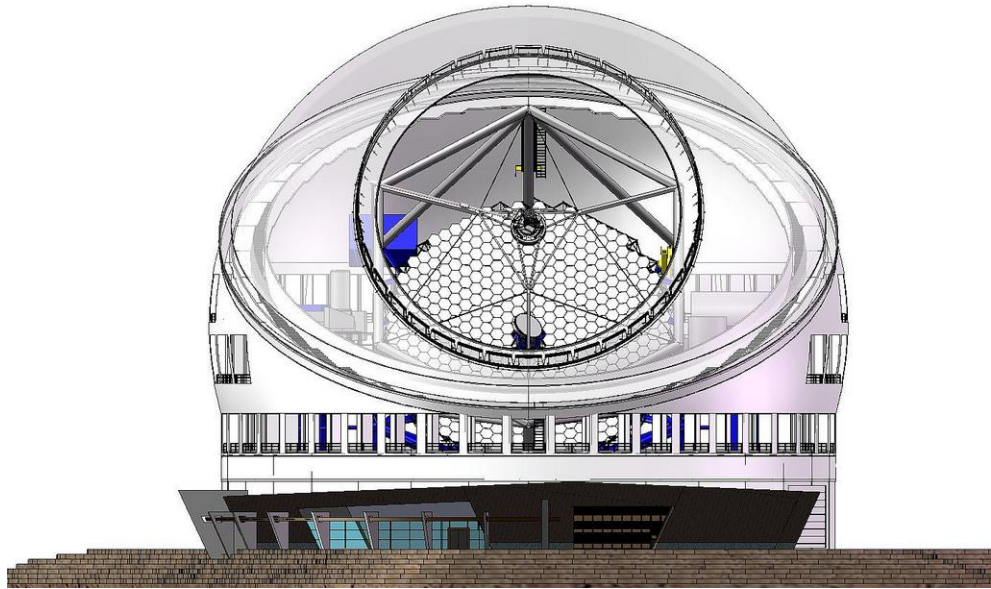
Fig. 3.3 Schematic diagram of the TMT [picture taken from
http://www.tmt.org/gallery/renderings]

In this chapter, the basic operating blocks of an AO system are described, with an AO control loop featuring the three main components of most AO systems being introduced in section 3.2. Section 3.3 describes several types of DMs. A variety of practical applications using AO techniques in astronomy, bio-microscopy, ophthalmology and laser systems will be presented in section 3.4.

3.2 AO system components

A typical AO system normally consists of three main components, a WFS, a wavefront modulator (WFM) and a control system (see Fig. 3.4). Optical aberrations of an incoming optical wavefront are assessed by the WFS and sent to the control system as an electronic signal. Then, the control system introduces a deformation pattern on the WFM to compensate for the distorted wavefront according to the information from the WFS.
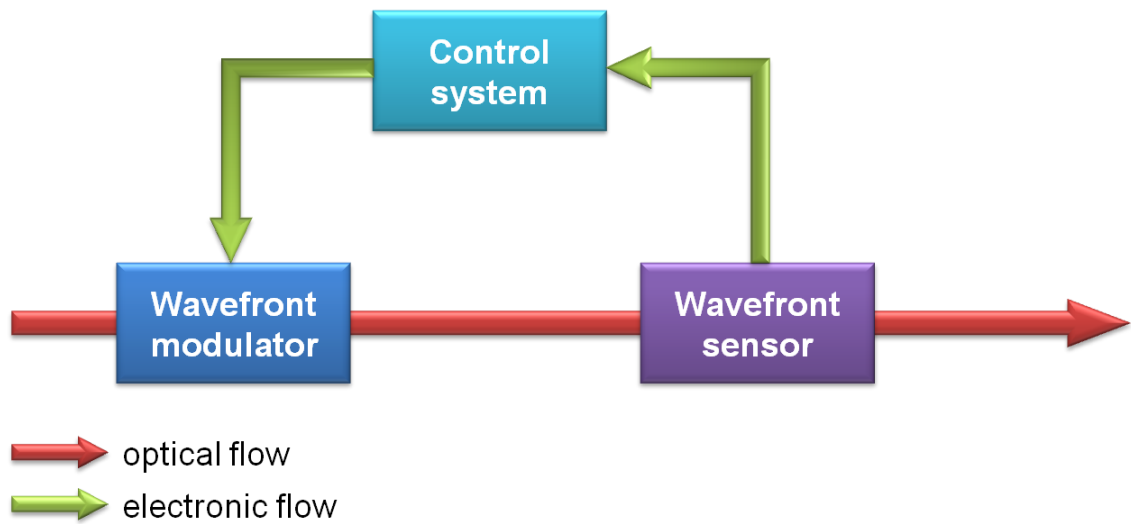
Fig. 3.4 Schematic diagram of an AO control loop system

3.2.1 Wavefront sensor

In an AO control loop system, the accurate measurement of the optical properties of an incoming wavefront is paramount for the ensuing wavefront modulation. Several measuring approaches can be used to detect the distortion of a wavefront, such as a Shack-Hartmann WFS [3.6], a shearing interferometer [3.7], or a phase retrieval technique [3.8]. Out of these the Shack-Hartmann WFS has been mostly utilised in AO systems due to its simple principle and high accuracy for the wavelength distortion in real time measurement.
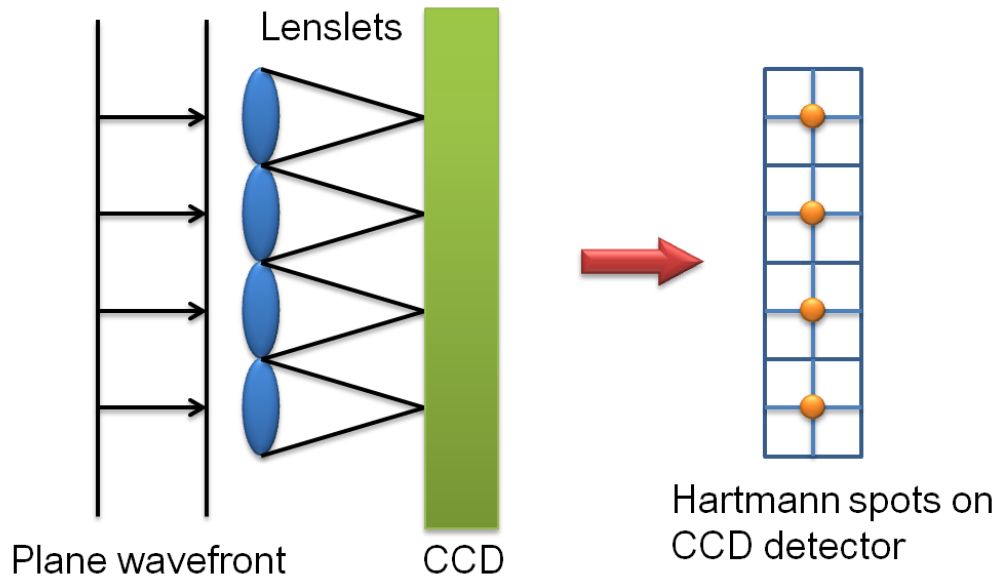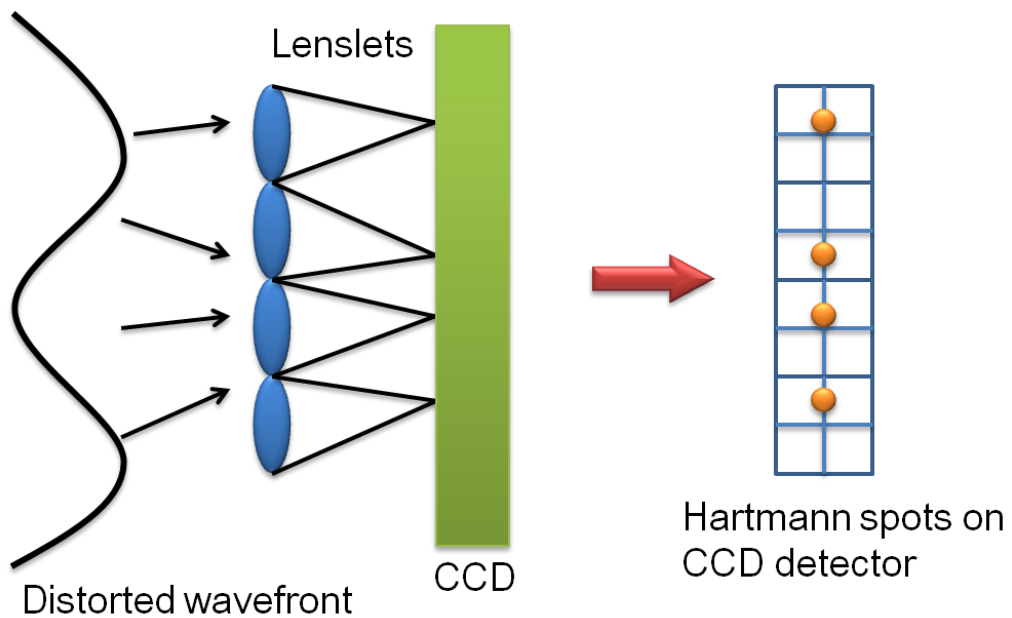
Fig. 3.5 Schematic diagram of the principle of a Shack-Hartmann WFS, (a) reference wavefront; (b) distorted wavefront

A Shack-Hartmann WFS consists of a two-dimensional microlens array (called lenslets) with all having identical focal lengths. A CCD detector is placed at the focal plane of the lenslets. As displayed in Fig. 3.5, when a planar wavefront is incident on the lenslets, the wavefront is divided into a 2D array of light

beams and separately focused onto the centre of each specific CCD grid (see Fig. 3.5 (a)). If the wavefront is distorted, it results in lateral shift of the focal spots (see Fig. 3.5 (b)). In this way, the wavefront shape can be approximated by measuring the displacement of the distorted wavefront focal spots.

The properties of the wavefront patterns can be represented by Zernike coefficients which are a series of orthogonal polynomials that arise in the expansion of a wavefront function for optical systems with circular pupils. Fig 3.6 descripts the first 6 orders of Zernike polinomials and their resulting wavefront deformation. An example of a Shack-Hartmann WFS is shown in Fig. 3.7, made by Thorlabs [3.9] (WFS150-7AR).
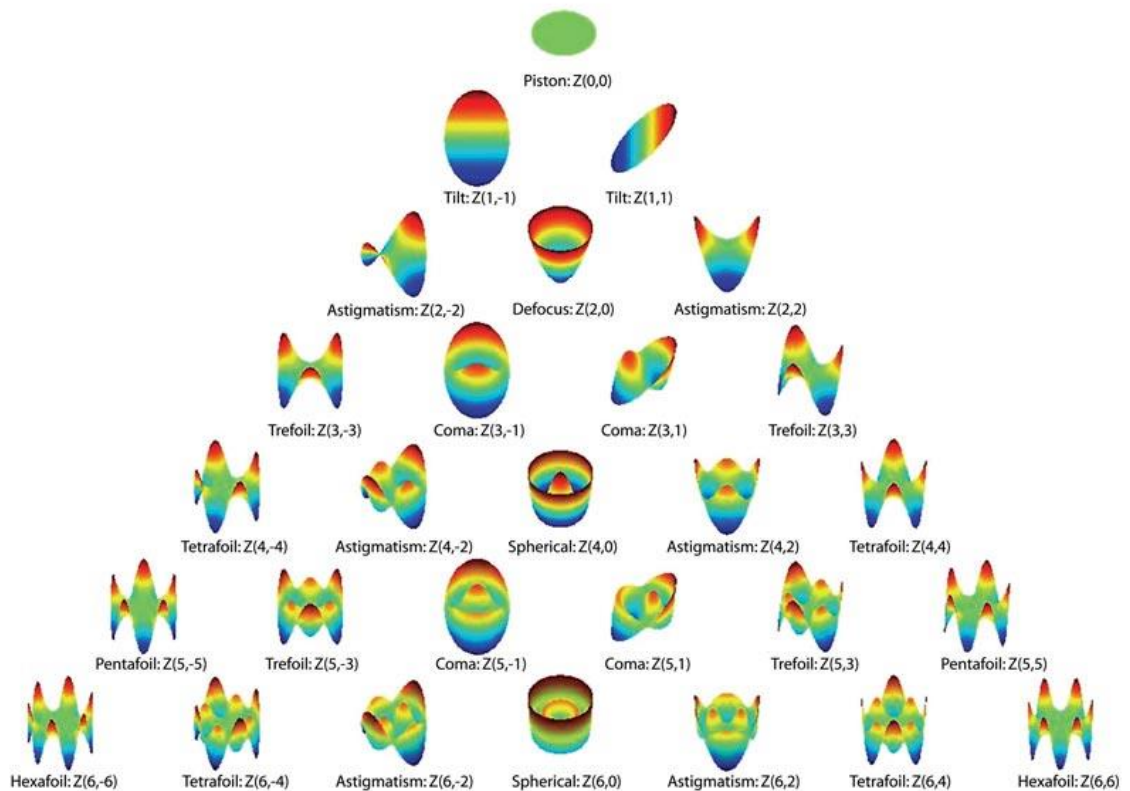
Fig. 3.6 Six orders of Zernike Polynomials [Picture taken from
http://astro.if.ufrgs.br/telesc/aberracao.htm]

Fig. 3.7 Thorlab's Shack-Hartmann Wavefront Sensors (WFS150-7AR) [Picture taken from https://www.thorlabschina.cn/newgrouppage9.cfm?objectgroup_id=2946&]

3.2.2 Wavefront modulator

The WFM plays an important role in AO systems as it is commonly used to compensate for the wavefront aberrations or to modify the phase profiles of light beams. WFMs can be divided into two categories due to their different modes of correction, namely reflective modulation and transmissive modulation (see Fig. 3.8).

(a)   (b)
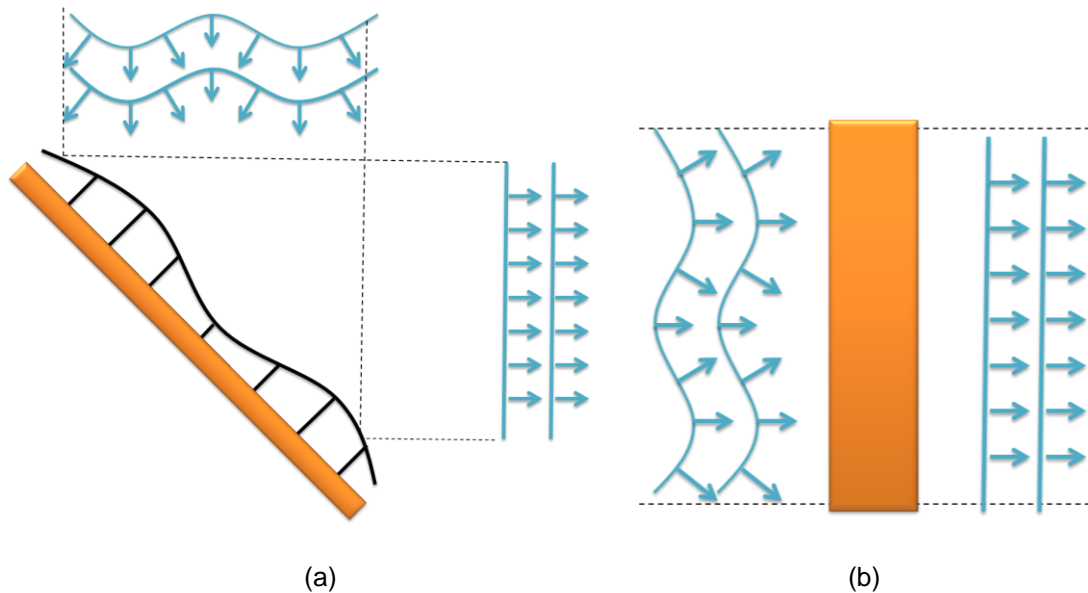
Fig. 3.8 Different types of wavefront correction, (a) reflective modulation; (b) transmissive modulation

The most common transmissive modulator is based on a nematic Liquid Crystal (LC) lens which provides a large birefringence to achieve a wide range of variable focal lengths [3.10]. As displayed in Fig. 3.9 (a), a typical LC device contains a nematic LC layer sandwiched by two glass substrates with thin transparent indium-tin-oxide layers. The LC layer is made up of a set of elongated nematic molecules which have different molecular polarisabilities corresponding to the long (along n_e direction in Fig. 3.9 (b)) and short axes (along n_o direction in Fig. 3.9 (b)). When a linearly polarised beam is incident onto the molecules, the effective refractive index can be varied according to the incident angle. For instance, if the incoming light is polarised along the long axis, the refractive index is n_e; if it is polarised along the short axis, the index of refraction would be changed to n_o; if the polarisation orientation has an arbitrary angle θ along the long axis of the molecules, the refractive index would be changed to n_{eff} which is a constant number between n_e and n_o.

(a)   (b)
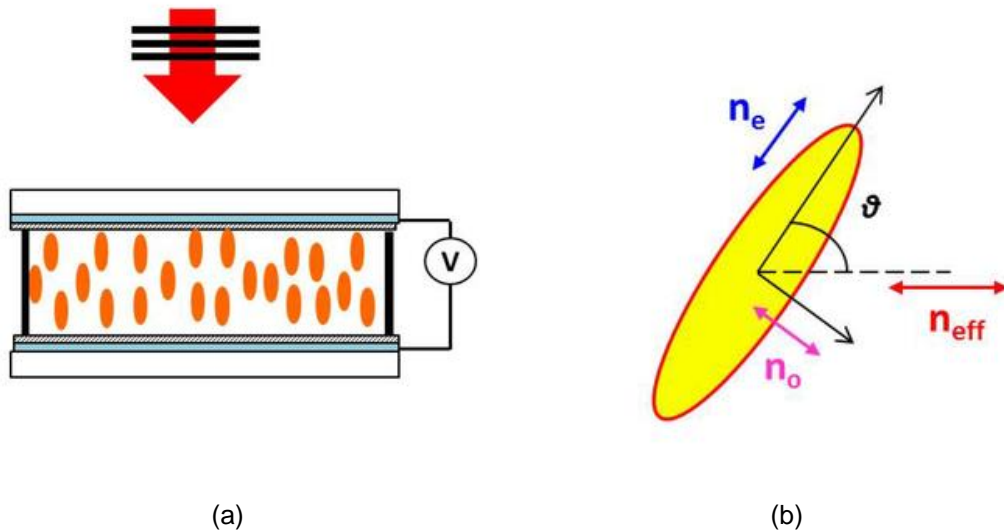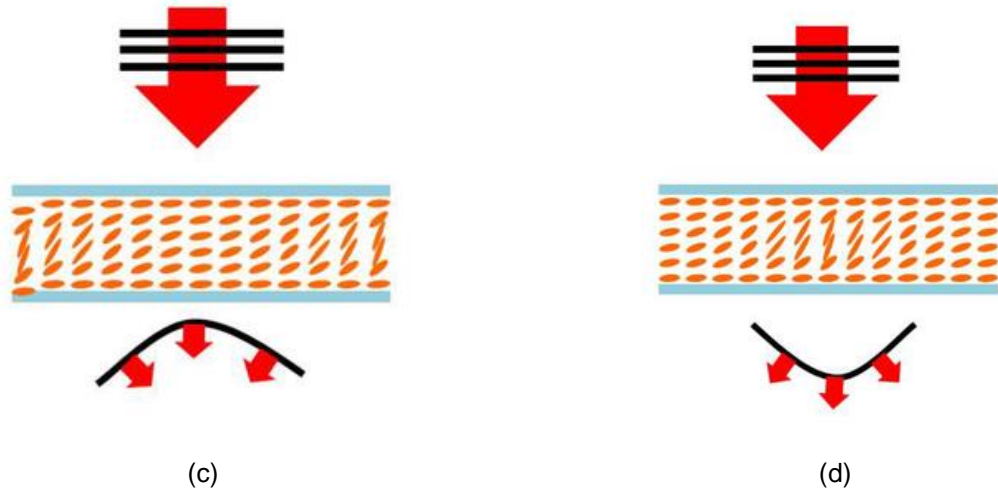
Fig. 3.9 Principle of a nematic LC lens, (a) schematic cross-section of LC lens; (b) nematic LC molecules, polarisation dependent refractive index; (c) positive LC lens shape; (d) negative LC lens shape (Pictures taken from [3.10])

Therefore, by applying a driving voltage on opposing surfaces of the LC device, an electric field can be generated inside the LC layer which alters the orientation of the LC molecules resulting in a variation of the effective refractive index. In this way, the refractive index in different local areas of the LC layer can be spatially controlled by applying a specific pattern of drive voltages. As a result, it can modify the propagating wavefront such as introducing a tilt, a bend or a desired curvature (see Fig. 3.9 (c) and (d)).

The LC lenses present a great potential in AO systems, especially for the lower-order aberration corrections (i.e. defocus and astigmatism) due to its low control voltage (i.e. a few volts), low power consumption and high reliability [3.11, 3.12]. Moreover, the cost of LC lenses (i.e. a few thousands of US $) is relatively low compared to most types of DMs since the manufacturing of LC lenses is based on a well-development LC display technology. Against these advantages, LC lenses are mainly limited by their slow response time (~ 100 ms) and polarisation dependence.

Since all of the work related in this thesis is focused on using DMs, more details of these reflective technologies will be introduced in the next section.

3.3 Deformable mirrors

The most prevalent technology used for wavefront correction is based on DMs which consist of a flexible reflective surface whose shape can be adjusted using a variety of physical actuator mechanisms such as magnetic force, electrostatic force or piezoelectricity. Micro-Electro-Mechanical Systems (MEMS) DMs are currently the most widely used technology in AO systems thanks to the rapid development of silicon device and fabrication technologies. MEMS actuators are commonly produced on a silicone substrate using photo-lithography and etching methods [3.13]. To better understand the different types of DMs and how they affect the AO systems, several important characteristics of DMs will be introduced below.

Inter-actuator coupling describes a mechanical coupling effect on all adjacent actuators when one individual actuator is driven. Spatial resolution represents the capability of DM compensation for the complicated (i.e. high order) aberration wavefront which is determined by the inter-actuator coupling and actuator numbers. Typically, a high spatial resolution corresponds to a large numbers of actuators with a low effect of inter-actuator coupling. For instance, the number of actuators in a mirror array is ranging from 19 actuators used for intracavity laser beam correction to up to 4000 actuators of a MEMS DM which can be utilised in astronomy. The maximum distance of DM deflection is called DM stroke which exhibits a significant trade-off with the spatial resolution. The maximum stroke can be achieved when all actuators are at maximum (for a circular DM, it corresponds to a near-spherical mirror shape which can be approximately represented by the ROC or the focusing power). The response frequency represents the reaction speed of a DM to the input control signal. It is mainly influenced by the structure and the material properties of the DM. A high response frequency is critical for real-time wavefront correction as needed in many intracavity laser applications. In addition, hysteresis is also an important property for DMs (especially for piezoelectric actuated DMs). As shown in Fig. 3.10, it describes the discrepancy of the focusing power variation

of the DM surface corresponding to whether the driving voltage is increased or decreased.
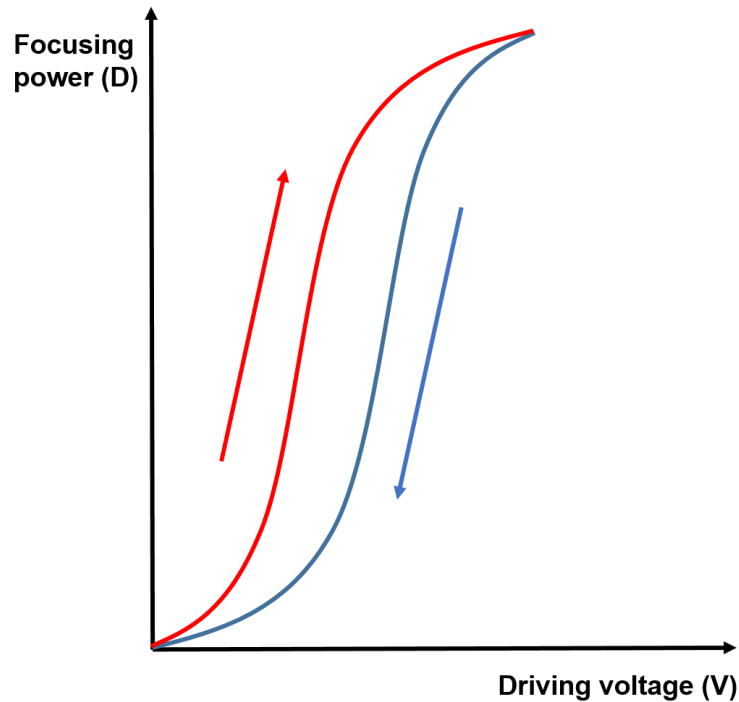
Fig. 3.10. Hysteresis phenomenon

DMs can in general be divided into either segmented DMs or continuous DMs due to the different types of reflective surface (see Fig. 3.11). The DMs have in general a membrane reflective surface connected to an actuator surface via several actuator posts. The actuator surface is supported by another set of posts and placed on top of a layer of actuators (i.e. electrodes or electromagnets). When the actuators are charged, the actuator surface is deformed by the effect of the electrostatic or electromagnetic force. Therefore, the deformation of the membrane reflective surface can be achieved by the movement of its underlying actuator posts. It should be noted that some types of continuous DMs do not have any actuator posts. Mirrors with that particular characteristic will be described in more details in the following sub-sections.
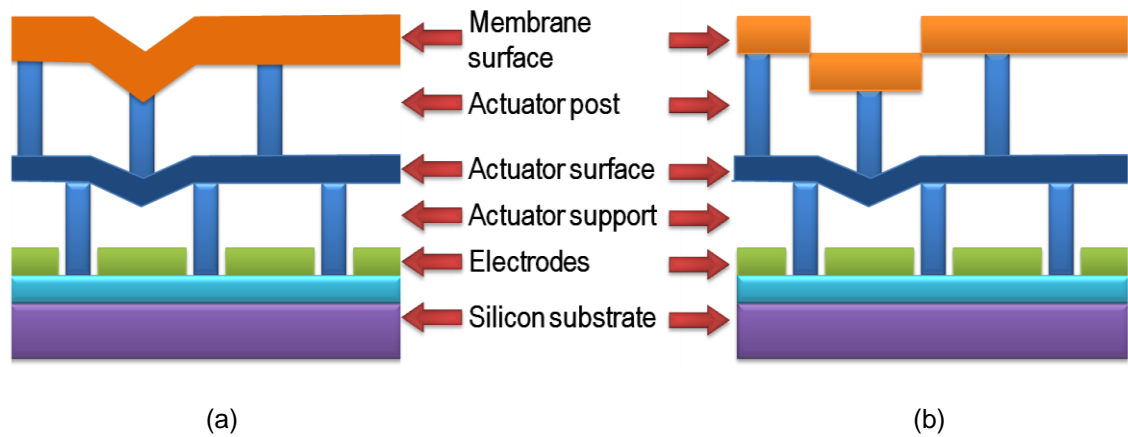
Fig. 3.11 A cross sectional schematic of DMs, (a) continuous DMs, (b) segmented DMs

3.3.1 Segmented DMs

As displayed in Fig. 3.11 (b), in segmented DMs, the mirror surface is discretely separated into a set of flat segments. Each individual mirror surface can lead to a local deformation corresponding to three degrees of freedom (piston, tip and tilt). Because each mirror segment can be controlled by one actuator post separately which does not affect the shape of the whole surface (i.e. no inter-actuator coupling which is also called "zonal" correction), it is particularly suitable to be utilised for some high-order or discontinuous wavefront correction. However, the edge gaps between adjacent actuators can lead to some diffraction effects and fitting errors which can significantly limit its utilisation in laser or high-precision applications.

In astronomy, it is difficult to construct a telescope whose aperture is over 10 metres using a single monolithic mirror surface due to a variety of limitations such as deformation and thermal issues, risk of breakage, coating problems, and the massive cost for the fabrication and transport [3.14]. Because of that, the segmented surfaces are essential for creating a solution. They were widely used for a variety of key astronomy telescopes such as the Keck Observatory telescope on Mauna Kea [3.15], and will be also utilised in several observatory projects in the future (i.e. TMT [3.5]).

The primary reflecting surface of one of the Keck telescope is displayed in Fig. 3.12 which contains 36 hexagonal segmented mirrors corresponding to a total aperture diameter of 10 metres.
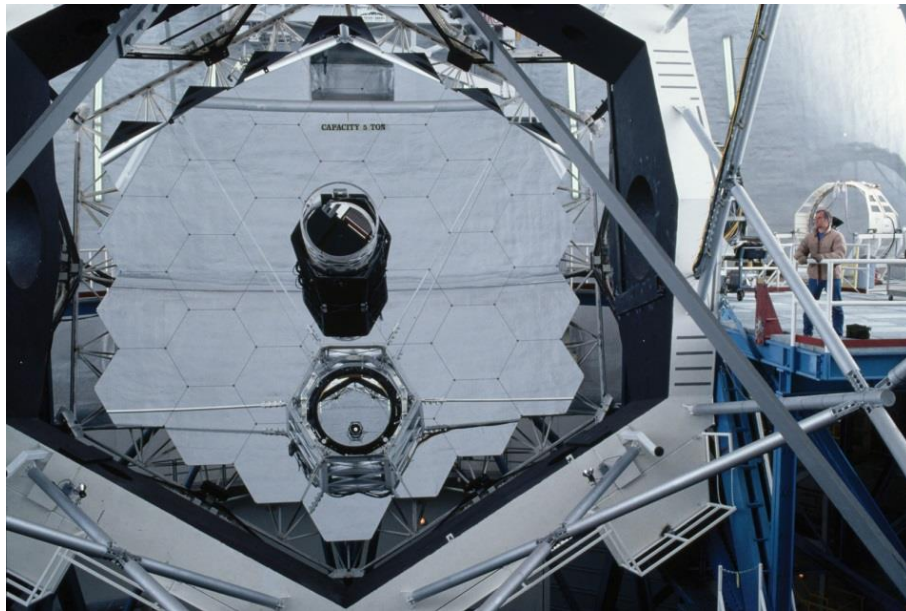
Fig. 3.12 Keck Observatory: primary segmented mirrors of Keck 1[picture taken from http://kids.britannica.com/comptons/art-90825]

Due to the expanding area of silicon device manufacturing, the smaller and compact segmented DMs were rapidly developed based on MEMS technology at a relatively low cost (i.e. a few thousands of dollars). A large number of micro-electro-mechanical actuators (from several hundreds to a few thousands) can be fabricated on silicon wafers and can be driven by electrostatic forces. The segmented MEMS DMs have been produced by many companies, such as the Iris AO [3.16] who developed a small-packaging PTT489 DM containing 163 piston-tip-tilt actuators within an inscribed aperture of 7.7 mm (see Fig. 3.13).

(a)   (b)
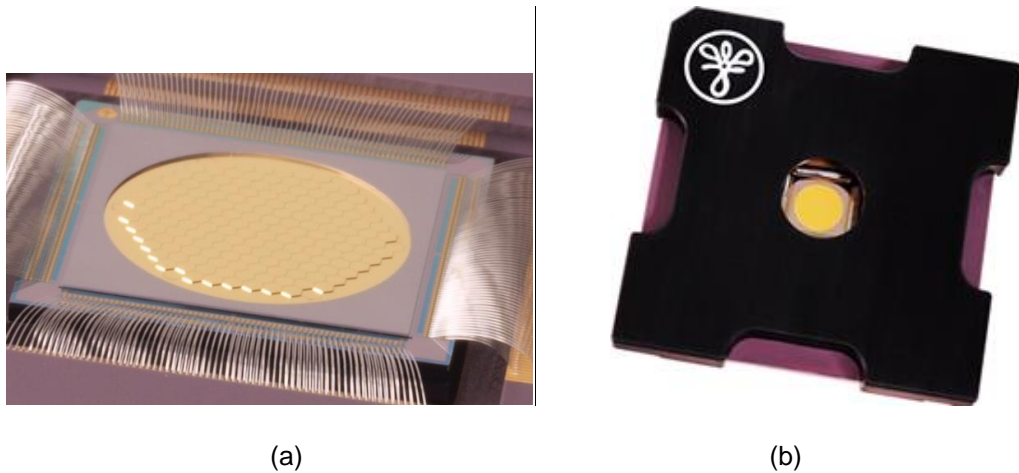
Fig. 3.13 Segmented MEMS DM (PTT489), (a) reflecting surface; (b) general view of the DM
[Picture taken from http://www.irisao.com/product.ptt489.html]

3.3.2 Continuous DMs

Different from the uncoupled control of segmented DMs, the continuous DMs
provide a smooth mechanism correction for the incoming wavefront phase
without any scattering effect (as see Fig. 3.11 (a)). They consist of only one
continuous reflecting surface controlled by a range of discrete actuators. A
global change of the whole mirror surface can be achieved by the adjustment
of each individual actuator which is also called "modal" correction. In this way,
the inter-actuator coupling effect needs to be taken into account due to each
single actuator being mechanically coupled to the surrounding actuators.
These types of DMs are particularly appropriate for some low-order corrections
such as the wavefront distortions induced in a laser system which requires a
continuous adjustment. Two types of continuous DMs are widely produced and
utilised in many practical applications, one is the membrane DM, and the other
is the bimorph DM.

3.3.2.1 Membrane DMs

Membrane DMs are constructed by a thin (i.e. from 0.5 µm to 10 µm thick),
high-reflective membrane surface mounted on top of a serial two-dimensional

electrode array (see Fig. 3.14). The membrane layer is normally fabricated using a bulk micromachining technique to produce membrane diameters ranging from 5 mm to 50 mm [3.13]. The application of driving voltages to the electrodes results in a deformation of the membrane layer towards the electrodes by the electrostatic force. Therefore, by applying a variety of drive voltages to different electrodes, a specific shape can be formed on the membrane surface corresponding to the different patterns of wavefront distortions. However, membrane DMs can only represent "concave optical shapes" since the membrane surface can only be "pulled" by the electrodes due to the electrostatic attraction. In some cases, the membrane surface is initially pre-set at a slightly concave reference (normally in the middle of the maximum stroke). In this way, the shape of membrane DMs can be adjusted to both directions of the surface deformation.
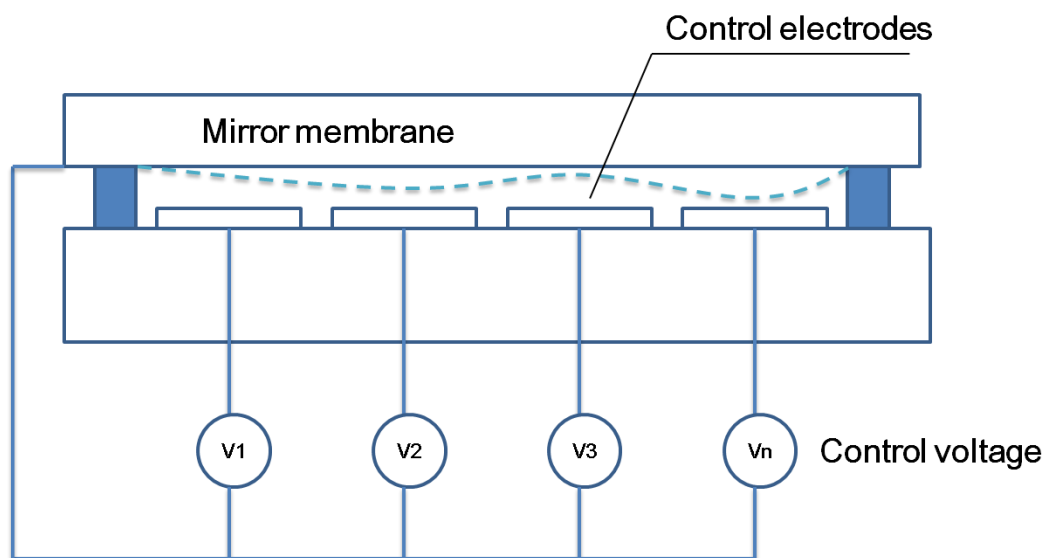
Fig. 3.14 Schematic cross-section of membrane DMs

Moreover, membrane DMs feature negligible hysteresis during surface deformation which can be utilised in automatic feedback control systems without any additional calibration. Another advantage of membrane DMs is that the electrostatic electrodes of membrane DMs are possible to be mass-produced at low cost (i.e. ~ \$ 2000) due to inexpensive fabrication techniques. For instance, OKO Technologies [3.17] have produced a series of Micro-

machined Membrane Deformable Mirrors (MMDM, see Fig. 3.15 (a)) consisting of a range of actuator numbers from 17 to 79 within a surface aperture between 15 mm to 50 mm. The maximum mirror strokes can be achieved from 9 μm to 18 μm based on the actuator numbers. The Mirao 52-e DM developed by Imagine Optics [3.18] has also been widely utilised in wavefront correction applications, especially for microscopy. 52 electromagnetic actuators are in its case allocated to a 15 mm pupil corresponding to a Stroke variation range of ± 50 μm. It should be noted that Boston Micromachines Corporation [3.19] developed a MMDM containing 4096 actuators arranged as a 64 × 64 grid pattern in an active aperture of 25 mm (see Fig. 3.15 (b)). The maximum mirror stroke of this particular DM can be up to 3.5 μm with ~ 13 % interactuator coupling. The mechanical responds time was measured as less than 100 μs.

<div align="center">(a)   (b)</div>
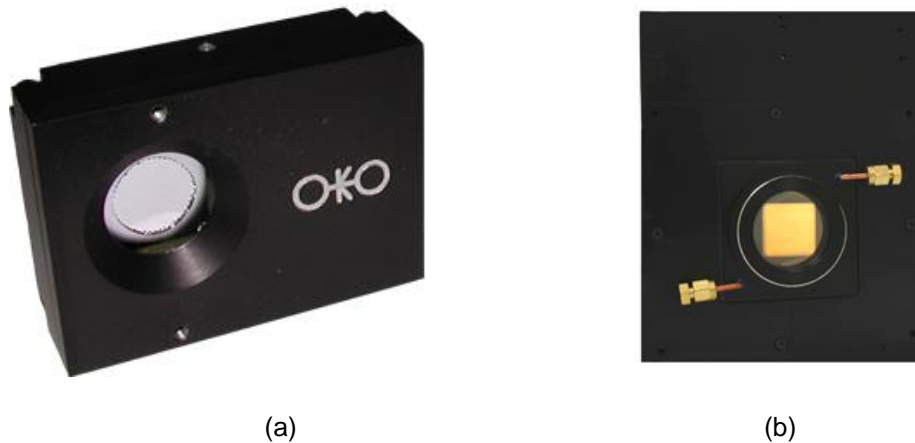
Fig. 3.15 General view of MMDM, (a) OKO 30 mm, 39-actuator MMDM; (b) Boston 4K-DM
[Picture taken from http://www.okotech.com/mmdm and
http://www.bostonmicromachines.com/plus-kilo.htm]

The main drawback of membrane DMs is related to thermal issues. Any heat deposited within the membrane surface can lead to a significant thermal deformation of the original mirror shape. This restricts several applications related to high power laser beams such as the intracavity laser control investigations presented in this thesis. However, by combining the thin membrane surfaces with metal/dielectric HR coating techniques (i.e achieving R > 99.9 %), it is possible now to implement membrane DMs inside a laser

cavity at power levels up to 600 W operating in the CW regime. Another drawback of membrane DMs is the high interactuator coupling due to the integrative membrane surface which results in a limitation for the high-order wavefront correction. For example, in OKO's 50 mm diameter, 79-actuator MMDM, the interactuator coupling is measured at 0.7 µm for a maximum mirror stroke of 18 µm.

Another type of membrane DM is based on the ferromagnetic attraction between the membrane surface and magnetic actuators (see Fig. 3.7 (a)). These devices enable a high stroke with a relatively low interactuator coupling. For instance, ALPAO SAS [3.20] developed a series of ferromagnetic DMs containing a number of actuators from 69 to 820 within a pupil diameter range from 10.5 mm to 45 mm. A maximum stroke of up to 40 µm can be achieved with a low hysteresis (i.e. < 3 %). The mechanical response time was measured as larger than 500 µs. The main limitation however is the complex and expensive manufacturing process. In practice it is utilised in many communication and astronomical applications mainly focusing on the high amplitude and low resolution wavefront aberrations.

(a)   (b)
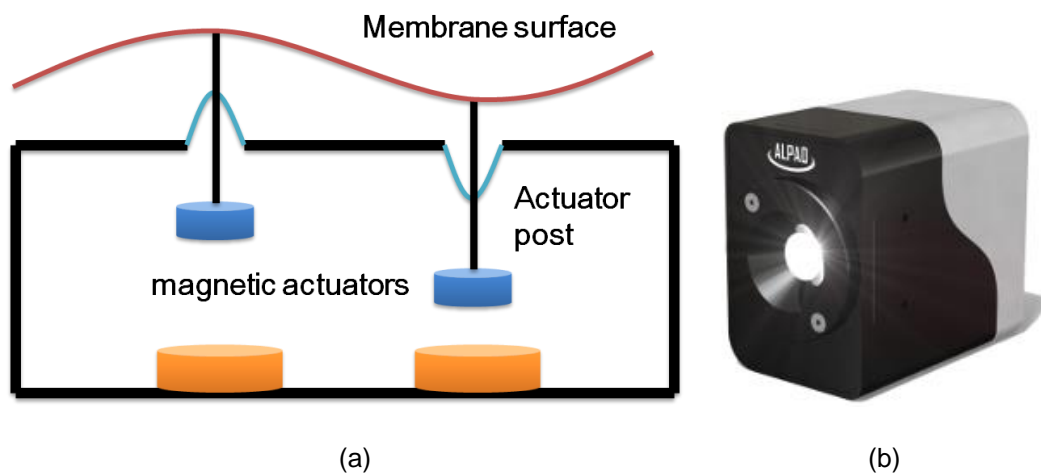
Fig. 3.16 ALPAO ferromagnetic DMs, a) cross-section schematic; b) general view [Picture taken from http://www.alpao.com/Products/Deformable_mirrors.htm]

3.3.2.2 Bimorph DMs

The surface of bimorph DMs is manufactured by two or more layers which consist of an active layer and several passive layers. The passive layers can be made of glass, fused silica or silicon which can be coated with a HR surface (i.e. R > 99.99 %). The active layer is composed of a piezo-electric material that is able to convert electric power into a mechanical stress. A set of discrete electrodes is arranged on the lower layer surface to adjust the deformation via applying a set of driving voltages (see Fig. 3.17).
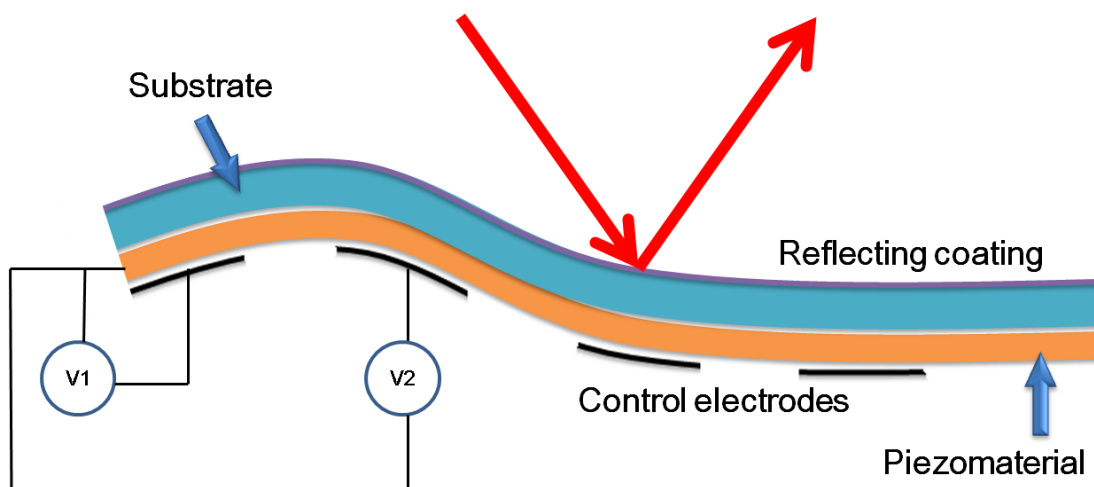
Fig. 3.17 Schematic cross-section of bimorph DMs

Unlike DMs, the piezo-electric actuators can achieve both concave and convex deformation of the reflecting surface. When a positive voltage is applied to the actuators, a stress would be generated which "pulls" the mirror surface towards the electrode structure, corresponding to a concave deformation shape; on the other hand, when the actuators have a negative drive voltage applied to them, the mirror surface would be "pushed" by the stress corresponding to a convex deformation shape. Therefore, a high stroke (i.e. + / - 40 µm for the AKA Optics DMs [3.21]) can be achieved by bimorph DMs which is beneficial for the high amplitude low-order wavelength correction. Like membrane DMs, because of the high interactuator coupling (i.e. 8 µm maximum stroke corresponding to an interactuator coupling of 2 µm for the OKO DMs [3.17]), it is struggling to

modify high-order wavefront aberration. Another main difference between bimorph DMs and membrane DMs is the ability to design the bimorph reflecting surface with many layers, resulting in a significant improvement of the damage threshold. Consequently, bimorph mirrors are widely utilised in high-power laser systems. The main drawback of bimorph DMs is the high cost of the devices (i.e. a bimorph DM with only 19-actuator can cost above $ 10000). Moreover, because it also experiences a noticeable hysteresis during the surface deformation (i.e. < 10 % hysteresis error typically [3.17]) it needs to be re-calibrated in some continuous precise adjustment.

Fig. 3.17 AKA Optics bimorph DMs [Picture taken from http://www.akaoptics.com/index.php]

Due to their advantages for high power laser systems a variety of bespoke bimorph DMs manufactured by BAE systems advanced technology centre [3.22] were utilised in this thesis (see Fig. 3.19). The characteristics of these DMs will be fully described in chapter 5 and 6.
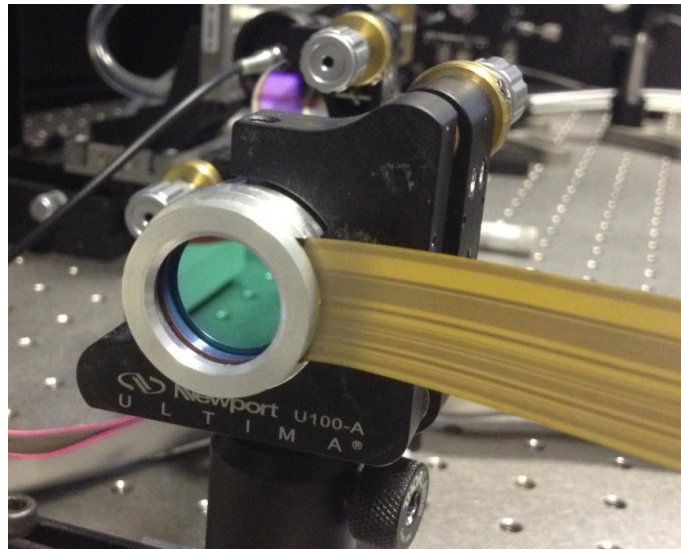
Fig. 3.18 37-actuator bimorph DM produced by BAE systems advanced technology centre
[image extracted from chapter 1 Fig. 1.10]

3.4 AO system applications

As described in section 3.1, AO systems were originally introduced to correct for the atmospheric turbulence in astronomy [3.23-3.25]. Nowadays, it has been developed into a well-established technology and is utilised in most of the major astronomical telescopes. Meanwhile, due to the rapid development of silicon manufacturing and fabrication technologies, the decreasing size (i.e. centimetre scale) and cost (i.e. a few thousands of dollars), AO components (specifically the WFMs) have been developed for a wide range of applications such as microscopy [3.26-3.29], ophthalmology [3.30-3.36], laser systems [3.36-3.48], defence industry and communications [3.35]. A selection of AO applications will be described in this section.

3.4.1 Astronomical AO system

In recent years, with the rapid development of astrophysics and cosmology, the requirements for high angular resolution observations have become more and more important [3.25]. Hindering this increased resolution requirement is

a blurring effect to the image of astronomical objects, introduced by distortion by atmospheric turbulences when a light beam from a distant star or galaxy passes through the earth's atmosphere.

These undesirable effects can be avoided by two approaches. One is placing the astronomical telescope above the earth's atmosphere, such as done with the Hubble Space Telescope. (See Fig. 3.19).

Another way is using adaptive optics to correct for the blurring effects caused by earth's atmosphere to the wavefront incident to the ground-based telescopes. As shown in Fig. 3.20, the incoming distorted wavefront is reflected by a DM and divided into two beams to illuminate a High-Resolution Camera and WFS respectively by using a beam splitter. The distorted wavefront can be measured by the WFS and sent to the control system. Following this, the reflecting surface of the DM is adjusted by a set of drive voltages from the control system to compensate for the deviation between the reference and distorted wavefront. Through this, the wavefront aberrations are corrected upon reflection. In real-time operation, this process of correction must be changed at least thousands of times each second to response to the rapid variable atmospheric turbulences [3.29].
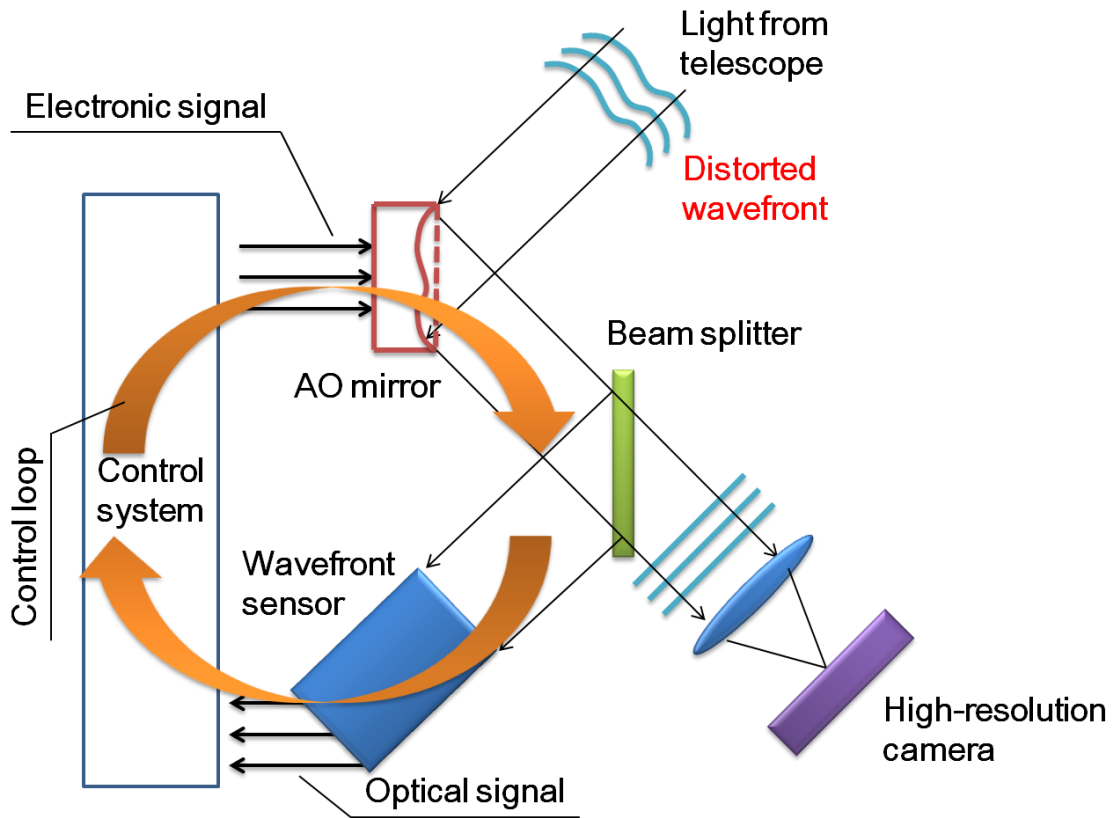
Fig. 3.20 Schematic diagram of an astronomical AO system

(a)	(b)
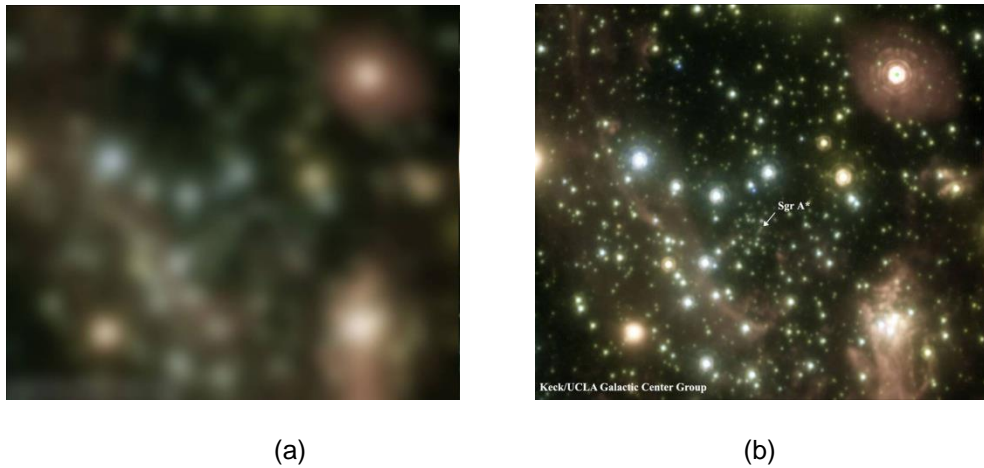
Fig. 3.21 The image of galactic center obtained by Keck Observatory, (a) without AO correction, (b) with AO correction [Picture taken from http://cosmicmatters.keckobservatory.org/2007/dec]

Fig. 3.21 displays an image of the galactic centre obtained by the Keck Observatory. A significant blurring effect can be observed in Fig. 3.21 (a).

However a much clearer image can be seen in Fig. 3.21 (b) with an AO correction implemented in the system. Due to the significantly improved resolution by using the AO correction, a black hole was also found from this image [3.25].

3.4.2 Adaptive Scanning Optical Microscope

A trade-off problem between a wide field of view and image resolution has always been encountered in conventional microscopes. Two approaches have been developed to solve this problem, using either a fast-scanning stage or a fast-scanning lens [3.29]. The fast-scanning stage enables to move different parts of the sample under the objective in a fixed time interval to obtain a series of images which can be stitched together to compose the full view of the sample. The main limitation for a fast-scanning stage is that some new optical aberrations can be introduced by the moving stage. For the second approach, the fast-scanning lens does not exhibit any mechanical-induced-aberrations. However, off-axis lens aberrations would be the main challenge in this approach.

As displayed in Fig. 3.22, an Adaptive Scanning Optical Microscope (ASOM) contains a large-area fast steering mirror (FSM shown in Fig. 3.22),a large-aperture scanning lens and a DM which was developed by Potsaid et.al in 2005 [3.28]. In this way, the off-axis aberrations can be efficiently compensated by the DM and lead to a high image resolution with a wide field of view. Nowadays, the ASOM technology has been utilised in many areas such as in bio-photonics microscopy and electronic fabrication monitoring (see Fig. 3.23).

(a)   (b)
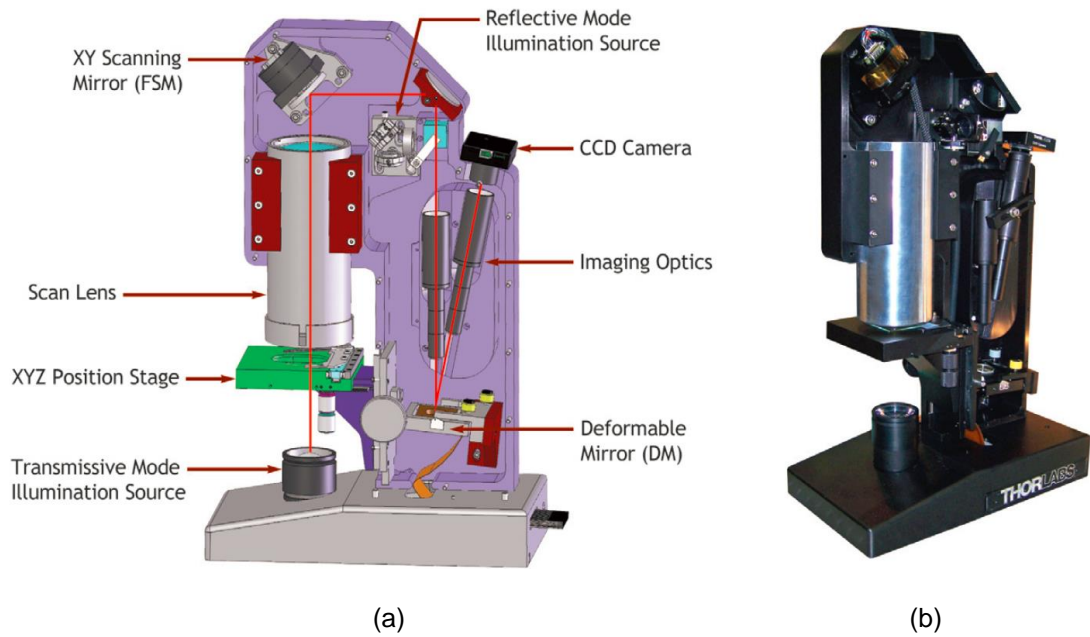
Fig. 3.22, (a) Schematic diagram of adaptive scanning optical microscope; (b) General view (Thorlabs ASM960, picture taken from [3.29])

(a)   (b)
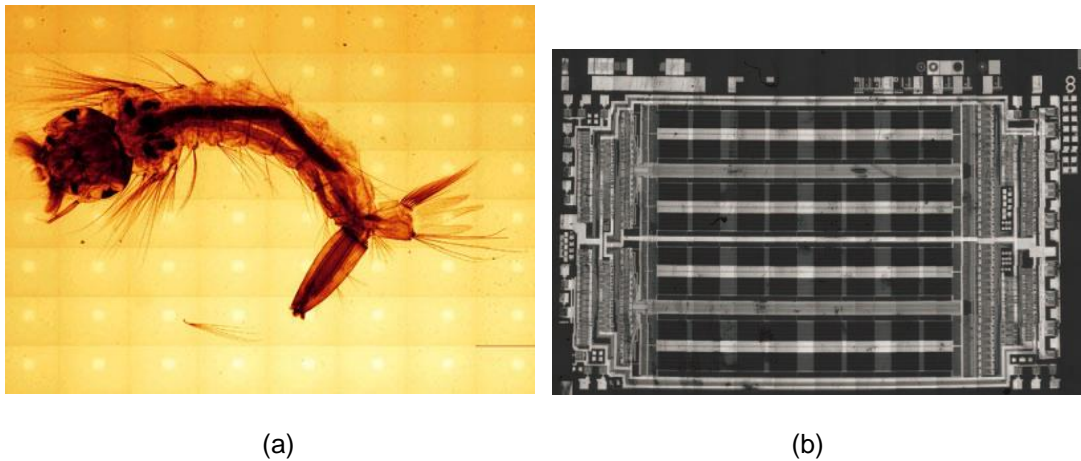
Fig. 3.23 ASOM image, (a) mosquito larva with a high resolution of 8192×6144 pixels; (b) computer memory chip with a high resolution of 14336 × 6144 pixels (Picture taken from [3.29])

3.4.3 AO in ophthalmology

In ophthalmology, it is meaningful to improve the resolution of cellular-level images of the human retina for the rapid detection and diagnosis of ophthalmic diseases. Optical Coherence Tomography (OCT) is a non-invasive imaging

technology which enables to provide rapid three-dimensional retinal images with micrometre resolution [3.30]. However, the further improvement of the image resolution is mainly restricted by the nature of imperfections in parts of the human eyes, such as the cornea and crystalline lens. In 2002, Roorda et. al first demonstrated that AO techniques can be utilised as an efficient approach to measure and correct the wavefront aberrations caused by the human eye [3.31]. Since then, a variety of works focusing on the combination between AO and OCT have been widely investigated and summarised by Pircher and Zawadzki [3.33]. A significant improvement of the retina image resolution can be observed in Fig. 3.24 [3.34].

(a)   (b)
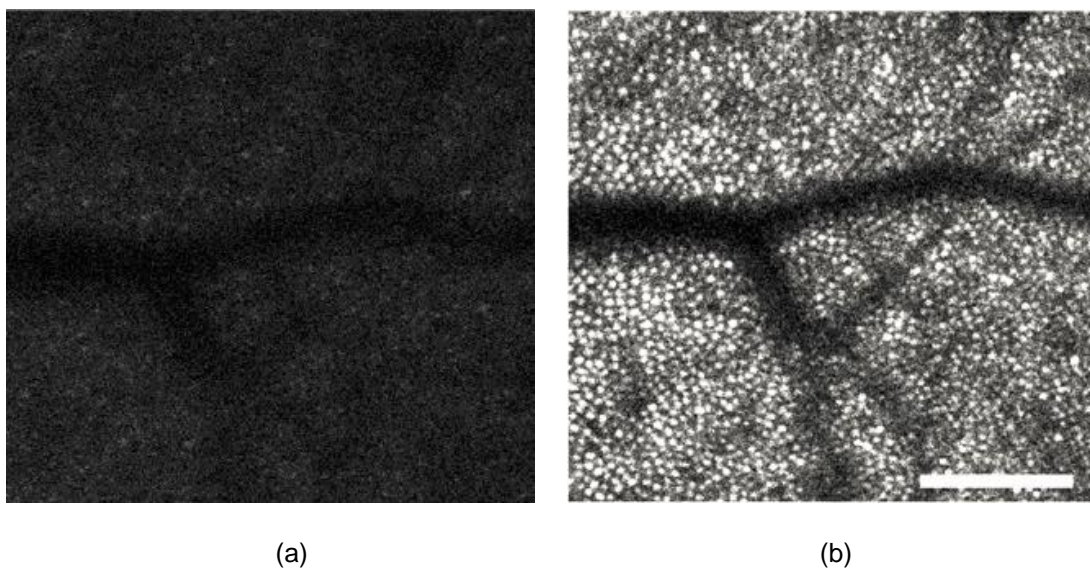
Fig. 3.24 Image of human retina, (a) without AO correction; (b) with AO correction (Picture taken from [3.34])

3.4.4 AO in laser systems

As described in sub-section 1.3.4, thermal lensing build up within the laser gain medium has long been recognised as the main limitation in the performance of solid-state lasers. In the early 1990s, several active mirrors (i.e. metal active mirror [3.50] or adjustable-curvature mirror [3.51]) were implemented inside solid-state lasers to partially compensate for the thermal lens effect by manually adjusting its ROC. However, the compensation of thermal lensing by

this method is not efficient since each change of the intracavity wavefront modulation can establish a new thermal equilibrium and lead to a high and dynamic dependence during solid-state laser operation.
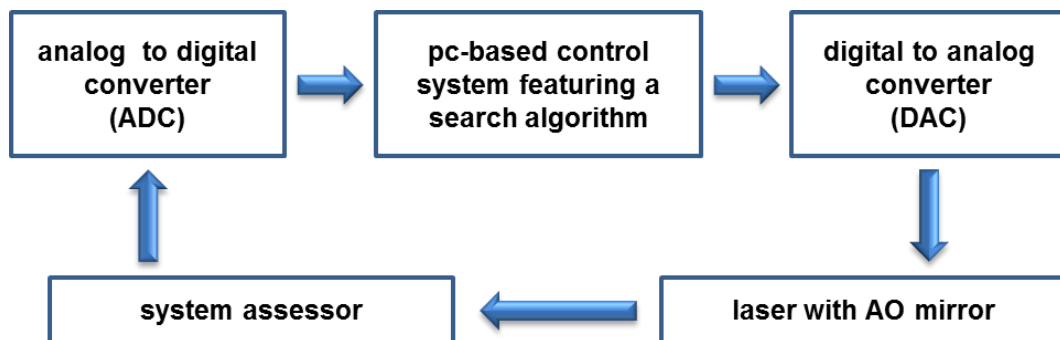
Fig. 3.25 Flow chart of the AO-closed-loop used for CW intracavity solid-state lasers

An efficient approach to automatically compensate for this variable thermal lensing in real-time is based on an iterative AO-based feedback control loop featuring a search algorithm (see Fig. 3.25). Typically, a search algorithm is employed to approach the optimum AO mirror shape corresponding to a self-optimisation of the laser output performance (i.e. either the laser output power or/and beam profiles) according to the detected feedback signals from the system assessor (e.g. a wavefront sensor, a photodiode or/and a beam profiler). In this way, an automatic enhancement of the laser output performance can be achieved efficiently. Various investigations for AO optimisation in solid-state lasers have been done since the early 2000s [3.37-3.48]. An improvement of the beam profiles from a 6 W Nd:YAlO laser by an AO-based closed-loop optimisation is displayed in Fig. 3.26 [3.46]. More literature reviews of intracavity CW solid-state laser improvements based on the use of an AO-closed loop will be presented in section 5.2.
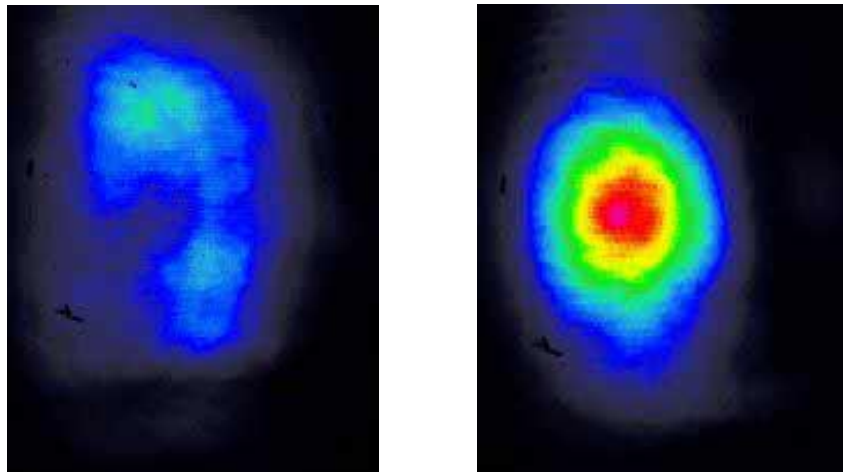
<center>(a)   (b)</center>

Fig. 3.26 Beam profiles taken from the 6W Nd:YAlO laser, (a) before AO optimisation; (b) after AO optimisation (Picture taken from [3.46])

In addition to enhancing the solid-state laser output performance by compensating for the thermal lens effect, AO systems are also widely used for beam profile control [3.52], pulse shaping [3.53] and free-space laser communication [3.54], especially with an extra-cavity laser configuration design.

3.5 Conclusion

In this chapter, the development of AO systems has been reviewed. Three main components of a typical AO control loop have been introduced, while different types of DMs were described with more details since some of them are utilised in this thesis work. At last, a range of AO applications were introduced with details of selected practical examples.

As detailed in this chapter, AO systems, especially the iterative AO-based feedback control loop featuring a search algorithm, have exhibited a noteworthy potential to be implemented inside self-Raman lasers to compensate for the occurring significant thermal lens effect and enhance the Raman laser output performance. This will be fully presented in chapter 5 with

a CW Nd:YVO$_4$ self-Raman laser emitting in the near-infrared regime (i.e. λ = 1109 nm or 1176 nm) and in chapter 6 with a CW frequency-doubled Nd:GdVO$_4$ self-Raman laser emitting in the visible regime (λ = 586.5 nm).

3.6 References

3.1   R. K. Tyson, *Principles of adaptive optics,* (Academic Press, 1991).

3.2   H. W. Babcock, "The possibility of compensating astronomical seeing," Publ. Astron. Soc. Pac. **65**, 229-236 (1953).

3.3   C. C. Wilcox, J. R. Andrews, S. R. Restaino, T. Martinez, S. W. Teare, "Atmospheric Turbulence Generator Using a Liquid Crystal Spatial Light Modulator," Proceedings of the IEEE 2007 Aerospace Conference, 1-8 (2007).

3.4   F. Merkle, P. Kern, P. Lena, F. Rigaut, J. C. Fontanella, G. Rousset, Onera, C. Boyer, J. P. Gaffard, P. Jagourel, Laserdot, "Successful Tests of Adaptive Optics," The Messenger, **58**, 1-4 (1989).

3.5   Thirty meter telescope, 1111 South Arroyo Parkway, Suite 200, Pasadena, CA 91105, United States, www.tmt.org.

3.6   S. Chenais, F. Druon, F. Balembois, G. Lucas-Leclin, Y. Fichot, P. Georges, R. Gaume, B. Viana, G. P. Aka, D. Vivien, "Thermal lensing measurements in diode-pumped Yb-doped GdCOB, YCOB, YSO, YAG and KGW," Opt. Mater. **22**, 129-137 (2003).

3.7   T. Omatsu, M. Okida, A. Lee, H. M. Pask, "Thermal lensing in a diode-end-pumped continuous-wave self-Raman Nd-doped $GdVO_4$ laser," Appl. Phys. B **108**, 73-79 (2012).

3.8   G. R. Brady, M. Guizar-Sicairos, and J. R. Fienup, "Optical wavefront measurement using phase retrieval with transverse translation diversity," Opt. Express. **17**, 624-639 (2009).

3.9   THORLABS, 56 Sparta Avenue, Newton, New Jersey, 07860, United States, www.thorlabs.com.

3.10   S. Xu, Y. Li, Y. Liu, J. Sun, H. Ren, and W. Shin-Tson, "Fast-Response Liquid Crystal Microlens," *Micromachines* **5**, 300-324 (2014).

3.11   A. F. Naumov, M. Y. Loktev, I. R. Guralnik and G. Vdovin, "Liquid-crystal adaptive lenses with modal control," Opt. Lett. **23**, 992-994 (1998).

3.12   S. P. Kotova, M. Y. Kvashnin, M. A. Rakhmatulin, O. A. Zayakin, I. R. Guralnik, N. A. Klimov, P. Clark, G. D. Love, A. F. Naumov, C. D. Saunter, M. Y. Loktev, G. V. Vdovin and L. V. Toporkova, "Modal liquid crystal wavefront corrector," Opt. Express. **22**, 1258-1272 (2002).

3.13   Boston Micromachines Corporation, *Adaptive Optics 101 Technical Whitepaper*, www. bostonmicromachines.com (2011).

3.14   T. D. Oswalt, I. S. McLean, *Planets, Stars and Stellar Systems, Volume 1, Telescopes and Instrumentation* (Springer Press, 2013).

3.15   W. M. Keck Observatory, 65-1120 Mamalahoa Hwy, Kamuela, HI 96743, United States, www.keckobservatory.org.

3.16   Iris AO, 2680 Bancroft Way Berkeley, CA 94704, United States, www.irisao.com.

3.17   Flexible Optical B.V, Polakweg 10-11, 2288 GG Rijswijk ZH, Netherlands, www.okotech.com.

3.18   Imagine Optics, 18 rue Charles de Gaulle, 91400 ORSAY, France, www.imagine-optic.com.

3.19   Boston Micromachines Corporation, 30 Spinelli Place, Cambridge, MA 02138, United Kingdom, www.bostonmicromachines.com.

3.20   ALPAO SAS, Inovallée, 345 rue Lavoisier, 38330 Montbonnot St. Martin, France, www.alpao.com.

3.21   AKA Optics, 2 rue Marc Donadille, 13013 MARSEILLE, CSB0001, France, www.akaoptics.com.

3.22   BAE systems advanced technology centre, Stirling Square, 6 Carlton Gardens, London, SW1Y 5AD United Kingdom, www.baesystems.com.

3.23   C. Higgs, H. T. Barclay, D. V. Murphy, and C. A. Primmerman, "Atmospheric compensation and Tracking Using Active Illumination," LLABJ. **11**, 1-26 (1998).

3.24   Z. Zhao, S. D. Lyke, and M. C. Roggemann, "Adaptive Optical Communication Through Turbulent Atmospheric Channels," IEEE Trans. Commun. **50**, 5432-5436 (2008).

3.25   J. W. Hardy, *Adaptive Optics for Astronomical Telescopes,* (Oxford University Press, 1998).

3.26   L. Sherman, J. Y. Ye, O. Albert† & T. B. NORRIS, "Adaptive correction of depth-induced aberrations in multiphoton scanning microscopy using a deformable mirror," J. Microsc. **206**, 65-71 (2002)

3.27   M. J. Booth, M. A. A. Neil, R. Juskaitis, and T. Wilson, "Adaptive aberration correction in a confocal microscope," PNAS. **99**, 5788-5792 (2002).

3.28   B. Potsaid, Y. Bellouard, and J. T. Wen, "Adaptive Scanning Optical Microscope (ASOM): A multidisciplinary optical microscope design for large field of view and high resolution imaging," Opt. Express. **13**, 6504-6518 (2005).

3.29   Thorlabs, Inc. *Insight advantage image and microscopy: Adaptive Optics*, www.thorlabs.com (2009).

3.30   E. J. Fernández, I. Iglesias, and P. Artal, "Closed-loop adaptive optics in the human eye," Opt. Lett. **26**, 476-478 (2001).

3.31   A. Roorda, F. Romero-Borja, W. J. Donnelly III, H. Queener, T. J. Hebert and M. C. W. Campbell, "Adaptive optics scanning laser ophthalmoscopy," Opt. Express. **10**, 405-412 (2002).

3.32   J. Carroll, D. C. Gray, A. Roorda, and D. R. Williams, "Recent Advances in Retinal Imaging With Adaptive Optics," Optics & Photonics News. **16**, 36-42 (2005).

3.33 M. Pircher, and R. J. Zawadzki, "Combining adaptive optics with optical coherence tomography: unveiling the cellular structure of the human retina in vivo," Expert Review of Ophthalmology **2**, 1019-1035 (2007).

3.34 R. Zawadzki, B. Cense, Y. Zhang, S. Choi, D. Miller, J. Werner, "Ultrahigh-resolution optical coherence tomography with monochromatic and chromatic aberration correction", Opt. Express. **16**, 8126-8143 (2008).

3.35 B. Tyson, *Topics in Adaptive Optics*, (InTech Press 2012).

3.36 I. Kozak, "Retinal imaging using adaptive optics technology," Saudi J Ophthalmol. **28**, 117-122 (2014).

3.37 L. Zhu, P. Sun, D. Bartsch, W. R. Freeman, and Y. Fainman, "Wave-front generation of Zernike polynomial modes with a micromachined membrane deformable mirror," Appl. Opt. **38**, 6019-6026 (1999).

3.38 G. Vdovin, V. Kiyko, "Intracavity control of a 200-W continuous-wave Nd:YAG laser by a micromachined deformable mirror," Opt. Lett. **26**, 798-800 (2001).

3.39 Y. Seo, S. Baik, S. Park and C. Kim, "Closed-Loop Adaptive Optics System for Wave-Front Correction," J. Korean Phys. Soc. **39**, 891-894 (2001).

3.40 A. L. Rukosuev, A. Alexandrov, V. Y. Zavalova, V. V. Samarkin, A. V. Kudryashov, "Adaptive optical system based on bimorph mirror and Shack-Hartmann wavefront sensor," Proc. SPIE **4493**, 261-268 (2002).

3.41 W. Lubeigt, G. Valentine, J. Girkin, E. Bente, D. Burns, "Active transverse mode control and optimization of an all-solid-state laser using an intracavity adaptive-optic mirror," Opt. Express. **10**, 550-555 (2002).

3.42   U. Wittrock and P. Welp, "Adaptive laser resonator control with deformable MOEMS mirrors," SPIE Proceedings, paper **6113**, 1-13 (2006).

3.43   P. Yang, Y. Liu, W. Yang, M. Ao, S. Hu, B. Xu, W. Jiang, "Adaptive mode optimization of a continuous-wave solid-state laser using an intracavity piezoelectric deformable mirror," Opt. Commun. **278**, 377-381 (2007).

3.44   W. Lubeigt, G. Valentine and D. Burns, "Enhancement of laser performance using an intracavity deformable membrane mirror," Opt. Express. **16**, 10943-10955 (2008).

3.45   L. Dong, P. Yang, B. Xu, "Adaptive aberration correction based on ant colony algorithm for solid-state lasers: numerical simulations," Appl. Phys. B **96**, 527-533 (2009).

3.46   W. Lubeigt, S. P. Poland, G. J. Valentine, A. J. Wright, J. M. Girkin, and D. Burns, "Search-based active optic systems for aberration correction in time-independent applications," Appl. Opt. **49**, 307-314 (2010).

3.47   P. Yang, Y. Ning, X. Lei, B. Xu, X. Li, L. Dong, H. Yan, W. Liu, W. Jiang, L. Liu, C. Wang, X. Liang, and X. Tang, "Enhancement of the beam quality of non-uniform output slab laser amplifier with a 39-actuator rectangular piezoelectric deformable mirror," Opt. Express. **18**, 7121-7130 (2010).

3.48   J. Li, X. Chen, "A Novel Intra-cavity Adaptive Optical System for high Power Solid-state Lasers," Symposium on Photonics and Optoelectronics, (2010).

3.49   D. Huang, E. A. Swanson, C. P. Lin, J. S. Schuman, W. G. Stinson, W. Chang, M. R. Hee, T. Flotte, K. Gregory, C. A. Puliafito, J. G. Fujimoto, "Optical Coherence Tomography", Science. **254**, 1178-1181 (1991).

3.50   U. J. Greiner and H. H. Klingenberg, "Thermal lens correction of a
diode-pumped Nd:YAG laser of high TEM_{00} power by an adjustable-
curvature mirror," Opt. Lett. **19**, 1207-1209 (1994).

3.51   V. V. Apollonov, G. V. Vdovin, L. M. Ostrovskaya, V. N. Rodin, and S.
A. Chetkin, "Active correction of a thermal lens in a solid-state laser. I.
Metal mirror with a controlled curvature of the central region of the
reflecting surface," Quantum Electronics. **21**, 116-118 (1991).

3.52   R. El-Agmy, H. Bulte, A. H. Greenaway and D. T. Reid, "Adaptive
beam profile control using a simulated annealing algorithm," Opt.
Express. **13**, 6085-6091 (2005).

3.53   T. Baumert, T. Brixner, V. Seyfried, M.Strehle, G. Gerber,
"Femtosecond pulse shaping by an evolutionary algorithm with
feedback," Appl. Phys. B **65**, 779-782 (1997).

3.54   S. Bloom, "Photonic design & solution -Fiber-free: Laser
communications soar to unheard of heights," Photon. Spectra. **31**, 36-
42 (2002).

Chapter 4

Continuous-wave Nd:YVO$_4$ self-Raman lasers based on 379 cm^{-1} and 893 cm^{-1} Raman shifts

4.1 Introduction

In 2004, Chen demonstrated that Neodymium-doped orthovanadates, such as Nd:GdVO$_4$ [4.1] or Nd:YVO$_4$ [4.2], could be used inside Raman lasers as both the laser and Raman gain media, as previously predicted by Kaminskii et al. in 2001 [4.3]. Since then, Neodymium-doped orthovanadates have been widely utilised in Raman lasers, especially in a diode-pumped intracavity self-Raman configuration where both lasing and SRS occur within the same active crystal. Until now, most of the investigations have been focused on the use of the primary Raman shifts of these vanadate crystals (~ 882 cm^{-1} and 893 cm^{-1} for Nd:GdVO$_4$ and Nd:YVO$_4$ respectively) corresponding to a first Stokes Raman output wavelength range from λ = 1173 nm to 1180 nm when pumped with a Nd-based laser source [4.1, 4.2, 4.4-4.6]. When combined with SHG or SFG, the Raman laser output beams emit in the visible spectrum [4.7-4.14], with applications in many fields such as medicine (retinal laser photocoagulation) [4.15], laser projection displays, and remote sensing (bathymetry or underwater detection) [4.16].

The use of a secondary Raman shift inside vanadate crystals can add a significant number of narrowly-spaced wavelength outputs [4.17, 4.18]. When combined with SHG or SFG, these Raman lasers can produce an even more-closely spaced set of visible lines in the green-lime-yellow region compared to

lasers purely based on the primary Raman shifts. These can benefit many applications, especially in medicine and bio-photonics. For instance, the detection of blood effects induced by carbon monoxide poisoning requires light emitting at λ = 555 nm due to the peak absorption of hemoglobin in this region [4.19]. In addition, light operating around λ = 550 nm is absorbed by numerous red fluorescent dyes and markers for single-molecule detection [4.20]. A review of the previous vanadate crystalline lasers using the secondary Raman shift is given in the following paragraphs.

In 2011, Shuzhen et al. reported a Q-switched self-Raman laser operating at λ = 1097 nm using a secondary Raman shift of 259 cm^{-1} in a c-cut Nd:YVO$_4$ crystal [4.17]. A fibre-coupled laser diode emitting at λ = 880 nm was used to pump the self-Raman gain medium while the pulsed laser was produced using an acousto-optic Q-switch with a PRF of 50 kHz and pulse duration of 33 ns. The schematic diagram of this 2-mirror self-Raman laser configuration is displayed in Fig. 4.1. A maximum Raman laser average output power of 1.45 W was obtained for an absorbed diode power of 12.4 W corresponding to an absorbed pump power to Raman output power conversion efficiency of 11.7 %.
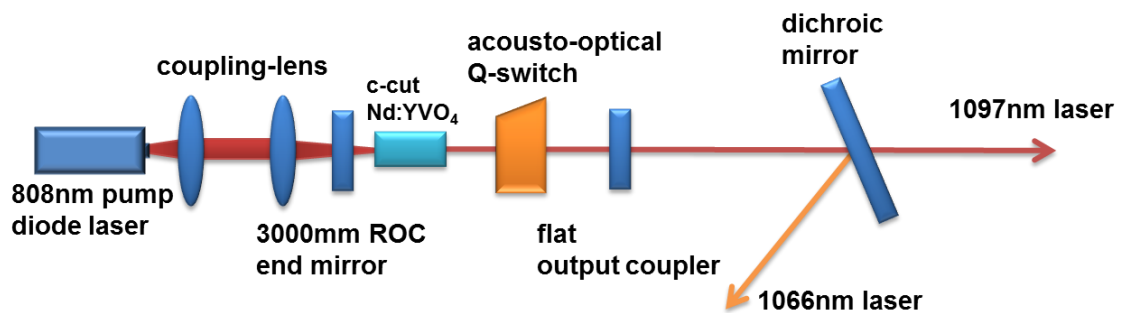
Fig 4.1 λ = 1097 nm self-Raman laser configuration [image extracted from 4.17]

In the same year, Li et al. observed two parasitic output beams emitting at λ = 1108 nm and 1132 nm when they characterised the first Stokes Raman laser output at λ = 1176 nm [4.12]. They concluded that these additional Raman lines originated from the conversion of the primary (λ = 1064 nm) and

secondary (λ = 1086 nm) fundamental emission based on a 376 cm^{-1} secondary Raman shift in an YVO$_4$ crystal. Since the aim of this experiment was to optimise the Raman laser output at λ = 587.8 nm by SHG in a miniature self-Raman laser cavity, these two parasitic Stokes lines were not fully characterised.

Most notably, in 2012, Lin et al. demonstrated several QCW self-Raman lasers emitting at λ = 1108 nm, 1156 nm and 1227 nm utilising the 882 cm^{-1} primary and 382 cm^{-1} secondary Raman shifts for an a-cut Nd:GdVO$_4$ [4.18] crystal.
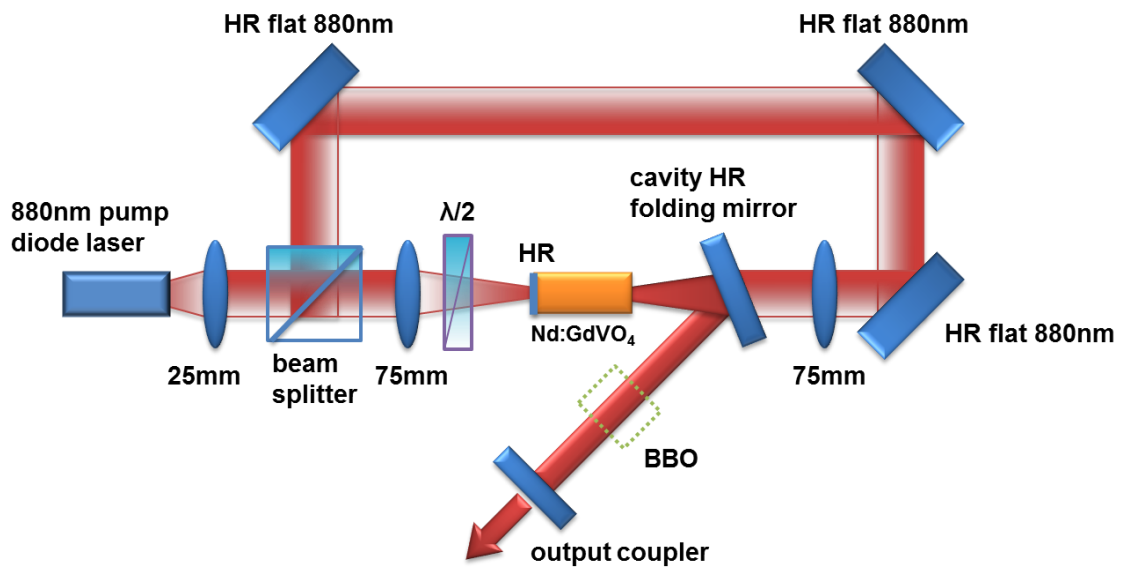
Fig. 4.2 Cascaded Nd:GdVO$_4$ self-Raman laser configuration with double-end polarised pumping [image extracted from 4.18]

The schematic diagram of the cascaded self-Raman laser configuration is displayed in Fig. 4.2. A double-end polarised pumping scheme at λ = 880 nm (as fully described in [4.14]) was utilised to improve the conversion efficiency. Laser outputs at λ = 1108 nm and 1156 nm were observed, corresponding to the first and second Stokes output resulting from the 382 cm^{-1} secondary Raman transition of the GdVO$_4$ crystal. This led to maximum QCW output powers measured at 1.41 W and 120 mW at λ = 1108 nm and 1156 nm and corresponding absorbed pump power to Raman output power conversion efficiencies of 4.7 % and 0.35 % respectively. Moreover, a λ = 1227 nm

Raman line was obtained resulting from the combination of the first Stokes conversion using the 882 cm^{-1} primary Raman shift and the 382 cm^{-1} secondary Raman shift sequentially. At this wavelength, the maximum QCW output power was measured at 1.01 W corresponding to an absorbed pump power to Raman output power conversion efficiency of 2.7 %.
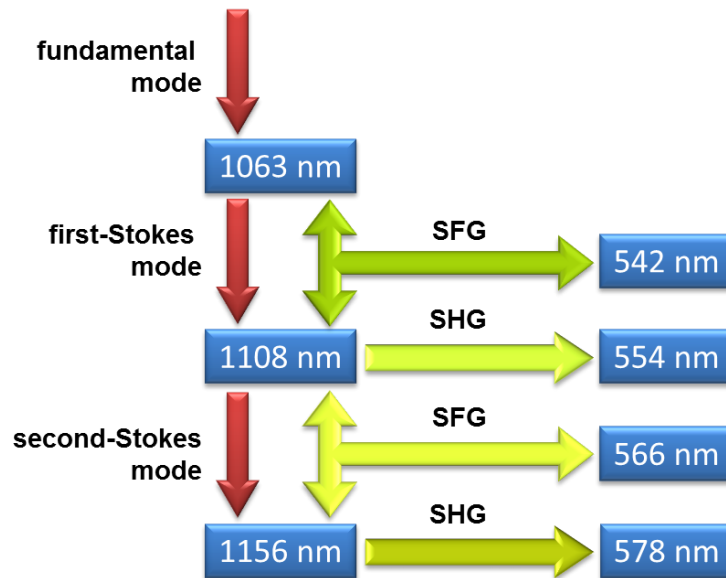
Fig. 4.3 Wavelengths generation combined with the SHG and SFG

In addition, these lines were combined with a SHG and SFG process, resulting in four discrete visible wavelengths as summarised in Fig. 4.3. Maximum QCW output powers of 3.4 W, 2.8 W, 1.4 W and 0.8 W were measured at λ = 542 nm, 554 nm, 566 nm and 577 nm corresponding to a set of overall pump diode-to-visible conversion efficiencies of 11.7 %, 9.7 %, 4.8 % and 2.7 % respectively. However, the strong thermal lens effect inherent to the fundamental laser conversion and the non-elastic nature of SRS present inside the Nd:GdVO$_4$ crystal prevented true CW operation. For this reason, the duty cycle of the pump modulation was limited at 50 %.

In this chapter, for the first time to my knowledge, several CW Nd:YVO$_4$ self-Raman lasers based on a 379 cm^{-1} secondary Raman shift emitting at λ = 1109 nm, 1158 nm and 1231 nm are demonstrated. A two-mirror Raman laser configuration with 26 mm cavity length was designed, utilising a strongly-

concave output coupler (ROC = 100 mm) and a flat end-mirror. In this way, the strong thermal lens effect on the cavity dynamics and particularly the resonator stability was significantly alleviated. Therefore, true CW Raman laser outputs using the secondary Raman transition could be obtained.

In section 4.2, the Raman spectrum for the a-cut Nd:YVO$_4$ crystal used in this work will be measured. The 2-mirror self-Raman laser configuration will be presented in section 4.3. In section 4.4, several CW self-Raman laser outputs will be characterised while the relevant discussion points will be provided in section 4.5.

4.2 Raman spectrum measurement for the a-cut Nd:YVO$_4$ crystal

Nd:YVO$_4$ crystals belong to the group of oxide compounds, crystallising in a zircon tetragonal structure with space group D$_{4h}$ [4.21]. As referred in Fig. 4.4, the uniaxial Nd:YVO$_4$ crystals include a four-fold-symmetry axis (which is called the crystallographic c-axis) while two distinguishable a-axes (a$_1$ and a$_2$) are defined in an orthogonal plane to the c-axis. In general, Nd:YVO$_4$ crystals can be divided into two types according to the orientation of their cut. When the crystal is cut along the a-axis (which is called a-cut crystal), the laser output is polarised along the c-axis and propagates along the a$_1$-axis (see Fig. 4.4 (a)). That is due to the natural birefringence of Nd:YVO$_4$ crystals as the stimulated emission cross section parallel to the c-axis ($\sigma\|$, ~ 25 × 10^{-19} cm^2) has been measured to be ~ four times higher than the cross section orthogonal to the c-axis ($\sigma\perp$, ~ 6.5 × 10^{-19} cm^2) at λ = 1.06 µm [4.3]. Therefore, in an a-cut crystal, a laser beam can oscillate easier by using the higher stimulated emission cross section of $\sigma\|$ rather than $\sigma\perp$, which presents a strong polarisation-dependent laser output. Conversely, a c-cut crystal is cut along the c-axis while the laser output is unpolarised (due to both transverse axes having a similar cross section) and propagates along the c-axis (see Fig. 4.4

(b)). In a c-cut crystal, the laser oscillation is only dominated by the stimulated emission cross section of $\sigma_\perp$.
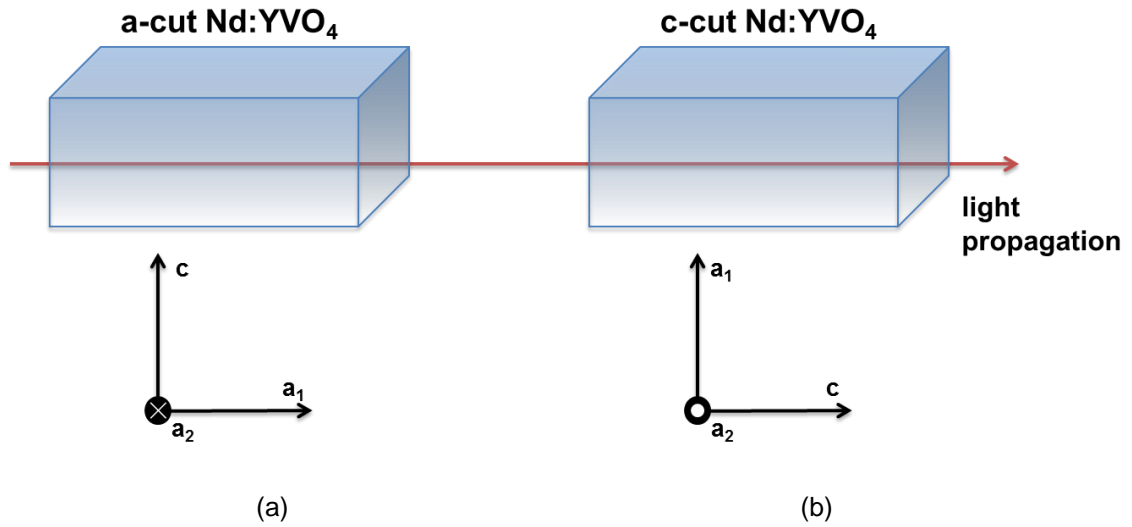
Fig. 4.4 Definitions of the (a) a-cut Nd:YVO₄ crystal and (b) c-cut Nd:YVO₄ crystal

In general, a-cut Nd:YVO$_4$ crystals have been widely used for CW laser operation with a lower pump threshold and more efficient laser generation [4.6, 4.12, 4.13]. However, in the Q-switched laser regime, energy storage capacity can be constrained by a large stimulated emission cross section. So c-cut Nd:YVO$_4$ crystals are more appropriate in Q-switched regime [4.3, 4.17].

In this work, an a-cut, 20 mm long, 2 mm diameter, 0.3 at. % doped Nd:YVO$_4$ rod (from Casix Ltd [4.22]) was used as self-Raman gain medium. Using a relatively low doping concentration of Nd^{3+} ions has the advantage of reducing the thermal lens effect and improving self-Raman conversion as demonstrated by Chen [4.4]. The spontaneous Raman spectrum was measured using a Renishaw Invia Raman microscope [4.23] operating in a back scattering mode (see Fig 4.5). A $\lambda = 514$ nm pump beam propagated along the a_1-axis while both the excitation and backscattered Raman signals were polarised along the crystal c-axis. The scattering configuration can be expressed as X(ZZ)X̄ corresponding to the Porto notations [4.24].

Fig. 4.5 Renishaw Invia Raman microscope used in this work
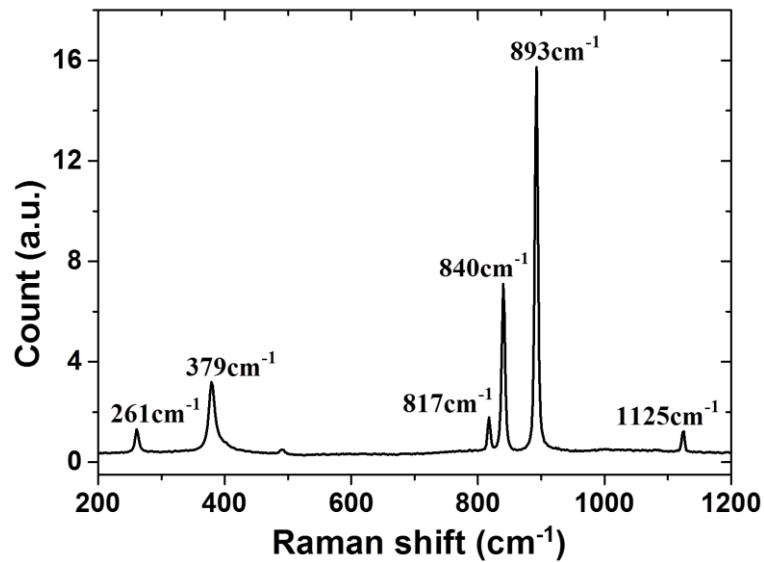
Fig. 4.6 Spontaneous Raman spectrum for the a-cut Nd:YVO$_4$ crystal

Three main Raman shifts can be observed at 893 cm^{-1}, 840 cm^{-1} and 379 cm^{-1} in Fig. 4.6. The Full Width at Half Maximum (FWHM) of these three Raman transitions could be measured at ~ 6 cm^{-1}, 6 cm^{-1} and 14 cm^{-1} respectively with a 2 cm^{-1} data resolution. Based on the Raman gain of 4.5 cm / GW measured for the 893 cm^{-1} primary Raman shift in [4.3], the Raman gain for the 379 cm^{-1} shift can be estimated to be 0.9 cm / GW using the relative ratio measured in Fig 4.6.

The relationship between the fundamental laser wavelength, Stokes Raman wavelength and Raman shift can be expressed using the following equation

$$\frac{1}{\lambda_R} = \frac{1}{\lambda_f} - n * R_s \qquad (4\text{-}1)$$

where R_s denotes the Raman shift, n the Raman Stokes series number, λ_f and λ_R the wavelengths of the fundamental and Raman laser field respectively.

4.3 Experimental laser configuration
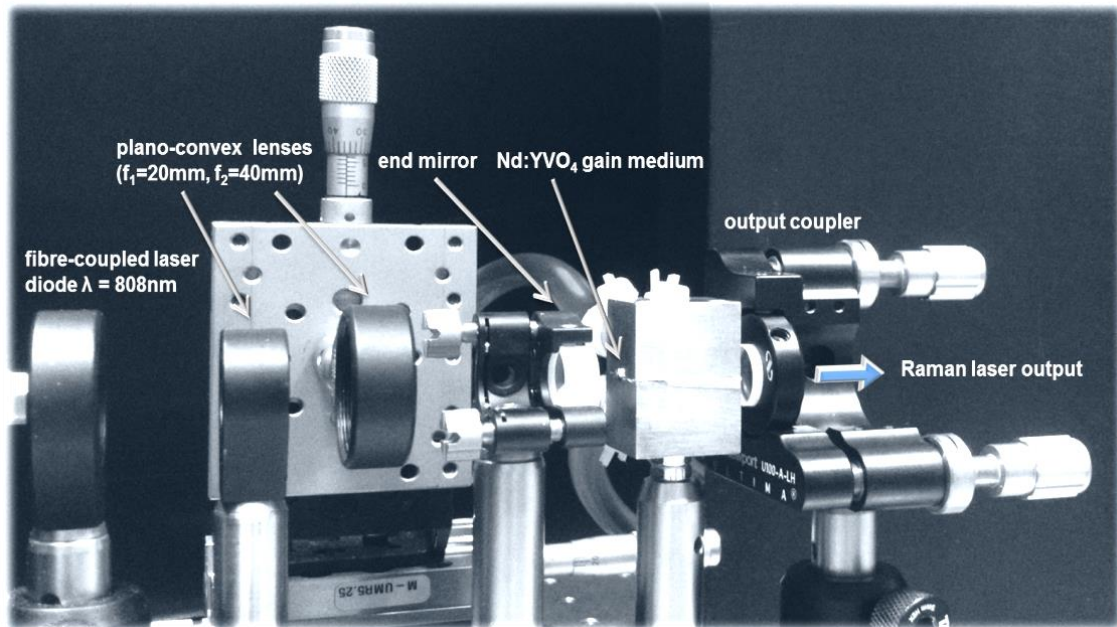
Fig. 4.7 Two-mirror Nd:YVO$_4$ self-Raman laser configuration

In this work, a 26 mm-long, two-mirror Nd:YVO$_4$ self-Raman laser cavity was built to generate various Raman laser outputs using different output couplers (see Fig. 4.7). The distances between the end mirror and the front surface of the gain medium, and between the rear surface of the gain medium and the output coupler were set to 4 and 2 mm respectively. The flat end-mirror had a HR coating estimated to be R > 99.95 % at $\lambda = 1064$nm and between 1109 and 1230 nm. All output couplers (R > 99.97 % at $\lambda = 1064$ nm) have a

strongly-concave ROC of 100 mm for alleviating the thermal lens effect on the cavity dynamics and resonator stability.
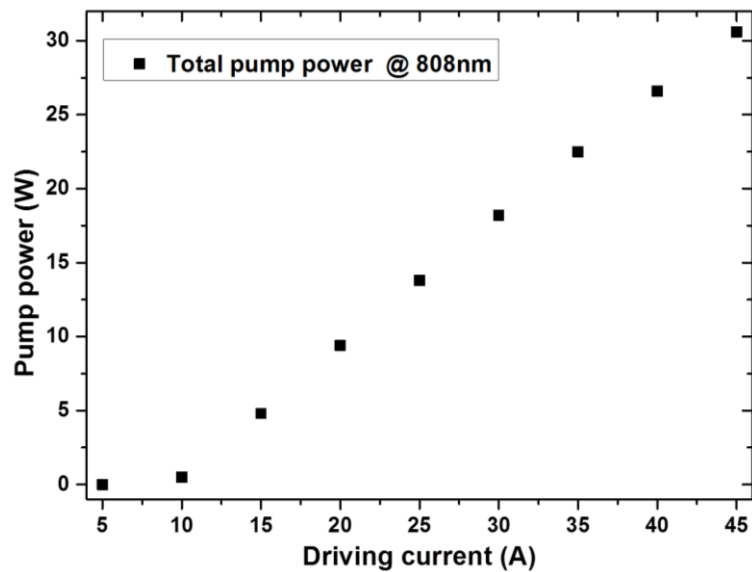
Fig. 4.8 Incident pump power to the laser gain medium as a function of the diode current

A 100 µm-diameter fibre-coupled (NA ~ 0.22) laser diode (from Dilas Ltd, M1F1S22-808.3-35C-SS2.1 [4.25]) operating at $\lambda = 808$ nm was used as a pump source. A temperature-feedback cooling system (from Elite Thermal Engineering, Model OCP-110-24 [4.26]) was used to keep a constant temperature of the pump laser diode at 27˚C. Using a Thorlabs power-meter (PM100A, [4.27]) the pump power incident to the gain medium was measured as a function of the current supplied to the laser diode as displayed in Fig. 4.8.

The size of both pump and fundamental laser fields need to be matched within the gain medium to optimise laser conversion of the fundamental laser. Two plano-convex lenses AR-coated at $\lambda = 808$ nm were used to collimate and focus the pump beam into the centre of the self-Raman crystal with a 1:2 magnification ratio. As Fig 4.9 and 4.10 show, the pump beam waist along the x and y axes were both measured at ~ 100 µm with a ~ 7 mm Rayleigh range for a diode pump power of 2 W, using a Thorlabs beam profiler (BP104-IR, [4.27]).
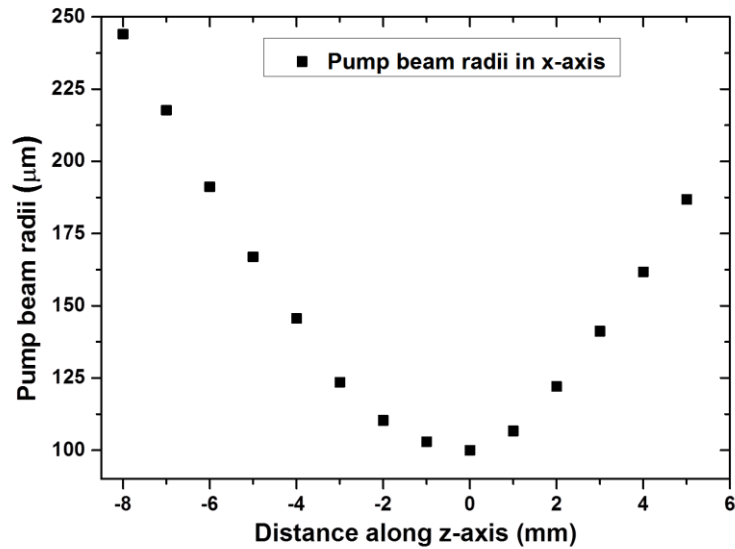
Fig. 4.9 Pump beam radii in x-axis corresponding to the distance along z-axis
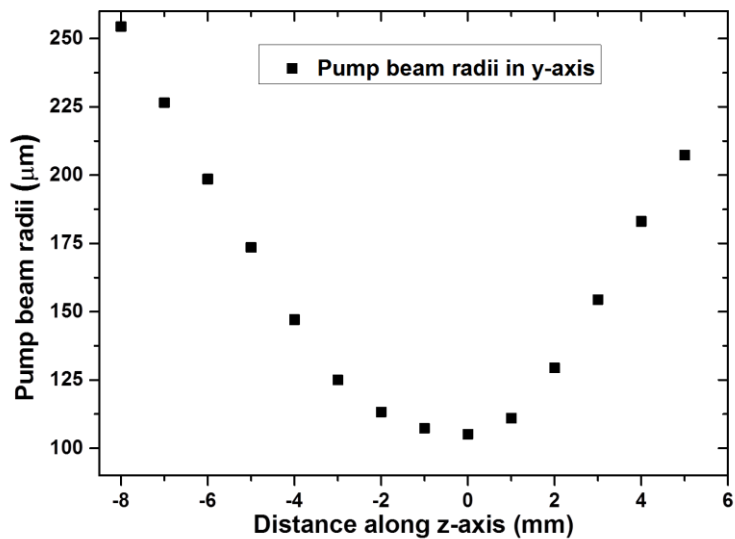
Fig. 4.10 Pump beam radii in y-axis corresponding to the distance along z-axis

The Nd:YVO$_4$ rod described in section 4.2 was wrapped with indium foil and fixed in a home-made copper block which was water-cooled at 22 °C by a recirculating chiller (from ThermoFisher Scientific, Neslab-ThermoFlex-1400 [4.28]). The c-axis of the crystal was located parallel to the horizontal plane, which resulted in a horizontal polarisation for the laser outputs. Both side surfaces of the crystal were AR coated with R < 0.1 % at λ = 1064,

1109 - 1176 nm. The residual pump power transfer after passing through the laser crystal was measured as a function of the laser diode current as displayed in Fig 4.11.
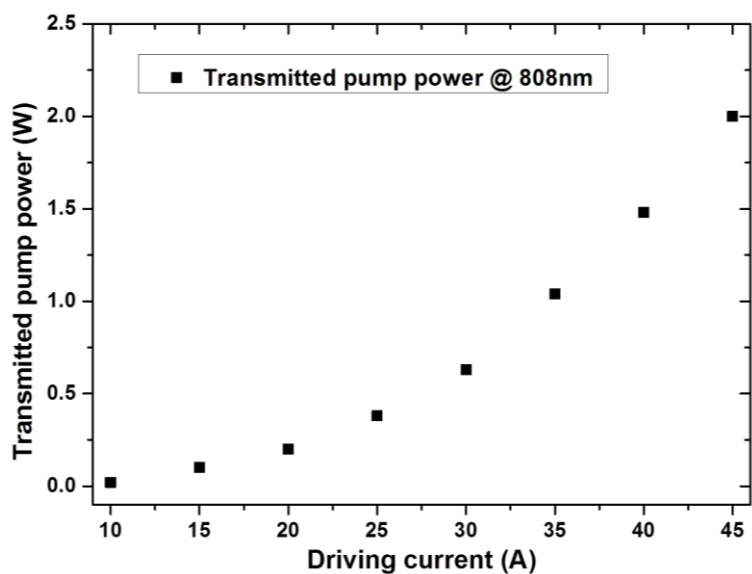
Fig. 4.11 Transmitted pump power after the Nd:YVO₄ crystal correspond to the driving current
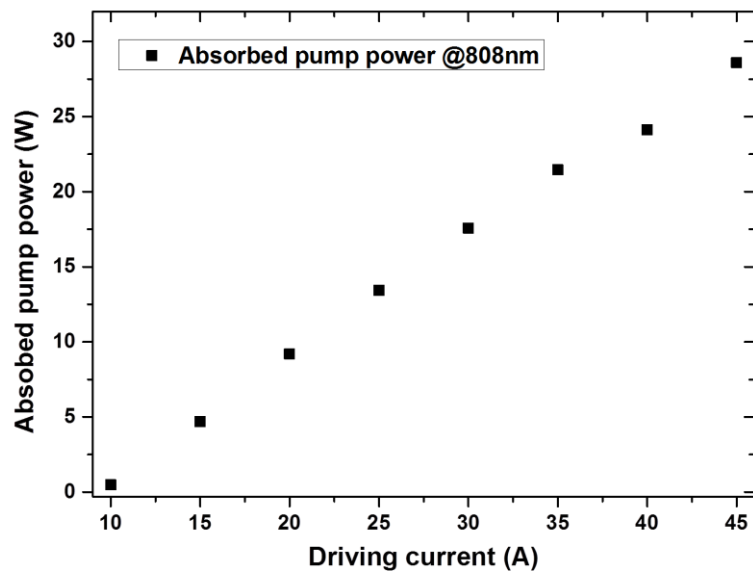
Fig. 4.12 Absorbed pump power transfer within the Nd:YVO₄ crystal as a function of the driving current

Therefore, the absorbed laser diode pump power as a function of the diode current can be estimated by the difference between the data displayed in Fig. 4.8 and 4.11 (see Fig. 4.12).

Fig. 4.13 Laser output beams view

The laser output beam emitting in the near-infrared could be observed using an infrared sensor card (from Newport Corporation F-IRC4-S [4.29]). As shown in Fig 4.13, the fundamental and Raman output beam overlapped in the small bright spot in the centre, surrounded by a divergent pump beam. To separate the different output beams, a prism-based system was built at the laser output as shown in Fig. 4.14.
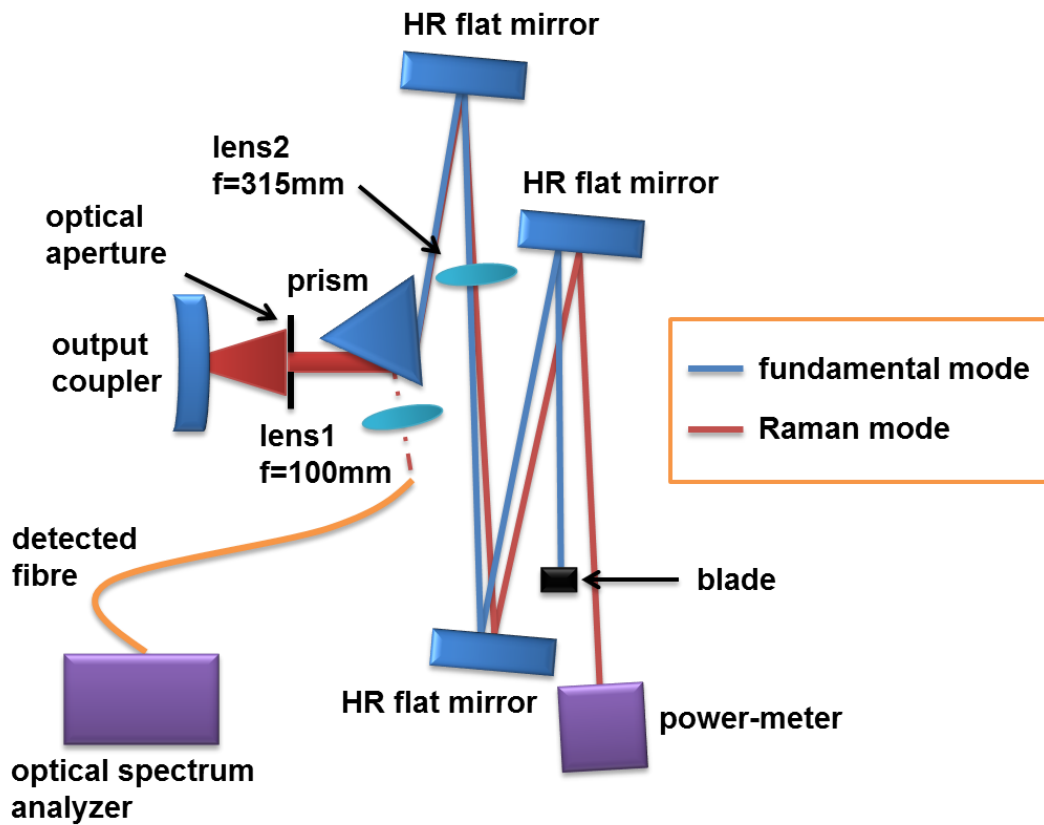
Fig. 4.14 Schematic diagram for the measurement system

First, an optical aperture was used to block most of the pump beam. The fundamental and Raman outputs could be separated by a prism placed at the Brewster angle (~ 56 degree) in the horizontal plane. Using a Gentec-EO power-meter (SOLO PE, [4.30]), the laser power reflected by the surface of the prism was measured at ~ 1 % of the total laser power incident to the prism. This reflected laser beam was focused using a f = 100 mm plano-convex lens (lens 1) into a fibre-coupled optical spectrum analyzer (from Agilent technologies, 86140B [4.31]). A f = 315 mm plano-convex lens (lens 2) was employed to focus the refracted beams of different wavelength. Three plane HR mirrors (R > 99.95 % at λ = 1064 & 1109 - 1230 nm) were used to extend the optical path. After this, the fundamental and Stokes Raman output beams could be easily separated using a blade located near the focusing point of lens 2. As displayed in Fig 4.15, since longer wavelengths lead to larger refractive angles, the distance between the two beam spots at λ = 1064 nm and 1176 nm (see Fig. 4.15(a)) is higher than that for the beam spots at λ = 1064 nm and

1109 nm. The total optical losses induced by this system were measured to be ~ 3 % of the total output power.

(a)   (b)
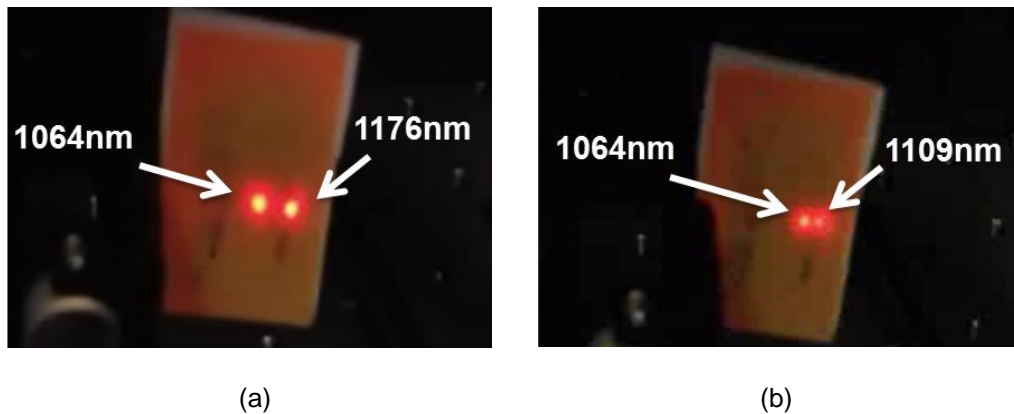
Fig. 4.15 Separated output beams (a) λ = 1064 and 1176 nm and (b) λ = 1064 and 1109 nm

4.4 Results

4.4.1 Fundamental field laser output at λ = 1064 nm

First, the power transfer of the fundamental laser obtained using a T = 10 % output coupler and operating at λ = 1064 nm was measured as shown in Fig. 4.16. The threshold of the fundamental field was achieved for an absorbed laser diode pump power of 1.48 W. A maximum laser output of 11.5 W was obtained for an absorbed laser diode pump power of 28.6 W corresponding to an absorbed pump power to fundamental output power conversion efficiency of 40.2 %. No sign of thermal rollover could be detected at this level of pump power.
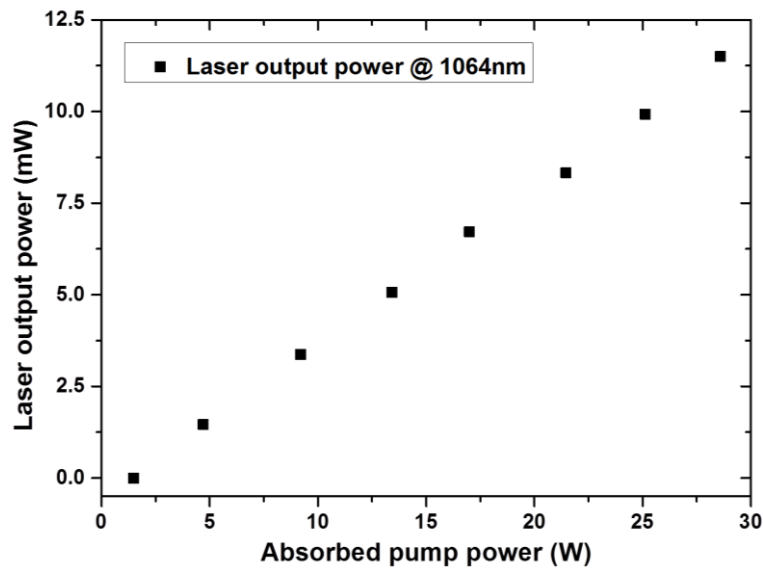
Fig. 4.16 Fundamental field output power transfer at λ = 1064 nm

4.4.2 First Stokes Raman laser at λ = 1109 nm

The CW first Stokes Raman laser output at λ = 1109 nm, based on the secondary Raman shift of 379 cm^{-1}, was characterised using an output coupler with T ~ 0.2 % at λ = 1109 nm and T > 7 % at λ = 1158 - 1176 nm. The pump threshold for the first Stokes SRS was reached with an absorbed laser diode pump power of 2.2 W. At this pump level, 64 mW of fundamental laser output power (λ = 1164 nm) could also be observed. A maximum Raman output power of 1.0 W was obtained for an absorbed laser diode pump power of 11.9 W while the λ = 1064 nm fundamental output power was measured at 70 mW. This corresponded to an absorbed pump power to Raman output power conversion efficiency of 8.4 %.
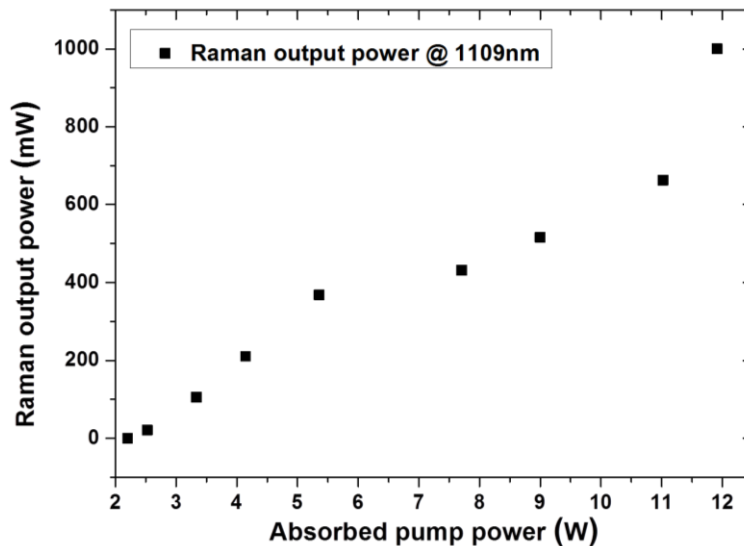
Fig. 4.17 First Stokes Raman laser output power transfer at λ = 1109 nm

The first Stokes Raman laser output power transfer is shown in Fig. 4.17. With a change of the diode pump power, the dynamic laser oscillation is strongly influenced by the variation of thermal lensing occurring within the gain medium. This inevitably has a direct effect on the transverse mode profile of the fundamental beam and therefore impacts the Raman conversion efficiencies between the fundamental and first Stokes outputs or first Stokes and second Stokes modes. It should be noted that the laser cavity was only manually aligned to achieve maximum Raman laser output power at the highest absorbed pump power (11.9 W). This is probably the reason behind the drop in conversion efficiency between 6 W and 11.9 W seen in Fig. 4.17. The same approach was also taken for the subsequent experimental Raman laser configurations mentioned in this chapter. Moreover, in each Raman laser configuration in this chapter, a thermal rollover of the desired Raman output power could be detected when the laser diode pump was above the maximum point shown for the four Raman configurations. This rollover might lead to a significant power decrease or even directly to the instability of the laser cavity.

The beam quality factors M^2 along the x-and y axes of the laser outputs were manually measured using a beam profiler combined with a $f = 200$ mm

focusing lens. The same approach was also taken for the subsequent Raman lasers in this chapter.

As shown in Fig. 4.18 and 4.19, at the maximum Raman output power of 1.0 W, the beam quality factors of M^2 were measured at 2.3 and 3.1 at the x and y axes for the first Stokes Raman output and 4.9 and 5.4 for the fundamental laser output respectively.
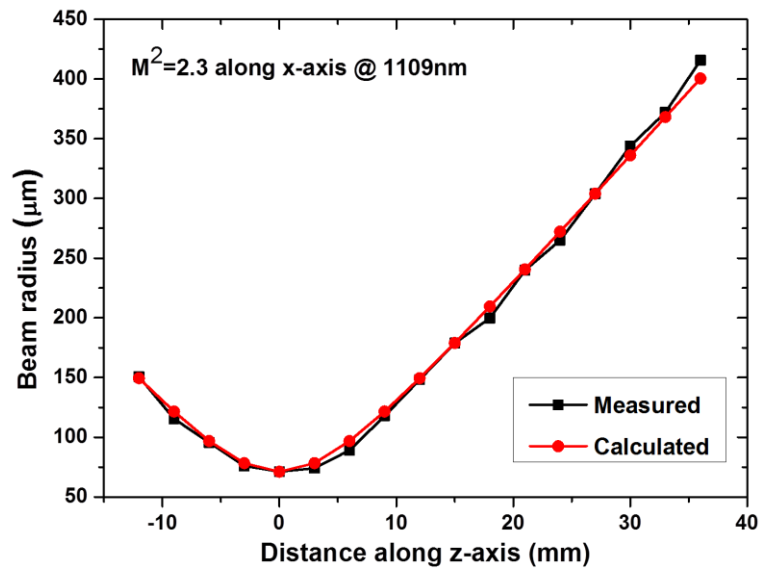
Fig. 4.18 Beam quality factors M^2 along x-axis at λ = 1109 nm
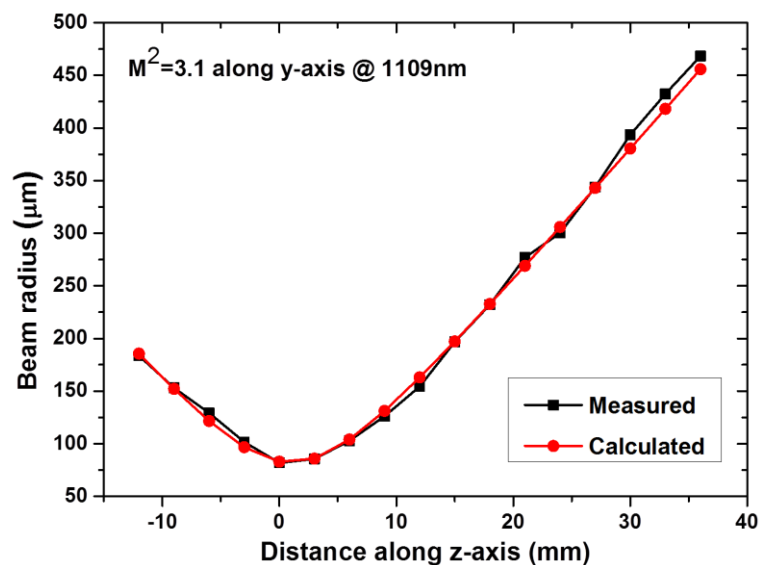
Fig. 4.19 Beam quality M^2 factors along y-axis at λ = 1109 nm

The output optical spectrum was recorded and is displayed in Fig. 4.20. The far-field beam profiles for both fundamental and first Stokes fields were captured using a laser beam profiling digital camera (from Data Ray, WincamD-UCD12-1310 [4.31]) and are displayed in Fig. 4.21.
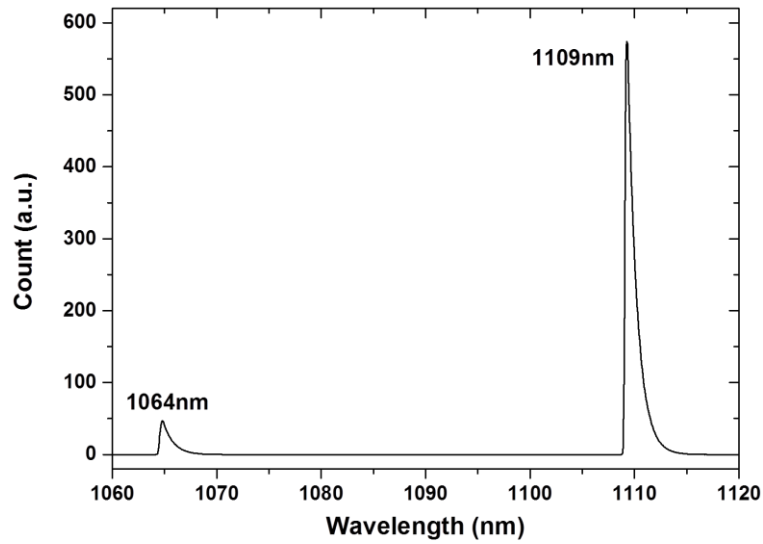
Fig. 4.20 Optical spectrum for the first Stokes Raman output at λ = 1109 nm

(a)   (b)
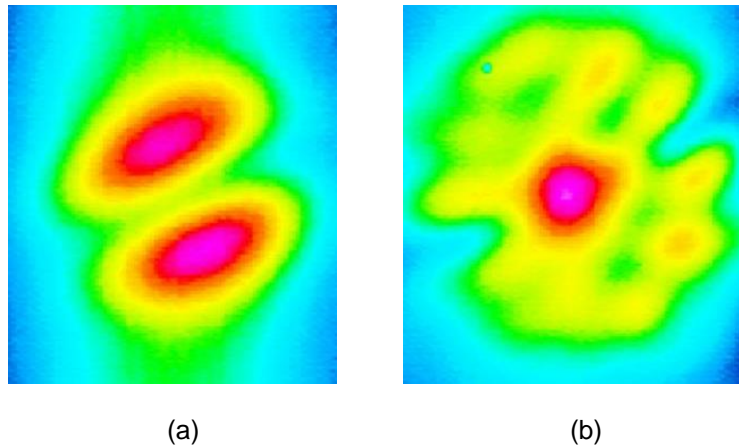
Fig. 4.21 Far-field beam profiles for (a) fundamental field and (b) λ = 1109 nm first Stokes mode

4.4.3 Second Stokes Raman laser at λ = 1158 nm

An output coupler with T ~ 1.2 %, 0.1 % and > 5.0 % at λ = 1158 nm, 1109 nm, and 1176 - 1231 nm respectively was utilised to obtain the λ = 1158 nm Raman laser line resulting from the second Stokes conversion of the 379 cm^{-1} shift. The SRS threshold for the first Stokes (λ = 1109 nm) output was achieved for an absorbed laser diode pump power of 2.9 W with 64 mW fundamental output. The second Stokes Raman threshold was observed for an absorbed laser diode pump power of 8.6 W, with the first Stokes and fundamental output powers being 185 mW and 100 mW respectively. A maximum output power of 700 mW at λ = 1158 nm was obtained for an absorbed laser diode pump power of 12.9 W while the first Stokes and fundamental output powers were measured at 200 mW and 150 mW respectively. This corresponded to an absorbed pump power to second Stokes Raman output power conversion efficiency of 5.4 %. As shown in Fig. 4.22, the power transfer of the second Stokes output exhibited a linear trend without significant influence of thermal lensing. A slight decrease of the conversion efficiency could be observed starting already at the maximum point in Fig. 4.22. Above this pump power, the Raman output power would drop significantly with increasing laser diode pump power.
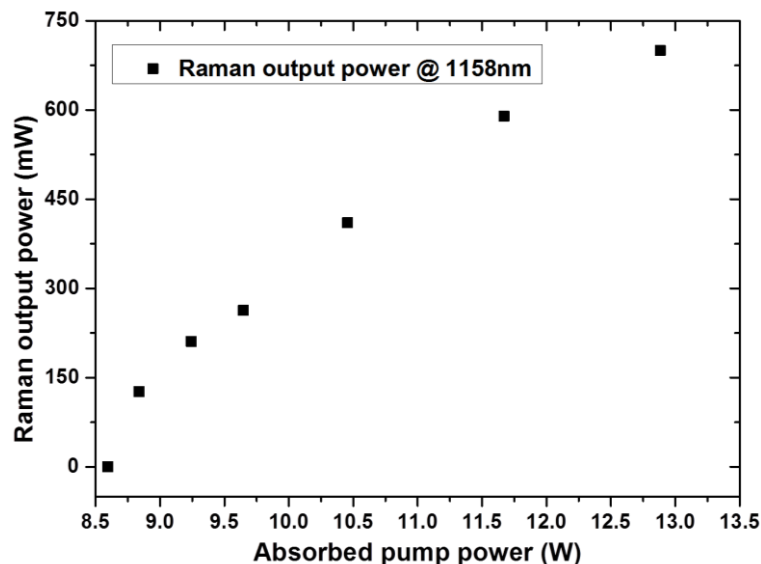
Fig. 4.22 Second Stokes Raman laser output power transfer at λ = 1158 nm

At the maximum Raman output power of 700 mW, the beam quality factors M^2 along x and y axes were both measured at 1.2 for the $\lambda = 1158$ nm laser output, 1.8 and 1.9 for the $\lambda = 1109$ nm laser output and 3.4 and 3.6 for the $\lambda = 1064$ nm laser output. The optical spectrum was measured and is displayed in Fig. 4.23 while the far-field beam profiles of each mode are shown in Fig. 4.24.
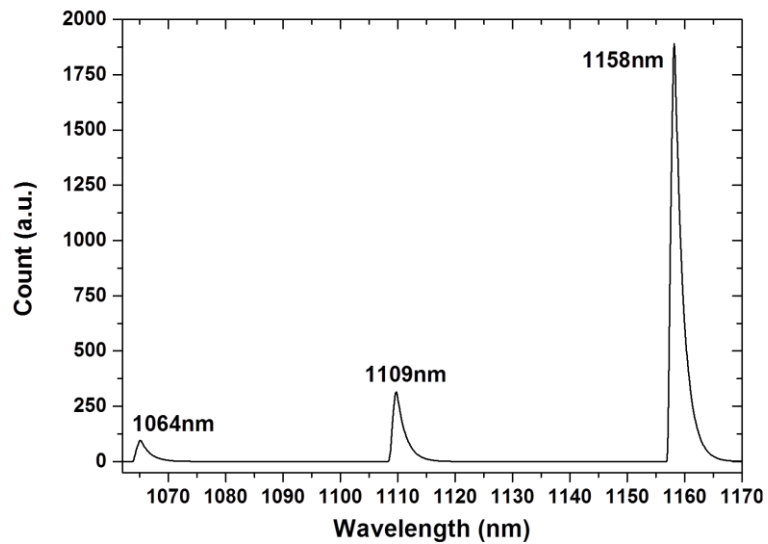
Fig. 4.23 Optical spectrum for the second Stokes Raman output at λ = 1158 nm
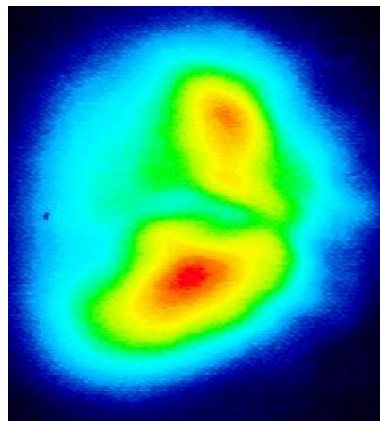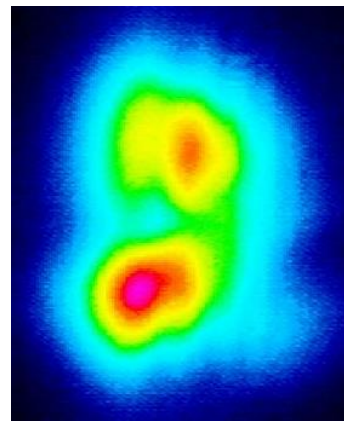
<div align="center">(a)   (b)</div>
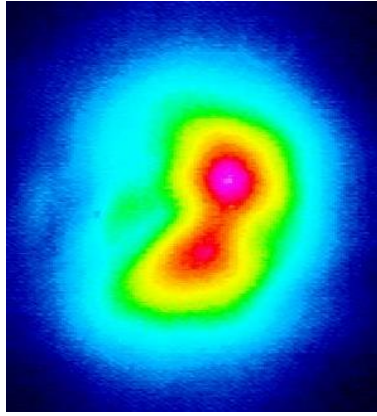
(c)

Fig. 4.24 Far-field beam profiles for (a) fundamental signal and (b) λ = 1109 nm first Stokes signal and (c) λ = 1158 nm second Stokes signal

4.4.4 Second Stokes Raman laser at λ = 1231 nm

A λ = 1231 nm Raman laser was observed resulting from the combination of the first Stokes conversion based on the secondary 379 cm^{-1} shift and the cascaded second Stokes conversion on the primary 893 cm^{-1} shift. The output coupler for this laser was coated for T ~ 2.4 %, 0.5 %, 0.1 % and 2.5 % at λ = 1231 nm, 1158 nm, 1109 nm and 1176 nm respectively. The higher transmission (T ~ 2.5 %) at λ = 1176 nm combined with the lower transmission at λ = 1109 nm (T ~ 0.1 %) of the output coupler resulted in the fundamental laser being first converted into the λ = 1109 nm first Stokes mode based on the 379 cm^{-1} secondary Raman transition before experiencing the 893 cm^{-1} transition. 1.3 W of absorbed diode pump power was required to reach the threshold for the first Stokes conversion with a fundamental laser output power of 40 mW. Beyond that, the threshold for the second Stokes Raman output was observed with an absorbed diode pump power of 3.5 W. At this pump level, 181 mW of output power at λ = 1109 nm and 68 mW of fundamental laser output power were measured. This significantly reduced pump power threshold, when compared with the previous one in subsection 4.4.3 (i.e. 8.6 W), could be attributed to the ~ 5 times higher Raman gain of the primary Raman shift compared to the secondary one, even if the transmission of the

output coupler at the second Stokes Raman output in this case (T ~ 2.4 % at λ = 1231 nm) is twice higher than that in case 4.4.3 (T ~ 1.2 % at λ = 1158 nm).

A Raman output power of 540 mW at λ = 1231 nm was measured for an absorbed diode pump power of 10 W. At the same time, 350 mW of first Stokes output power and 120 mW of fundamental output power were also present. This corresponded to an absorbed pump power to λ = 1231 nm Raman output power conversion efficiency of 5.4 %. As described in subsection 4.4.2, a reduction of the desired second Stokes Raman conversion efficiency could be observed at a range of absorbed diode pump power between 5.9 W and 9.8 W in Fig. 4.25.
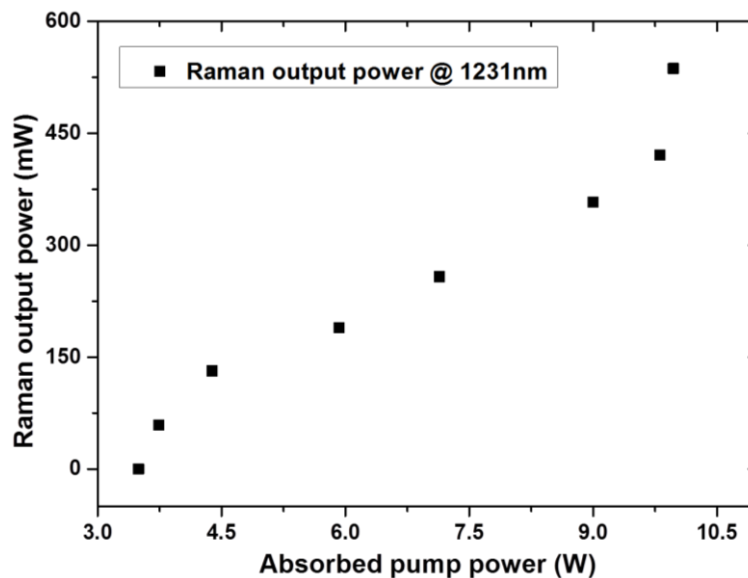
Fig. 4.25 Second Stokes Raman laser output power transfer at λ = 1231 nm

At the maximum output power of 540 mW, the beam quality factors M^2 along the x and y axes were measured at 1.2 and 1.3 for the λ = 1231 nm laser output; 1.8 and 2.3 for the λ = 1109 nm mode laser output and 4 and 3.8 for the fundamental field laser output.

The optical spectrum for the Raman laser output was measured as shown in Fig. 4.26. It should be noted that, in this case, when the diode pump power was slightly increased above the maximum level shown in Fig. 4.25, the

Raman laser output suddenly collapsed, either induced by the strong thermal lensing or the competition between different Stokes modes. With this collapse of SRS conversion, all the laser diode pump power automatically converted to the fundamental field. Due to the extremely high-Q for the fundamental field inside the laser cavity (i.e. R > 99.95 % at λ = 1064 nm for the end mirror and R > 99.97 % at λ = 1064 nm for the output coupler), an excessive intracavity power intensity of the fundamental field was produced which resulted in damage to the Nd:YVO$_4$ crystal coating. For this reason, the beam profiles of the Raman output could unfortunately not be measured.
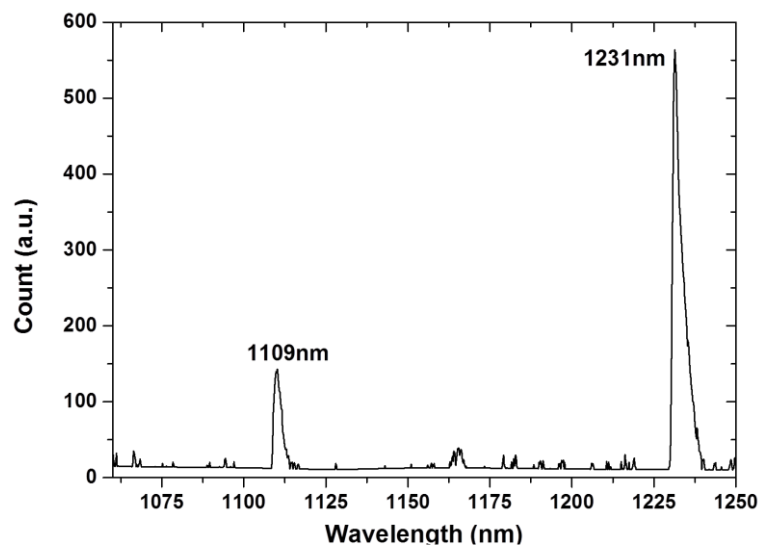
Fig. 4.26 Optical spectrum for the second Stokes Raman output at λ = 1231 nm

4.4.5 First Stokes Raman laser at λ = 1176 nm

An output coupler with T ~ 1.0 % at λ = 1176 nm and T ~ 0.2 % at λ = 1109 nm was used to obtain a "conventional" first Stokes Raman laser output at λ = 1176 nm based on the main 893 cm^{-1} shift. The threshold for the first Stokes Raman output was observed with an absorbed diode pump power of 2.12 W. At this pump level, 70 mW of fundamental laser output power could also be measured. A maximum Raman output power of 1.14 W at λ = 1176 nm and 200 mW of output power at λ = 1064 nm were obtained with 12.2 W of absorbed pump power. This corresponds to an absorbed pump power to

114

Raman output power conversion efficiency of 9.3 %. The Raman output power transfer was measured as shown in Fig. 4.27. At pump powers above 12 W, a thermal rollover was observed.
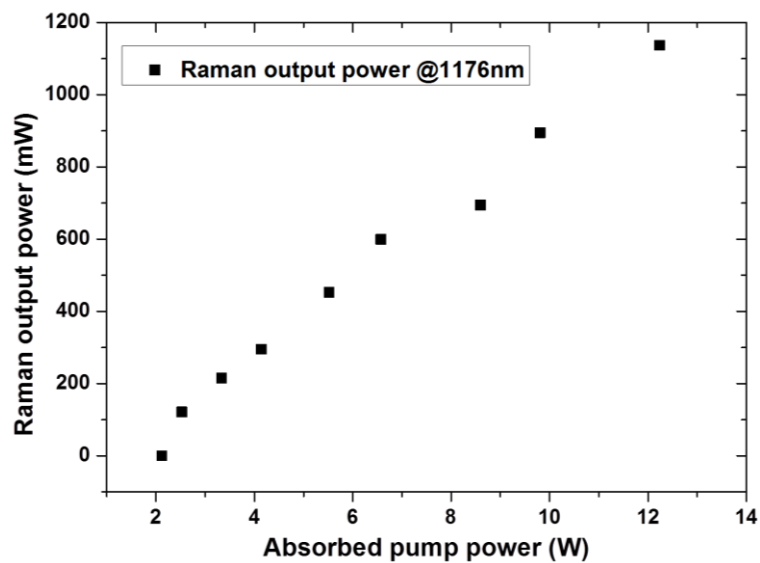
Fig. 4.27 First Stokes Raman laser output power transfer at λ = 1176 nm

At the maximum Raman output power, the beam quality factors M^2 along the x and y axes were measured at 2.0 and 2.5 for the first Stokes mode laser and both 2.7 for the fundamental field laser output. The optical spectrum and beam profiles were measured and are shown in Fig. 4.28 and 4.29.
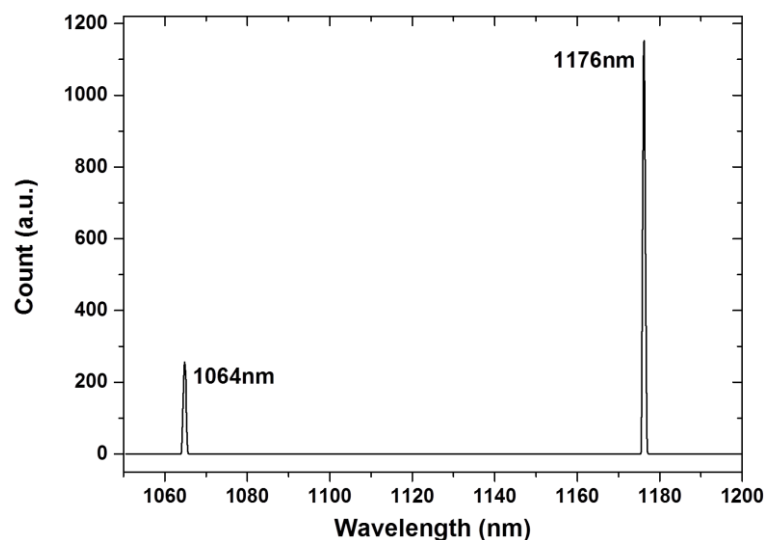
Fig. 4.28 Optical spectrum for the first Stokes Raman output at λ = 1176 nm

(a)   (b)
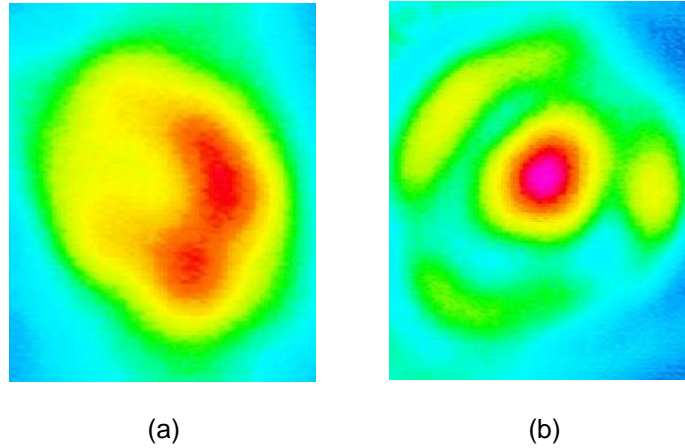
Fig. 4.29 Far-field beam profiles for (a) fundamental field and (b) λ = 1176 nm first Stokes mode

4.5 Discussion

4.5.1 Compensation for the beam radii variation influenced by the thermal lensing

As explain in subsection 1.3.4, thermal lensing scales directly with the Raman laser output power and has been recognised as the main limitation in the power-scaling of CW Raman lasers [4.33]. The fundamental (λ = 1064 nm) and Raman (λ = 1176 nm) TEM_{00} radii w at the centre of the gain medium under the influence of thermal lensing with different focal lengths (f_{thl} = 200 mm, 100 mm and 30 mm) could be simulated using an ABCD-matrix software (Winlase 2.1 pro [4.34]). These calculations were undertaken for different curvatures of output couplers ranging from 1m to 0.1m as displayed in Tables 4.1-4.3.

	With f_{thl} = 200 mm	With f_{thl} = 100 mm	With f_{thl} = 30 mm
ω_{1064nm}	132 µm	114 µm	88 µm
ω_{1176nm}	139 µm	120 µm	93 µm

Table 4.1 The radii varying influenced by thermal lensing with a ROC = 1000 mm output coupler

	With f_{thl} =200 mm	With f_{thl} = 100 mm	With f_{thl} = 30 mm
ω_{1064nm}	127 µm	112 µm	88 µm
ω_{1176nm}	133 µm	117 µm	92 µm

Table 4.2 The radii varying influenced by thermal lensing with a ROC = 500 mm output coupler

	With f_{thl} = 200 mm	With f_{thl} = 100 mm	With f_{thl} = 30 mm
ω_{1064nm}	104 µm	98 µm	83 µm
ω_{1176nm}	110 µm	103 µm	88 µm

Table 4.3 The radii varying influenced by thermal lensing with a ROC = 100 mm output coupler

	ROC = 1000 mm	ROC = 500 mm	ROC = 100 mm
$\Delta\omega_{1064nm}$	44 µm	39 µm	21 µm
$\Delta\omega_{1176nm}$	46 µm	41 µm	22 µm

Table 4.4 Summary of the variation ranges of the beam radii with different curved output couplers

The variations of the fundamental and Raman single mode beam radii as influenced by the varying range of the thermal lensing (from f_{thl} = 200 to 30 mm) with output couplers of different ROC are summarised in Table. 4.4. The ROC = 100 mm output coupler leads to a minimum variation in the single mode beam size within the gain medium (~ half compared to the other cases) for the fundamental and Raman fields during the built up of the thermal lens.

This alleviation of the thermal lens effect will significantly benefit the Raman laser output performance and the cavity stability under a relative high diode pump power in the CW regime. However, using the strongly-concave output coupler will lead to a high intracavity power intensity, which has the potential to damage the AR coatings of the Nd:YVO$_4$ surfaces. Therefore, a balance between avoiding coating damage and obtaining a good resilience to the thermal lensing build up must be reached.

4.5.2 Raman clean-up effect

The spatial beam qualities of the different laser outputs are summarised in Table 4.5. An improvement of the beam quality factor M^2 could be observed in each of the Raman laser configurations either between the fundamental field and the first Stokes field or between the first Stokes mode and the second Stokes mode. This improvement is attributed to the Raman beam clean-up effect which has been well reported in [4.35-4.37]. Due to the high power intensity requirement for the SRS conversion, the weak Stokes signal originating from spontaneous Raman scattering will be amplified from the lowest-order propagation mode of the fundamental beam. In this way, SRS conversion will feature the transfer of energy between fundamental and Stokes fields without the transfer of distortions, even if the fundamental beam has a poor beam quality or a multi-mode profile. The Raman clean-up effect may then influence the beam profiles of the fundamental field due to the weak gain at the lowest-order propagation mode of the fundamental field induced by SRS conversion (i.e. Fig. 4.21 and 4.29).

An improved TEM of the first Stokes Raman output (~TEM$_{00}$) could be observed if compared with the fundamental field (~TEM$_{01}$) due to the Raman beam clean-up effect which will be described in the discussion section.

Type of output	M^2 at λ = 1064 nm	M^2 at λ = 1109 nm	M^2 at λ = 1158 nm	M^2 at λ = 1176 nm	M^2 at λ = 1231 nm
First Stokes output based on the 379 cm⁻¹ shift (4.4.2)	4.9 (x-axis) 5.4 (y-axis)	2.3 (x-axis) 3.1 (y-axis)			
Second Stokes output based on the 379 cm⁻¹ shift (4.4.3)	3.4 (x-axis) 3.6 (y-axis)	1.8 (x-axis) 1.9 (y-axis)	1.2 (x-axis) 1.2 (y-axis)		
Combination of the 379 cm⁻¹ shift with the 893 cm⁻¹ shift (4.4.4)	4.0 (x-axis) 3.8 (y-axis)	1.8 (x-axis) 2.3 (y-axis)			1.2 (x-axis) 1.3 (y-axis)
First Stokes output based on the 893 cm⁻¹ shift (4.4.5)	2.7 (x-axis) 2.7 (y-axis)			2.0 (x-axis) 2.5 (y-axis)	

Table 4.5 Summary of the beam quality factors M^2 in different Raman laser cavities

4.5.3 Comparison between the primary and secondary Raman shifts in YVO$_4$ crystal

The conversion efficiency of the Raman laser emitting at λ = 1109 nm (8.4 %) and that of the λ = 1176 nm Raman laser (9.3 %) were in the same range despite the significant discrepancy in Raman gain transition – the 893 cm⁻¹ Raman gain being ~ 5 times higher than that of the 379 cm⁻¹ transition. This can be explained by a combination of reasons elaborated in the following sub-sections.

4.5.3.1 Output coupling transmission

First, the output coupling transmissions at each first Stokes wavelength in these two Raman laser configurations are different. A $T \sim 0.2\,\%$ at $\lambda = 1109$ nm output coupler was utilised in 4.4.2 while a $T \sim 1.0\,\%$ at $\lambda = 1176$ nm output coupler was used in 4.4.5. To evaluate the influences induced by different output transmissions and Raman gains on the first Stokes Raman conversion efficiency, the modelling equations for CW intracavity Raman lasers developed by Spence et al. [4.38] (which were described in subsection 1.3.1) were utilised here:

$$\mathbf{P_S^{Out}/P_P} = \frac{\mathbf{T_S}}{\mathbf{(T_S+L_S)}}\,\frac{\mathbf{\lambda_P}}{\mathbf{\lambda_S}} - \frac{\mathbf{T_S(T_F+L_F)}}{\mathbf{4}}\,\frac{\mathbf{\lambda_F}}{\mathbf{\lambda_S}}\,\frac{\mathbf{\pi\omega^2}}{\mathbf{P_Pg_RL_R}} \qquad (4\text{-}2)$$

All relative parameters were summarised in Table 4.6 below.

	Subsection 4.4.2	Subsection 4.4.5
Fundamental beam radius (ω)	~ 100 µm	~ 100 µm
Output coupling transmissions for the fundamental field (T_F)	~ 0.03 %	~ 0.03 %
Round-trip losses for the fundamental field (L_F)	~ 0.48 %	~ 0.48 %
Output coupling transmissions for the Stokes field (T_S)	~ 0.2 %	~ 1.0 %
Round-trip losses for the Stokes field (L_S)	~ 0.45 %	~ 0.45 %
Pump wavelength (λ_P)	~ 808 nm	~ 808 nm
Fundamental wavelength (λ_F)	~ 1064 nm	~ 1064 nm

Stokes wavelength (λ_S)	~ 1109 nm	~ 1176 nm
Laser diode pump power (P_p)	~ 12 W	~ 12 W
Crystal length (L_R)	~ 20 mm	~ 20 mm
Raman gain coefficient (g_R)	~ 0.9 cm / GW	~ 4.5 cm / GW

Table 4.6 Summary of the relative parameters in subsection 4.4.2 and 4.4.5

Therefore, the first Stokes conversion efficiencies could be calculated at ~ 44% and ~ 19% for the cases described in subsection 4.4.5 and 4.4.2, corresponding to a ~ 2.3 times ratio difference. From the modelling equation 4.2, it is clear that the difference in output coupling and Raman gain coefficients will significantly influence the first Stokes conversion efficiency.

4.5.3.2 Thermal lensing effect

The modelling described above relies on several assumptions such as no optical losses due to the cavity alignment, fundamental beam radii in the gain medium are not varying over time and a perfect mode match between the fundamental and first Stokes lines is present. However, in a real experiment, strong thermal lensing will significantly reduce the conversion efficiency as calculated using the modelling equation. The similar Raman laser output conversion efficiency observed in subsection 4.4.2 and 4.4.5 leads to the assumption that the thermal lens effect in the $\lambda = 1109$ nm case is less pronounced than in the $\lambda = 1176$ nm case. This can be attributed to the quantum defect of the different wavelength conversions. The quantum defect can be represented as a heat transfer originating from the difference of energies between the pump photon of the Raman transition and its emitted Stokes photon, which can be expressed using the following equation:

$$q = h * \omega_f - h * \omega_s \qquad (4\text{-}3)$$

where q is the difference of energies due to the quantum defect, h is the Plank constant ($\sim 6.63 \times 10^{-34}$ m^2 kg / s), ω_f and ω_s are the frequencies of the fundamental and Stokes photons respectively. This can be rewritten as,

$$\mathbf{q} = \mathbf{h} * \mathbf{c} * (\frac{1}{\lambda_f} - \frac{1}{\lambda_s}) \qquad (4\text{-}4)$$

where c is the speed of light in vacuum, λ_f and λ_s are the wavelengths of fundamental and Stokes photons respectively.

Equation (4-4) describes that, assuming the same fundamental wavelength, a Stokes wavelength closer to the fundamental wavelength can lead to a lower quantum defect (thermal loading) during the SRS conversion. Therefore, in this work, the quantum defect in the λ_{s1} = 1176 nm case can be calculated to be 2.4 times larger than that in the λ_{s2} = 1109 nm case based on the fundamental pump wavelength of λ_f = 1064 nm.

4.5.3.3 Spectral broadening effect

In 2014, Bonner et al. demonstrated that SRS conversion occurring in an intracavity Raman laser configuration can extent the linewidth of the fundamental laser field, which in turn reduces the effective Raman gain [4.39]. However, this effect is dependent on the linewidth of the Raman gain. With a wider linewidth of the Raman transition, the SRS-induced loss of the fundamental laser field becomes spectrally broader. Therefore, this effect will discourage any side-stepping of the fundamental field wavelength. In this way, the conversion efficiency will be increased.

According to the above points, self-Raman lasers based on the secondary Raman shift have the potential to provide conversion efficiencies in the same range as those measured in self-Raman laser based on the primary Raman shift despite the significant reduction in Raman gain.

During the laser characterisations presented in subsection 4.4.4 and 4.4.5, both second Stokes (λ = 1158 and 1231 nm) or first Stokes (λ = 1109 and 1176 nm) Raman outputs could be observed simultaneously (see Fig. 4.30 and 4.31). This demonstrated a co-existing and competition state between these two Raman lines based on the same Stokes order but different Raman shifts. To deal with this competition and select the favourable wavelength, a balance between the Raman gain and optical cavity losses for each Raman laser configuration must be struck. Although the Raman gain in the primary 893 cm^{-1} Raman shift is ~ 5 times higher than that in the secondary 379 cm^{-1} shift, the reduced thermal lensing and spectral broadening effects occurring in the secondary Raman shift can partly compensate for this significant difference in Raman gain. By carefully managing the cavity optical losses for each Raman shift in the same Stokes mode such as changing the output coupler transmission or manually aligning the cavity, a desired Raman output wavelength can be optimised.
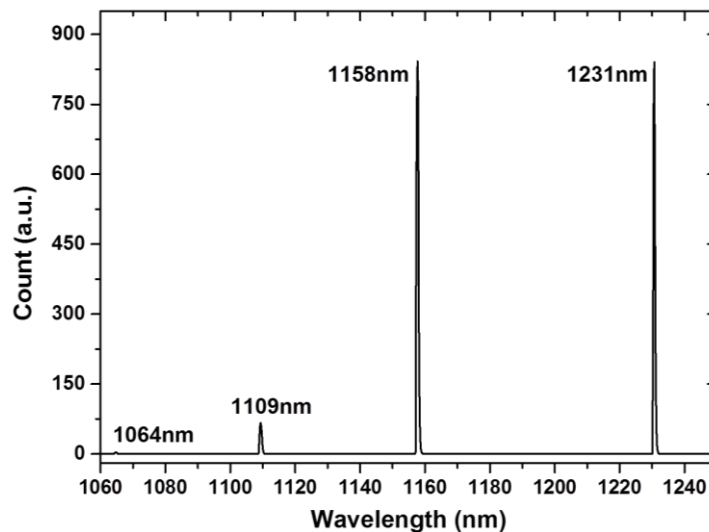
Fig. 4.30 Laser output spectrum for the laser presented in subsection 4.4.4
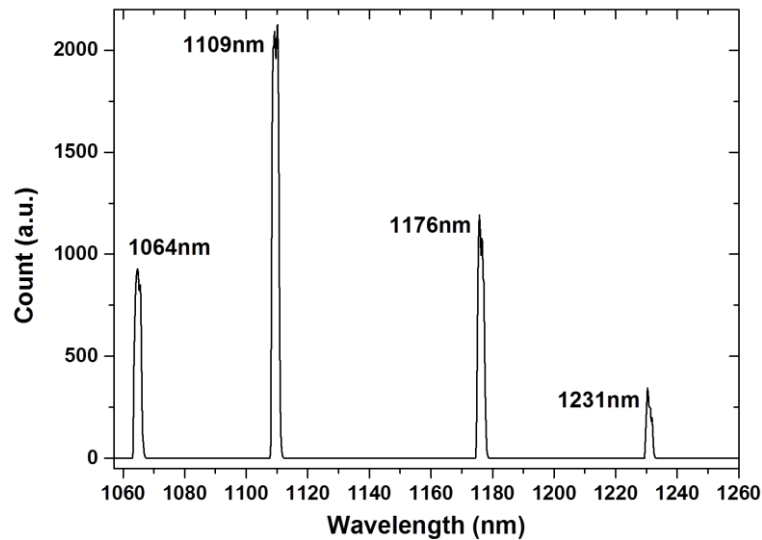
Fig. 4.31 Laser output spectrum for the laser presented in subsection 4.4.5

4.6 Conclusion

To the best of my knowledge, the first CW self-Raman lasers based on a 379 cm^{-1} secondary Raman shift of Nd:YVO$_4$ crystal have been achieved and presented in this chapter. The 5-times reduction in Raman gain did not significantly impact the conversion efficiency of the Raman laser operating at $\lambda = 1109$ nm. This was due to the significant reduction in thermal lensing and spectral broadening effects. Four configurations were investigated resulting in ~ Watt-level CW Raman laser outputs at $\lambda = 1109$ nm, 1158 nm, 1176 nm and 1231 nm. These lasers represent a first step towards the development of CW, narrowly-spaced, visible lines in the green-lime-yellow region for a range of medicine and bio-photonics applications.

In this work, the Raman laser output performances were mainly restricted by the thermal lens and spectral broadening effects, which could be improved by several approaches such as optimising the reflectivity of the output couplers, swapping the pump wavelength from $\lambda = 808$ nm to $\lambda = 880$ nm to further alleviate the thermal lens effect [4.8, 4.10, 4.40] and using linewidth narrowing elements to alleviate the spectral broadening effect [4.39, 4.41]. In addition, the significant thermal loading and internal Raman shifts competition both lead

to some potential opportunities to implement adaptive optics techniques inside self-Raman lasers to control the Raman laser output performance.

4.7 References

4.1   Y. F. Chen, "Compact efficient self-frequency Raman conversion in diode-pumped passively Q-switched Nd:GdVO$_4$ laser," Appl. Phys. B **78**, 685-687 (2004).

4.2   Y. F. Chen, "Efficient subnanosecond diode-pumped passively Q-switched Nd:YVO$_4$ self-stimulated Raman laser," Opt. Lett. **29**, 1251-1253 (2004).

4.3   A. A. Kaminskii, K. Ueda, H. J. Eichler, Y. Kuwano, H. Kouta, S. N. Bagaev, T. H. Chyba, J. C. Barnes, G. M. A. Gad, T. Murai, and J. Lu, "Tetragonal vanadates YVO$_4$ and GdVO$_4$ – new efficient $\chi^{(3)}$ - materials for Raman lasers," Opt. Commun. 1**94**, 201-206 (2001).

4.4   Y. F. Chen, "High-power diode-pumped actively Q-switched Nd:YVO$_4$ self-Raman laser: influence of dopant concentration," Opt. Lett. **29**, 1915-1917 (2004).

4.5   F. Su, X. Zhang, Q. Wang, S. Ding, P. Jia, S. Li, S. Fan, C. Zhang and B. Liu, "Diode pumped actively Q-switched Nd:YVO$_4$ self-Raman laser," J. Phys. D: Appl. Phys. **39,** 2090-2093 (2006).

4.6   L. Fan Y. X. Fan H. T. Wang, "A compact efficient continuous-wave self-frequency Raman laser with a composite YVO$_4$/Nd:YVO$_4$/YVO$_4$ crystal," Appl. Phys. B **101**, 493-496 (2010).

4.7   P. Dekker, H. M. Pask, D. J. Spence and J. A. Piper, "Continuous-wave, intracavity doubled, self-Raman laser operation in Nd:GdVO$_4$ at 586.5 nm," Opt. Express. **15**, 7038-7046 (2007).

4.8   A. J. Lee, H. M. Pask, P. Dekker, J. A. Piper, "High efficiency, multi-Watt CW yellow emission from an intracavity-doubled self-Raman laser using Nd:GdVO$_4$," Opt. Express. **16**, 21958-21963 (2008).

4.9   H. Zhu, Y. Duan, G. Zhang, C. Huang, Y. Wei, W. Chen, Y. Huang, and N. Ye, "Yellow-light generation of 5.7 W by intracavity doubling self-Raman laser of YVO$_4$ /Nd:YVO$_4$," Opt. Lett. **34**, 2763-2765 (2009).

4.10   A. J. Lee, H. M. Pask, D. J. Spence, and J. A. Piper, "Efficient 5.3 W cw laser at 559 nm by intracavity frequency summation of fundamental and first-Stokes wavelengths in a self-Raman Nd:GdVO$_4$ laser," Opt. Lett. **35**, 682-684 (2010).

4.11   A. J. Lee, D. J. Spence, J. A. Piper, and H. M. Pask, "A wavelength-versatile, continuous-wave, self-Raman solid-state laser operating in the visible," Opt. Express. **18**, 20013-20018 (2010).

4.12   X. Li, A. J. Lee, H. M. Pask, J. A. Piper and Y. Huo, "330 mW CW yellow emission from miniature self-Raman laser based on direct HR-coated Nd:YVO$_4$ crystal," IQEC/CLEO Pacific Rim, p. C289 (2011).

4.13   X. Li, H. M. Pask, A. J. Lee, Y. Huo, J. A. Piper, and D. J. Spence, "Miniature wavelength-selectable Raman laser: new insights for optimizing performance," Opt. Express. **19**, 25623-25631 (2011).

4.14   J. Lin, H. M. Pask, "Nd:GdVO$_4$ self-Raman laser using double-end polarised pumping at 880 nm for high power infrared and visible output," Appl. Phys. B **108**, 17-24 (2012).

4.15   J. H. Lock and K. C. Fong, "Retinal Laser Photocoagulation," Med. J. Malaysia **65**, 88-95, (2010).

4.16   H. M. Pask, P. Dekker, R. P. Mildren, D. J. Spence, and J. A. Piper, "Wavelength-versatile visible and UV sources based on crystalline Raman lasers," Prog. Quantum Electron. **32**, 121–158 (2008).

4.17   F. Shuzhen, Z. Xingyu, W. Qingpu, L. Zhaojun, L. Lei, C. Zhenhua, C. Xiaohan, Z. Xiaolei, "1097 nm Nd:YVO$_4$ self-Raman laser," Opt. Commun. **284** 1642-1644 (2011).

4.18   J. Lin and H. M. Pask, "Cascaded self-Raman lasers based on 382 cm^{-1} shift in Nd:GdVO$_4$," Opt. Express. **20**, 15180-15185 (2012).

4.19   H. Yu, K. Wu, H. Zhang, Z. Wang, J. Wang, and M. Jiang, "Nd:YGG crystal laser at 1110 nm: a potential source for detecting carbon monoxide poisoning," Opt. Lett. **36**, 1281-1283 (2011).

4.20   M. F. Garcia-Parajo, M. Koopman, E. M. van Dijk, V. Subramaniam, and N. F. van Hulst, "The nature of fluorescence emission in the red fluorescent protein DsRed, revealed by single-molecule detection," Proc. Natl. Acad. Sci. U.S.A. **98**, 14392-14397 (2001).

4.21   *Neodymium doped Yttrium Orthavanadate (Nd: YVO₄)* Crystal, LASER COMPONENTS GmbH, Werner-von-Siemens-Str. 15, Olching, 82140, Germany, www.lasercomponents.com.

4.22   CASIX, 20, Fuxing Street Fuxing Investment District, Fuzhou, Fujian, 350014, China, www.casix.com/technology/crystal-growing.shtml.

4.23   RENISHAW apply innovation, New Mills, Wotton-under-Edge, Gloucestershire, GL 12 8JR, United Kingdom, www.renishaw.com.

4.24   T. C. Damen, S. P. S. Porto, and B. Tell, "Raman Effect in Zinc Oxide," Phys. Rev. **142**, 570–574 (1966).

4.25   DILAS The diode laser company, Galileo-Galilei-Straße 10, Mainz-Hechtsheim, D-55129, Germany, www.dilas.com.

4.26   ELITE THERMAL ENGINEERING, 11th Avenue West, Bothell, Washington, 98021, United States, www.elitethermalengineering.com.

4.27   THORLABS, 56 Sparta Avenue, Newton, New Jersey, 07860, United States, www.thorlabs.com.

4.28   ThermoFisher Scientific, 81 Wyman Street, Waltham, Massachusetts, 02451, United States, www.thermofisher.com/en/home.html.

4.29   Newport Corporation, 1791 Deere Avenue Irvine, California, 92606, United States, www.newport.com.

4.30   GENTEC ELECTRO OPTICS, 445 St-Jean-Baptiste, Suite 160, Quebec, G2E 5N7, Canada, www.gentec-eo.com.

4.31   Agilent technologies, 5301 Stevens Creek Blvd, Santa Clara, California, 95051, United States, www.agilent.com/home.

4.32   DataRay, 14505 Seaman Gulch Road, Bella Vista, California, 96008, United States, www.dataray.com.

4.33   H. M. Pask, "The design and operation of solid-state Raman lasers," Prog. Quant. Electron. **27**, 3-56 (2003).

4.34   Winlase 2.1 Pro, Future Laser Technologies, 24221 Robledo Cir, Mission Viejo, California, 92600, United States, www.winlase.com.

4.35   R. S. F. Chang, R. H. Lehmberg, M. T. Duignan, and N. Djeu, "Raman Beam Cleanup of a Severely Aberrated Pump Laser," IEEE. J. Quant. Electron. **QE-21**, 477-487 (1985).

4.36   J. Reintjes, R. H. Lehmberg, R. S. F. Chang, M. T. Duignan, and G. Calame, "Beam cleanup with stimulated Raman scattering in the intensity-averaging regime," J. Opt. Soc. AM. **3**, 1408-1427 (1986).

4.37   J. T. Murray, W. L. Austin, R. C. Powell, "Intracavity Raman conversion and Raman beam cleanup," Opt. Mater. **11**, 353–371 (1999).

4.38   D. J. Spence, P. Dekker, and H. M. Pask, "Modelling of Continuous Wave Intracavity Raman Lasers," IEEE J. Sel. Topics Quantum Electron. **13**, 756-763 (2007).

4.39   G. M. Bonner, J. Lin, A. J. Kemp, J. Wang, H. Zhang, D. J. Spence, and H. M. Pask, "Spectral broadening in continuous-wave intracavity Raman lasers," Opt. Express. **22**, 7492-7502 (2014).

4.40   T. Omatsu, M. Okida, A. Lee, H. M. Pask, "Thermal lensing in a diode-end-pumped continuous-wave self-Raman Nd-doped GdVO$_4$ laser," Appl. Phys. B **108**, 73-79 (2012).

4.41   V. G. Savitski, "Experimental analysis of emission linewidth narrowing in a pulsed KGd(WO$_4$)$_2$ Raman laser," Opt. Express. **22**, 21767-21774 (2014).

Chapter 5

Advanced controllable continuous-wave Nd:YVO₄ self-Raman laser using intracavity adaptive optics

5.1 Introduction

Solid-state Raman lasers enable the generation of an extended range of "hard-to-reach" laser wavebands due to the wavelength conversion associated with SRS [5.1, 5.2]. However, the power scaling of these Raman lasers operating either in the CW regime or in the pulsed regime at high repetition rates is severely limited by the thermal lensing occurring within the Raman gain medium (especially for intracavity Raman configurations) [5.3, 5.4].

A number of approaches to reduce the thermal lens effect for a range of specific CW solid-state Raman lasers in an intracavity configuration have been introduced in sub-section 2.5.4. These methods are based on the use of synthetic diamond or artificial composite $YVO_4/Nd:YVO_4/YVO_4$ crystals as the Raman gain medium [5.5-5.9], or on the lengthening of Raman active crystals [5.10]. In addition, the quantum defect – one of the influencing factors for the thermal lens effect - can be reduced by using a higher pump wavelength (for instance, using diodes emitting at $\lambda = 880$ nm to pump Neodymium-doped orthovanadate Raman crystals [5.4, 5.10, 5.11]).

In this chapter, a novel approach to reduce the detrimental effects of thermal lensing during Raman laser oscillation is proposed, utilising adaptive optics inside the laser cavity. This method has the potential to be utilised in all solid-

state Raman laser configurations in order to power-scale the Raman laser output performance. A CW Nd:YVO$_4$ intracavity self-Raman laser was used as a test-bed for the implementation of this technique due to its simple cavity design and the complex superposition of thermal lensing induced by the residual pump loading and the non-elastic nature of SRS [5.3, 5.4, 5.11]. An AO-based feedback control loop featuring an intracavity bimorph DM, a photodiode sensor to assess the Raman output power and a PC-based control system was implemented into the self-Raman laser platform leading to an ~ 18 % improvement of the Raman laser output power. In addition to power-scaling, a wavelength control based on the selection of the primary or secondary Raman shift of the Nd:YVO$_4$ crystal (which has been described in chapter 4) was demonstrated using this AO technique.

Section 5.2 reviews several AO-closed-loops that were integrated in CW intracavity solid-state lasers to enhance the laser output performances. Section 5.3 describes the characterisations of five DMs using two different measuring approaches. In section 5.4, a Nd:YVO$_4$ self-Raman laser platform, a system assessor and a PC-based control program will be introduced. In section 5.5, the results for the Raman laser output power-scaling and wavelength selection using this AO technique will be presented, while several discussion points for the achieved results will be provided in section 5.6.

5.2 Reviews of the CW intracavity solid-state laser improvement using AO-closed-loop

This thesis presents work on the development of an advanced controllable CW self-Raman laser using AO techniques. A series of previous research related to the AO-closed-loop implementing inside CW intracavity crystalline lasers is reviewed below.

Using this concept, Lubeigt et al. improved in 2002 the laser output transverse mode from TEM$_{01}$ to TEM$_{00}$ while the laser output power was power-scaled

from 20 mW to 120 mW by implementing an AO-closed-loop for the first time inside an end-pumped all-solid-state Nd:YVO$_4$ laser cavity [5.23].
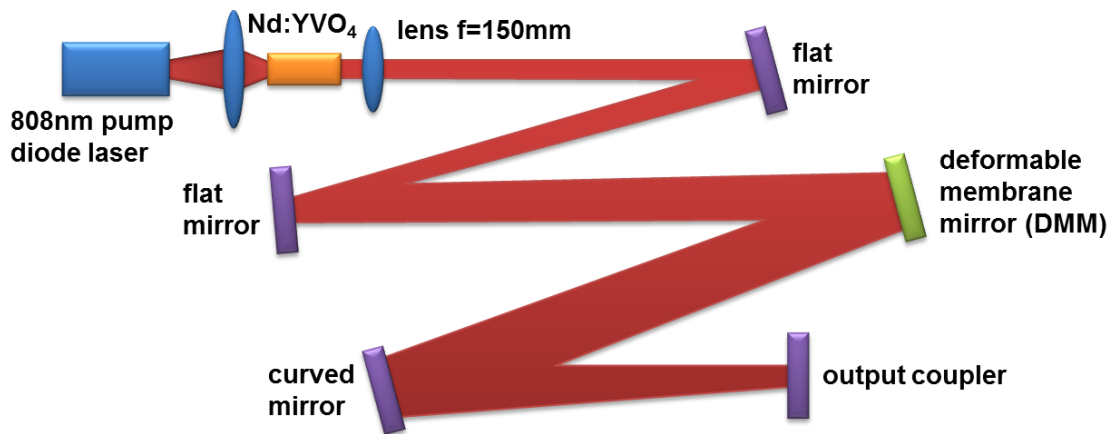
Fig. 5.3 Nd:YVO$_4$ laser configuration featuring an intracavity DMM [image extracted from 5.23]

A 15 mm-diameter deformable membrane mirror (DMM) containing 37 actuators distributed in a hexagonal pattern, was used as one of the HR folding mirror in a 6-mirror Nd:YVO$_4$ laser resonator shown in Fig. 5.3. During the AO optimisation, two approaches were used to assess the laser output performance. In the first method, the laser output intensity was detected by a silicon photodiode with a 100 μm-diameter pinhole which was placed to spatially filter the laser beam into a TEM$_{00}$ mode. Alternatively, an advanced measurement approach using a CCD camera in cooperation with a programmed software aperture was developed and tested. A hill-climbing search algorithm was employed to adapt the DMM shape providing an improved laser output performance.

In 2006, Wittrock et al. demonstrated the use of an AO-based closed-loop inside a solid-state laser cavity [5.25]. A feedback control network consisting of an intracavity 10 mm-diameter DMM comprised of 19 actuators with a hexagonal pattern was integrated within a 4-mirror Nd:YVO$_4$ laser configuration (see Fig. 5.4). A "power-in-the-bucket" fitness assessor (a photodiode sensor behind a far-field aperture) and a PC-based control program were used for the closed-loop control. A genetic algorithm was

developed to obtain an improved laser output performance. Compared to the manual laser alignment for the same cavity, the beam quality factor M^2 was enhanced from 5.0 to 3.6 after AO optimisation, while the maximum laser output power was increased from 5.6 W to 6.1 W for the same absorbed laser diode pump power of 26.6 W.
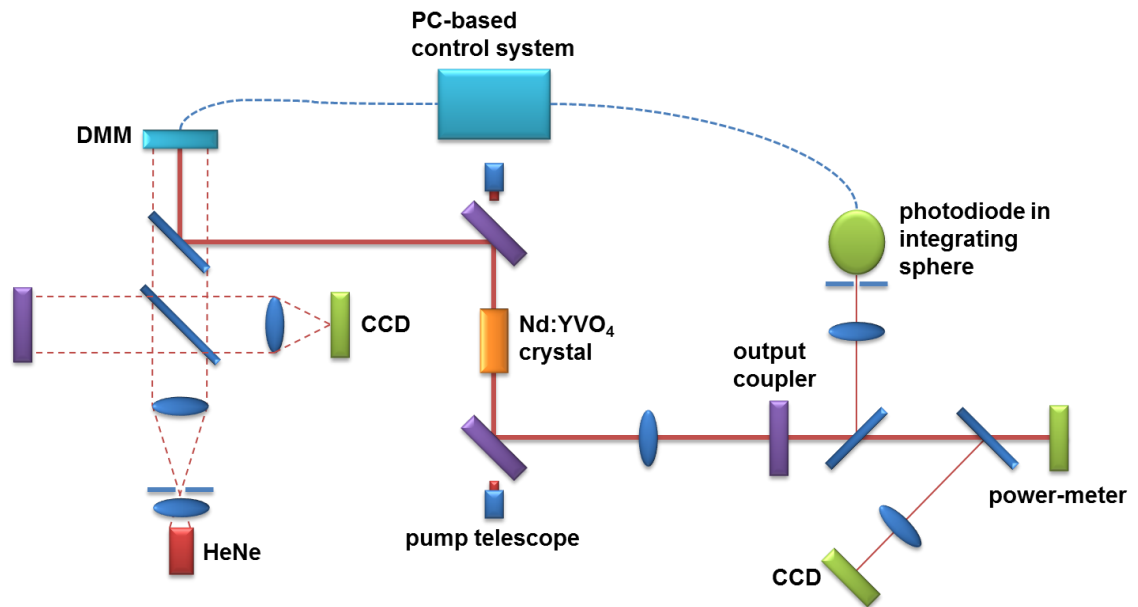
Fig. 5.4 AO-closed-loop combined with a 4-mirror Nd:YVO$_4$ solid-state laser cavity [image extracted from 5.25]

In 2007, several CW Nd:YAG lasers with different beam profiles (i.e. TEM_{11}, TEM_{10} and TEM_{20}) were optimised into a TEM_{00} mode by compensating for the thermal effects using an AO-closed-loop as reported by P. Yang et al. [5.26]. As shown in Fig. 5.5, an intracavity 19-element piezoelectric DM with a hexagonal actuator design was utilised as a cavity end-mirror of a flash lamp-pumped 2-mirror Nd:YAG laser cavity. The output beam profiles were detected using a PC-controlled CCD camera. The optimum DM pattern corresponding to a TEM_{00} beam after optimisation was achieved by a genetic algorithm-based search process.
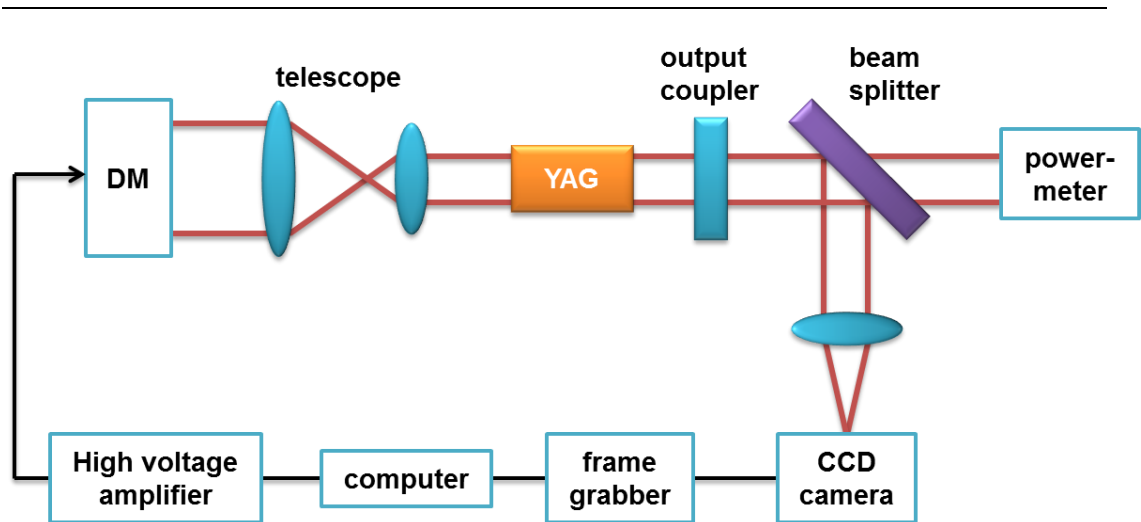
Fig. 5.5 AO-closed-loop in cooperation with the 2-mirror YAG laser cavity [image extracted from 5.26]

Similarly, in 2008 Lubeigt et al. successfully integrated an AO-closed-loop into two different side-pumped solid-state laser cavities to significantly enhance the laser output beam qualities [5.27]. A 15 mm-diameter intracavity DMM was utilised for both solid-state laser configurations. The DMM contained 37 electrostatic actuators designed in a hexagonal pattern.
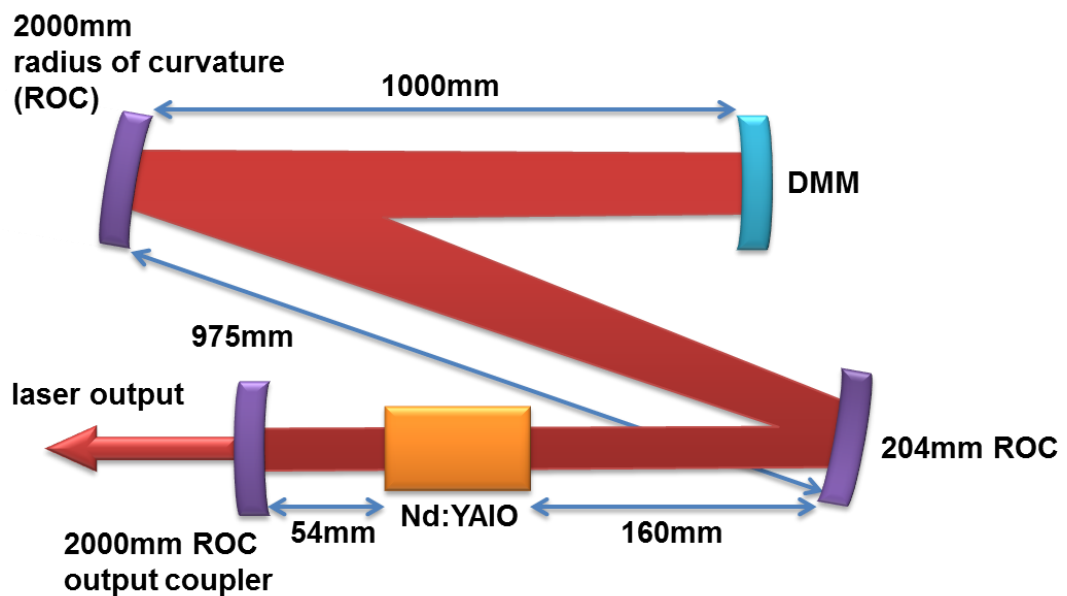
Fig. 5.6 Side-pumped Nd:YAlO laser configuration [image extracted from 5.27]

In the first instance, the AO-closed-loop featuring a genetic search algorithm was implemented into a side-pumped Nd:YAlO laser platform, as shown in Fig. 5.6. A highly multi-mode laser output beam profile was improved to a single-mode beam profile ($M^2 < 1.3$) with less than 5 % output power drop after the AO optimisation.
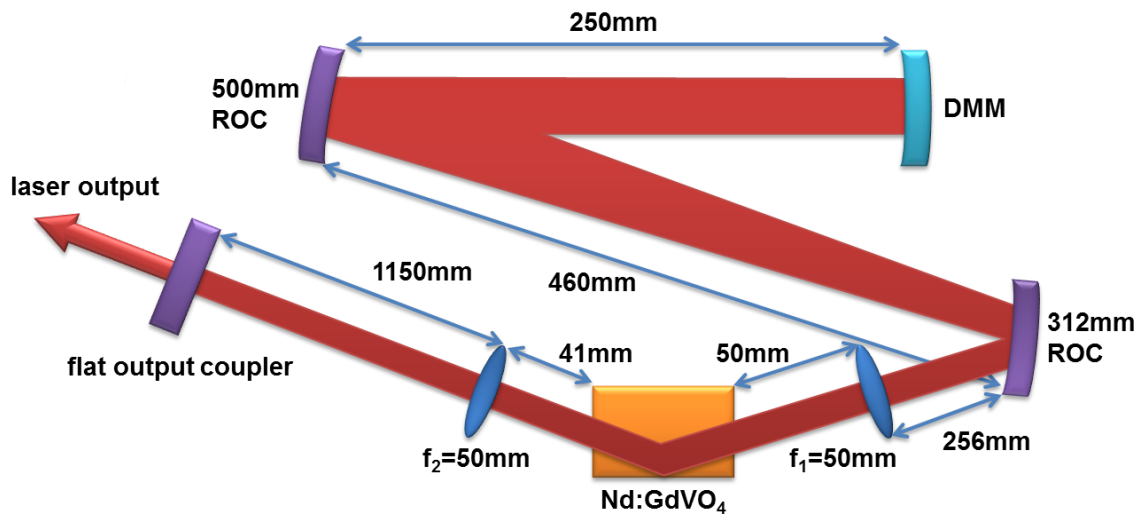
Fig. 5.7 Grazing-incidence Nd:GdVO$_4$ laser configuration [image extracted from 5.27]

In the second case, a grazing-incidence Nd:GdVO$_4$ laser was constructed as the AO optimisation platform as shown in Fig. 5.7. A similar genetic algorithm was used to optimise the beam mode. In this case, the laser output performance was assessed by a nonlinear KTP crystal since the conversion efficiency of the SHG scales directly with the brightness of the incoming beam. Therefore, it provided an indirect way to evaluate the incoming laser output performance by detecting the SHG output laser intensity using a photodiode sensor. After AO optimisation, the beam quality factors M^2 were optimised from 27 to 9 in the tangential plane and from 10.5 to 3 in the sagittal plane with an output power drop from 15 W to 14 W. This corresponded to a brightness improvement of one order of magnitude.

Furthermore, the investigation on CW intracavity SSL improvements using AO-closed-loop control was reported in 2010 by J. Li et.al. [5.31]. A 25 mm-diameter DMM containing 37 electrostatic actuators with a hexagonal

distribution was used as a cavity end-mirror inside a 2-mirror Nd:YAG laser cavity, which is similar to P. Yang's previously reported laser platform [5.26]. A Shack-Hartmann wavefront sensor was used to detect the thermally induced wavefront aberration of a probe HeNe laser for the global genetic algorithm search procedure. As a result, the laser output beam profile was optimised from TEM_{01} to TEM_{00} while the laser output power was power-scaled from 230 mW to 546 mW.

All reports above have demonstrated the feasibility of AO-closed-loop operation used in conventional solid-state lasers to enhance the laser output performances, either in respect of the output power and/or the beam profile. This shows the potential of the concept to be implemented inside Raman lasers to correct for the more complicated and stronger thermal lensing produced during SRS conversion.

5.3 Characterisations of INCAO bimorph DM

Five bespoke piezoelectric actuated bimorph DMs developed by BAE Systems Advanced Technology Centre [5.32] were available for AO correction. Their characteristics and performance will be described in this section and only the most suitable one will be chosen for our subsequent investigations.

(a)   (b)
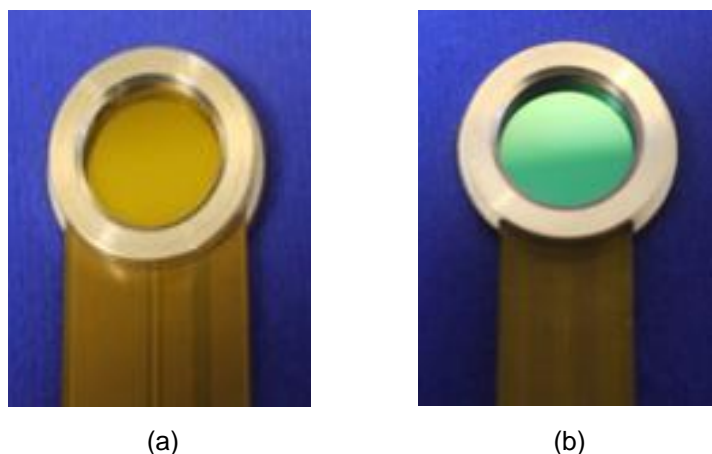
Fig 5.8 (a) Test mirrors (INCAO1-3); (b) Final mirrors (INCAO 4, 5)

The five DMs can be divided into the two groups of "test mirrors" and "final mirrors" due to their different characteristics (see Fig. 5.8).

Each test mirror (INCAO 1-3) contains 31 piezoelectric actuators with a corresponding driving voltage range from -50 V to 250 V [5.33]. As Fig. 5.9 (a) shows, 15 actuators are arranged in a 7mm active aperture while the other 16 boundary actuators extend the total DM diameter to 15 mm. All test DMs have a HR multi-layer dielectric coating for R > 99.8 % at λ = 1064 nm. The working principle of bimorph DMs has been described in chapter 3.

(a)   (b)
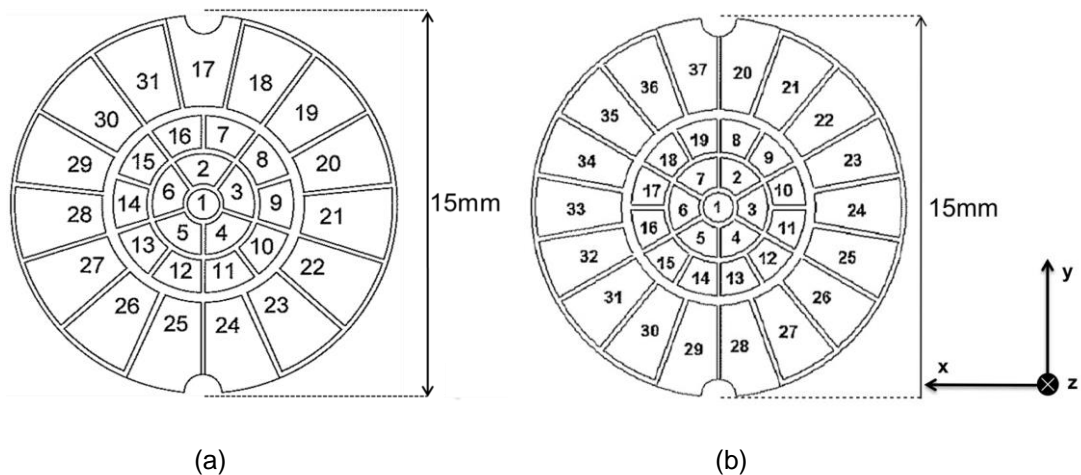
Fig. 5.9 Actuator designation of a) INCAO test mirror with 31 actuators, b) INCAO final mirror with 37 actuators (looking at the mirror surface when the flexi-circuit is on the right side) [image extracted from 5.33, 5.34]

37 actuators are allocated to the surface of the final mirrors (INCAO 4, 5), with a similar radial distribution as used in the test mirrors which can provide a higher spatial resolution for the wavefront correction (see Fig. 5.9 (b)) [5.34]. Both final DMs have a multi-layer HR dielectric coating of R > 99.9 % at λ = 1064 nm. However, the INCAO mirror 4 could only be driven at a voltage ranging from -30 V to 180 V while the INCAO mirror 5 has the same driving voltage range as the test DMs (from -50 V to 250 V).

In order to individually address all actuators with the required voltage range, the control system shown in Fig. 5.10 was developed. The 12-bit individual digital signals were produced by a LabView-based control program and

converted to a set of multi-channel voltages ranging from 0 to ~ 3.5 V using a USB-DAC (from OKO technologies [5.35]). A high voltage amplifier (from OKO technologies) was utilised to increase the voltage to the driving requirement of 300 V or 210 V, depending on the type of DMs used. An additional power supply (fixed at either 50 V or 30 V for the maximum voltage of 300 V or 210 V respectively) was used as a floating ground. In this way, a driving voltage range from -50 V to 250 V (or -30 V to 180 V) could be achieved, which corresponded to the full addressable range of the 12-bit values (from 0 to 4096) in the LabView program.
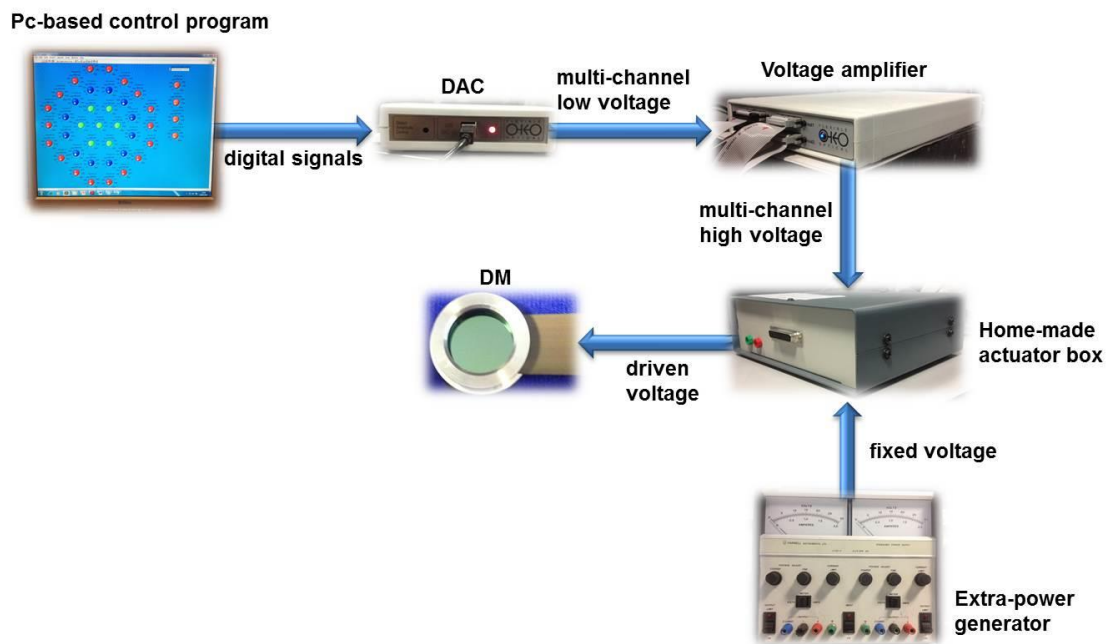
Fig. 5.10 Schematic diagram of the DM control system

When the same multi-channel driving voltage was applied to all actuators simultaneously, it led to a near-spherical deformation of the DM surface, corresponding to a ROC variation of the DM shape. This deformation can be quantitatively represented by the focusing power (F) that is commonly used to assess a converging or diverging light beam path through an optical element. The relationship between the ROC of the mirror surface and the focusing power can be expressed as:

$$F = \frac{2}{ROC} \qquad (5\text{-}1)$$

The response of the focusing power to variations in the DM actuation is a crucial characterisation of the DM, especially when it is used to adjust the defocus of each intracavity beam size to achieve a favourable mode matching between the fundamental and Stokes fields of the Raman laser. Two optical measuring approaches were undertaken to characterise the DMs in this work. One was based on a white light optical profiling system, while the other was using a Shack-Hartmann wavefront sensor.

The principle of the commercial white light optical profiling system used here (Wyko NT1100 from Veeco [5.36], see Fig. 5.11) is based on a Michelson interferometer. The focusing power responses of the three test mirrors were measured along their x and y axes with a ~ 0.3 nm vertical resolution for varying actuation voltages. [N.B. the x and y axes are as defined in Fig. 5.9]. The measurement results are displayed in Fig. 5.12-5.14, where the average ROC was calculated from:

$$ROC = \frac{ROC_x + ROC_y}{2} \qquad (5\text{-}2)$$
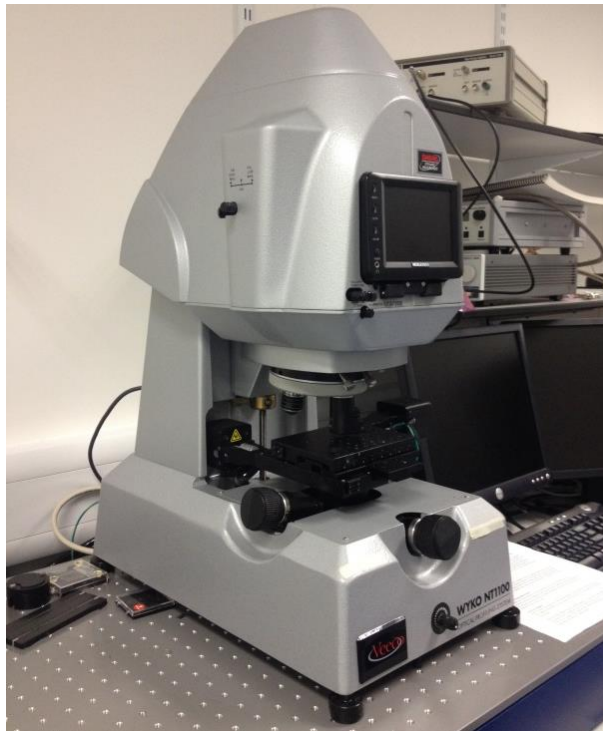
Fig. 5.11 White light optical profiling system Wyko NT1100
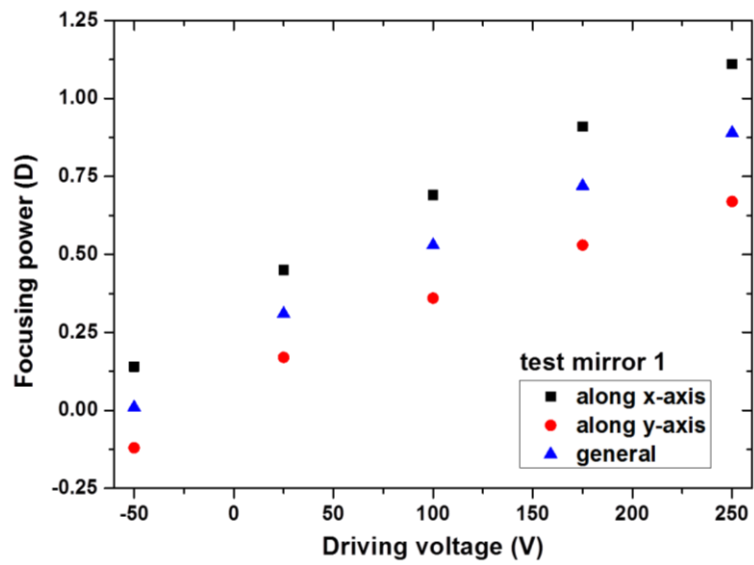
Fig. 5.12 Focusing power response of test mirror 1 measured using a white light interferometer
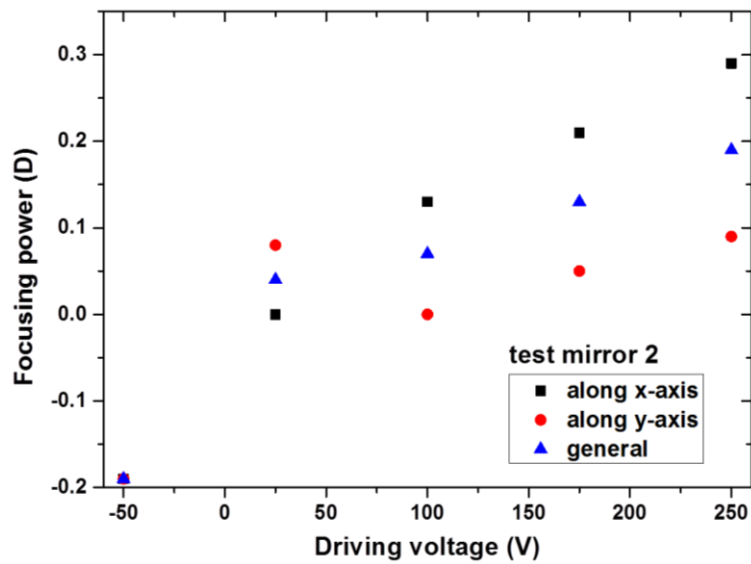
Fig. 5.13 Focusing power response of test mirror 2 measured using a white light interferometer
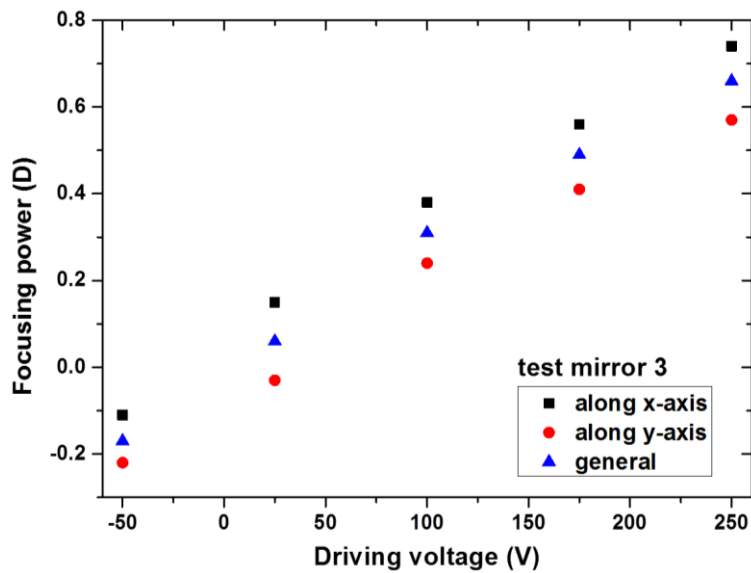
Fig. 5.14 Focusing power response of test mirror 3 measured using a white light interferometer

Unfortunately, this measurement could not be achieved with the final DM as its reflective surface was located too far away from the top of the protective ring (see Fig. 5.15). As a result, the objective lens of the profiler could not be moved close enough to focus on the mirror surface. Therefore, only the surface of the test mirrors could be assessed using this experimental set-up.
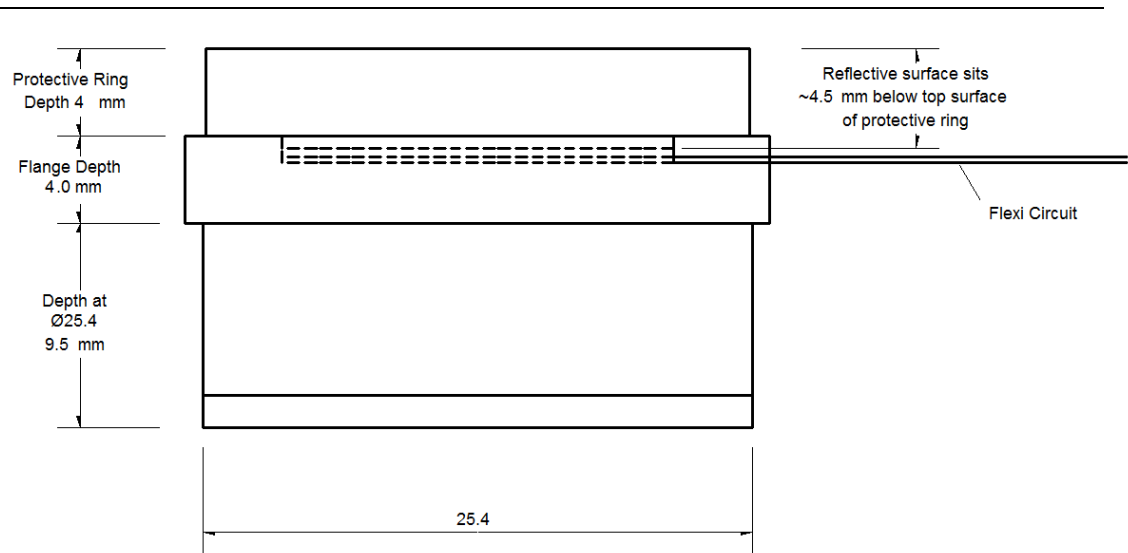
Fig. 5.15 Outlines drawing of INCAO final mirror [5.33]

To overcome the limitation of this measurement technique and to measure the maximum curvatures of the final DMs, a surface profile measurement system based on a Shack-Hartmann wavefront sensor was constructed as shown in Fig. 5.16. A $\times$ 4.5 telescope was used to expand a HeNe probe beam to ~ 3 mm diameter in order to obtain a large illumination area on the DM. The wavefront on the mirror surface plane was then imaged in the wavefront sensor using a pair of f = 12.5 cm lenses. Both the illumination and light collection beam paths were directed with a plane incident on the DM through the use of a 50 / 50 distribution beam-splitter.
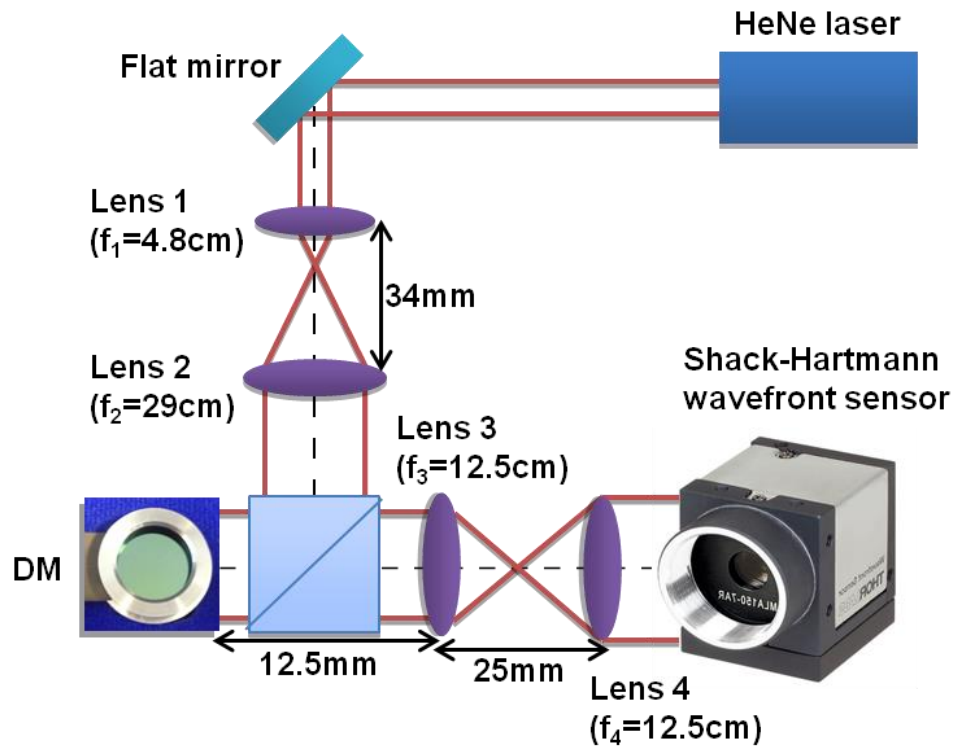
Fig. 5.16 Shack-Hartmann wavefront sensor measuring system

The Shack-Hartmann wavefront sensor from Thorlabs instruments [5.37] (WFS150-5C) contains an array of miniature lenses (lenslets) which all have the same focal length (~ 5 mm). When an incoming wavefront is incident on the lenslets, it is split into an array of light beams which are each focused onto a CCD detector. The Zernike Polynomials describing the properties of the incoming wavefront can be computed using the deviations of the different focus spots. The major Zernike coefficients relevant to this investigation were Z_5 (defocus) and Z_6 (astigmatism) which can be used to calculate the ROC of the wavefront as follows [5.38]:

$$Z_{5x} = Z_5 + \frac{Z_6}{\sqrt{2}} \tag{5-3}$$

$$Z_{5y} = Z_5 - \frac{Z_6}{\sqrt{2}} \tag{5-4}$$

$$ROC_x = \frac{-\Phi_x{}^2}{8\sqrt{3}\,Z_{5x}} \tag{5-5}$$

$$\mathbf{ROC_y} = \frac{-\Phi_y{}^2}{8\sqrt{3}\,Z_{5y}} \quad . \tag{5-6}$$

where Z_{5x} and Z_{5y} are the defocus term for the x and y axes respectively and Φ_x and Φ_y are the diameter of the measurement pupil along the x and y axes respectively. The ROC along the x and y axes (ROC_x and ROC_y) can therefore be calculated.

The focusing powers along the x and y axes for all five DMs were measured for varying driving voltages and are displayed in Fig. 5.17-5.21 respectively.
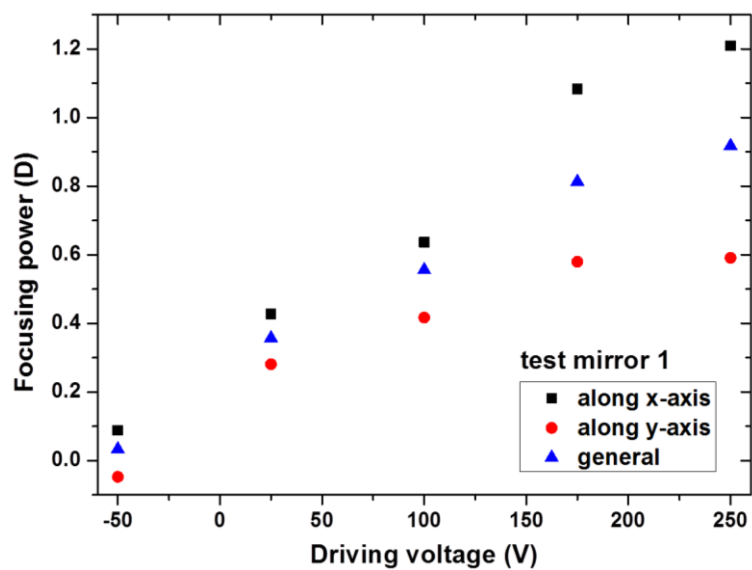
Fig. 5.17 Focusing power response of the test mirror 1 measured using a wavefront sensor
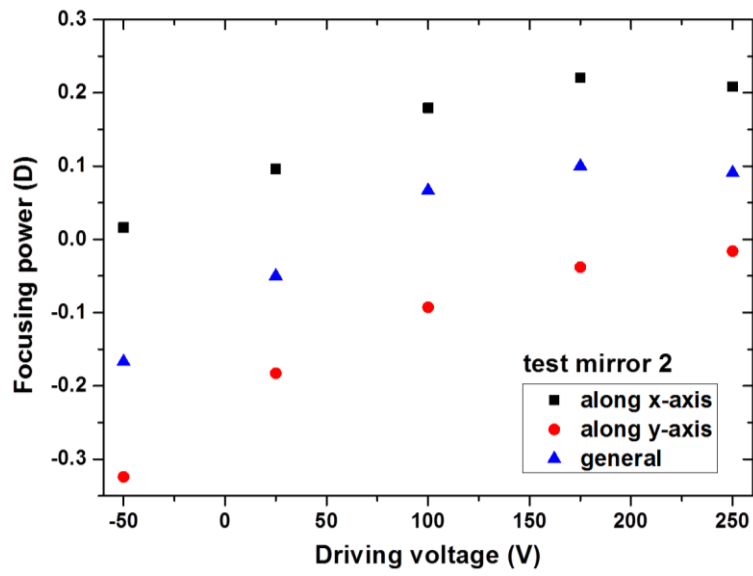
Fig. 5.18 Focusing power response of the test mirror 2 measured using a wavefront sensor
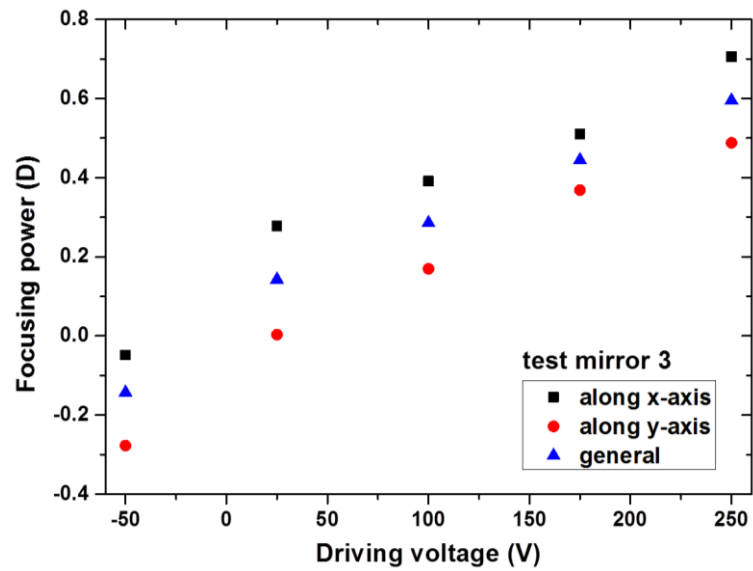
Fig. 5.19 Focusing power response of the test mirror 3 measured using a wavefront sensor
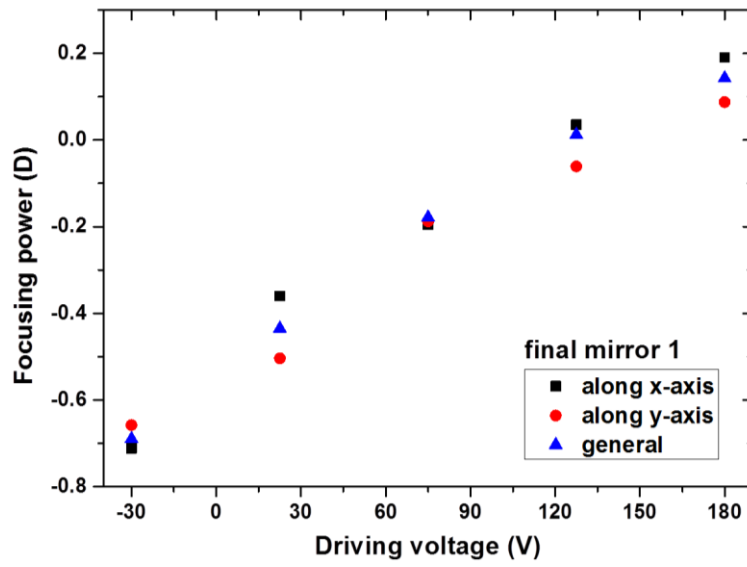
Fig. 5.20 Focusing power response of the final mirror 1 measured using a wavefront sensor
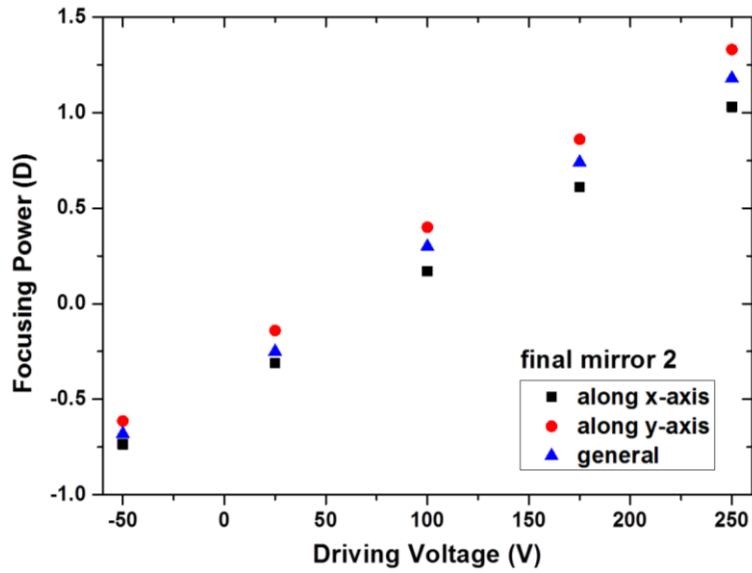
Fig. 5.21 Focusing power response of the final mirror 2 measured using a wavefront sensor

146

DM/Measuring approach	Minimum Focusing Power (D)	Maximum Focusing Power (D)	Focusing Power Range ΔF (D)
Test mirror 1 using a white light interferometer	0.01	0.89	0.88
Test mirror 1 using a wavefront sensor	0.03	0.92	0.89
Test mirror 2 using a white light interferometer	-0.19	0.19	0.38
Test mirror 2 using a wavefront sensor	-0.17	0.09	0.26
Test mirror 3 using a white light interferometer	-0.17	0.66	0.83
Test mirror 3 using a wavefront sensor	-0.14	0.60	0.74

Table 5.1 Summary of the general focusing powers of test mirrors measured using a white light interferometer and wavefront sensor

Table 5.1 compares the average achievable focusing powers of the three test mirrors, measured using either the optical profiling system or the wavefront sensor. Most of the results from both sets are in reasonable agreement (within ~ 10 %). Moreover, test mirror 1 and 3 exhibit a similar average focusing power range (ΔF ~ 0.8 D) while the test mirror 2 has a significantly reduced response range (ΔF ~ 0.4 D). In addition, test mirror 2 has a similar focusing power when actuated at 250 V compared to an actuation of 175 V for the other mirrors. This can possibly be explained by some unexpected faults that happened to the actuators of test mirror 2, such as physical shock or overload.

DM/Direction	Minimum Focusing Power (D)	Maximum Focusing Power (D)	Focusing Power Range ΔF (D)
Test mirror 1 along the x axis	0.09	1.21	1.12
Test mirror 1 along the y axis	-0.05	0.59	0.64
Test mirror 2 along the x axis	0.02	0.21	0.19
Test mirror 2 along the y axis	-0.32	-0.02	0.30
Test mirror 3 along the x axis	-0.05	0.71	0.76
Test mirror 3 along the y axis	-0.28	0.49	0.77

Table 5.2 Summary of the focusing powers of test mirrors along x and y axes measured using the wavefront sensor

Table 5.2 summaries the focusing power responses of all test mirrors along their x and y axes using the wavefront sensor only. The correction ranges observed along the x-axis are always larger than that observed along the y-axis. As far as the maximum focusing powers of the three test mirrors are concerned, the biases of the astigmatism between the two main axes were observed at ~ 0.6 D, ~ 0.2 D and ~ 0.2 D corresponding to test mirror 1 to 3 respectively. It can therefore be concluded that all test mirrors exhibit a high astigmatism.

The final mirrors were produced approximately one year after the test mirrors. The dielectric coating and focusing power range were both improved through advanced passive substrate materials and manufacturing. Table 5.3 displays a summary of the focusing powers of the final mirrors measured using the Shack-Hartman wavefront sensor. Final mirror 2 exhibits a much wider average focusing power range of $\Delta F = 1.86$ D compared with final mirror 1 ($\Delta F = 0.83$ D). This could be explained by the possibility of using an extended driving voltage range applied on final mirror 2. In addition, a lower astigmatism effect could be observed on both final mirrors compared to the test mirrors.

DM/Direction	Minimum Focusing Power (D)	Maximum Focusing Power (D)	Focusing Power Range ΔF (D)
Final mirror 1 along the x axis	-0.71	0.19	0.90
Final mirror 1 along the y axis	-0.66	0.09	0.75
Final mirror 1 average	-0.69	0.14	0.83
Final mirror 2 along the x axis	-0.74	1.03	1.77
Final mirror 2 along the y axis	-0.61	1.33	1.94
Final mirror 2 average	-0.68	1.18	1.86

Table 5.3 Summary of the focusing powers of final mirrors

In conclusion, only test mirror 2 had a limited correction range, corresponding to the shortest general focusing power range of $\Delta F = 0.4$ D. Since final mirror 2 presented the best focusing power range ($\Delta F = 1.86$ D) with a lower astigmatism effect, it was chosen to be implemented inside the self-Raman laser resonator.

5.4 AO-based feedback control network

The AO-control feedback loop integrated within a 4-mirror Nd:YVO$_4$ self-Raman laser configuration is displayed in Fig. 5.22. The Raman laser output power was recorded by a photodiode (Thorlabs PDA10CS-EC [5.37]) and sent to the PC-based control program. An iterative search algorithm was employed to find a shape of the DM that results in an improved Raman laser output power according to the feedback signal. The AO optimisation process was terminated after a pre-set loop iteration number was reached in the search algorithm. Therefore, an automatic power-scaling of the Raman laser output could be achieved.
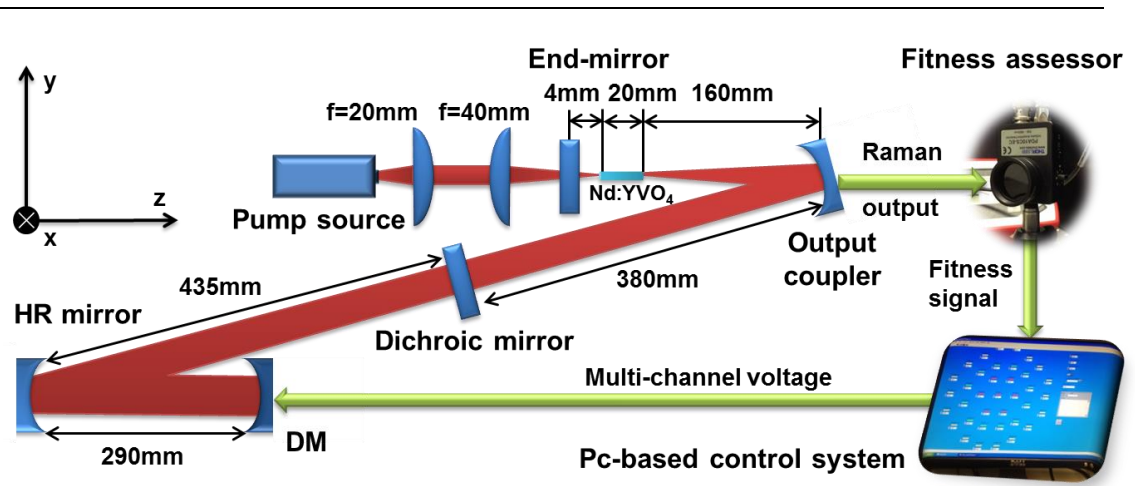
Fig. 5.22 Schematic diagram of the AO-based feedback control system

5.4.1 4-mirror Nd:YVO₄ self-Raman laser configuration

It is well known that, compared to the traditional $\lambda = 808$ nm pumping which involves the $^4I_{9/2}$ to $^4F_{5/2}$ absorption transition in the Nd^{3+} ion, pumping at $\lambda = 880$ nm enables direct excitation of the upper laser level of $^4F_{3/2}$. Bypassing the non-radiative $^4F_{5/2}$ to $^4F_{3/2}$ transition, it provides a lower quantum deficiency and weaker absorption coefficient leading to an important benefit of reducing the thermal load. Therefore, in this work, a $\lambda = 880$ nm pump source was utilised to alleviate the significant thermal loading within the self-Raman crystal and to allow the resonator to be operated at a higher pump power level [5.4, 5.10, 5.11, 5.39]. The laser diode (LM-B 0107, from LIMO [5.40]) was coupled with a high-power fibre (ø ~ 100 µm, NA ~ 0.22, QMMJ-5HPM, from Laser 2000 Ltd [5.41]) with a maximum pump power of 32 W. A temperature feedback controlled cooling system (Model OCP-11 from Elite Thermal Engineering [5.42]) was utilised to keep the diode at a constant temperature of 24 ˚C. The absorbed pump power within the laser gain medium as a function of the diode driving current was measured using a powermeter (PM100A, from Thorlabs [5.37]) and is displayed in Fig. 5.23.
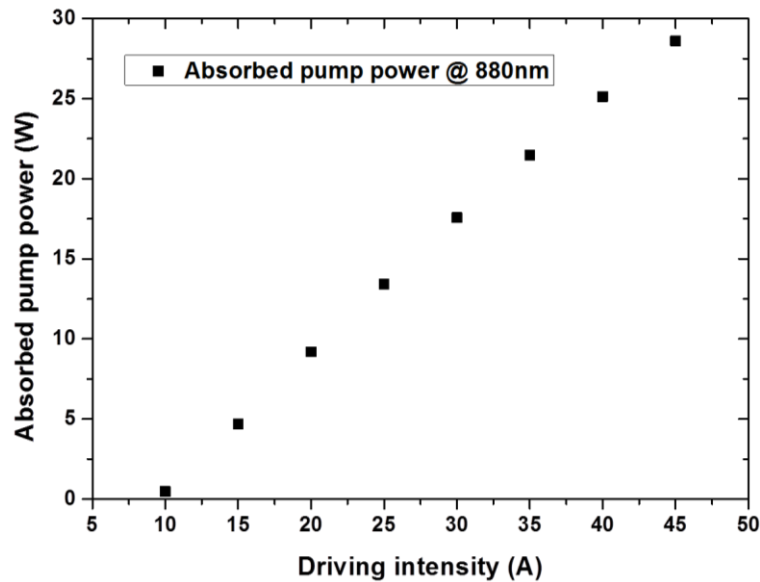
Fig. 5.23 Absorbed pump power corresponding to the driving current

The pump light was collimated and focused into the centre of the self-Raman crystal with a beam waist of 100 μm (measured by a BP104-IR beam profiler, from Thorlabs [5.37]) using a pair of plano–convex lenses. An a-cut, 2 mm-diameter, 20 mm-long, 0.3 at.% doped Nd:YVO$_4$ rod was used as self-Raman gain medium and mounted in a water-cooled copper block operating at 22 ˚C (as previously described in section 4.3). The rod was placed so that the c-axis of the Nd:YVO$_4$ crystal coincided with the x-axis of the DM. Therefore, the laser oscillation was linearly polarised along this axis. To maximise the effect of the intracavity DM to the oscillating laser field, a concave output coupler (ROC = 250 mm) and a curved folding mirror (ROC = 1000 mm) were used to build a x 4 intracavity telescope to expand the laser spot size incident to the DM. The spot diameter of the single transverse mode was calculated to be ~ 1.5 mm using an ABCD-matrix calculation software (Winlase 2.1 pro [5.43]). The plane end-mirror and curved folding mirror had a HR coating with R > 99.95 % at λ = 1064 and 1109 - 1176 nm while the concave output coupler was coated for R > 99.97 % at λ = 1064 nm, T = 1 % at λ = 1176 nm and T ~ 0.2 % at λ = 1109 nm. A folding angle of ~ 5° was arranged for both output coupler and HR mirror.

As concluded in section 5.3, the final INCAO mirror 2 was selected and inserted into this laser configuration. Since the DM was not coated for the Raman wavelength, a flat dichroic mirror (R < 1 % at λ = 1064 nm and R > 99.98 % at λ = 1109 and 1176 nm) was used to divide the Raman laser oscillator into a 3-mirror resonator and a 4-mirror resonator for the fundamental laser. The distance between the dichroic mirror and the output coupler was set to 380 mm to ensure mode matching of both Raman (λ = 1176 nm) and fundamental laser (λ = 1064 nm) fields inside the laser gain medium (TEM$_{00}$ mode radii calculated at ~ 100 μm using Winlase).

5.4.2 System assessment
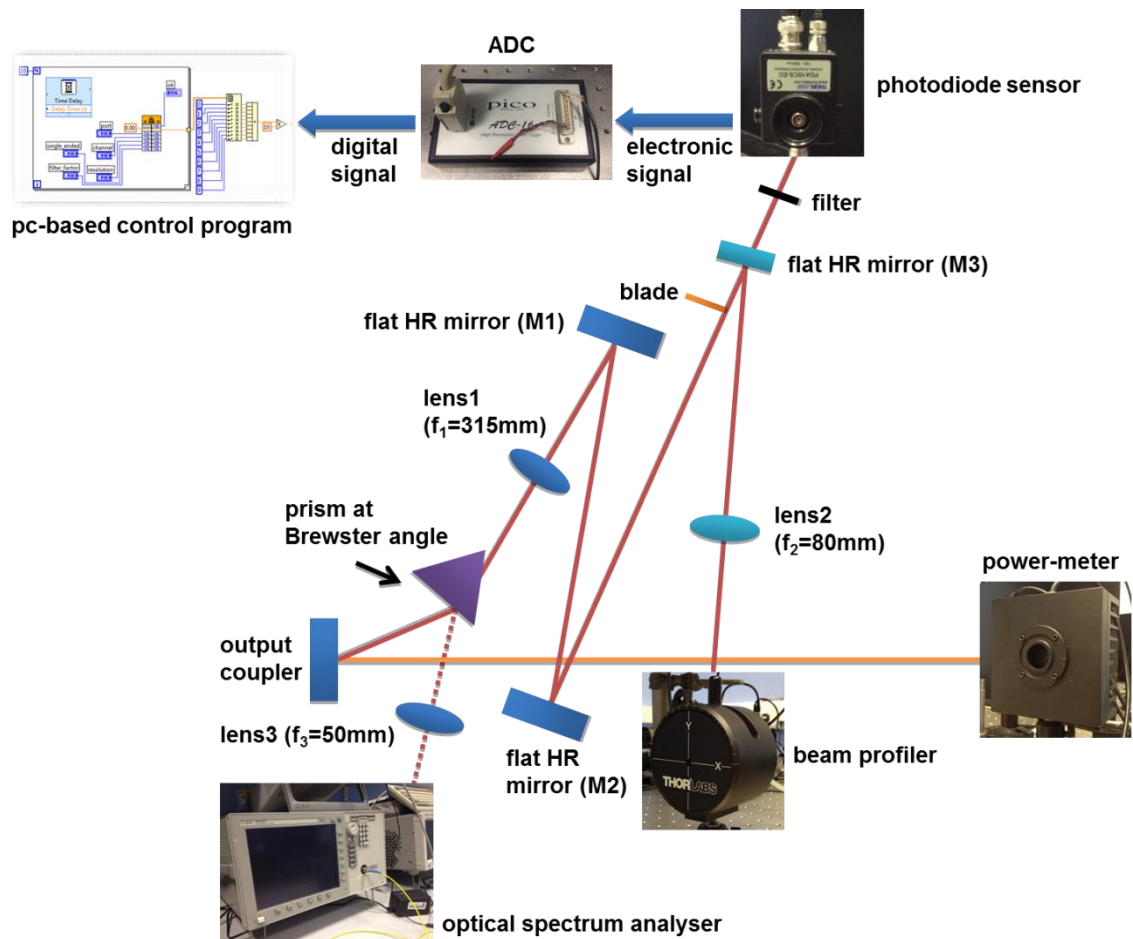
Fig. 5.24 Raman laser output measuring system

The schematic diagram of the Raman laser diagnostic system is shown in Fig. 5.24. Since the Raman laser output coupler acted as a cavity folding mirror, two output beams were produced. The output power of the first output beam (shown in orange in Fig. 5.24) was directly measured using a Thorlabs powermeter for monitoring the laser output power during the AO optimisation. It must be noted that a leakage from the fundamental laser field was also collected by this powermeter. The system previously described in section 4.3 based on a prism placed at Brewster's angle was used to separate the fundamental laser field from the Raman modes. The total optical losses induced by the prism, lens 1 and two flat folding mirrors (M1 and M2) were measured at ~ 5 %. The separated Raman output intensity was recorded by a photodiode sensor (PDA10CS-EC, from Thorlabs [5.37]) and sent to the PC-based control program via an ADC (206-4258, from RS [5.44]) as feedback signal for the search algorithm. The laser output wavelengths were measured using an optical spectrum analyser (86140B, from Agilent technologies [5.45]) while the beam quality factors M^2 were measured using a Thorlabs beam profiler and a $f = 80$ mm lens 2.

5.4.3 PC-based control system

Several search algorithms were considered in this work. The first search algorithm considered was a hill-climbing search algorithm, which is a simple procedure (corresponding to a low computer power requirement) with a reduced search duration (~ few tens of iterations).

The hill-climbing search algorithm is a rather simple mathematical optimisation approach. In Fig. 5.25 for instance, it starts with an initial variable (V_1) corresponding to a output power $P(V_1)$. Then, the initial variable is changed with a fixed span (i.e. $V_2 = V_1 + C$) before the new output power, $P(V_2)$, is measured. If this leads to an improved solution (i.e. $P(V_2) > P(V_1)$), the change will be accepted. If not, the change is rejected. The algorithm then goes to the next iteration (i.e. $V_3 = V_2 + C$) and the process is repeated n-times (n being

chosen by the user). The returned solution corresponds to the variable used after the last iteration.
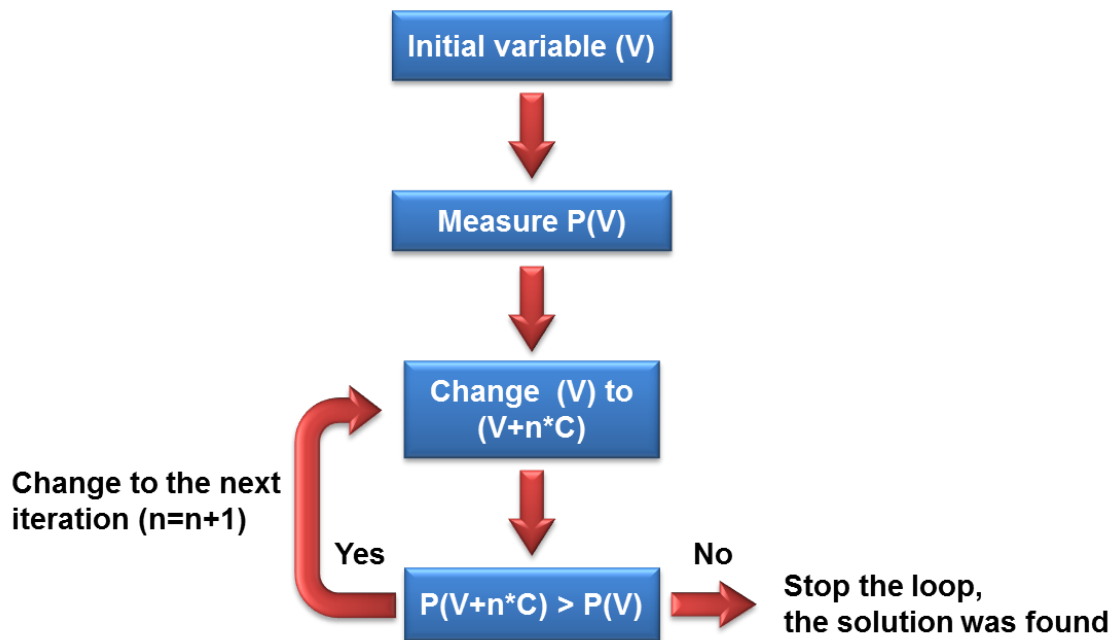
Fig. 5.25 Flowchart of the hill-climbing search algorithm

This rather simple search pattern has a main limitation: it only tends to lead to a local optimum result whereby the end result depends on the starting position. Taking a simple 2-dimension search space as shown in Fig. 5.26 for example, if the starting location is at A, the hill-climbing algorithm will lead to a local optimum result. However, if the optimisation process is started from B, a global optimum result will be located. In this work, the big size of the search space (37 actuators with a driving voltage ranging from -50 V to 250 V) significantly reduces the possibility to start at an initial position on the slope that would lead to reaching the global optimum result. Therefore, the hill-climbing search algorithm is not suitable to be applied in this platform. A more advanced search algorithm is required to locate a global solution.

Fig. 5.26 Graphic explanation for the local and global optimum in hill-climbing search
algorithm (the highest mountain in Britain - Ben Nevis, image extracted from
http://www.tarmachan-mountaineering.org.uk)

In [5.29], a number of more advanced search algorithms such as a genetic algorithm, a simulated annealing algorithm and a random search algorithm were tested on the same laser platform by Lubeigt et al. Although the genetic algorithm [5.46] tends to always provide a global optimum, the high number of iterations needed and the high requirement of computer resources were not entirely adequate for this application. On the other hand, an adapted version of the random search algorithm exhibited a satisfactory compromise between a near-global optimum, reduced number of iterations needed and lower required computer power in this application. This algorithm was therefore chosen in the work presented in this thesis.

The only difference between a hill climbing and a random search algorithm is that in the latter, each single element of the solution is randomly changed to provide any local optimum results. In this work, the variable elements are the voltages applied on each actuator of the DM while the Raman laser output intensity recorded by the photodiode sensor is used as the system feedback signal for assessing the influence of each actuator change.
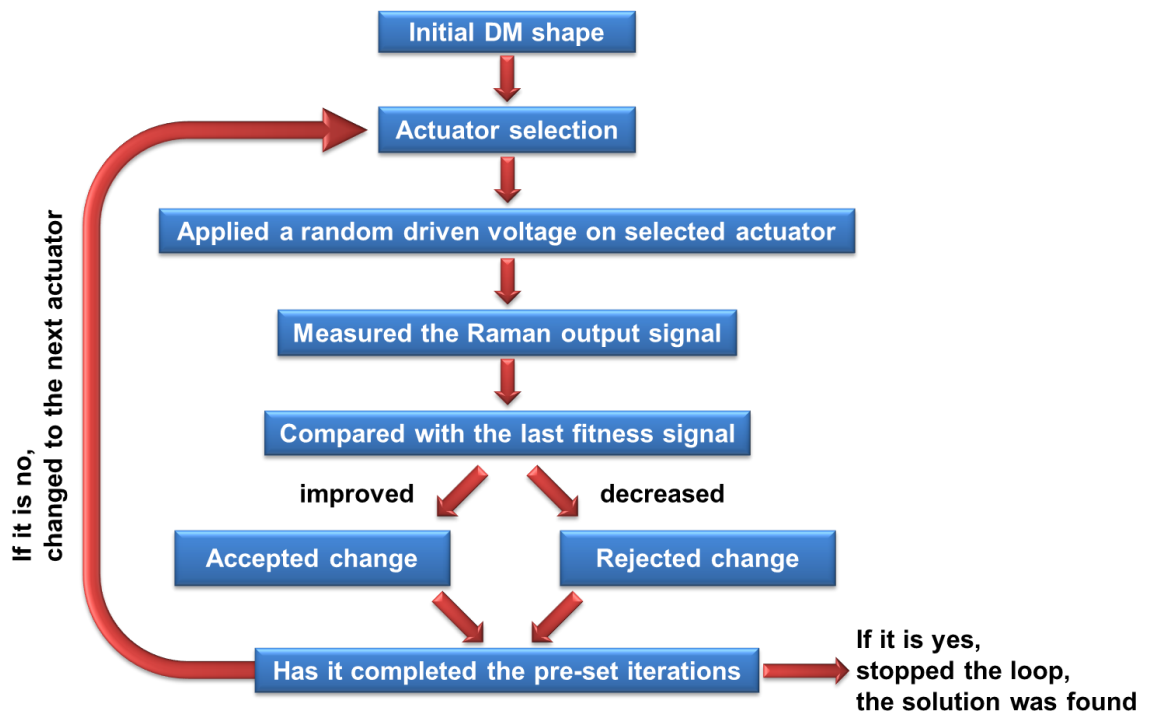
Fig. 5.27 Flowchart of the PC-based control system using a random search algorithm

An adapted version of the random search algorithm was developed using LabView (from National Instruments Corporation [5.47]). The search algorithm flowchart is displayed in Fig. 5.27. At first, the DM shape was initialised when all actuators were addressed with a similar user-defined voltage. Next, a random voltage was applied to the first actuator leading to a subtle deformation of the DM shape. Each DM mirror change modified the intracavity laser field leading to thermal changes within the gain medium. However, the establishment of this new thermal equilibrium is not instantaneous. This so-called thermal lag can vary in duration but is usually in the order of few hundreds of micro-seconds as described in [5.29]. Therefore a delay (600 ms used here) between the DM change and the output power measurement is required in the optimisation procedure. After this delay, a comparison between the new output power and the previous one was undertaken. If the output power was improved, the DM surface change was accepted. Otherwise, the DM surface was returned to its previous shape. This process was repeated on each selected actuator in sequence until a pre-set number of iterations was achieved. Consequently, the expected DM shape could be adapted

corresponding to an improved Raman laser output power. In addition, by the end of each loop, the Raman output power would be re-measured and utilised as the new feedback signal to avoid any long term laser fluctuations induced by mechanical or thermal instabilities.
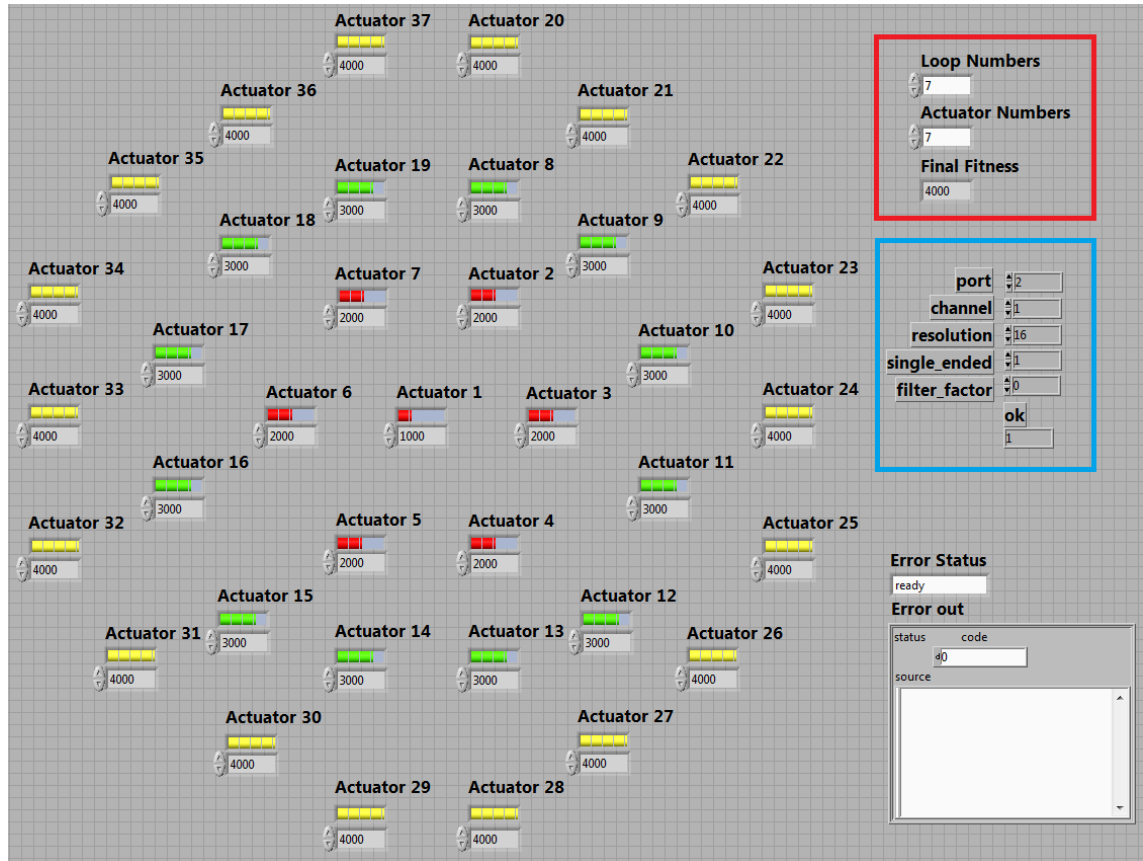
Fig. 5.28 LabView operation interface of the control system

The operation interface of the control system is shown in Fig. 5.28. In the red square (top right corner), the actuators number was entered by the user defining how many actuators were involved in each loop while the loop number (also defined by the user) determined how many loops were to be undertaken during the optimisation process. The optimised Raman output intensity recorded by the photodiode sensor was shown as the final output power. The blue square included a series of initial settings for the photodiode sensor measurement. The 37 single patterns represent the actuators distributed on the DM, while a range of 12-bit values from 0 to 4096 was used to express a driving voltage range from -50 V to 250 V correspondingly.

5.5 Results

In this section, two different types of experimental results are presented. In subsection 5.5.1, an automatic AO-loop optimisation was achieved and resulted in a power enhancement of the Raman laser output performance operating at $\lambda = 1176$ nm. In subsection 5.5.2, a wavelength switching between $\lambda = 1176$ nm and $\lambda = 1109$ nm was realised by manually changing the DM shape.

5.5.1 Power-scaling

At the initial stage, the Raman laser was manually aligned with no voltage applied to the actuators. This resulted in a maximum Raman output power of 500 mW for an absorbed laser diode pump power of 10.8 W. Without any voltage applied to the actuators, the focusing power of the DM was measured at -0.46 D and -0.38 D along the x and y axes respectively using the Shack-Hartmann wavefront sensor-based diagnostic system described in section 5.3.

In the following "pre-optimisation" state, all 37 actuators were supplied with a driving voltage of 60 V simultaneously, corresponding to a focusing power of 0.27 D along the x-axis and 0.50 D along the y-axis. Using the same pump power, the laser was manually aligned resulting in a Raman laser output power of 550 mW. Using the same method introduced in subsection 4.4.2, the beam quality factors M^2 were measured at 1.3 and 1.4 along the x and y axes respectively for the fundamental laser field at $\lambda = 1064$ nm and both less than 1.1 for the Raman laser mode at $\lambda = 1176$ nm. The Raman laser output power transfer was measured as displayed in Fig. 5.29 (except the red point). A thermal rollover could be observed for absorbed pump powers above 10.3 W and the maximum Raman output power was equal to 550 mW.
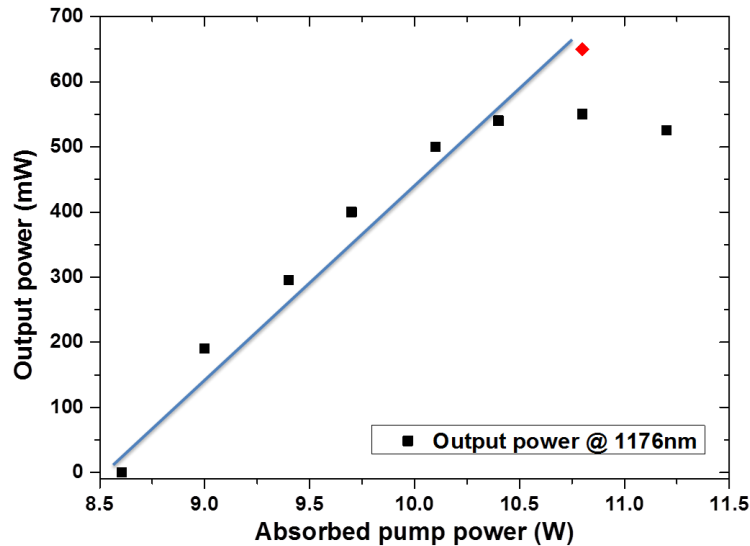
Fig. 5.29 Raman laser power transfer at pre-optimisation stage (the red point is the result after AO optimisation)

Then, a range of near-spherical DM shapes with different ROCs were applied by simultaneously applying the same voltage to all DM actuators. Past a certain voltage value, the Raman laser ceased oscillating. This enabled to define the boundary curvatures to be used in the forthcoming automatic optimisation. It was found that the Raman laser could only operate in a stable way with a driving voltage value applied to all actuators between 60 and 180 V (corresponding to a general focusing power range between ~ 0 and ~ 0.80 D). As a result, the voltage range used in this optimisation was limited to within these boundary values.

With a starting shape providing a Raman laser output power of 550 mW, the AO optimisation procedure using the random search algorithm described in subsection 5.4.3 was automatically undertaken. To speed up the AO-loop procedure, only the central 7 actuators were utilised with 6 loop iterations corresponding to a search duration of ~ 5 minutes. After this optimisation, a specific DM shape was found to deliver an improved maximum Raman output power of 650 mW (red point in Fig. 5.29) which led to a ~ 18 % Raman output power enhancement. The driving voltages applied on the central 7 actuators

were displayed in Table 5.4 while the rest of the actuators remained in a starting driving voltage of 112.5 V.

Actuator number	Driving voltage (V)
1	90.5
2	150.6
3	169.8
4	67.8
5	105
6	109.8
7	62
8-37	112.5

Table 5.4 Driving voltages on each actuators for the specific DM shape after AO optimisation

The output power measurements during the search process were recorded as shown in Fig. 5.30.
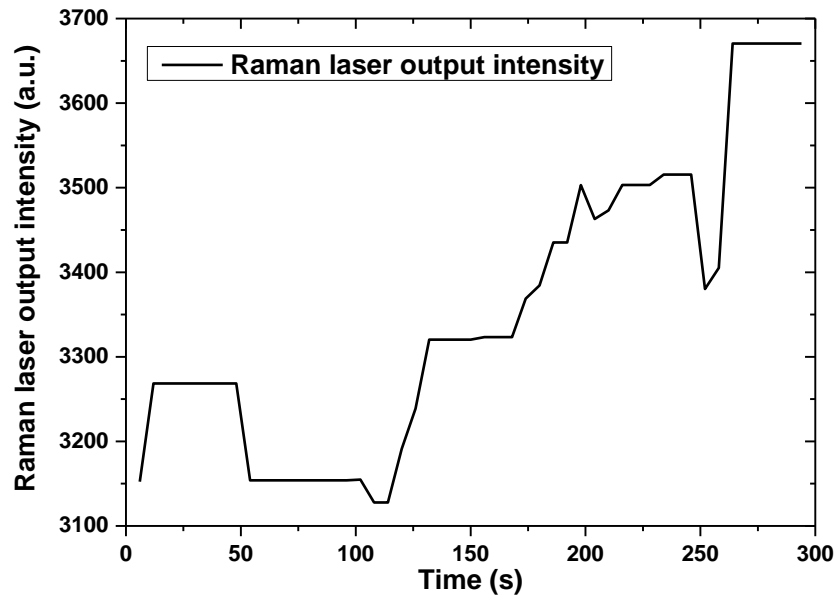
Fig. 5.30 Output power measurements tracking during the random search algorithm process

The beam quality factors M^2 were measured at 1.2 and 1.1 along the x and y axes for the fundamental field and both less than 1.1 for the Raman mode.

Zernike Coefficient Order	Starting Point (µm)	End Point (µm)	Error Range (µm)
1 (piston)	-18.59	−18.49	0.01
2 (tip y)	14.79	14.76	0.01
3 (tip x)	3.87	3.78	0.01
4 (astigmatism ±45°)	0.019	0.016	0.002
5 (defocus)	−0.125	−0.118	0.002
6 (astigmatism ±0°)	0.055	0.071	0.002
7 (trefoil y)	−0.001	−0.004	0.001
8 (coma x)	−0.004	−0.006	0.001
9 (coma y)	0.002	0.011	0.001
10 (trefoil x)	−0.002	−0.005	0.001

Table 5.5 Zernike coefficients before and after power scaling investigation

Using the Shack-Hartmann wavefront sensor system described in Fig. 5.16, the wavefront modification induced by the DM shape before and after the AO-loop optimisation can be measured and the related Zernike coefficients are shown in Table 5.5. The highest change revealed in Table 5.5 implies that the astigmatism at 0° and coma in the y-axis of the wavefront correction played a driving role for the high-order thermal lensing compensation.

5.5.2 Wavelength selection

Apart from the power-scaling of the 1176 nm Raman line, a wavelength selection between two first Stokes Raman outputs at $\lambda = 1176$ nm and $\lambda = 1109$ nm due to the use of two different Raman shifts in the Nd:YVO$_4$ crystal has also been undertaken. In this work, the DM mirror was used to favour the oscillation of one Raman line over the other.
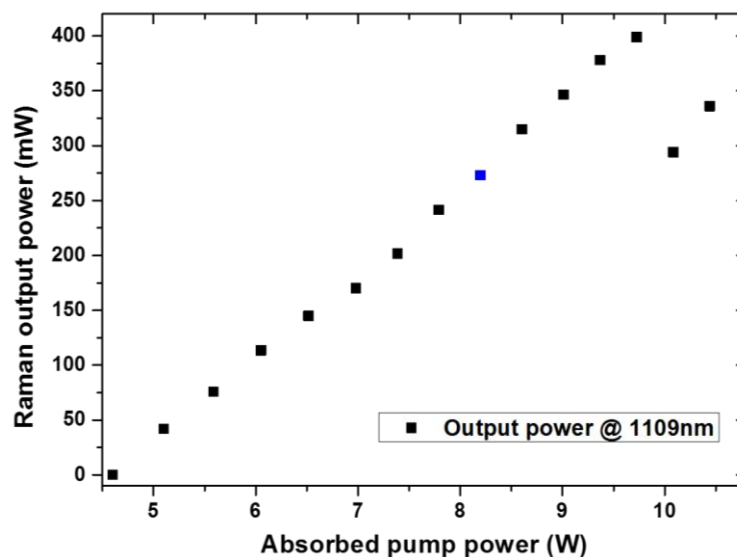
Fig. 5.31 Optical power transfer of $\lambda = 1109$ nm mode Raman laser outputs (the blue point is the wavelength switching point)

In this case, to favour the first Stokes Raman laser output at $\lambda = 1109$ nm, the distance between the DM and the curved folding mirror was slightly extended to 300 mm (see Fig. 5.22). At first, the Raman laser was manually aligned to

only emit at $\lambda = 1109$ nm with 0 V applied to all 37 actuators (corresponding to a DM general focusing power of ~ 0.38 D). The optical power transfer of the 1109nm Raman output was measured as displayed in Fig. 5.31.

At absorbed pump powers above 8.2 W, the $\lambda = 1176$ nm mode Raman output could be additionally observed and competed with the $\lambda = 1109$ nm mode, leading to a significant decline of the output power of the latter. With 10.1 W of absorbed pump power, the $\lambda = 1176$ nm mode was measured at ~ 100 mW. To avoid the parasitic oscillation of the $\lambda = 1176$ nm mode, the blue point shown in Fig. 5.31 was considered to be utilised as the wavelength switching point since it corresponded to an oscillation of solely the $\lambda = 1109$ nm mode Raman output corresponding to a Raman output power of 275 mW for an absorbed laser diode pump power of 8.2 W. The beam quality factors M^2 were measured to be 2.2 and 1.9 along the x and y axes for the fundamental field laser output and 1.3 and 1.6 for the $\lambda = 1109$ nm laser mode respectively.

Using an optical spectrum analyser, the spectrum of the $\lambda = 1109$ nm Raman output beam was measured as displayed in Fig. 5.32. The full width at half-maximum (FWHM) of the linewidth of the $\lambda = 1109$ nm mode could be estimated to be ~ 0.15 nm with a resolution of 0.06 nm.
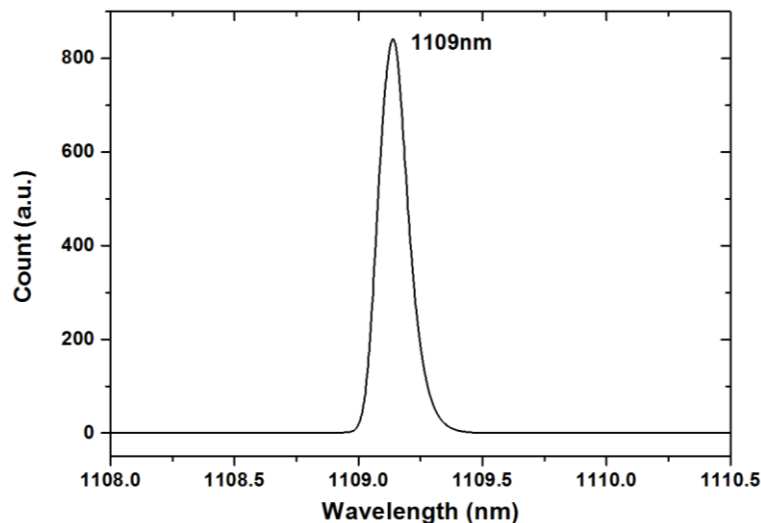
Fig. 5.32 Optical spectrum of the $\lambda = 1109$ nm mode Raman laser output at the switching point
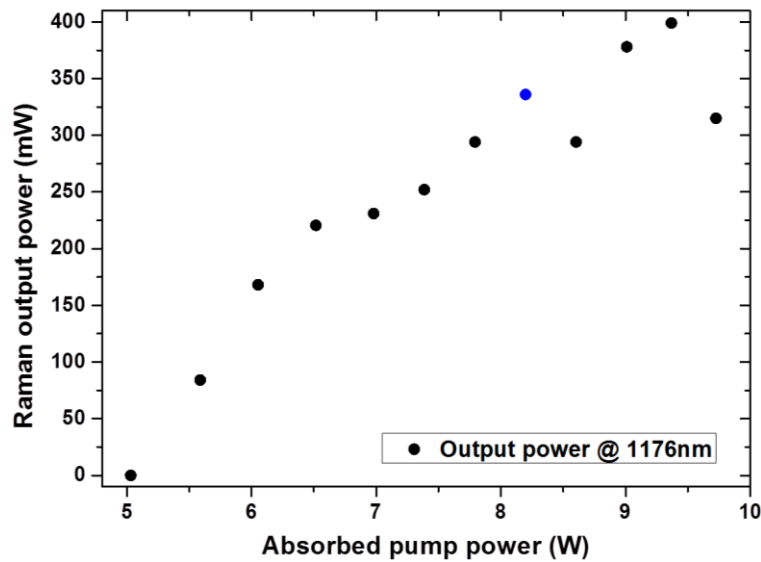
Fig. 5.33 Optical power transfer of λ = 1176 nm mode Raman laser outputs

At this pump power level, a driving voltage of 66 V was then applied to all actuators simultaneously, corresponding to a near flat DM shape. This led to the sole oscillation of the λ = 1176 nm mode with 340 mW of output power. Using this DM surface shape, the optical power transfer of the λ = 1176 nm mode was measured as shown in Fig. 5.33. Similar to the λ = 1109 nm case, both Raman outputs (λ = 1176 nm and 1109 nm) could be observed simultaneously at pump powers above 9.5 W.

At the switching point (blue dot in Fig. 5.33), the beam quality factors M^2 along the x and y axes were measured to be 1.4, 1.9 for the fundamental field and 1.3, 1.6 for the λ = 1176 nm mode respectively at the maximum Raman laser output.

The FWHM linewidth of the λ = 1176 nm mode Raman laser output was measured at 0.15 nm at a resolution of 0.06 nm (see Fig. 5.34). The transverse beam profiles of the two first-Stokes Raman modes obtained before and after wavelength switching are captured using the Thorlabs beam profiler and are displayed in Fig. 5.35.
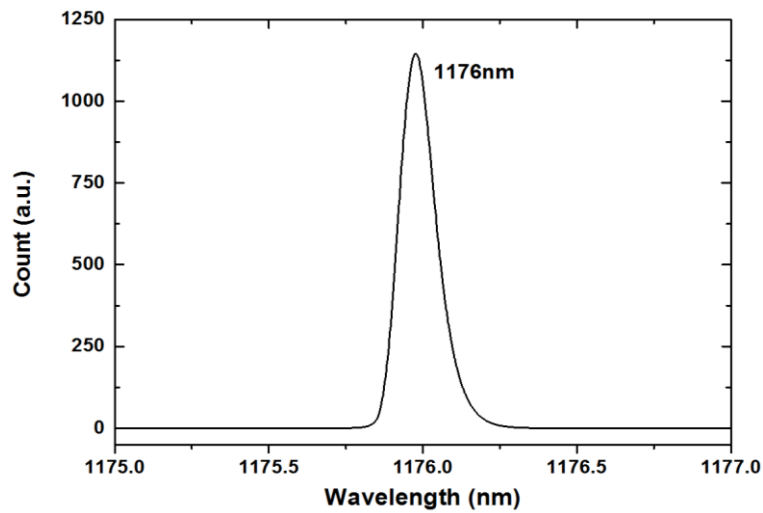
Fig. 5.34 Optical spectrum of the λ = 1176 nm mode Raman laser output at the switching point

| (a) | (b) |
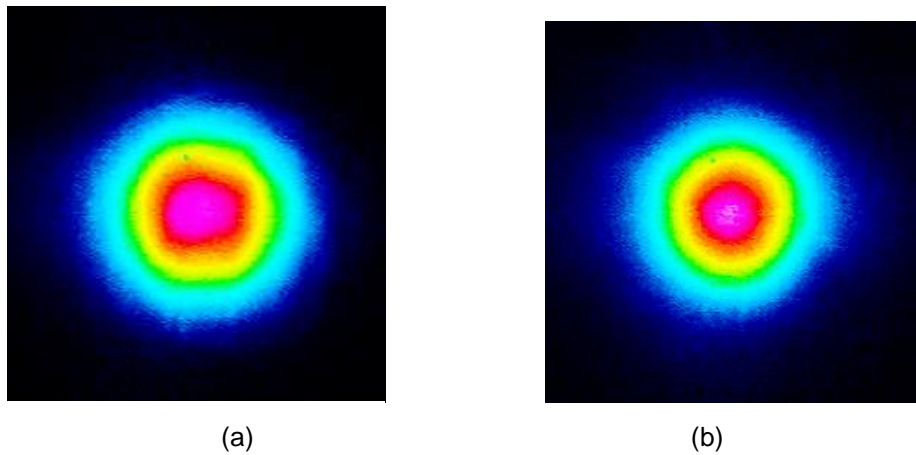
Fig. 5.35 Beam profiles of the Raman output (a) before wavelength switching (λ = 1109 nm), (b) after wavelength switching (λ = 1176 nm)

The related Zernike coefficients corresponding to the wavefront correction induced by the DM shape deformation before and after the wavelength selection are summarised in Table 5.6. The modification of the wavefront was mainly focused on changing the defocus.

Zernike Coefficient Order	Starting Point (µm)	End Point (µm)	Error Range (µm)
1 (piston)	-19.32	−18.99	0.01
2 (tip y)	15.38	15.06	0.01
3 (tip x)	3.77	3.83	0.01
4 (astigmatism ±45°)	0.016	0.016	0.002
5 (defocus)	0.121	−0.013	0.002
6 (astigmatism ±0°)	0.043	0.048	0.002
7 (trefoil y)	0.002	0.001	0.001
8 (coma x)	−0.001	−0.003	0.001
9 (coma y)	0.004	0.002	0.001
10 (trefoil x)	0.003	0.001	0.001

Table 5.6 Zernike Coefficients before and after wavelength switching investigation

5.6 Discussion

Several discussion points were presented from these two AO-based experiments.

In the power-scaling investigation, different orders of thermal lensing were alleviated by two stages (i.e. pre-optimisation and AO optimisation). In the initial state, the focal length of the first-order near-spherical thermal lensing (f_{thl}) was estimated to be ~ 50 mm when a maximum Raman output power of 500 mW was achieved for an absorbed laser diode pump power of 10.8 W (this estimation was based on the thermal lensing measurements in a similar Nd:GdVO$_4$ self-Raman laser system [5.4]). The comparisons of the fundamental (λ = 1064 nm) and the first Stokes (λ = 1176 nm) fields beam radii (TEM$_{00}$ mode) at the centre of the gain medium with and without thermal lens effect were calculated using the ABCD-matrix software and are summarised in Table. 5.7.

	No Thermal Lensing	With $f_{thl} = 50$ mm
Fundamental laser field radius along x axis (µm)	101	101
Fundamental laser field radius along y axis (µm)	95	95
First-Stokes laser mode radius along x axis (µm)	102	119
First-Stokes laser mode radius along y axis (µm)	103	119

Table 5.7 Radii of the fundamental and first Stokes fields affected by the thermal lensing

In this laser configuration, the fundamental and first Stokes laser fields were resonating using two coupled cavities due to the insertion of the dichroic mirror as represented in Fig. 5.36.
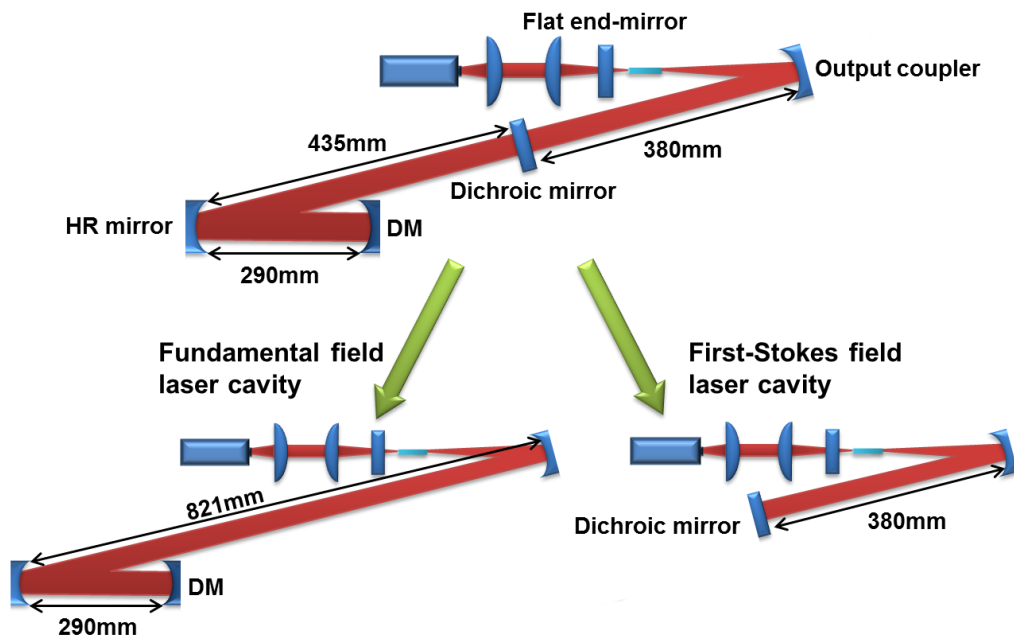
Fig. 5.36 Separation of the resonators for the fundamental and first-Stokes laser fields for visualisation purposes

As shown in Table 5.7, without thermal lens effect, the radii of the fundamental and first Stokes fields presented a near-perfect mode match on both x and y

axes. However, the strong thermal lensing led to a ~ 20 % increase of the first-Stokes mode radii while the fundamental field radii were not affected. Therefore, the Raman laser conversion efficiency was significantly limited due to the mode mismatch under strong thermal lensing.

After the pre-optimisation corresponding to a large variation of the DM shape from concave (i.e. -4.35 m along x-axis and -5.26 m along y-axis) to convex (i.e. 7.41 m along x-axis and 4 m along y-axis), the TEM_{00} mode radii of the two laser modes at the centre of the gain medium were calculated and are displayed in Table 5.8.

	Before pre-optimisation	After pre-optimisation
Fundamental laser field radius along x axis (μm)	101	121
Fundamental laser field radius along y axis (μm)	95	116
First-Stokes laser mode radius along x axis (μm)	119	119
First-Stokes laser mode radius along y axis (μm)	119	119

Table 5.8 Radii of the fundamental and first-Stokes fields affected by the pre-optimisation

A ~ 20 % radii increase of the fundamental laser field on both the x and y axes is shown in Table 5.8 by the near-spherical deformation of the DM shape. Meanwhile, the mode sizes of the Raman laser field were not modified since the DM could not directly affect the first Stokes laser resonator. In this way, compensating for the mode mismatch induced by the first-order spherical thermal lensing enabled a ~ 10 % (i.e. from 500 mW to 550 mW) power-scaling of the Raman laser output.

However, after the pre-optimisation, an obvious rollover of the laser power transfer curve could still be observed with diode pump powers above 10.4 W

as seen in Fig. 5.29. This was mainly due to the complex superposition of the high-order thermal lensing which was difficult to alleviate by the near-spherical compensation. After the automated AO-loop, the maximum Raman laser output power at 10.8 W pumping was observed to be less influenced by this rollover and improved back to the original linear trend observed at lower pump power values (see the red point and blue line in Fig. 5.29). The fundamental laser output power was measured and remained at 315 mW before and after the AO optimisation. This experiment shows that the high-order thermal lens effect has been reduced resulting in a measurable enhancement of the first Stokes Raman laser conversion efficiency using this AO-based feedback control loop.

In the wavelength selection investigation, the variation of ROCs along the x and y axis on the DM could be calculated using the equations from (5-3) to (5-6) and the defocus (Z5) and astigmatism (Z6) terms shown in Table 5.6. Before the wavelength selection experiment (i.e. emission of the $\lambda = 1109$ nm line only), the ROC_x and ROC_y of the DM were calculated to be -4.29 m and -7.17 m respectively while an ROC_x of > 30 m and ROC_y of 13.8 m were obtained post-wavelength selection (i.e. emission of the $\lambda = 1176$ nm line only). The TEM_{00} mode sizes of the fundamental laser field at the centre of the gain medium before and after the wavelength switching were calculated and are shown in Table 5.9.

	Before wavelength switching	After wavelength switching
Fundamental laser field radius along x axis (µm)	101	113
Fundamental laser field radius along y axis (µm)	95	109

Table 5.9 Radii of the fundamental field affected by the wavelength switching

A ~ 15 % increase in the fundamental single mode size could be observed after wavelength switching in Table 5.9. The origin of this effect is not currently clear to us but the dynamic interaction of all intracavity laser fields will undoubtedly play a part in this.

To make an easier comparison between these two Raman laser outputs before and after the wavelength selection, the Fig. 5.31 and 5.33 were combined as shown in Fig. 5.37.
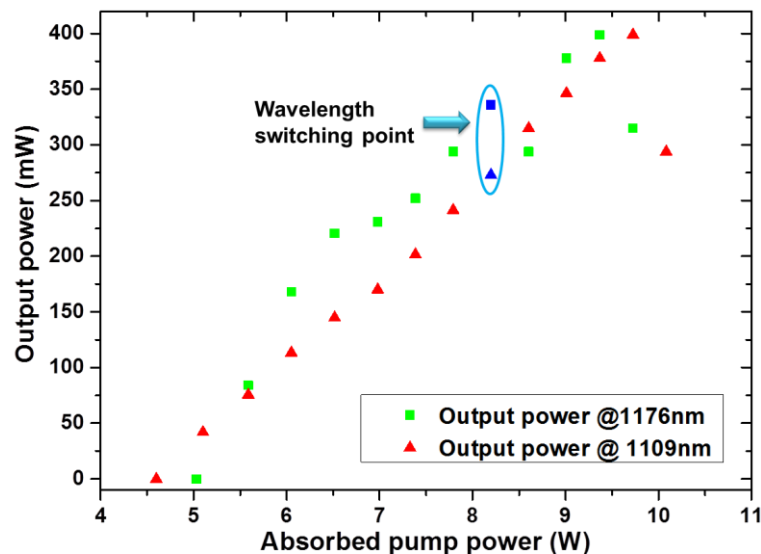
Fig. 5.37 Power transfer of Raman lasers resulting from different Raman transitions

The Raman thresholds for both first Stokes modes were achieved at 4.6 W and 5.0 W diode pump powers corresponding to the output wavelengths of $\lambda = 1109$ nm and 1176 nm respectively. The lower Raman threshold for the $\lambda = 1109$ nm mode was attributed to reduced cavity losses due to the reduced output coupling used for the wavelength of interest (T = 1 % at $\lambda = 1176$ nm and T ~ 0.2 % at $\lambda = 1109$ nm). For absorbed pump powers of 8.2 W corresponding to a single first Stokes mode operating for each wavelength, the Raman output power at $\lambda = 1176$ nm was higher by ~ 23 % than the $\lambda = 1109$ nm mode. With diode pump powers above 8.2 W, the two first Stokes Raman outputs coexisted and interacted with each other. However, the total sum of both first Stokes Raman output powers appeared in line with the slope efficiency observed at lower pumping levels. Further investigation would be

required to explain the full interaction between these competing Raman modes.

In addition, while the wavelength selection described in this work could always be repeated with consistency, the power scaling experiment could not. This could be imputed to the hysteresis phenomena inherent to bimorph deformable mirrors. As shown in Fig. 5.38, significant focusing power discrepancies are displayed by applying different driving voltage trends (either upward or downward). The maximum hysteresis value observed at a driving voltage range from 40 to 80 V resulted in a variation of focusing power of ~ 0.2 D. So it can be concluded that, when a moderate surface change of the DM is required (such as in the power-scaling case), the hysteresis phenomena will significantly affect the optimisation. Whereas when a stronger correction is needed such as in the wavelength switching, this hysteresis has less impact. A possible solution for reducing this hysteresis effect will be mentioned in the future work chapter.
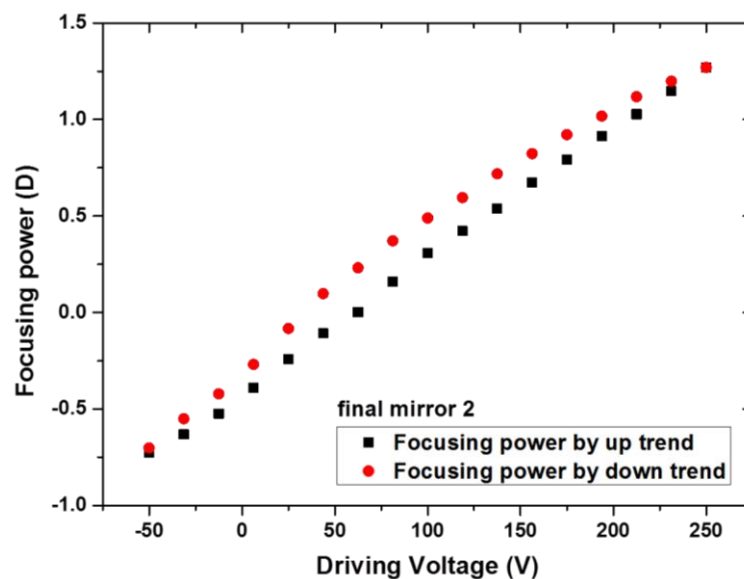
Fig. 5.38 Focusing power response of the final mirror 2 with the hysteresis phenomena

5.7 Conclusion

In conclusion, for the first time, an AO-based feedback control loop was successfully integrated to improve the performance of a Raman laser. In this proof-of-concept experiment, a bimorph deformable mirror was inserted inside a self-Raman laser in a coupled cavity configuration. At first, a ~ 10 % increase of the first Stokes Raman laser output power (at λ = 1176 nm) from 500 mW to 550 mW was achieved by manually adjusting the intracavity DM shape (i.e. from -0.46 D to 0.27 D for the x axis and from -0.38 D to 0.50 D for the y axis) for an absorbed pump power of 10.8 W. Based on this "pre-optimisation" point, another ~ 18 % improvement of the Raman laser output power was demonstrated from 550 mW to 650 mW by an automatic AO-loop optimisation. The thermal rollover phenomenon observed at the pre-optimisation point in Fig. 5.30 occurred at higher pump powers after the AO-loop optimisation. The absorbed pump power was limited to 10.8 W to prevent any damage to the self-Raman laser crystal coating in case the Raman laser oscillation collapses during the AO-loop optimisation.

The shape of the DM was assessed using a Shack-Hartmann wavefront sensor measuring a range of Zernike coefficients. High-order correction (mainly involving astigmatism and coma) was found to play an important role during the AO-loop optimisation since the first-order of the spherical thermal lensing had mostly been compensated for by the defocus correction at the pre-optimisation stage. From pre-optimisation to the AO-loop optimisation, the beam quality factors M^2 were slightly enhanced for the fundamental field (i.e. from 1.3 to 1.2 for the x axis and from 1.4 to 1.1 for the y axis) while the first Stokes Raman laser outputs were always measured at less than 1.1 due to the Raman beam clean-up effect described in sub-section 4.5.2.

As the DM used in this work was not coated at any of the Stokes wavelengths, only the fundamental field was optimised during the AO-loop optimisation. This probably restrained the improvement of SRS conversion efficiency (i.e. ~ 18 %) since the first Stokes mode was not directly optimised by changing the

DM. However, it can be further improved using a new DM with an HR coating for both fundamental and Stokes wavelengths.

In addition, repeatable wavelength selection between two first Stokes Raman output wavelengths ($\lambda = 1176$ nm and 1109 nm) has been demonstrated by a large stroke variation of the DM shape (i.e. from a general ROC of -5.25 m to flat). The Raman laser output powers were measured to be 275 mW and 340 mW for operating at $\lambda = 1109$ nm and 1176 nm respectively at the same absorbed pump power of 8.2 W. The beam quality factors M^2 were measured to be 1.3 and 1.6 for the x and y axis at $\lambda = 1109$ nm while both were less than 1.1 at $\lambda = 1176$ nm.

This proof-of-concept experiment represents an attractive method to improve the solid-state Raman lasers to new power levels by alleviating the strong thermal lens inherent to Raman lasers. It will benefit a wide range of applications especially combined with nonlinear optical techniques (i.e. SHG and SFG), for instance to obtain yellow Raman lasers for astronomy (guide star generation [5.48]), and medicine (retinal laser photocoagulation [5.49]). In addition, the wavelength selection of Raman laser outputs achieved using the AO technique represents a first step towards the development of CW, narrowly-spaced Raman lasers at visible lines, which is of significant interest for medicine (carbon monoxide poisoning monitoring [5.50]), bio-photonics (single-molecule detection [5.51]) and environmental remote sensing (underwater detector [5.52]).

5.8 References

5.1   P. Cerny, H. Jelinkova, P. G. Zverev, T. T. Basiev, "Solid state lasers with Raman frequency conversion," Prog. Quantum Electron. **28**, 113-143 (2004).

5.2   J. A. Piper and H. M. Pask, "Crystalline Raman Lasers," IEEE J. Sel. Top. Quantum Electron. **13**, 692-704 (2007).

5.3   P. Dekker, H. M. Pask, D. J. Spence and J. A. Piper, "Continuous-wave, intracavity doubled, self- Raman laser operation in Nd:GdVO$_4$ at 586.5 nm," Opt. Express. **15**, 7038-7046 (2007).

5.4   T. Omatsu, M. Okida, A. Lee, H. M. Pask, "Thermal lensing in a diode-end-pumped continuous-wave self-Raman Nd-doped GdVO$_4$ laser," Appl. Phys. B **108**, 73-79 (2012).

5.5   A. Sabella, J. A. Piper, and R. P. Mildren, "1240 nm diamond Raman laser operating near the quantum limit," Opt. Lett. **35**, 3874-3976 (2010).

5.6   W. Lubeigt, V. G. Savitski, G. M. Bonner, S. L. Geoghegan, I. Friel, J. E. Hastie, M. D. Dawson, D. Burns, and A. J. Kemp, "1.6 W continuous-wave Raman laser using low-loss synthetic diamond," Opt. Express. **19**, 6938-6944 (2011).

5.7   O. Kitzler, A. McKay, and R. P. Mildren, "Continuous-wave wavelength conversion for high-power applications using an external cavity diamond Raman laser," Opt. Lett. **37**, 2790-2792 (2012).

5.8   R. J. Williams, O. Kitzler, A. McKay, and R. P. Mildren, "Investigating diamond Raman lasers at the 100 W level using quasi-continuous-wave pumping," Opt. Lett. **39**, 4152-4155 (2014).

5.9   L. Fan Y. X. Fan H. T. Wang, "A compact efficient continuous-wave self-frequency Raman laser with a composite YVO$_4$/Nd:YVO$_4$/YVO$_4$ crystal," Appl. Phys. B **101**, 493-496 (2010).

5.10   A. J. Lee, H. M. Pask, P. Dekker, J. A. Piper, "High efficiency, multi-Watt CW yellow emission from an intracavity-doubled self-Raman laser using Nd:GdVO$_4$," Opt. Express. **16**, 21958-21963 (2008).

5.11   A. J. Lee, H. M. Pask, D. J. Spence, and J. A. Piper, "Efficient 5.3 W cw laser at 559 nm by intracavity frequency summation of fundamental and first Stokes wavelengths in a self-Raman Nd:GdVO$_4$ laser," Opt. Lett. **35**, 682-684 (2010).

5.12   A. McKay, O. Kitzler, and R. P. Mildren, "Thermal lens evolution and compensation in a high power KGW Raman laser," Opt. Express. **22**, 6707-6718 (2014).

5.13   F. Merkle, P. Kern, P. Lena, F. Rigaut, J. C. Fontanella, G. Rousset, Onera, C. Boyer, J. P. Gaffard, P. Jagourel, Laserdot, "Successful Tests of Adaptive Optics," The Messenger, **58**, 1-4 (1989).

5.14   R. K. Tyson, *Principles of adaptive optics,* (Academic Press, 1991).

5.15   L. Sherman, J. Y. Ye, O. Albert† & T. B. NORRIS, "Adaptive correction of depth-induced aberrations in multiphoton scanning microscopy using a deformable mirror," J. Microsc. **206**, 65-71 (2002)

5.16   M. J. Booth, M. A. A. Neil, R. Juskaitis, and T. Wilson, "Adaptive aberration correction in a confocal microscope," PNAS. **99**, 5788-5792 (2002).

5.17   A. Greenaway and J. Burnett, *Industrial and Medical Applications of Adaptive Optics,* (Technology Tracking, London, 2003).

5.18   J. Carroll, D. C. Gray, A. Roorda, and D. R. Williams, "Recent Advances in Retinal Imaging With Adaptive Optics," Optics & Photonics News **16**, 36-42 (2005).

5.19   L. Zhu, P. Sun, D. Bartsch, W. R. Freeman, and Y. Fainman, "Wave-front generation of Zernike polynomial modes with a micromachined membrane deformable mirror," Appl. Opt. **38**, 6019-6026 (1999).

5.20   G. Vdovin, V. Kiyko, "Intracavity control of a 200 W continuous-wave Nd:YAG laser by a micromachined deformable mirror," Opt. Lett. **26**, 798-800 (2001).

5.21   Y. Seo, S. Baik, S. Park and C. Kim, "Closed-Loop Adaptive Optics System for Wave-Front Correction," J. Korean Phys. Soc. **39**, 891-894 (2001).

5.22   A. L. Rukosuev, A. Alexandrov, V. Y. Zavalova, V. V. Samarkin, A. V. Kudryashov, "Adaptive optical system based on bimorph mirror and Shack-Hartmann wavefront sensor," Proc. SPIE **4493**, 261-268 (2002).

5.23   W. Lubeigt, G. Valentine, J. Girkin, E. Bente, D. Burns, "Active transverse mode control and optimization of an all-solid-state laser using an intracavity adaptive-optic mirror," Opt. Express. **10**, 550-555 (2002).

5.24   R. El-Agmy, H. Bulte, A. H. Greenaway and D. T. Reid, "Adaptive beam profile control using a simulated annealing algorithm," Opt. Express. **13**, 6085-6091 (2005).

5.25   U. Wittrock and P. Welp, "Adaptive laser resonator control with deformable MOEMS mirrors," SPIE Proceedings, paper **6113**, 1-13 (2006).

5.26   P. Yang, Y. Liu, W. Yang, M. Ao, S. Hu, B. Xu, W. Jiang, "Adaptive mode optimization of a continuous-wave solid-state laser using an intracavity piezoelectric deformable mirror," Opt. Commun. **278**, 377-381 (2007).

5.27   W. Lubeigt, G. Valentine and D. Burns, "Enhancement of laser performance using an intracavity deformable membrane mirror," Opt. Express. **16**, 10943-10955 (2008).

5.28   L. Dong, P. Yang, B. Xu, "Adaptive aberration correction based on ant colony algorithm for solid-state lasers: numerical simulations," Appl. Phys. B **96**, 527-533 (2009).

5.29   W. Lubeigt, S. P. Poland, G. J. Valentine, A. J. Wright, J. M. Girkin, and D. Burns, "Search-based active optic systems for aberration correction in time-independent applications," Appl. Opt. **49**, 307-314 (2010).

5.30   P. Yang, Y. Ning, X. Lei, B. Xu, X. Li, L. Dong, H. Yan, W. Liu, W. Jiang, L. Liu, C. Wang, X. Liang, and X. Tang, "Enhancement of the beam quality of non-uniform output slab laser amplifier with a 39-actuator rectangular piezoelectric deformable mirror," Opt. Express. **18**, 7121-7130 (2010).

5.31   J. Li, X. Chen, "A Novel Intra-cavity Adaptive Optical System for high Power Solid-state Lasers," Symposium on Photonics and Optoelectronics, (2010).

5.32   BAE systems advanced technology centre, Stirling Square, 6 Carlton Gardens, London, SW1Y 5AD United Kingdom, www.baesystems.com.

5.33   *Test Mirror INCAO 002 Technical Passport*, GST/070061/108404, (2007).

5.34   *INCAO Final Mirror Edition 02 Technical Passport*, GSE/080195/108404, (2008)

5.35   Flexible OKO Optical, Polakweg 10-11, Rijswijk, 2288 GG, Netherlands, www.okotech.com.

5.36   Veeco, 2650 E. Elvira Road, Tucson, AZ 85706, United States, www.veeco.com.

5.37   THORLABS, 56 Sparta Avenue, Newton, New Jersey, 07860, United States, www.thorlabs.com.

5.38   D. Malacara, *Optical Shop Testing*, 2nd ed. (Wiley, 1992).

5.39   J. Lin, H. M. Pask, "Nd:GdVO$_4$ self-Raman laser using double-end polarised pumping at 880 nm for high power infrared and visible output," Appl. Phys. B **108**, 17-24 (2012).

5.40   LIMO, Bookenburgweg 4-8, Dortmund, 44319, Germany, www.limo.de/en.

5.41   Laser 2000, Unit 9, Avro Court, Ermine Business Park, Huntingdon, Cambridgeshire, PE29 6XS, United Kingdom, www.laser2000.co.uk.

5.42   ELITE THERMAL ENGINEERING, 11th Avenue West, Bothell, Washington, 98021, United States, www.elitethermalengineering.com.

5.43   Winlase 2.1 Pro, Future Laser Technologies, 24221 Robledo Cir, Mission Viejo, CA 92691, United States, www.winlase.com

5.44   RS Components, Birchington Road, Corby, Northants, NN17 9RS, United Kingdom, uk.rs-online.com/web.

5.45   Agilent technologies, 5301 Stevens Creek Blvd, Santa Clara, California, 95051, United States, www.agilent.com/home.

5.46   K. F. Man, K. S. Tang, S. Kwong, *Genetic Algorithm: Concept and Designs*, (Springer, 1999).

5.47   National Instruments Corporation, 11500 N Mopac Expy, Austin, TX 78759-3563, United States, www.ni.com.

5.48   S. Wada, N. Saito, M. Kato, K. Akagawa, A. Takazawa, Y. Hayano, H. Takami, "High Power Yellow Light Generation for Laser Guide Star," in Advanced Solid-State Photonics, paper MB5, (2006).

5.49   J. H. Lock and K. C. Fong, "Retinal Laser Photocoagulation," Med. J. Malaysia **65**, 88-95, (2010).

5.50   H. Yu, K. Wu, H. Zhang, Z. Wang, J. Wang, and M. Jiang, "Nd:YGG crystal laser at 1110 nm: a potential source for detecting carbon monoxide poisoning," Opt. Lett. **36**, 1281-1283 (2011).

5.51   M. F. Garcia-Parajo, M. Koopman, E. M. van Dijk, V. Subramaniam, and N. F. van Hulst, "The nature of fluorescence emission in the red fluorescent protein DsRed, revealed by single-molecule detection," Proc. Natl. Acad. Sci. U.S.A. **98**, 14392-14397 (2001).

5.52   H. M. Pask, P. Dekker, R. P. Mildren, D. J. Spence, and J. A. Piper, "Wavelength-versatile visible and UV sources based on crystalline Raman lasers," Prog. Quantum Electron. **32**, 121–158 (2008).

Chapter 6

Power-scaling and intracavity second harmonic generation of self-Raman lasers using 2nd generation deformable mirror

6.1 Introduction

In chapter 5, the power-scaling of a CW Nd:YVO$_4$ self-Raman laser has been demonstrated using an AO-based feedback control loop system featuring an intracavity bimorph DM, a photodiode sensor and a PC-based control system [6.1]. As the DM used in that work was not coated at any of the Stokes wavelengths (i.e. $\lambda = 1109$ or 1176 nm), the phase correction was only applied on the fundamental laser field during the AO optimisation. Therefore, the efficiency of the Raman laser power-scaling (which was shown as a ~ 18 % output power improvement in the previous chapter) might have been restrained since the first Stokes mode was not directly optimised by adjusting the DM. To correct for both the intracavity fundamental and Stokes fields, a new bimorph DM with high reflectivity coating for the fundamental and Stokes wavelengths was inserted inside either a CW Nd:YVO$_4$ self-Raman laser or a CW frequency-doubled Nd:GdVO$_4$ Raman laser to obtain further Raman output power-scaling.

Section 6.2 describes the characterisation of the new bimorph DMs using the Shack-Hartmann wavefront sensor. Two Raman laser platforms (i.e. a intracavity Nd:YVO$_4$ self-Raman laser and a frequency-doubled Nd:GdVO$_4$ Raman laser) combined with the AO-based feedback control network described in section 5.4 will be introduced in section 6.3. In section 6.4, the

power-scaling for both Raman laser outputs emitting at either the near-infrared or the yellow regime will be presented, while several discussion points for the achieved results will be provided in section 6.5.

6.2 Characterisation of new bimorph DMs

Two new bimorph DMs developed by BAE Systems Advanced Technology Centre [6.2] were utilised in the work presented in this chapter. The general characteristics of the DM diameter, driving mode, driving voltage range, numbers of actuators and their distribution (shown again in Fig. 6.1) were similar to the DM (i.e. final mirror 2) used in chapter 5.
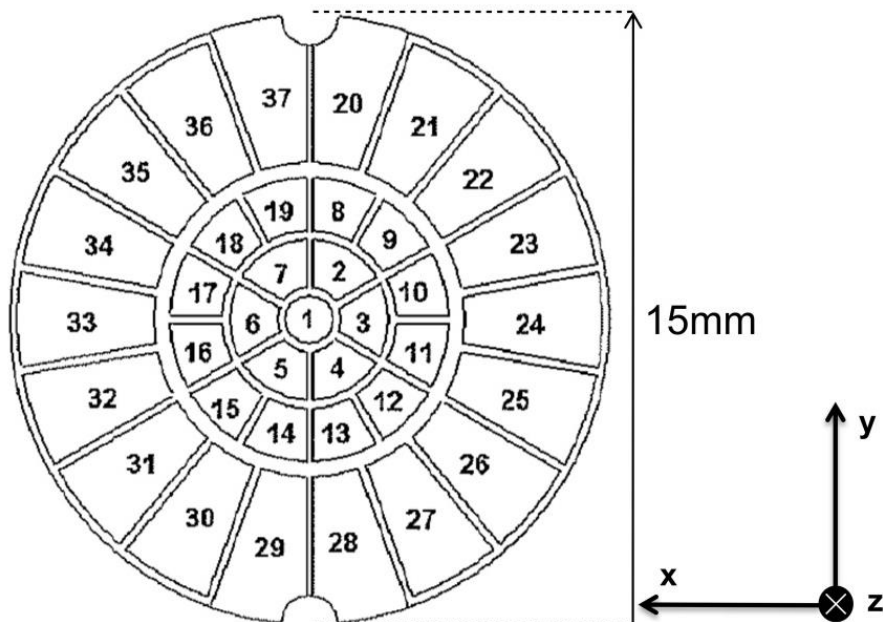
Fig. 6.1 Piezoelectric actuator designation of new DM (looking at the mirror surface when the flexi-circuit is on the right side, driving voltage can be delivered from -50 V to 250 V) [image extracted from chapter 5 Fig. 5.9]

The main difference compared to the previous DM family is the HR coating for both the fundamental and Stokes wavelength (i.e. R > 99.9 % @ λ = 1064 nm and 1170 - 1180 nm) on these new bimorph DMs, which provides the possibility to adjust for both the intracavity fundamental and Stokes fields

during the AO optimisation. The actuation system of the new DMs is similar to the one described in section 5.3, with the focusing power responses of these two new DMs being measured using a Shack-Hartmann wavefront sensor and displayed in Fig. 6.2 and 6.3.
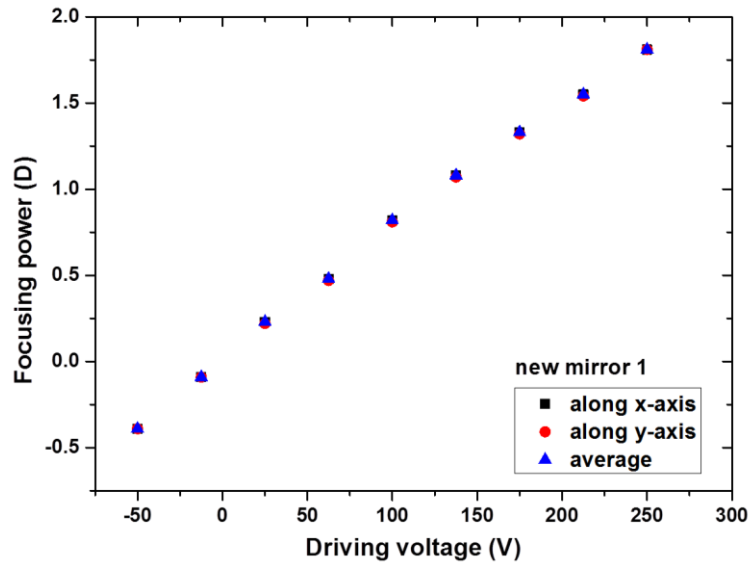
Fig. 6.2 Focusing power response of the new mirror 1 measured using a wavefront sensor
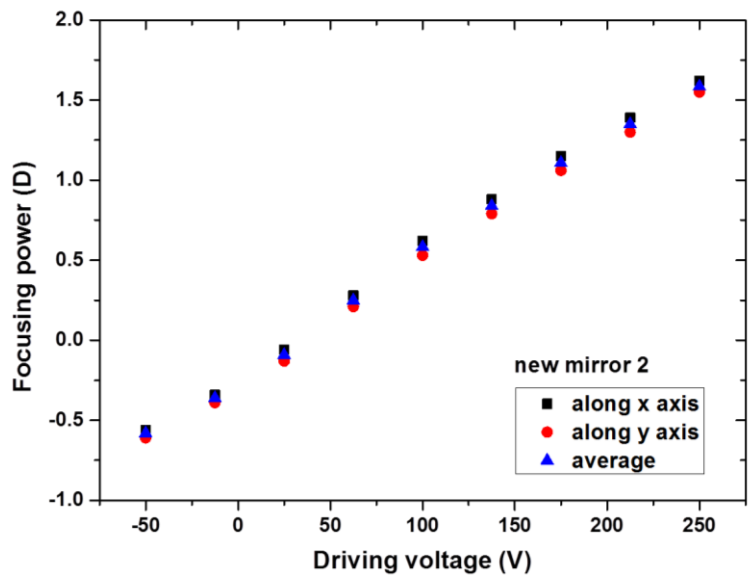
Fig. 6.3 Focusing power response of the new mirror 2 measured using a wavefront sensor

DM/Direction	Minimum Focusing Power (D)	Maximum Focusing Power (D)	Focusing Power Range ΔF (D)
new mirror 1 along the x axis	-0.39	1.81	2.20
new mirror 1 along the y axis	-0.39	1.81	2.20
new mirror 1 average	-0.39	1.81	2.20
new mirror 2 along the x axis	-0.56	1.62	2.18
new mirror 2 along the y axis	-0.61	1.55	2.16
new mirror 2 average	-0.58	1.59	2.17
Final mirror 2 along the x axis	-0.74	1.03	1.77
Final mirror 2 along the y axis	-0.61	1.33	1.94
Final mirror 2 average	-0.68	1.18	1.86

Table 6.1 Summary of the focusing powers of new DMs compared with the final mirror 2

The focusing power responses along the x and y axes are summarised in Table 6.1. The focusing power range and biases of the astigmatism were both improved compared to those of the final mirror 2 that was utilised in chapter 5. This is due to the advanced passive substrate material and manufacturing processes used for these 2nd generation mirrors. Since the new mirror 1 exhibited the longest focusing power range ($\Delta F = 2.2$ D) and nearly no astigmatism effects, it was considered to be the best candidate for the following experiments in this chapter.

6.3 Experimental platforms

6.3.1 AO-controlled intracavity Nd:YVO₄ self-laser system

As shown in Fig. 6.4, the AO-based feedback control network in this work was similar to the one described in section 5.4. It included an intracavity bimorph DM for the wavefront modulation, a photodiode sensor to measure the Raman output intensity as a feedback signal and a PC-based control program featuring a random-search algorithm to evaluate the shape of the DM corresponding to an optimised Raman laser output. It should be noted that no dichroic mirror was used in this platform since the new DM was coated at both the fundamental and the Stokes wavelengths.
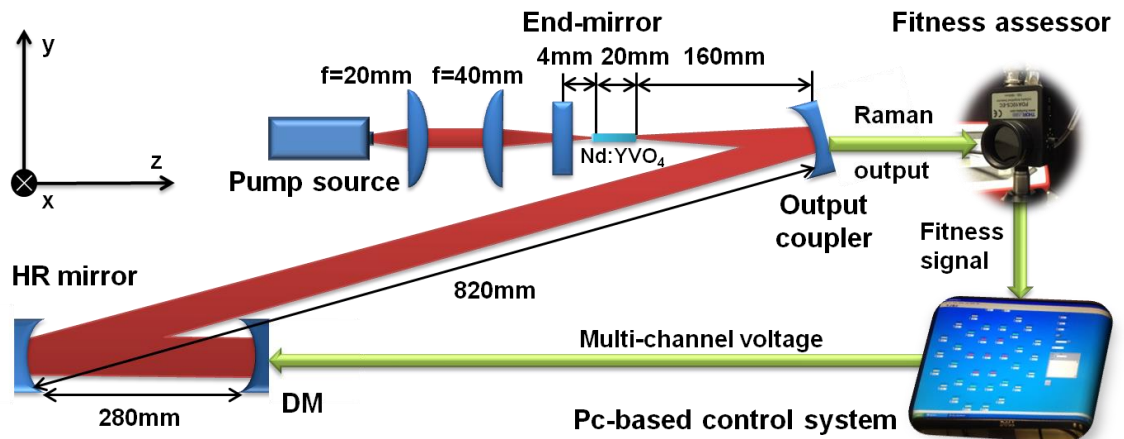
Fig. 6.4 Diagram of the Nd:YVO₄ self-Raman laser incorporating the AO feedback control loop

6.3.2 AO-controlled frequency-doubled intracavity Nd:GdVO$_4$ Raman laser system
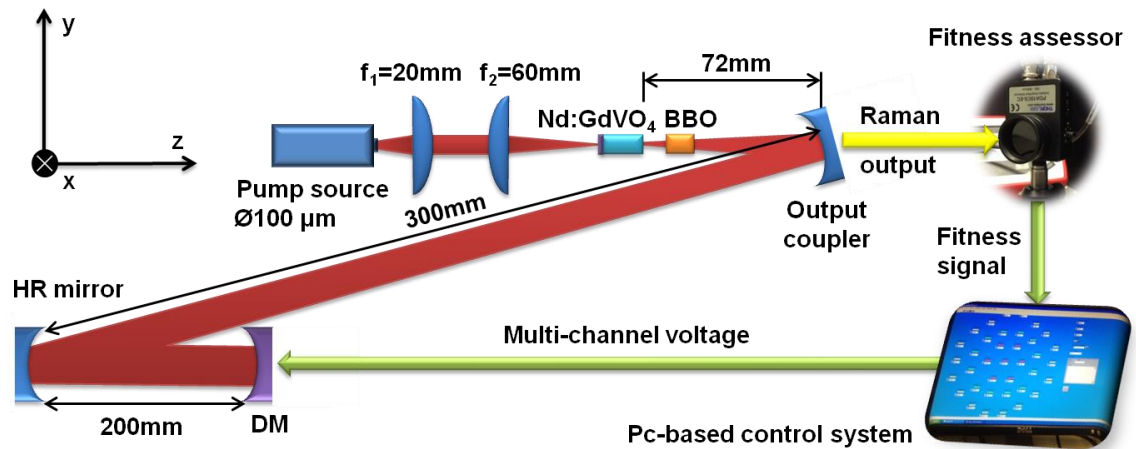
Fig. 6.5 Diagram of the frequency-doubled Nd:GdVO$_4$ Raman laser incorporating the AO feedback control loop

For the investigation of a frequency doubled Raman output, an a-cut, 4 × 4 × 13 mm-long, 0.3 at.% doped Nd:GdVO$_4$ crystal was used as both laser and Raman gain medium as shown in Fig. 6.5. One end surface of the crystal was HR coated at λ = 1064 and 1173 nm and AR coated for λ = 880 nm, while the second end surface was all AR coated for λ = 880, 1064 and 1173 nm. The spontaneous Raman spectrum for the Nd:GdVO$_4$ crystal used in this work was measured using a Renishaw Invia Raman microscope [6.3] with the same operation procedures as described in section 4.2 and displayed in Fig. 6.6.
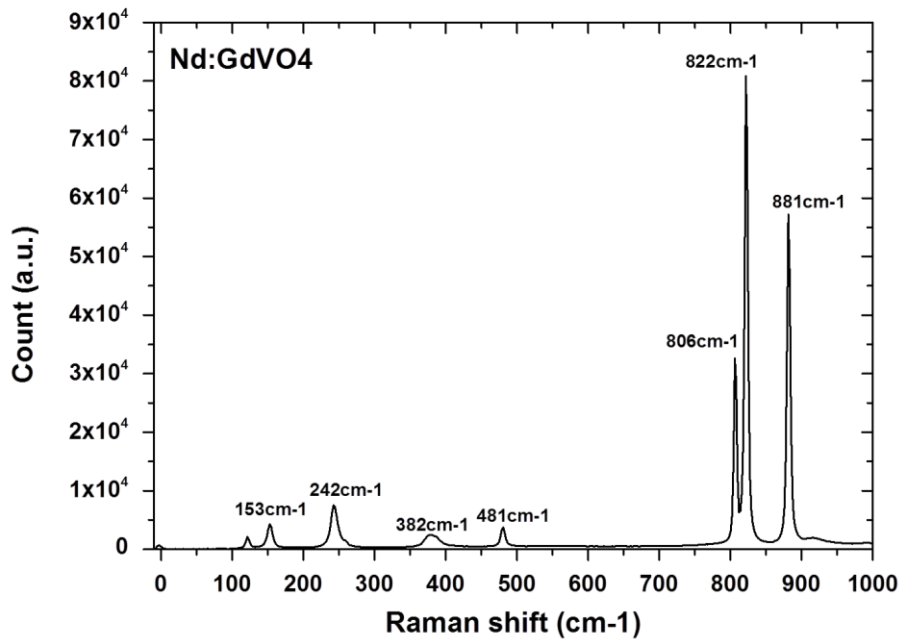
Fig. 6.6 Spontaneous Raman spectrum for the a-cut Nd:GdVO$_4$ crystal

The crystal was end-pumped by a fibre-coupled laser diode (100 µm core diameter, NA ~ 0.22), capable of producing up to 25 W pump power at λ = 880 nm. Two plano-convex lenses were used to obtain a 300 µm pump beam waist at the centre of the self-Raman gain medium. A four-mirror cavity (including the HR coating at the end surface of the Nd:GdVO4 crystal) was constructed with a similar configuration to the one in section 6.3.1. An intracavity 4 × 4 × 7 mm-long BBO doubling-frequency crystal was used to provide an efficient SHG process (see Fig. 6.7). The nonlinear crystal was AR coated at λ = 880, 1064 and 1173 nm and cut for type I critical phase matching (θ = 21:5°, φ = 0). A narrow bandwidth optical filter (λ = 1173 nm) was used to ensure that only the Stokes wavelength could be detected by the photodiode sensor.
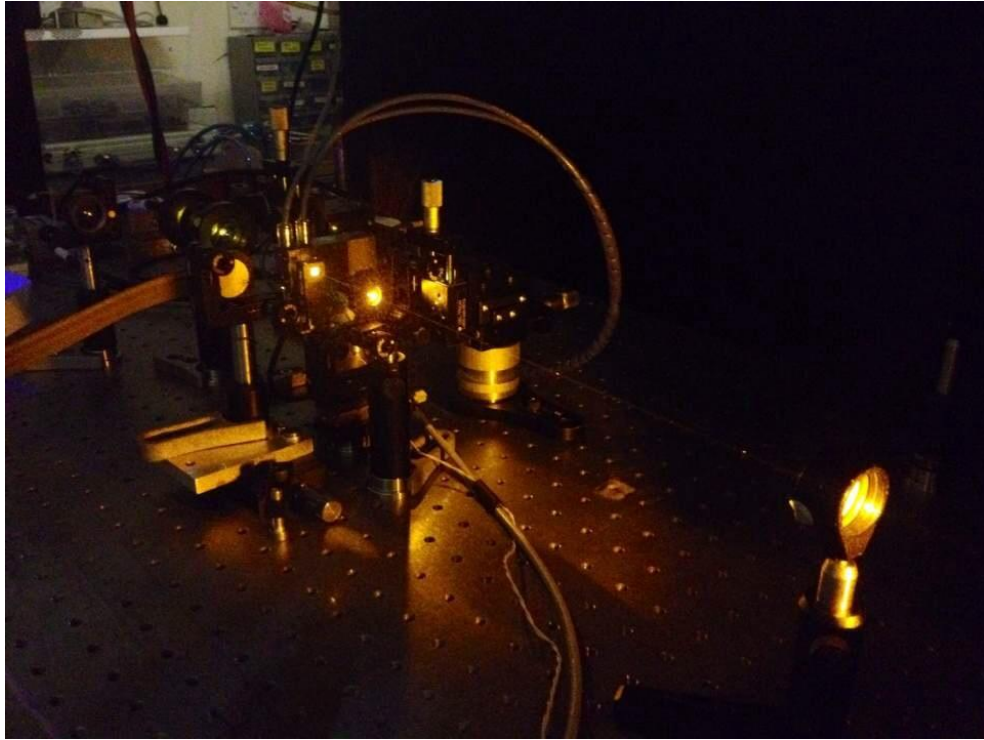
Fig. 6.7 AO controlled intracavity frequency-doubled Nd:GdVO₄ Raman laser operated in the CW regime

6.4 Results

6.4.1 Power-scaling of intracavity Nd:YVO₄ self-Raman laser

First, with 11.2 W of absorbed pump power and no voltage applied to the DM (corresponding to an average focusing power of ~ 0.02 D), the laser cavity of the Nd:YVO₄ self-Raman laser was manually aligned to deliver a maximum Raman output power of 380 mW at $\lambda = 1176$ nm. Then, a pre-optimisation experiment was undertaken with all actuators manually and simultaneously changed to obtain a maximum Raman output power, which was measured at 420 mW with all actuators set at 17.5 V (corresponding to an average focusing power of ~ 0.17 D). The beam quality M^2 factors of the Raman laser output beam were found to be similar for both transverse axes and measured as less than 1.1. The optical power transfer of the Raman laser was measured in Fig. 6.8. The black dots represent the power transfer after a pre-optimisation stage

while the red dot shows the output power obtained after the full AO optimisation described below.
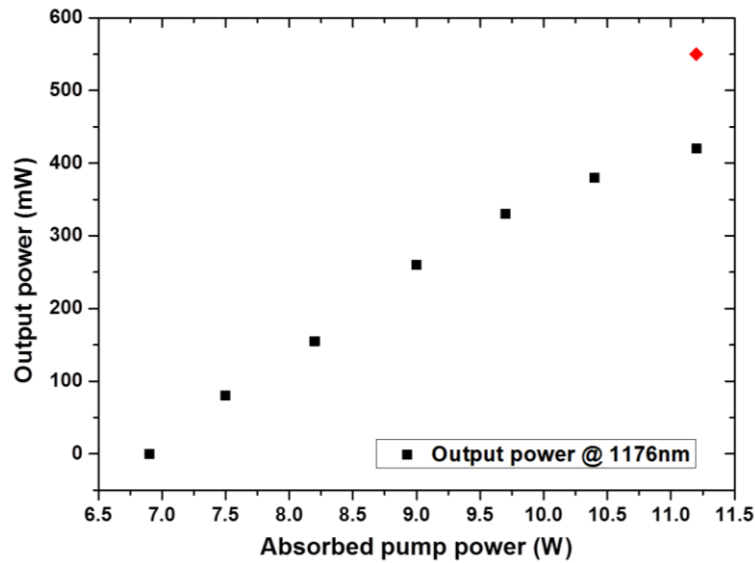
Fig. 6.8 Power transfer of the λ = 1176 nm output (optimisation point for an absorbed laser diode pump power of 11.2 W)

Subsequently, an AO optimisation procedure consisting of 42 actuator changes (which corresponded to a search duration of ∼ 5 min) was automatically run and returned a DM shape enabling a Raman laser output power of 550 mW, showing a power improvement of ∼ 31 %. The beam quality factors M^2 along the x and y transverse axes were both measured as less than 1.1 for the first Stokes laser output. This optimised power value has been added to the power transfer shown in Fig. 6.8 (red dot). The beam profiles of the first Stokes output before and after AO optimisation are both displayed in Fig. 6.9.
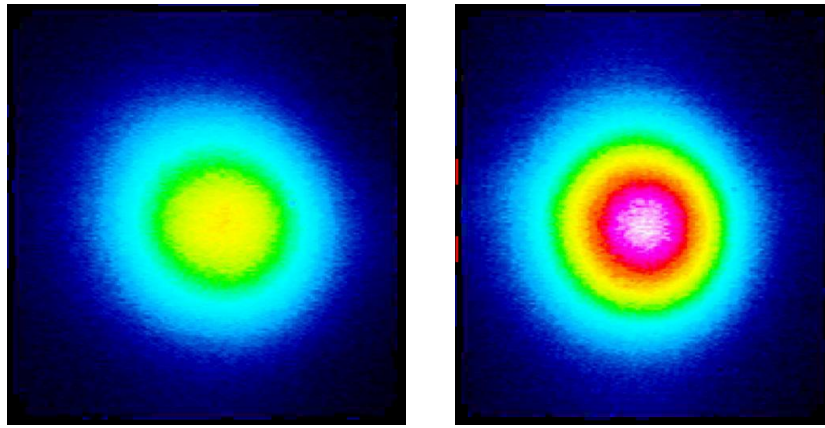
<center>(a)   (b)</center>

Fig. 6.9 *Beam profiles of the λ = 1176 nm outputs before (a) and after (b) AO optimisation*

6.4.2 Power-scaling of intracavity frequency-doubled Nd:GdVO₄ Raman laser

At the initial stage, the laser cavity including the Nd:GdVO$_4$ and BBO crystals was manually aligned with no voltage applied to the DM actuators. This resulted in a maximum yellow Raman output power of 320 ± 20 mW for an absorbed pump power of 11.3 W.
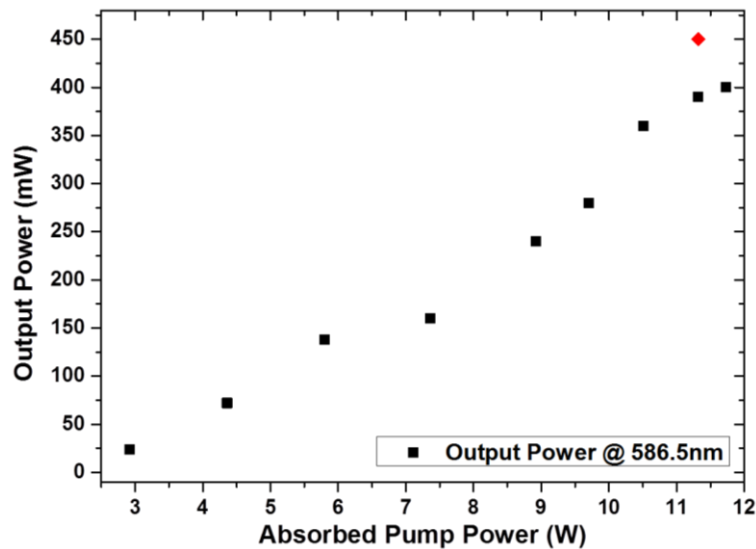
Fig. 6.10 *Power transfer of the λ = 586.5 nm output (optimisation point for an absorbed laser diode pump power of 11.3 W)*

Then, a pre-optimisation experiment was performed whereby all actuators were manually and simultaneously changed to a driving voltage of 25V (corresponding to an average focusing power of ~ 0.23 D). This mirror shape led to a yellow Raman output power of 390 ± 20 mW. The power transfer after this pre-optimisation is shown in Fig. 6.10. An automatic AO optimisation loop was employed at this highest output power, which after approximately 50 actuator changes (which corresponds to a search duration of ~ 7 min) returned an optimum mirror shape delivering a yellow Raman laser output power of 450 ± 20 mW, resulting in a power improvement of ~ 15 %. The beam profile of the first Stokes mode (λ = 1173 nm) was measured from a first Stokes beam leakage after the HR folding mirror and is displayed in Fig. 6.11. A significant beam mode improvement can be observed after the AO loop optimisation.

(a)   (b)
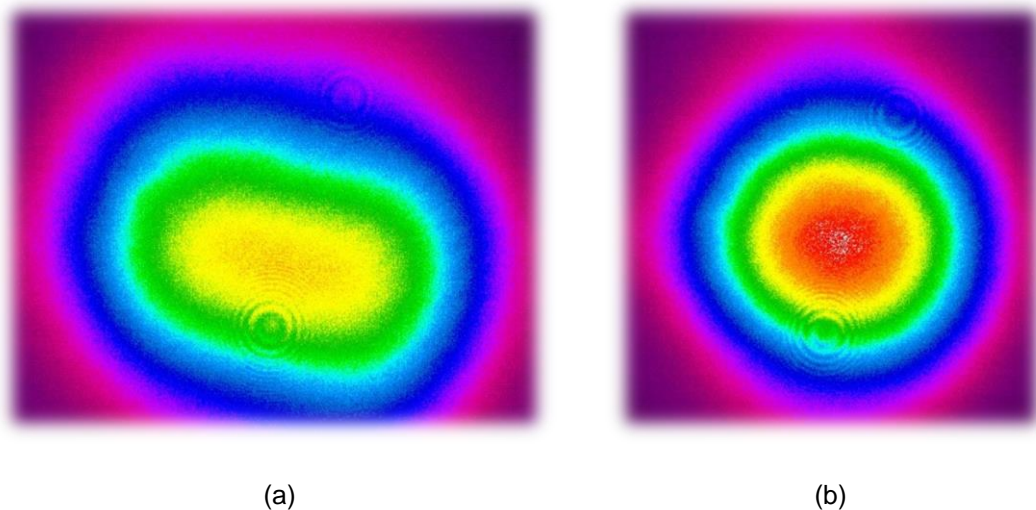
Fig. 6.11 *Beam profile of the λ = 1173 nm outputs before (a) and after (b) AO optimisation*

6.5 Discussions

Several discussion points are presented from these two AO-based experiments.

For the power-scaling of the intracavity Nd:YVO$_4$ self-Raman laser, a distinct rollover could be observed at pump powers above 10.4 W which is due to the strong thermal lens effect within the Nd:YVO$_4$ crystal. After AO optimisation,

the optimised point (red dot in Fig. 6.8) exhibited a linear trend with the output power transfer obtained at lower pump powers. This disappearance of a thermal rollover behaviour shows a significant reduction of the thermal lens effect after the AO-loop optimisation. Most notably, a higher power-scaling enhancement (~ 31 %) was obtained compared with the previous AO optimisations presented in chapter 5 (~ 18 %). This is mainly attributed to the phase correction applied to both the first Stokes and the fundamental fields using the new intracavity DM. A further experiment to investigate the influences of the thermal lens compensation by the intracavity wavefront modulation applied on the fundamental or Stokes field individually will be described in chapter 7.

For the power-scaling of the intracavity frequency-doubled $Nd:GdVO_4$ Raman laser, the power-scaling improvement (~ 15 %) is not as high as the previous results presented in the $Nd:YVO_4$ self-Raman case. This could be mainly explained by the intracavity multi-mode competition in the frequency-doubled Raman laser regime. For the CW intracavity frequency-doubled crystalline Raman laser, a strong output power instability was commonly observed at a relatively high absorbed pump power (> 10 W) due to the complex coupling between different intracavity modes from the fundamental laser conversion, SRS, SHG and SFG [6.4-6.7] and also the complex superposition of thermal lens effects induced by different intracavity modes. This high dynamic regime was even more complicated when the intracavity DM modulation was involved. A ± 20 mW yellow Raman output instability range was measured when the absorbed pump power reached 11.3 W, corresponding to a high output noise of 6.25 %. This amplitude fluctuation can significantly disturb the comparison between each two adjacent feedback signals when the random search algorithm of the AO loop was running. To obtain a relative accurate output power measurement, a longer delay of 1000 ms (compared with the previously chosen delay of 600 ms in chapter 5) between the DM changes and the output power measurement was set during the AO optimisation procedure. Therefore, a small expense of additional correction complexity of the search algorithm and a slightly longer optimisation time has been necessary in this case. It

should be noted that, since the HR coating at the yellow output wavelength was applied on neither the end mirror nor any surface of the self-Raman and frequency-doubling crystals, the yellow Raman laser output was also exiting the laser cavity at the end mirror, with the output power being roughly equivalent to the power measured on the output coupler side. In order to collect as much yellow emission from one direction, an intracavity dichroic mirror (i.e. AR at pump, fundamental and Stokes wavelengths and HR in the yellow regime) could be inserted between the self-Raman and frequency-doubling crystals in further investigations [6.5]. In this way, the amplitude fluctuation may also be alleviated since the dichroic mirror will have the potential to reduce thermal lens effects by preventing the absorption of yellow light within the self-Raman crystal.

6.6 Conclusion

An intracavity adaptive optics system featuring a new DM, which was HR coated for both the fundamental and the Stokes wavelengths, was implemented inside two Raman laser platforms to automatically power-scale the Raman laser outputs. A ~ 31 % power improvement of a CW intracavity Nd:YVO$_4$ self-Raman laser operating at $\lambda = 1176$ nm was achieved using an AO-based feedback control network. The significant enhancement of the power-scaling efficiency, compared with the previous results presented in chapter 5, exhibited the potential of phase correction applied on both the fundamental and the first Stokes fields for alleviating the detrimental effects of thermal lensing in self-Raman lasers.

Moreover, for the first time to the author's knowledge, an AO correction applied in a frequency-doubled Raman laser emitting at the yellow regime was demonstrated. A ~ 15 % power-scaling of a CW frequency-doubled Nd:GdVO$_4$ Raman laser was obtained after the AO loop optimisation. This technique presented the potential to reduce the effects of thermal lensing in crystalline Raman lasers and further push the boundaries of high-power yellow lasers for

astronomy and medical applications [6.8, 6.9]. Further investigations should focus on looking to apply the automatic power-scaling investigations at higher pump powers (> 15 W) using a more advanced search algorithm (i.e. genetic algorithm [6.10]).

6.7 References

6.1   R. Li, M. Griffith, L. Laycock, W. Lubeigt, "Controllable continuous-wave Nd:YVO₄ self-Raman lasers using intracavity adaptive optics," Opt. Lett. **39**, 4762-4765 (2014).

6.2   BAE systems advanced technology centre, Stirling Square, 6 Carlton Gardens, London, SW1Y 5AD United Kingdom, www.baesystems.com.

6.3   RENISHAW apply innovation, New Mills, Wotton-under-Edge, Gloucestershire, GL 12 8JR, United Kingdom, www.renishaw.com.

6.4   J. Lin, H. M. Pask, A. J. Lee, and D. J. Spence, "Study of Amplitude Noise in a Continuous-Wave Intracavity Frequency-Doubled Raman Laser," IEEE J. Quant. Electron. **47**, 314-319 (2011).

6.5   A. J. Lee, H. M. Pask, P. Dekker, J. A. Piper, "High efficiency, multi-Watt CW yellow emission from an intracavity-doubled self-Raman laser using Nd:GdVO4," Opt. Express. **16**, 21958-21963 (2008).

6.6   A. J. Lee, D. J. Spence, J. A. Piper, and H. M. Pask, "A wavelength-versatile, continuous-wave, self-Raman solid-state laser operating in the visible," Opt. Express. **18**, 20013-20018 (2010).

6.7   A. J. Lee, J. Lin, and H. M. Pask, "Near-infrared and orange–red emission from a continuous-wave, second Stokes self-Raman Nd:GdVO4 laser," Opt. Lett. **35**, 3000-3002 (2010).

6.8   S. Wada, N. Saito, M. Kato, K. Akagawa, A. Takazawa, Y. Hayano, H. Takami, "High Power Yellow Light Generation for Laser Guide Star," in Advanced Solid-State Photonics, paper MB5, (2006).

6.9   J. H. Lock and K. C. Fong, "Retinal Laser Photocoagulation," Med. J. Malaysia **65**, 88-95, (2010).

6.10 W. Lubeigt, S. P. Poland, G. J. Valentine, A. J. Wright, J. M. Girkin, and D. Burns, "Search-based active optic systems for aberration correction in time-independent applications," Appl. Opt. **49**, 307-314 (2010).

Chapter 7

Conclusion

The work presented in this thesis demonstrates the development of an advanced controllable solid-state Raman laser operating in either the near-infrared or the visible regime for astronomy and medical applications [7.1, 7.2]. The schematic diagram of the thesis work can be concluded in Fig. 7.1.
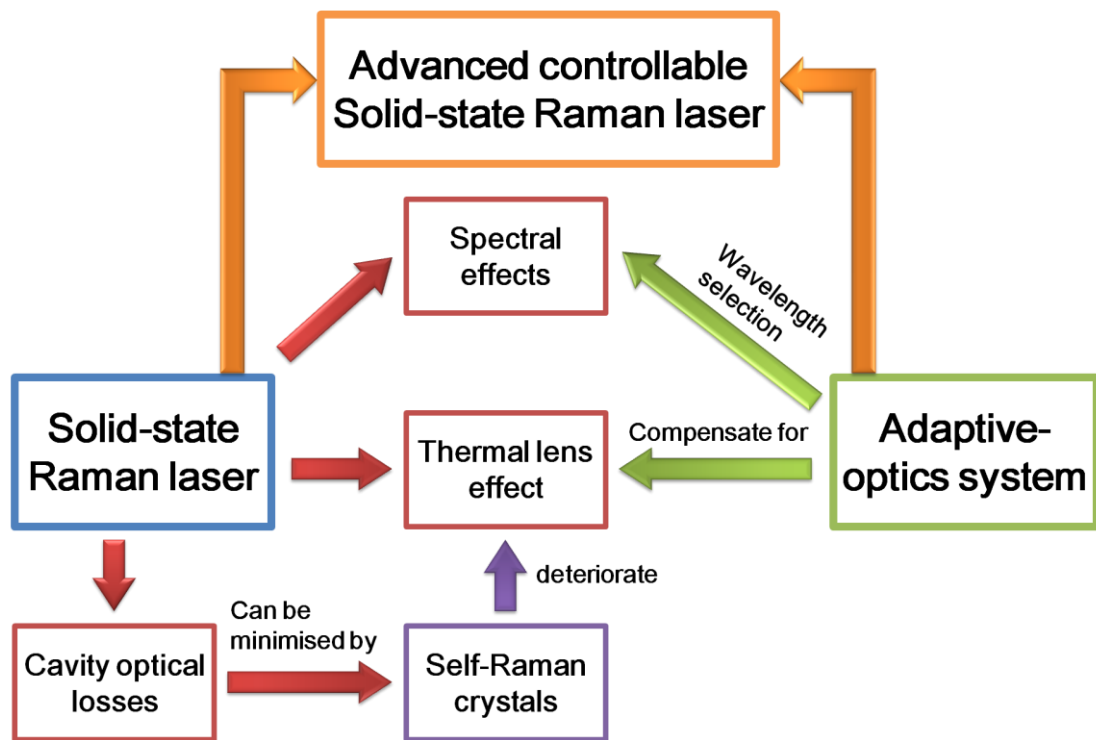
Fig. 7.1 Schematic diagram of the thesis work

As shown in Fig. 7.1, this thesis was entirely focused on dealing with two major issues restricting the output performance of intracavity solid-state Raman laser operating in the CW regime, which are the thermal lens effect and spectral effects.

To minimise the cavity optical losses and provide a simple intracavity Raman laser configuration design, two self-Raman crystals (i.e. Nd:YVO$_4$ and Nd:GdVO$_4$) have been utilised in this thesis. This self-Raman configuration was strongly influenced by the effect of thermal lensing, which therefore represented an ideal test-platform for the investigations. In this thesis the use of an AO-based feedback control loop system is proposed, for the first time to the author's knowledge, to compensate for the strong thermal lens effect inherent within the crystalline self-Raman laser configuration. A series of proof-of-concept experiments were undertaken based on two different self-Raman laser platforms at a relative low pump power (i.e. < 15 W). The power-scaling of CW Raman laser outputs emitting at near-infrared and visible wavebands has been demonstrated through the integrated AO optimisation. It exhibits a great potential to alleviate the detrimental effect of thermal lensing using an automatic intracavity AO correction and open avenues to enable solid-state Raman lasers to reach new output power levels.

Regarding the intracavity Raman spectral effects, several novel CW Raman output lines based on the primary and secondary Raman shifts of Nd:YVO$_4$ have been obtained and characterised for the first time, using different Raman output couplers. Comparing the Raman output performances of different Raman transitions in the same laser configuration has led to the proof that a wider linewidth of the Raman shift may have the potential to improve the Raman conversion efficiency by restricting the spectral broadening effect. Moreover, a wavelength switching between two Raman outputs based on different Raman transitions has been achieved using an intracavity AO modulation which represents the way towards automatic wavelength selectable high power Raman lasers.

7.1 Summary

7.1.1 CW Nd:YVO$_4$ self-Raman lasers based on the 379 cm^{-1} and 893 cm^{-1} shifts

In chapter 4, the first CW Nd:YVO$_4$ self-Raman lasers based on a secondary Raman transition of 379 cm^{-1} were demonstrated in a 2-mirror intracavity Raman laser configuration using different output couplers [7.3].

desired output wavelength	output coupler transmissions (T)	type of output	max output power	M^2 at max output power	absorbed pump power to desired output power conversion efficiency
1109 nm	T = 0.2 % at λ = 1109 nm T > 7 % at λ = 1158 - 1176 nm	1st Stokes output of the 379 cm^{-1} shift	1 W	2.3 along x-axis 3.1 along y-axis	8.4 %
1158 nm	T = 1.2 % at λ = 1158 nm T = 0.1 % at λ = 1109 nm T = 5 % at λ = 1176 nm	2nd Stokes output of the 379 cm^{-1} shift	700 mW	1.2 along x-axis 1.2 along y-axis	5.4 %
1231 nm	T = 2.4 % at λ = 1231 nm T = 0.5 % at λ = 1158 nm T = 0.1 % at λ = 1109 nm T = 2.5 % at λ = 1176 nm	combination of the 379 cm^{-1} shift with the 893 cm^{-1} shift	540 mW	1.2 along x-axis 1.3 along y-axis	5.4 %
1176 nm	T = 1 % at λ = 1176 nm T < 0.4 % at λ = 1109 - 1158 nm	1st Stokes output of the 893 cm^{-1} shift	1.14 W	2.0 along x-axis 2.5 along y-axis	9.3 %

Table. 7.1 Summary of Raman laser output performances at different wavelengths

This was made possible by the use of strongly curved output couplers (i.e. ROC ~ 100 mm) which alleviated the significant thermal lens effect inherent within the self-Raman crystal. All Raman laser output performances based on different Raman transitions were summarised in table 7.1.

Although the Raman gain coefficient of the 379 cm^{-1} shift was measured to be ~ 5 times lower than that of the 893 cm^{-1} shift, no significant discrepancy was shown between the first Stokes Raman conversion efficiency emitting at λ = 1109 nm (~ 8.4 %) and that of the λ = 1176 nm Raman laser (~ 9.3 %). This can be explained by a combination of multiple reasons, including 1) output coupling transitions, 2) the thermal lens effect and 3) the spectral broadening effect.

The strongly curved output coupler used in this work significantly reduced the beam radius of the fundamental transverse mode inside the gain medium and induced a high intracavity power intensity which has the potential to damage the AR coatings of the Nd:YVO$_4$ surfaces. Therefore, a compromised solution between maintaining a good resilience to thermal lensing and the avoidance of coating damage limited the absorbed laser diode pump power level (~ 13 W). Moreover, a strong thermal lens effect, originating due to the simultaneous residual pump loading and the nonelastic nature of SRS occurring within the self-Raman gain medium, also ultimately limits the maximum attainable output powers. This could be enhanced by alleviating the significant thermal lensing by for example changing the pump wavelength from λ = 808 nm to λ = 880 nm. Finally, the Raman laser output performances could be also improved by optimising the reflectivity of the output couplers for each output wavelength.

These lasers represent a first step towards the development of CW Raman lasers emitting at narrowly-spaced green-lime-yellow regions when frequency-doubled, benefiting many applications especially for medicine and bio-photonics [7.4, 7.5].

7.1.2 Intracavity AO control of CW Nd:YVO$_4$ self-Raman laser

In chapter 5, an AO-based feedback control loop including an intracavity bimorph DM, a photodiode sensor and a PC-based control system featuring a random-search algorithm was implemented for the first time inside a Nd:YVO$_4$ self-Raman laser configuration for Raman output power-scaling and wavelength control [7.6]. A total ~ 30 % Raman laser output power improvement (i.e. from 500 mW to 650 mW for an absorbed pump power of 10.8 W) emitting at λ = 1176 nm was achieved via two stages (pre-optimisation and AO optimisation) corresponding to a first-order spherical thermal lensing compensation and a high-order thermal lensing compensation respectively. At the pre-optimisation stage, a near-spherical manually adjustment of the intracavity DM shape was undertaken (from -0.46 D to 0.27 D for the x axis and from -0.38 D to 0.50 D for the y axis) resulting in an power enhancement of the Raman laser output from 500 mW to 550 mW. Then, a further Raman output power-scaling was obtained from 550 mW to 650 mW after an automatic AO-loop optimisation with the subtle changes of the DM shape (mainly due to the astigmatism and coma wavefront correction). From the pre-optimisation to AO optimisation, the beam quality factors M^2 were slightly improved for the fundamental field (from 1.3 to 1.2 for the x axis and from 1.4 to 1.1 for the y axis) while the first Stokes Raman laser outputs were always measured at less than 1.1 due to the Raman beam clean-up effect.

At the pre-optimisation stage, an obvious thermal rollover phenomenon could be observed when the absorbed pump power increased above 10.4 W. However, it was found to be eliminated after the AO optimisation at the same pump level, which presented a significant reduction of the thermal lens effect in the Nd:YVO$_4$ crystal.

However, as the DM used in this work was not coated at any of the Stokes wavelengths (λ = 1109 to 1176 nm), the phase correction was only applied on the fundamental field during the AO optimisation. Therefore, the power-scaling

improvement (i.e. ~ 18 %) might be restrained since the first Stokes mode was not directly optimised through the changes of the intracavity DM.

Moreover, a repeatable wavelength switching between $\lambda = 1109$ nm and $\lambda = 1176$ nm has been demonstrated for the first time by manually changing the intracavity DM shape corresponding to a near spherical surface deformation from concave (~ -0.47 D along the x axis and ~ -0.28 D along the y axis) to flat. The Raman laser output powers were measured to be 275 mW and 340 mW at $\lambda = 1109$ nm and 1176 nm respectively for an absorbed laser diode pump power of 8.2 W. The beam quality factors M^2 along x and y were measured at 1.3 and 1.6 for the $\lambda = 1109$ nm Raman output and both less than 1.1 for the $\lambda = 1176$ nm output.

7.1.3 Power-scaling of CW self-Raman lasers using new intracavity DM

In chapter 6, a new intracavity DM coated at $\lambda = 1063 - 1064$ nm and 1173 - 1176 nm was utilised to control both the fundamental and the Stokes fields during the AO-loop optimisation. It has been tested on two different self-Raman laser platforms, an intracavity Nd:YVO$_4$ self-Raman laser and a frequency-doubled Nd:GdVO$_4$ Raman laser, showing power-scaling for both the Raman laser outputs in the near-infrared ($\lambda = 1176$ nm) and the visible yellow regime ($\lambda = 586.5$ nm). An output beam profile improvement was also observed in both platforms.

Compared with the previous results presented in chapter 5, a higher power-scaling enhancement (total ~ 45 %, from 380 mW to 550 mW for an absorbed pump power of 11.2 W) has been achieved in a similar Nd:YVO$_4$ self-Raman laser configuration than the one utilised in chapter 5. This could be attributed to the dual-phase adjustment applied on both the intracavity fundamental and Stokes fields.

In addition, for the first time to the author's knowledge, a yellow Raman output power improvement has been achieved using an intracavity AO-loop optimisation with a total power-scaling efficiency of ~ 41 % (from 320 mW to 450 mW for an absorbed pump power of 11.3 W). It represents the potential to significantly compensate for the detrimental thermal lens effect and open avenues which will enable crystalline Raman lasers to reach new output power levels. Due to the highly dynamic intracavity competition between several nonlinear effects (i.e. SRS, SFG and SHG) an output power instability of ~6% was observed. This instability can potentially be reduced in future investigations using an intracavity dichroic mirror to prevent the visible, yellow, laser field from entering the self-Raman gain medium and therefore reduce mode competition in it.

7.2 Future work

While a series of "proof-of-principle" experiments having been undertaken which demonstrated a successful implementation of intracavity AO techniques inside self-Raman laser configurations for solid-state Raman output power-scaling and wavelength selection, there still remain several scopes in either theoretical or experimental investigations for the future work.

7.2.1 Investigation of thermal lensing properties in self-Raman lasers

Understanding the behaviour of thermal lensing in self-Raman lasers is crucially important to power-scale crystalline Raman laser outputs. However, it is difficult to characterise the effect since the thermal lensing occurring within the self-Raman crystal is a highly dynamic and complex effect. Intracavity AO techniques can be a desired "tool" to find out how intracavity phase changes

affect the thermal lensing properties, which is vital for the thermal lensing compensation.
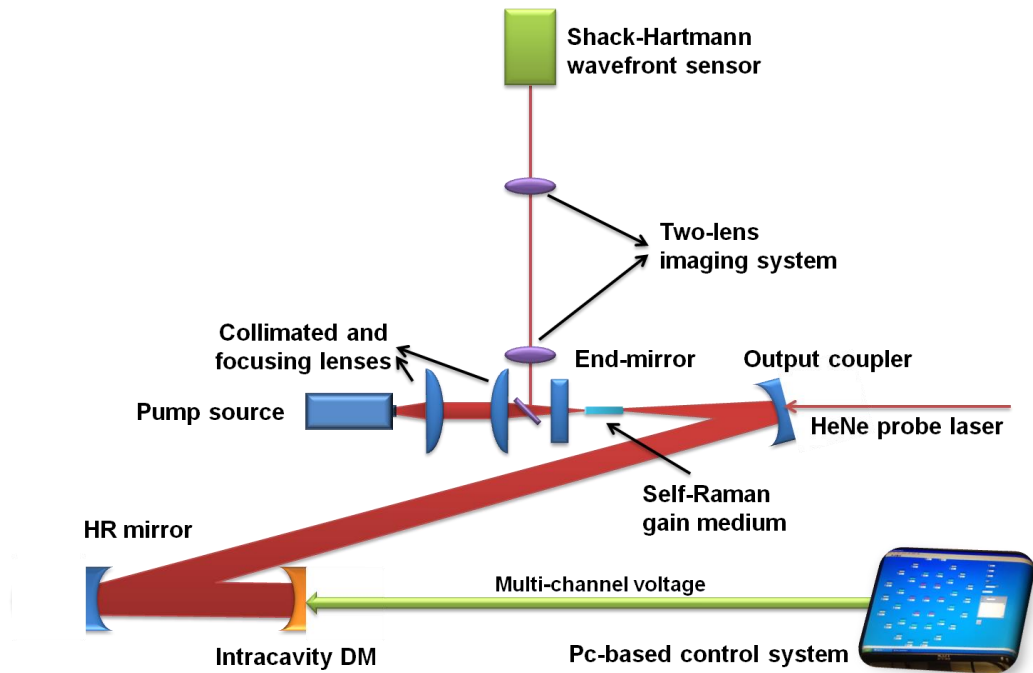
Fig. 7.2 *Schematic diagram of the experimental set-up for monitoring the thermal lensing within the self-Raman laser gain medium*

To achieve that, a measurement system for monitoring the variation of the thermal lensing in real-time during laser operating is required. The Shack-Hartmann wavefront sensor measurement system described in chapter 5 to measure the ROC of DMs can be considered for application in this experiment. As shown in Fig. 7.2, a HeNe probe beam passes through the self-Raman gain medium from the outside of the output coupler. The wavefront after the thermal lens effect (assumed to be occurring in the middle of the self-Raman crystal) will then be re-imaged on the Shack-Hartmann wavefront sensor via a pair of imaging lenses. Therefore, the variation of thermal lens properties can be described through the measured Zernike Polynomials in the Shack-Hartmann wavefront sensor, corresponding to each phase modulation change by the intracavity DM.

A further investigation could even consider the use of two intracavity DMs (see Fig. 7.3).
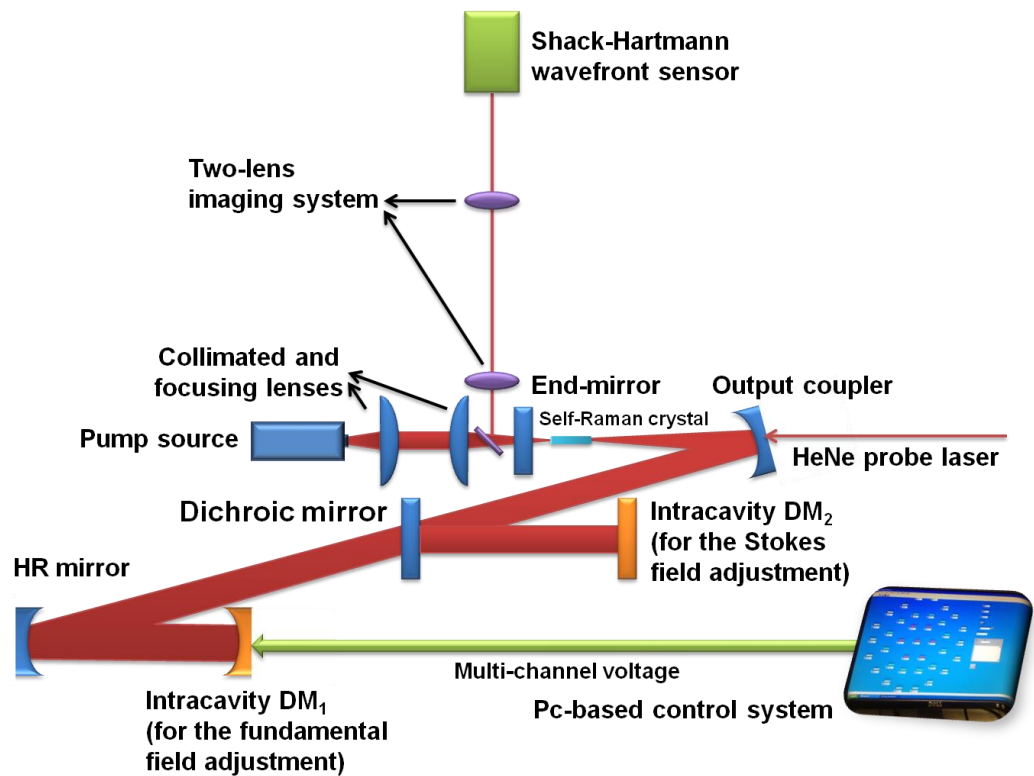
Fig. 7.3 *Schematic diagram of the experimental set-up for the separate intracavity phases adjustment*

With this configuration it could be possible to modulate the spatial and spectral properties of the fundamental or the Stokes fields separately by using different DMs. This could have the potential to reveal how different intracavity modes affect the properties of thermal lensing and the Raman laser output performance, which may benefit the current analytic model research on CW intracavity Raman lasers [7.7].

7.2.2 AO technique implementation in different types of laser sources

7.2.2.1 AO optimisation for a wavelength-versatile CW self-Raman laser

In chapter 6, an automatic AO-loop optimisation in an intracavity frequency-doubled Nd:GdVO$_4$ self-Raman laser emitting in the yellow regime ($\lambda = 586.5$ nm) has been demonstrated. More visible Raman lines can be accessed in the same configuration by phase-matching the nonlinear crystal for SHG or sum-frequency-generation of the fundamental and/or first Stokes wavelengths. However, with the output wavelength tuning between different lines a decreased Raman output performance compared to the optimisation point would occur due to the spatial and spectral variation within different intracavity laser modes. Nevertheless it could be possible to automatically correct for this change using a further intracavity AO optimisation, which exhibits the potential to further push the boundaries of high-power Raman lasers operating in a multi-visible spectra produced in one laser cavity.

7.2.2.2 AO optimisation for Stimulated Polariton Scattering (SPS) THz laser source

As described in [7.8], a crystalline laser source based on SRS and SPS nonlinear optical processes provides an attractive potential to generate frequency-tunable CW THz radiation at room temperature. The schematic diagram of a possible experimental set-up is displayed in Fig. 7.4.
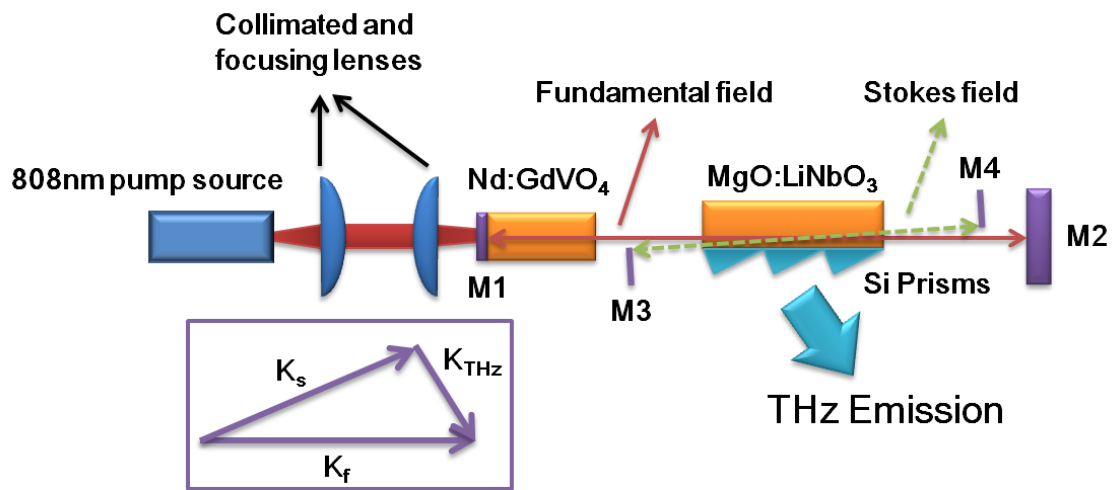
Fig. 7.4 Intracavity coupled THz SPS configuration. The wavevectors representing the interaction of the fundamental (K_f), Stokes (K_s) and THz fields (K_{THz}) [image extracted from 7.8]

In this system, a 2-mirror (M1 and M2) Nd:GdVO$_4$ cavity was constructed around the bottom surface of a MgO:LiNbO$_3$ nonlinear crystal to produce the fundamental laser field. Then, a near-infrared Stokes field can be generated via the SPS process in the 2-mirror Stokes cavity (M3 and M4). Simultaneously, the polariton field was also generated corresponding to an output frequency range between 1 and 4 THz and emitted from the Si prisms at an angle that satisfies the conservation of momentum of the fundamental, Stokes and polariton fields.

The main limitation of power-scaling the THz output is again due to the strong thermal lens effect inherent within the Nd:GdVO$_4$ crystal, which leads to a significant instability of the fundamental field. Moreover, a strong distortion of the fundamental beam profile was also observed because of the free-carrier-induced photorefractive effects within the MgO:LiNbO$_3$ crystal. Both of these undesired issues represent a significant potential to implement AO techniques inside SPS lasers to optimise the output performance of the THz generation for a wide range of applications, especially in THz imaging and spectroscopy [7.9-7.11].

7.3 References

7.1   S. Wada, N. Saito, M. Kato, K. Akagawa, A. Takazawa, Y. Hayano, H. Takami,"High Power Yellow Light Generation for Laser Guide Star," in Advanced Solid-State Photonics, paper MB5, (2006).

7.2   J. H. Lock and K. C. Fong, "Retinal Laser Photocoagulation," Med. J. Malaysia **65**, 88-95, (2010).

7.3   R. Li, R. Bauer, and W. Lubeigt, "Continuous-Wave Nd:YVO$_4$ self-Raman lasers operating at 1109 nm, 1158 nm and 1231 nm," Opt. Express. **21**, 17745-17750 (2013).

7.4   H. Yu, K. Wu, H. Zhang, Z. Wang, J. Wang, and M. Jiang, "Nd:YGG crystal laser at 1110 nm: a potential source for detecting carbon monoxide poisoning," Opt. Lett. **36**, 1281-1283 (2011).

7.5   M. F. Garcia-Parajo, M. Koopman, E. M. van Dijk, V. Subramaniam, and N. F. van Hulst, "The nature of fluorescence emission in the red fluorescent protein DsRed, revealed by single-molecule detection," Proc. Natl. Acad. Sci. U.S.A. **98**, 14392-14397 (2001).

7.6   R. Li, M. Griffith, L. Laycock, W. Lubeigt, "Controllable continuous-wave Nd:YVO$_4$ self-Raman lasers using intracavity adaptive optics," Opt. Lett. **39**, 4762-4765 (2014).

7.7   D. J. Spence, "Spatial and Spectral Effects in Continuous-Wave Intracavity Raman Lasers," IEEE J. Sel. Topics Quantum Electron. **21**, 1400108 (2015).

7.8   A. J. Lee and H. M. Pask, "Continuous wave, frequency-tunable terahertz laser radiation generated via stimulated polariton scattering," Opt. Lett. **39**, 442-445 (2014).

7.9   A. J. Fitzgerald, E. Berry, N. N. Zinovev, G. C. Walker, M. A. Smith and J. M. Chamberlain, "An introduction to medical imaging with coherent terahertz frequency radiation," Phys. Med. Biol. **47**, 67-84 (2002).

7.10   J. F. Federici, B. Schulkin, F. Huang, D. Gary, R. Barat, F Oliveira and D. Zimdars, "THz imaging and sensing for security applications—explosives, weapons and drugs," Semicond. Sci. Technol. **20**, 266-280 (2005).

7.11   X. Wang, W. Sun, Y. Zhang, "A novel normal reflection terahertz spectrometer," Optik **121**, 1148-1153 (2010).

Publications

Journal Publications

[1] R. Li, R. Bauer, and W. Lubeigt, "Continuous-Wave Nd:YVO$_4$ self-Raman lasers operating at 1109 nm, 1158 nm and 1231 nm," Optics Express **21**, (2013).

[2] R. Li, M. Griffith, L. Laycock, and W. Lubeigt, "Controllable continuous-wave Nd:YVO$_4$ self-Raman lasers using intracavity adaptive optics," Optics letters **39**, (2014).

[3] L. Li, R. Li, W. Lubeigt, and D. Uttamchandani, "Design, simulation and characterisation of a bimorph varifocal micromirror and its application in an optical imaging system," IEEE Journal of Microeletromechanical Systems **22**, (2013).

Conference Publications

[1] R. Li, R. Bauer, and W. Lubeigt, "Continuous-Wave Nd:YVO$_4$ self-Raman lasers based on the 379 cm^{-1} and 893 cm^{-1} shifts," Advanced Solid-state Lasers Congress 2013, paper ATu3A.41, Optical Society of America, Washington (2013).

[2] R. Li, M. Griffith, L. Laycock, and W. Lubeigt, "Power-scaling continuous-wave solid-state Raman lasers using intracavity adaptive optics," paper SM2F.4, CLEO 2014, Optical Society of America, Washington (2014).

[3] R. Li, M. Griffith, L. Laycock, and W. Lubeigt, "Power-scaling a continuous-wave Nd:YVO$_4$ Raman lasers using intracavity adaptive optics," paper 14675, Photon 14 conference, Institute of Physics, London (2014).

[4] R. Li, M. Griffith, L. Laycock, and W. Lubeigt, "Intracavity adaptive optics control of continuous-wave Nd:YVO$_4$ self-Raman lasers," Advanced Solid-state Lasers Congress 2014, paper AM5A.34, Optical Society of America, Washington (2014).

[5] R. Li, A. J. Lee, H. M. Pask, and W. Lubeigt, "A continuous-wave frequency-doubled Nd:GdVO$_4$ Raman laser at 586.5 nm using intracavity adaptive optics," paper CA_7_4, European Conference on Lasers and Electro-Optics Conference, Optical Society of America, Munich (2015).

[6] L. Li, R. Li, W. Lubeigt, and D. Uttamchandani, "Thermoeletrically-controlled varifocal micromirror for near aberration free imaging, " IEEE Optical MEMS and Nanophotonics 2013, paper MM-S2.7, Kanazawa (2013).

[7] R. Bauer, W. Lubeigt, R. Li, C. Clark, E. McBrearty, and D. Uttamchandani, "Power-scaling MEMS Q-switched solid-state lasers", Advanced Solid-state Lasers Congress 2013, paper ATu3A.39, Optical Society of America, Washington (2013).